Polarization observables for single and double charged pion photo-production with polarized HD target

Peng Peng
Houma, Shanxi, China

M. S., Xi'an Jiaotong University, 2007
B. S., Xi'an Jiaotong University, 2004

A Dissertation presented to the Graduate Faculty
of the University of Virginia in Candidacy for the Degree of
Doctor of Philosophy

Department of Physics

University of Virginia
December, 2015

Abstract

A complete picture of hadron spectroscopy is important for the understanding of the degrees of freedom inside the hadron in the medium energy region. This study will bridge the gap between the hadron/pion picture in the low-energy region and the quark/gluon picture in the high-energy region. However, while only the low-energy resonances have been well identified, the high-energy excited states are broad and overlapping, so can only be disentangled with Partial Wave Analysis (PWA). The present PWA still has ambiguities due to the lack of experimental data, especially data using a polarized neutron target.

The G14 experiment in Hall B of Jefferson Lab was designed and conducted to measure polarization observables from both polarized proton and neutron targets. The reaction channels studied in this dissertation are the single pion ($\gamma n \to p\pi^-$) and double pion ($\gamma p \to p\pi^+\pi^-$, and $\gamma n \to n\pi^+\pi^-$) photo-production. The E asymmetry in the single pion channel shows good agreement at lower energy with the prediction from two PWA groups: SAID from George Washington University and Bonn-Gatchina from University of Bonn. At higher energy, there is a big discrepancy between the experimental result and PWA prediction. This result is significant since the "missing resonances" are in this higher energy region. The polarization observables($I^{\odot}, P_z, P_z^{\odot}$) in the two-pion channel with polarized neutron target are the first results that have been measured, and these three observables($I^{\odot}, P_z, P_z^{\odot}$) in the two-pion channel with polarized proton target are compared with a previous CLAS experiment (G9a). The results are essential for the study of high-energy excited states since this channel has a bigger cross section than the single pion channel in the high-energy region.

Acknowledgments

First of all, I would like to thank my adviser, Blaine Norum, for his guidance in my PhD study, and for providing me with great freedom to pursue my ideas. I really appreciate his help to get me in his group in my fourth year, and to introduce me to the G14 experiment and the HDice group at Jefferson Lab. During the time I was doing the experiment and the data analysis at Jefferson Lab, he drove to the Lab almost every week to have a meeting with me, this helped me to keep a good pace with my project. During the last year, when I moved back to UVa, Blaine and I were working together on the explanation of an unexpected peak in the missing momentum plot. Even though the peak turned out to be caused by the gaps of the CLAS detectors, his way to pursue an explanation for the peak and his attitude to be careful for a new discovery have taught me a very good lesson of how to do research. I would like to thank Donal Day and Kent Paschke for serving on my thesis committee, and for their precious comments on my thesis. I also would like to thank Nilanga Liyanage and Krishni Wijesooriya for giving me a chance to work with them on nuclear physics and medical physics.

None of this work would have been possible without the help from the people in G14 collaboration and the HDice group. I would like to thank my supervisor at Jefferson Lab, Andy Sandorfi. His knowledge of nuclear physics and polarized target have helped me a lot in my PhD project. I have also been inspired by his project management skill and his passion for wine and coffee. I would like to thank Xiangdong Wei, Tsuneo Kageya, Michael Lowry, Vivien Laine, Alexandre Deur, and Gary Dezern from the HDice group for their help on my analysis of the target polarization. I would like to thank Franz Klein, Reinhard Schumacher, Annalisa D'Angelo, Eugene Pasyuk, Igor Strakovsky and Winston Roberts for their help in my data analysis. I am indebted to my officemate, Charles Hanretty, who gave me a lot of guidance when I started doing the data analysis, and I really enjoyed the beer he brewed. I would like to thank Dao Ho, Irene Zonta, and Natalie Walford for the valuable discussions during the G14 experiment analysis. My thanks also go to the Hall B staffs and technicians for their help in the G14 experiment. I also would like to thank the professors in the Physics department at UVa, who have taught me, and the staff members, especially Dawn Shifflett, who have supported me in my PhD study. I also would like to thank Yi Qiang, Jie Liu and Wenze Xi for their friendship, which makes my life at Newport News much fun.

Lastly but most importantly, I would like to thank my parents: Tianfu Peng and Xiaoxia Shi, for their unconditional love and limitless support.

Contents

List of Figures

xii

List of Tables

Chapter 1

Introduction

The science of Physics we know so far tells us there are four fundamental forces in nature: gravitational, electromagnetic, strong and weak. Depending on the scale and the speed of the system we are studying, there are four realms of mechanics: classical mechanics, relativistic mechanics, quantum mechanics, and quantum field theory. The hadron spectroscopy studies the system with quarks and gluons, which are small and fast, thus it falls under the category of quantum field theory. The quarks carry color charges, and interact with each other by the strong force. The strong interaction is mediated by gluons; the theory for this mechanism is referred as quantum chromodynamics (QCD). The classification of quarks, and how quarks bind into different hadrons are described by the quark model.

1.1 The Quark Model

The quark model can be described in several levels: from the simple dynamics-free picture of particles as bound states of quarks and anti-quarks, to models with dynamics described by phenomenological theories, to models derived directly from QCD. For the simplest case, the properties of hadrons are derived from the additive quantum numbers of quarks. Table 1.1 shows the properties for the six flavors of quarks.

Flavor	Down	Up	Strange	Charm	Bottom	Top
Symbol	d	u	s	c	b	t
Charge (e)	-1/3	+2/3	-1/3	+2/3	-1/3	+2/3
Mass (MeV/c^2)	3 - 7	1.5 - 3.0	95 ± 25	1250 ± 90	4200 ± 70	$1.725 \pm 0.023 \times 10^5$
I (isospin)	1/2	1/2	0	0	0	0
I_z	-1/2	1/2	0	0	0	0
S (strangeness)	0	0	-1	0	0	0
C (charm)	0	0	0	+1	0	0
B (bottomness)	0	0	0	0	-1	0
T (topness)	0	0	0	0	0	+1

Table 1.1: Properties for the six flavors of quarks.

Quarks are spin 1/2 fermions with positive parity, and each quark has a baryon number

1/3. The Gell-Mann-Nishijima formula relates the quantum numbers for quarks:

$$Q = I_z + \frac{\mathbf{B} + S + C + B + T}{2}, \tag{1.1}$$

where $\mathbf{B}$ is the baryon number. There is also a "hidden" color quantum number for quarks, which has three values: red, green and blue. It is "hidden" in the sense that all the particles or quark bound states are colorless (color singlets). Each quark has its antiquark with the quantum numbers having the opposite sign. In the quark model, the bound states of quarks are referred as hadrons, and there are two kinds of hadrons: mesons and baryons, in which a meson has a two quark configuration with baryon number $\mathbf{B} = 0$ and a baryon has a three quark configuration with baryon number $\mathbf{B} = 1$ [1].

Mesons

Mesons are bound states of quarks and antiquarks ($q\bar{q}'$). They are classified using J^{PC} multiplets, where $J = L + S$ is total angular momentum, $P = (-1)^{l+1}$ is the parity, $C = (-1)^{l+s}$ is the charge parity. Since quarks are spin 1/2 particles, $1/2 \otimes 1/2 = 0 \oplus 1$ gives states with total spin $S = 0$ or $S = 1$. For orbital angular momentum $l = 0$, there are two states: pseudo-scalars (0^{-+}) and vectors(1^{--}) as in Figure 1.1. $l = 1$ has scalars (0^{++}), axial vectors (1^{++} and 1^{+-}), and tensors (2^{++}). Mesons with exotic quantum numbers are predicted by QCD, which take into account gluon excitations. The "GlueX" experiment conducted in Hall D at Jefferson Lab was designed to search for these states.
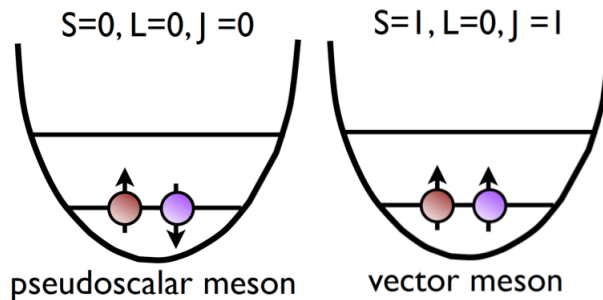
Figure 1.1: Spin states of mesons.

Considering only the three lightest quarks: up, down and strange, the three flavors form an approximate SU(3) group. Mesons can be classified in the Eightfold Way using the following decomposition:

$$3 \otimes 3 = 8 \oplus 1. \tag{1.2}$$

The nine states (nonet) are made of a octet and a singlet, as shown in Figure 1.2.

Baryons

Baryons are bound states of three quarks. The total state functions should be antisymmetric, since baryons are fermions:

$$|qqq>_A = |color>_A \times |space, spin, flavor>_S, \tag{1.3}$$

(a) Pseudo-scalar mesons ($J^{PC} = 0^{-+}$). (b) Vector mesons ($J^{PC} = 1^{--}$).
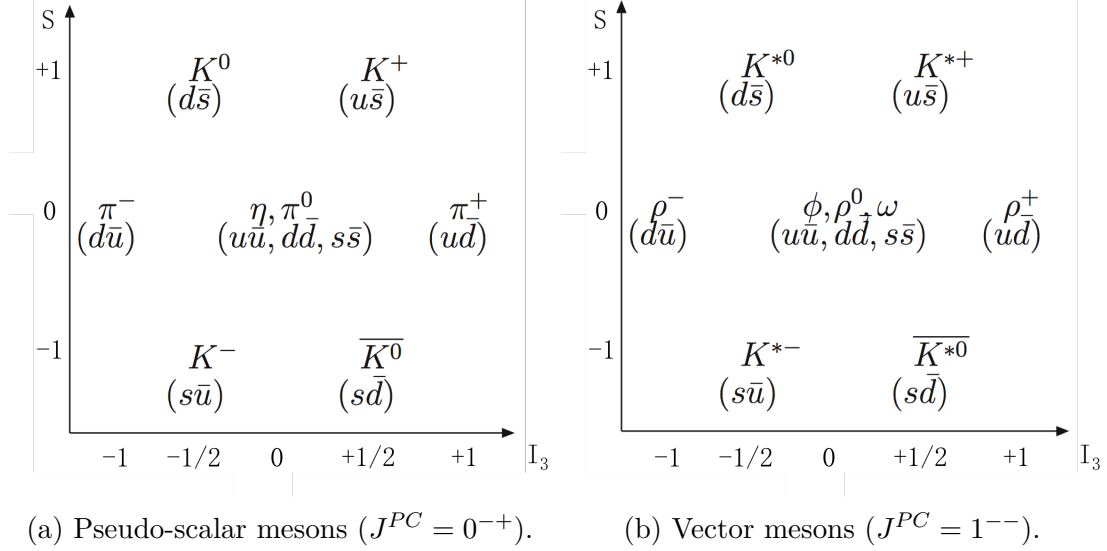
Figure 1.2: Nonets for pseudo-scalar and vector mesons. The y-axis is the strangeness, the x-axis is z-component of isospin.

where the subscripts S and A are indicators for symmetric or antisymmetric functions. The color part is an SU(3) singlet (antisymmetric); this makes the | space, spin, flavor > part symmetric. When decomposing baryons in the Eightfold way, it's more clear to use the flavor-spin SU(6) group as below:

$$6 \otimes 6 \otimes 6 = 56_S \oplus 70_M \oplus 70_M \oplus 20_A, \tag{1.4}$$

where subscripts S, M, A represent symmetric, mixed-symmetric, or antisymmetric functions. For ground state particles ($l = 0$), the space part is symmetric, this makes the | spin, flavor > part symmetric, so only 56_S states in the above equation are allowed, the 70_M and 20_A states require nonzero orbital angular momenta. 56_S can be further decomposed into flavor SU(3) multiplets as:

$$56 = 10^4_{3/2} \oplus 8^2_{1/2}, \tag{1.5}$$

where $10_{3/2}$ is a spin 3/2 baryon decuplet, $8_{1/2}$ is a spin 1/2 baryon octet as in Figure 1.3.

So far, we only looked at the classification of the ground states of the hadrons (mesons and baryons), there is no information about their excited states and the mass values for these states in the simple quark model. This information can be obtained in the more advanced quark models, which consider the dynamics between quarks. The quark model considering the dynamics will be introduced in the next section, this model is often referred as the constituent quark model (CQM).

1.2 Baryon Spectroscopy

Experimental results from deep inelastic scattering tell us that the nucleon has a more complicated structure than the three quark configuration. Other than the three valence

(a) S=1/2 baryon octet.

(b) S = 3/2 baryon decuplet.
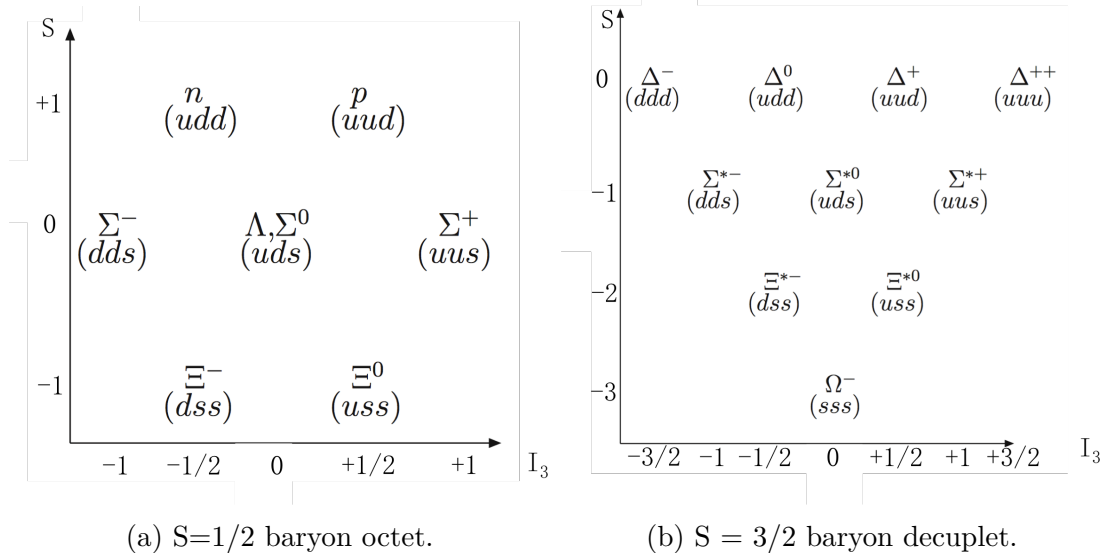
Figure 1.3: Octet and decuplet for baryons. The y-axis is the strangeness, the x-axis is the z-component of isospin.

quarks, sea quarks (quark-antiquark pair) and gluon fields also play important roles. A natural question to ask is: what are the effective degrees of freedom for this complicated system? As in atomic physics, the degrees of freedom for the system can be revealed in the spectrum of the excited states.

The spectrum of strongly-interacting particles is predicted by the QCD Lagrangian:

$$L_{QCD} = \hbar\phi_i[i(\gamma^\mu D_\mu) - m\delta_{ij}]\phi_j - \frac{1}{4}G^a_{\mu\nu}G^{\mu\nu}_a, \tag{1.6}$$

where $\phi_i(x)$ is the quark field, and $G^a_{\mu\nu} = \partial_\mu A^a_\nu - \partial_\nu A^a_\mu + gf^{abc}A^b_\mu A^c_\nu$ is the gluon field strength tensor, A^a_ν are the gluon fields, m and g are the quark mass and coupling constant. In the renormalized theory, the QCD coupling decreases as energy increases as shown in Figure 1.4. This phenomenon is referred as "asymptotic freedom".

The consequence of "asymptotic freedom" is that only at very high energy, the Lagrangian equation can be solved in a perturbative way. In the energy region of nucleon resonances, there is no analytic solution using a first principle calculation. Two methods have been developed to solve this problem. One method is to use phenomenological models, whose ingredients are abstracted from QCD, or from the low-energy limit of QCD (chiral Lagrangians). The most successful phenomenological models in making predictions of hadron properties are constituent quark models (CQMs). The other method is to use a numerical method (Lattice QCD).

1.2.1 Constituent Quark Models

In constituent quark models, the three constituent quarks are the only relevant degrees of freedom in the hadron. The constituent quark can be viewed as a low momentum "current quark" dressed with a cloud of low momentum gluons. It has a effective mass of about one third of the nucleon mass (350 - 400 MeV). Based on different models to describe the effective interaction between the constituent quarks, several versions of the constituent

4
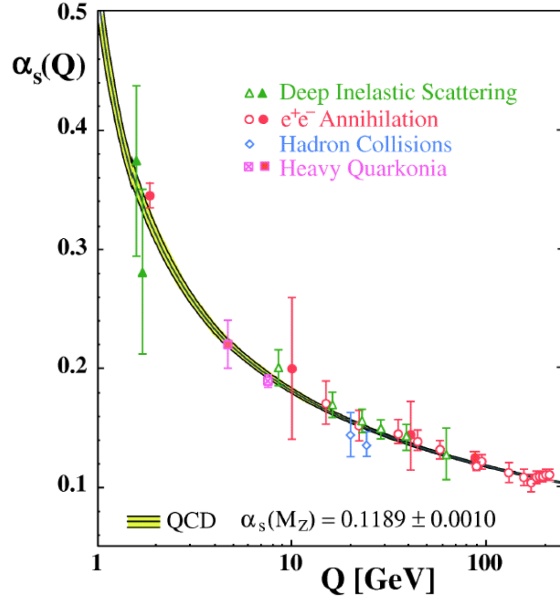
Figure 1.4: QCD coupling constant as a function of gluon momentum transfer Q.

quark model have been proposed. An overview of different quark models for baryons can be found in [1] and [2]. Most models include two kinds of interaction. The first interaction is a spin-independent confining interaction, such as harmonic or linear confinement. The second interaction is a spin-dependent force, the Isgur-Karl (IK) model uses a color-magnetic flavor-independent interaction modeled in terms of the gluon exchange in QCD [3], the instanton model uses a flavor-dependent short-range quark forces from instanton effects [8], other models use quark dynamics, such as: algebraic [5], hyper-central [6], Goldstone Boson Exchange [7].

In the Isgur-Karl (IK) model [3], the non-relativistic three valence quarks are dressed quarks with effective mass of 200-300 MeV for u and d quarks, the gluon fields provide a confining potential between quarks. The potential has a spin independent part V^{ij} and a spin dependent part V^{ij}_{hyp}. V^{ij} can be written as the sum of a harmonic oscillator potential $Kr^2_{ij}/2$, and an anharmonicity potential U_{ij}, which is treated as a perturbation. The spin dependent potential V^{ij}_{hyp} is the sum of a contact term $S_i \cdot S_j \delta^3(r_{ij})$ and a tensor term. It is a hyperfine interaction, which causes the $\Delta - N$ and $\Sigma - \Lambda$ splittings. The Hamiltonian is written as:

$$H = \sum_i (m_i + p_i^2/(2m_i)) + \sum_{i<j} (V^{ij} + V^{ij}_{hyp}). \tag{1.7}$$

The wave function is the product of a antisymmetric color wave function and a sum form of $\sum \psi \chi \phi$, in which ψ, χ, ϕ are the spatial, spin and flavor wave functions. The spatial wave functions ψ are the harmonic-oscillator eigenfunctions $\psi_{NLM}(\rho, \lambda)$ in the zeroth order of the perturbation calculation, in which $\rho = (r_1 - r_2)/\sqrt{2}$ and $\lambda = (r_1 + r_2 - 2r_3)/\sqrt{6}$, $N = 2(n_\rho + n_\lambda) + l_\rho + l_\lambda$. The ground states (N = 0 band, N(938) and $\Delta(1232)$) have positive parity ($l_\rho = l_\lambda = 0$). The N=1 excited resonances are "P waves" ($l_\rho = 1$ or $l_\lambda = 1$) with negative-parity. The N=2 band includes positive-parity excited states with radial excitations in one of the two oscillators ($n_\rho = 1, n_\lambda = 0$ or $n_\rho = 0, n_\lambda = 1$) or $l_\rho + l_\lambda = 2$.

5

The Schrödinger equation is solved in first-order perturbation theory for the anharmonic terms U_{ij} and V_{hyp}^{ij}. This model is quite successful in describing the low-lying baryon resonances. However, the baryons are strongly bound systems, so the approximation of non-relativistic kinematics and dynamics is not proper.

In the relativized model, the Hamiltonian is given by:

$$H = \sum_i \sqrt{p_i^2 + m_i^2} + V, \qquad (1.8)$$

where $V = V_{string} + V_{Coul} + V_{hyp} + V_{so(cm)} + V_{so(Tp)}$. V_{string} is the potential generated by adding the lengths of the gauge-invariant string configuration and multiplying by the meson string tension. $V_{Coul}, V_{hyp}, V_{so(cm)}, V_{so(Tp)}$ are color-Coulomb, color-hyperfine, color-magnetic spin-orbit, and Thomas-precession spin-orbit potentials [4]. The spectroscopy derived from the relativized model is comparable to that of the Isgur-Karl model. However, the relativized model is more tightly constrained with fewer fitting parameters than in the Isgur-Karl model. The wave functions from the relativized model are also very different from those of the Isgur-Karl model, due to the more realistic treatment of the spin-independent potential and inclusion of the configuration mixings.

The most recent CQM predictions for hadron spectroscopy are three papers published in 2001 [8], a relativistic quark model with instanton-induced quark forces was used in these papers. The instantaneous force is flavor-dependent, and was originally designed to solve the $\pi - \eta - \eta'$ puzzle, which exists in quark models of mesons based on one-gluon exchange. An expansion of the Euclidean action around single-instanton solutions of the gauge fields assuming zero-mode dominance in the fermion sector leads to an effective contact interaction between quarks, which acts only if the quarks are in a flavor anti-symmetric state.

In this model, quarks are confined by a linearly rising string potential, which is a three-quark string potential $V^{(3)}$. In addition, 't Hooft's instanton-induced two quark interaction is chosen as residual two-body force $V^{(2)}$. The non-strange baryon spectrum is calculated on the basis of the three-fermion Bethe-Salpeter equation. Figure 1.5 shows the comparison of calculated values with the experimental results for Δ (isospin T=3/2) and N^* (isospin T=1/2) resonances.

Overall, the model predictions are in good agreement with the experimental results. However, there are two problems: the assignment problem, and the missing resonance problem.

The assignment problem refers to the discrepancy between the model predicted values and experimentally identified states up to the fourth shell ($0\hbar\omega$, $1\hbar\omega$, $2\hbar\omega$ and $3\hbar\omega$) in the harmonic oscillation basis. Most states in the first three shells predicted by the model have been identified, but for some states, the predicted values are outside the error bars of the experimental measurements, such as $\Delta\frac{3}{2}^-(1700)$, $\Delta\frac{3}{2}^+(1600)$, $N\frac{1}{2}^+(1440)$, $N\frac{1}{2}^-(1530)$ (as seen in Figure 1.5). Moreover for the $3\hbar\omega$ shell in the Δ spectrum, three states $\Delta\frac{1}{2}^-(1900)$, $\Delta\frac{3}{2}^-(1940)$ and $\Delta\frac{5}{2}^-(1930)$ from the experimental measurements have values significant lower than the model predicted values. The assignment of experimentally observed states is only complete and well established up to the N = 1 band, the assignment for N = 2, N = 3 bands and beyond are still tentative.

The missing resonance problem refers to the situation that there are many more excited states predicted by the modern quark models than experimentally observed. A

detailed discussion of the missing resonance problem will be presented in the next section.

1.2.2 Missing resonances

The constituent quark models predict a large number of baryon resonances. However, as shown in the previous subsection, in the mass region above 1.8 GeV, only a few have been observed in experiment. The discrepancy between the theoretical predictions and experimental results needs more work from both the theory side and the experiment side.

On the theory side, a possible explanation for the fewer observed resonance states is the "quark-diquark" model [9]. This model assumes a tightly bound di-quark. Thus only two degrees of freedom are relevant at low energies, and fewer resonances are predicted. However, the Lattice QCD calculation of the hadron spectroscopy gives results in agree with the traditional Constituent Quark Models, thus the "quark-diquark" model has not been considered as the solution for the missing resonance problem.

On the experimental side, most data for the study of nucleon resonances are from the πN elastic scattering. This biases the results for resonances coupling weakly to the πN channel. Some quark models have predicted several unobserved resonances to have large decay branching ratios for the emission of mesons other than pions. The use of a photon beam provides a way to study the resonances which couple strongly to other branching channels.

Moreover, as shown in figure 1.7, the nucleon resonances have broad widths in the cross section plot, which makes the method of peak hunting impossible to identify all the resonances. Thus using the right way to decode the experimental results is crucial for the test of the theoretic models. The method used most often to identify the nucleon resonances is partial wave analysis (PWA). In the framework of PWA, the cross section and other experimentally measured quantities, such as polarization observables, are fitted using minimal set of partial waves (resonances), the discovery of a new resonance requires that the inclusion of the new state improves the fitting results in a significant way. The next section will present an introduction to the partial wave analysis for photo-production reactions, and introduce the methods from three PWA groups.

1.3 Partial Wave Analysis

The reaction between the photon beam and the nucleon involves two processes. One process is the electro-magnetic excitation of the nucleon, the other process is the strong decay in the s and u channels, or a meson exchange in the t channel. The tree level Feynman diagrams for the single-pion photo-production for these processes are shown in Figure 1.8.

The process of photo-production of a pseudo-scalar meson from a nucleon can be described by four complex amplitudes, which are most commonly parameterized in terms of the Chew-Goldberger-Low-Nambu (CGLN) amplitude[11]:

$$F = iF_1 \cdot \vec{\sigma} \cdot \vec{\epsilon} + F_2(\vec{\sigma} \cdot \vec{q})(\vec{\sigma} \cdot (\vec{k} \times \vec{\epsilon})) + iF_3(\vec{\sigma} \cdot \vec{k})(\vec{q} \cdot \vec{\epsilon}) + iF_4(\vec{\sigma} \cdot \vec{q})(\vec{q} \cdot \vec{\epsilon}), \qquad (1.9)$$

where $\vec{k}, \vec{q}$ are unit vectors for the momentum of the photon and meson, $\vec{\epsilon}$ is the polarization vector for a real photon, and $\vec{\sigma}$ are the nucleon's spin matrices. The differential cross
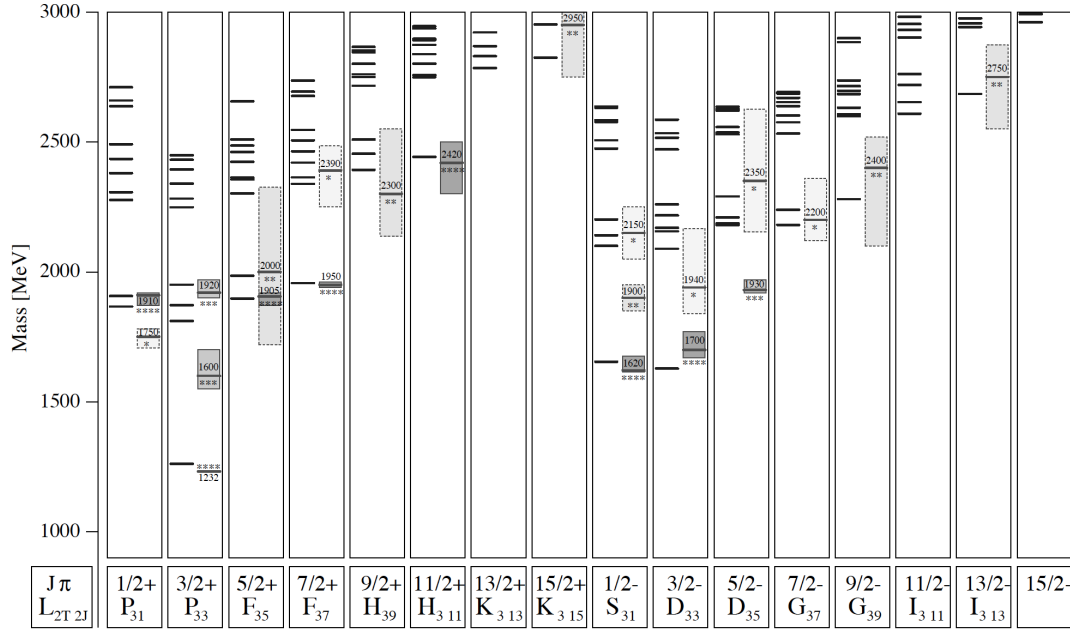
(a) Δ resonances (isospin T = 3/2).
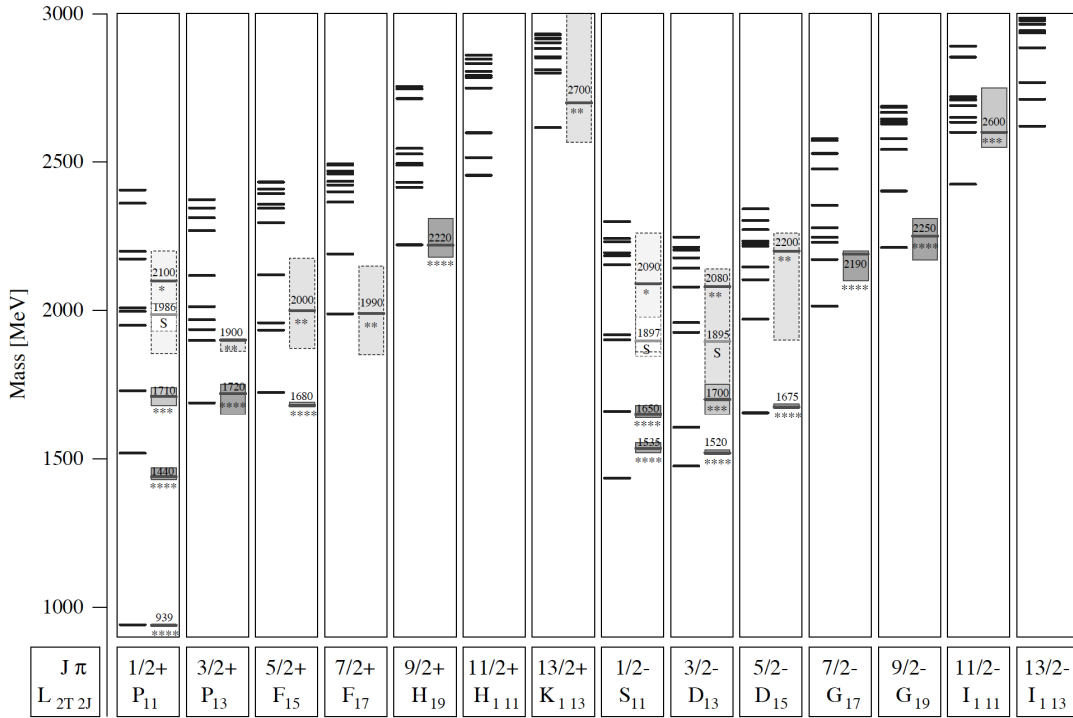
(b) N^* resonances (isospin T=1/2).

Figure 1.5: Calculated hadron spectrum from the instanton-induced quark model (black lines on the left side of each column), and the experimentally measured resonances (black lines with shaded box on the right side of each column). The resonances in each column are denoted by J^π, where J is total spin and π is parity; a detailed description of how J^π is determined can be seen in Figure 1.6. Another way to denote the states is $X_{2I+1,2J+1}$, where X = S, P, D, ... is the orbital angular momentum $l = 0, 1, 2, ...$ for the pion-nucleon system (for the reason that most old experimental data are from pion nucleon scattering). I is the total isospin, which can be 1/2 or 3/2, and $J = |l \pm \frac{1}{2}|$. For the experiment results, the lines indicate the position of the resonance, the shaded boxes are the uncertainties, and the stars under the lines indicate the status of the resonances, more stars correspond to better establishment. Image source: [8]

N sym	L^P	S	$N(I=1/2)$	$\Delta(I=3/2)$
2 A	1^+	1/2	$1/2^+$ $3/2^+$	
2 M	2^+	3/2	$1/2^+$ $3/2^+$ $5/2^+$ $7/2^+$	
2 M	2^+	1/2	$3/2^+$ $5/2^+$	$3/2^+$ $5/2^+$
2 M	0^+	3/2	$3/2^+$	
2 M	0^+	1/2	$1/2^+$ $N(1710)$	$1/2^+$ $\Delta(1750)$
2 S	2^+	3/2		$1/2^+$ $\Delta(1910)$ $3/2^+$ $\Delta(1920)$ $5/2^+$ $\Delta(1905)$ $7/2^+$ $\Delta(1950)$
2 S	2^+	1/2	$3/2^+$ $N(1720)$ $5/2^+$ $N(1680)$	
2 S	0^+	3/2		$3/2^+$ $\Delta(1600)$
2 S	0^+	1/2	$1/2^+$ $N(1440)$	
1 M	1^-	3/2	$1/2^-$ $N(1650)$ $3/2^-$ $N(1700)$ $5/2^-$ $N(1675)$	
1 M	1^-	1/2	$1/2^-$ $N(1535)$ $3/2^-$ $N(1520)$	$1/2^-$ $\Delta(1620)$ $3/2^-$ $\Delta(1700)$
0 S	0^+	3/2		$3/2^+$ $\Delta(1232)$
0 S	0^+	1/2	$1/2^+$ $N(938)$	

Figure 1.6: N and Δ states for the N = 0,1,2 harmonic oscillator bands from PDG [1]. A denotes the states with antisymmetric spatial wave fuction, S is for symmetric states, M is for mixed symmetric states. L^P is for angular momentum and parity. S is the three-quark spin.
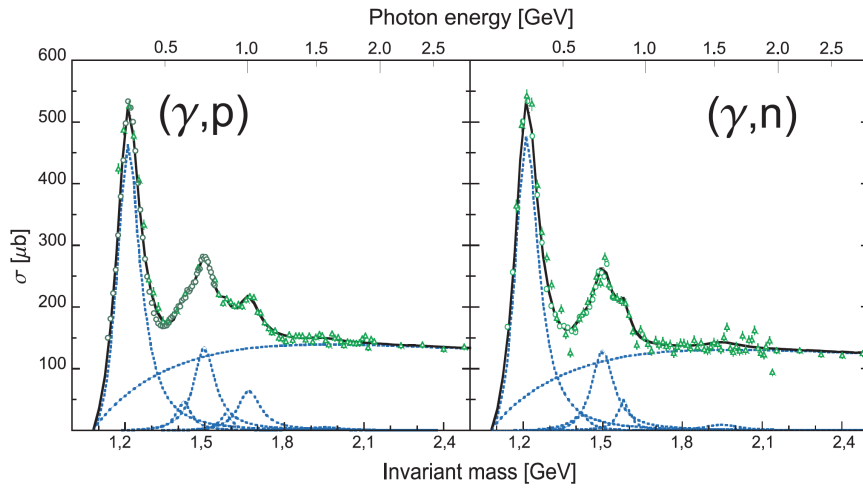
Figure 1.7: Total photonabsorption cross section with proton and neutron target. Points are measured data, curves are fitting results of Breit-Wigner shapes for nucleon resonances $P_{33}(1232)$, $D_{13}(1520)$, $S_{11}(1535)$, $F_{15}(1680)$ (only for proton), $F_{37}(1950)$ and a smooth background. Image source: [10]

(a) s-channel   (b) u-channel   (c) t-channel
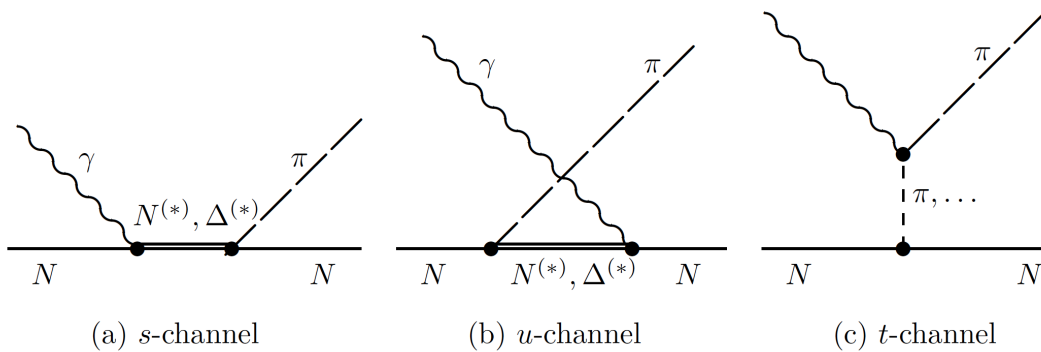
Figure 1.8: Tree level Feynman diagrams for single pion photoproduction.

section expressed in terms of the CGLN-amplitudes in the center of momentum frame is:

$$
\begin{aligned}
\frac{k}{q}\frac{d\sigma}{d\Omega} =& |F_1|^2 + |F_2|^2 + \frac{1}{2}|F_3|^2 + \frac{1}{2}|F_4|^2 + Re(F_1 F_3^*) \\
& + [Re(F_3 F_4^*) - 2Re(F_1 F_2^*)]cos(\theta_{cm}) \\
& - [\frac{1}{2}|F_3|^2 + \frac{1}{2}|F_4|^2 + Re(F_1 F_4^*) + Re(F_2 F_3^*)]\cos^2(\theta_{cm}) \\
& - [Re(F_3 F_4^*)]\cos^3(\theta_{cm}),
\end{aligned}
\tag{1.10}
$$

where q, k are momenta for the meson and photon in center of momentum frame, θ_{cm} is cm polar angle for the meson.

The four complex amplitudes can also be expressed in terms of helicity amplitudes. There are 8 helicity amplitudes, which come from the combination of two helicity states $\lambda_\gamma = \pm 1$ for real photon, two spin states $\nu_i = \pm 1/2, \nu_f = \pm 1/2$ for the initial and final state nucleons respectively. The 8 matrix elements can be reduced into four by parity conservation:

$$
\begin{aligned}
H_1 &= H_{+1/2,+3/2} = H_{-1/2,-3/2}, \\
H_2 &= H_{+1/2,+1/2} = -H_{-1/2,-1/2}, \\
H_3 &= H_{-1/2,+3/2} = -H_{+1/2,-3/2}, \\
H_4 &= H_{+1/2,-1/2} = -H_{-1/2,+1/2},
\end{aligned}
\tag{1.11}
$$

The relationship between the CGLN and helicity amplitudes is given in [12]. The differential cross section expressed in terms of the helicity amplitudes has a very simple form:

$$
\frac{k}{q}\frac{d\sigma}{d\Omega} = \frac{1}{2}(H_1^2 + H_2^2 + H_3^2 + H_4^2)
\tag{1.12}
$$

Using the selection rules and parity conservation, we can relate the intermediate resonance to the initial states and final states of the reaction.

For the initial state, the photon has total angular momentum $\vec{L}_\gamma = \vec{l} + \vec{s}_\gamma$, where $\vec{l}$ is the orbital angular momentum of photon relative to the target nucleon , and spin $\vec{s}_\gamma$ (s=1) is the spin of the photon, the photon has parity $P_\gamma = (-1)^L$ for EL- and $P_\gamma = (-1)^{L+1}$ for ML- multipoles of the photon field. The initial nucleon has spin $J_N = 1/2$, and parity $P_N = 1$. For a resonance with spin J_{N^*} and parity P_{N^*}, the selection rules and parity conservation gives:

$$
\begin{aligned}
&|L_\gamma - J_N| = |L_\gamma - 1/2| \leq J_{N^*} \leq |L_\gamma + 1/2| = |L_\gamma + J_N|, \\
&P_{N^*} = P_N \cdot P_\gamma = P_\gamma.
\end{aligned}
\tag{1.13}
$$

For the strong decay process of the resonance, the intermediate and final states have the following relations:

$$
\begin{aligned}
&|L_{meson} - J_N| = |L_m - 1/2| \leq J_{N^*} \leq |L_{meson} + 1/2| = |L_{meson} + J_N|, \\
&P_{N^*} = P_N \cdot P_{meson} \cdot (-1)^{L_{meson}} = (-1)^{L_{meson}+1}.
\end{aligned}
\tag{1.14}
$$

From the above four equations, we can relate the initial photon field multipoles (EL- and ML-) and the multipoles for meson photo-production ($E_{l\pm}$ and $M_{l\pm}$) to the resonance states (N^*), the results for several low order multipole amplitudes are shown in

photon M-pole	Initial state	Final state	Multipoles	N^*	N^*
EL/ML	(L_γ^P, J_N^P)	(J_N^P, L_{meson}^P)	$(E/M)_{l\pm}$	Jπ	$L_{2I,2J}$
E1	$(1^-, 1/2^+)$	$(1/2^+, 0^-)$	E_{0+}	1/2-	$S_{1,1}$ or $S_{3,1}$
E1	$(1^-, 1/2^+)$	$(1/2^+, 2^-)$	E_{2-}	3/2-	$D_{1,3}$ or $D_{3,3}$
M1	$(1^+, 1/2^+)$	$(1/2^+, 1^+)$	M_{1-}	1/2+	$P_{1,1}$ or $P_{3,1}$
M1	$(1^+, 1/2^+)$	$(1/2^+, 1^+)$	M_{1+}	3/2+	$P_{1,3}$ or $P_{3,3}$
E2	$(2^+, 1/2^+)$	$(1/2^+, 1^+)$	E_{1+}	3/2+	$P_{1,3}$ or $P_{3,3}$
E2	$(2^+, 1/2^+)$	$(1/2^+, 3^+)$	E_{3-}	5/2+	$F_{1,5}$ or $F_{3,5}$
M2	$(2^-, 1/2^+)$	$(1/2^+, 2^-)$	M_{2-}	3/2-	$D_{1,3}$ or $D_{3,3}$
M2	$(2^-, 1/2^+)$	$(1/2^+, 2^-)$	M_{2+}	5/2-	$D_{1,5}$ or $D_{3,5}$
E3	$(3^-, 1/2^+)$	$(1/2^+, 2^-)$	E_{2+}	5/2-	$D_{1,5}$ or $D_{3,5}$
E3	$(3^-, 1/2^+)$	$(1/2^+, 4^-)$	E_{4-}	7/2-	$G_{1,7}$ or $G_{3,7}$
M3	$(3^+, 1/2^+)$	$(1/2^+, 3^+)$	M_{3-}	5/2+	$F_{1,5}$ or $F_{3,5}$
M3	$(3^+, 1/2^+)$	$(1/2^+, 3^+)$	M_{3+}	7/2+	$F_{1,7}$ or $F_{3,7}$
...	...	...	...	...	...
...	...	...	...	...	...

Table 1.2: Relating the initial states and final states to the intermediate resonance states. The resonances N^* are shown in two different representations in the fifth and sixth columns. The corresponding photon multipoles and photo-production multipoles are shown in the first and fourth columns. For the photo-production multipoles $(E/M)_{l\pm}$, l is the relative angular momentum for the meson-nucleon system L_{meson}, $\pm$ indicates whether the spin 1/2 of the nucleon should be added to or subtracted from l to give the total angular momentum J_{N^*} for the resonances.

Table 1.2. From the table, we can see that if we can determine the components of the photo-production multipoles in the reaction, we can identify the corresponding nucleon resonances.

The CGLN amplitudes can be decomposed into the partial wave multipoles as 1.15:

$$F_1 = \sum_{l=0}^{\infty} \{(lM_{l+} + E_{l+})P'_{l+1}(\theta_{cm}) + [(l+1)M_{l-} + E_{l-}]P'_{l-1}(\theta_{cm})\},$$

$$F_2 = \sum_{l=0}^{\infty} [(l+1)M_{l+} + lM_{l-}]P'_l(\theta_{cm}),$$

$$F_3 = \sum_{l=0}^{\infty} [(E_{l+} - M_{l+})P''_{l+1}(\theta_{cm}) + (E_{l-} + M_{l-})P''_{l-1}(\theta_{cm})],$$

(1.15)

$$F_4 = \sum_{l=0}^{\infty} (M_{l+} - E_{l+} - M_{l-} - E_{l-})P''_l(\theta_{cm}),$$

where the P'_l, P''_l are derivatives of Legendre polynomials. From these equations, we know that if we can determine the partial wave multipoles in the reaction amplitude F_i for the reaction channel, the resonances that couple to this channel can be determined. The determination for the four complex amplitudes F_1, F_2, F_3, F_4 need eight independent measurements. For the single and double meson photo-production, there are 64 polarization observables [24]:

$$\begin{aligned}
\rho_f I =& I_0 \Big\{ (1 + \vec{\Lambda}_i \cdot \vec{P} + \vec{\sigma} \cdot \vec{P}' + \Lambda_i^\alpha \sigma^{\beta'} O_{\alpha\beta'}) \\
& + \delta_\odot (I^\odot + \vec{\Lambda}_i \cdot \vec{P}^\odot + \vec{\sigma} \cdot \vec{P}'^\odot + \Lambda_i^\alpha \sigma^{\beta'} O_{\alpha\beta'}^\odot) \\
& + \delta_l \Big[\sin 2\beta (I^s + \vec{\Lambda}_i \cdot \vec{P}^s + \vec{\sigma} \cdot \vec{P}'^s + \Lambda_i^\alpha \sigma^{\beta'} O_{\alpha\beta'}^s) \\
& + \cos 2\beta (I^c + \vec{\Lambda}_i \cdot \vec{P}^c + \vec{\sigma} \cdot \vec{P}'^c + \Lambda_i^\alpha \sigma^{\beta'} O_{\alpha\beta'}^c) \Big] \Big\},
\end{aligned}$$

(1.16)

where I is the reaction rate, Λ is the degree of polarization for the target, $\rho_f = (1 + \vec{\sigma} \cdot \vec{P}')/2$ is the density matrix of the recoil nucleon, $\delta_\odot$ is the degree of circular polarization of the photon beam, δ_l is the degree of linear polarization for the photon beam. There are 9 single polarization observables: $\vec{P}$ is the polarization observable related to the target nucleon polarization (P_x, P_y, P_z give three observables for target asymmetries), $\vec{P}'$ is the polarization observable relate to the recoil nucleon polarization ($P'_{x'}, P'_{y'}, P'_{z'}$ give three observables for recoil asymmetries), $I^\odot, I^s, I^c$ are photon beam asymmetries. There are 27 double polarization observables: $\vec{P}^\odot, \vec{P}^s, \vec{P}^c$ are beam-target asymmetries, $\vec{P}'^\odot, \vec{P}'^s, \vec{P}'^c$ are beam-recoil asymmetries, $O_{\alpha\beta'}$ is the target-recoil asymmetry. There are 27 triple polarization observables: $O_{\alpha\beta'}^\odot$, $O_{\alpha\beta'}^s$, and $O_{\alpha\beta'}^c$. Adding I_0, which is the unpolarized differential cross section, gives a total of 64 observables. There are 28 relations relating their amplitudes, and 21 equations relating their phases, which give 15 independent quantities. A complete set of experiments for the determination of the reaction amplitude will need measurements of the differential cross section and the single, double and triple polarization observables.

However, the complete set of experiments is often out of reach for most reaction channels. The extraction of the multipoles will have to rely on model dependent analysis. There are three groups updating their solutions for multipoles regularly with the inclusion of the most recent experiment results: Bonn-Gatchina [13], MAID [14], and SAID [15].

The three groups are using different phenomenological models to parametrize the multipoles. In the Bonn-Gatchina method, a combined analysis is used to analyze large number of reactions at the same time, which include the interference between different states. In the MAID method, the unitary isobar model contains both a common background, which is unitarized according to the K-matrix prescription, and 13 resonance terms, which are assumed to have the Breit-Wigner forms for the resonance shape. In the SAID method, the multipoles are parametrized in the form: $M = (Born + A)(1 + iT_{\pi N}) + BT_{\pi N}$, where $T_{\pi N}$ is the associated elastic pion-nucleon T matrix, A and B are purely phenomenological polynomials with correct threshold properties. Figure 1.9 shows the comparison of the multipoles calculated from these three models. The positions of the poles of the curve indicate the resonance energy of the multipoles. For example, for the M_1^+ multipole, the curve peaks at around 1232 MeV, which is the prominent $P_{33}(1232)$ peak as shown in Figure 1.7 for the cross section for single pion production reaction.
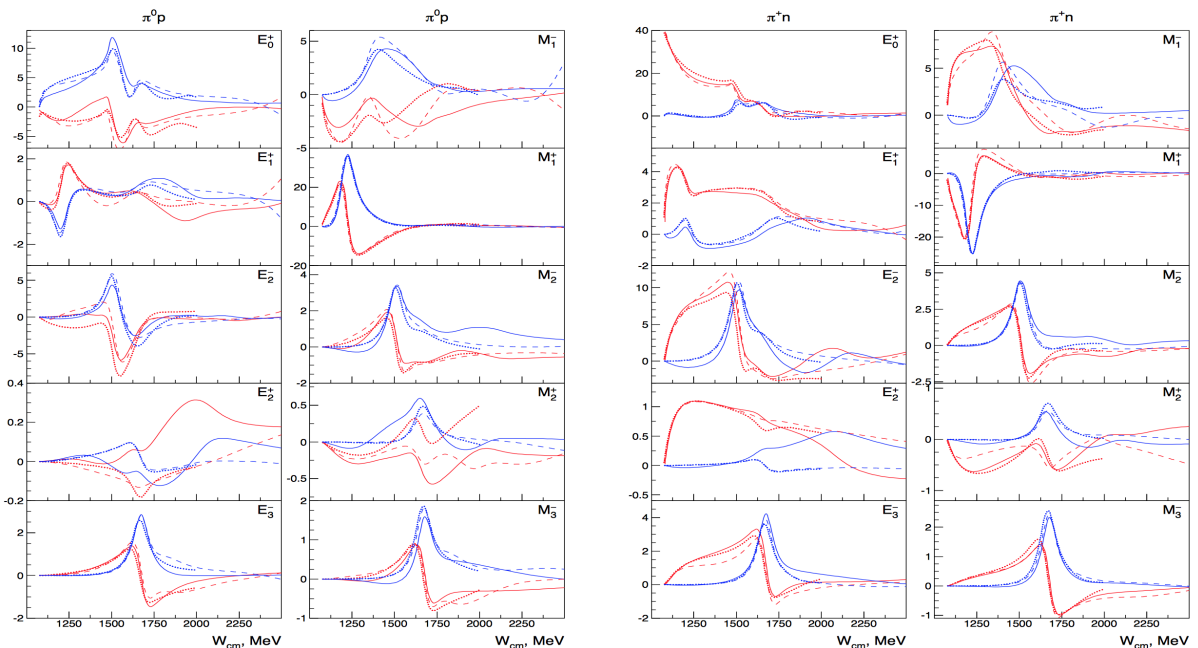
Figure 1.9: The multipoles for single pion production. Red curves are real part of the multipoles, Blue curves are imaginary part of the multipoles. Solid curves are BoGa solutions, dashed curves are SAID solutions, dotted curves are MAID 2009 solutions. Image Source: [25]

1.4   Previous Measurements

For the last two decades, with the advent of the high duty accelerator and advances in nearly 4π detectors (CLAS at JLab, Crystal Ball and TAPS at MAMI and ELSA), a lot of data have been collected for the reactions of single and double meson photo-production. Table 1.3 shows the observables and number of kinematic data points that have been included in the Bonn-Gatchina PWA model. For the reaction of double pion photo-production: $\gamma p \rightarrow p\pi^+\pi^-$, three more data sets have been acquired recently in CLAS

at Jefferson lab. The first is the circular beam helicity asymmetry $I^{\odot}$ measurement [20] using a circularly polarized photon beam and unpolarized proton target (CLAS g1c). The second is the linear beam helicity asymmetries I^s and I^c using a linearly polarized photon beam and unpolarized proton target (CLAS g8b). The third is the beam helicity asymmetry $I^{\odot}$, target asymmetry P_z, and beam target asymmetry $P_z^{\odot}$ using a circularly polarized photon beam and longitudinally polarized proton target (CLAS g9a). From table 1.3, we notice that most of the data are taken on a proton target, and the data from the double meson reaction are much less than those from the single meson reaction.

In this study, we will report the first measurement of the beam target asymmetry E for the reaction: $\gamma n \to p\pi^-$ with a circularly polarized photon beam and longitudinally polarized neutron target. Moreover, we will compare the asymmetries $I^{\odot}$, P_z and $P_z^{\odot}$ with the result from CLAS g1c and g9a for the reaction $\gamma p \to p\pi^+\pi^-$, and then report the first measurement of $I^{\odot}$, P_z and $P_z^{\odot}$ for the reaction $\gamma n \to p\pi^+\pi^-$.

Observable	N_{data} (Institute)
$d\sigma/d\Omega(\gamma p \to p\pi^0)$	1106 (CB-ELSA), 861 (GRAAL), 592 (CLAS), 1692 (TAPS@MAMI)
$\Sigma(\gamma p \to p\pi^0)$	540 (CB-ELSA), 1492 (SAID db)
$E(\gamma p \to p\pi^0)$	140 (A2-GDH)
$P(\gamma p \to p\pi^0)$	607 (SAID db)
$T(\gamma p \to p\pi^0)$	389 (SAID db)
$H(\gamma p \to p\pi^0)$	71 (SAID db)
$G(\gamma p \to p\pi^0)$	75 (SAID db)
$O_x(\gamma p \to p\pi^0)$	7 (SAID db)
$O_z(\gamma p \to p\pi^0)$	7 (SAID db)
$d\sigma/d\Omega(\gamma p \to n\pi^+)$	484 (CLAS), 1583 (SAID db), 408 (A2-GDH)
$\Sigma(\gamma p \to n\pi^+)$	899 (SAID db)
$E(\gamma p \to n\pi^+)$	231 (A2-GDH)
$P(\gamma p \to n\pi^+)$	252 (SAID db)
$T(\gamma p \to n\pi^+)$	661 (SAID db)
$H(\gamma p \to n\pi^+)$	71 (SAID db)
$G(\gamma p \to n\pi^+)$	86 (SAID db)
$d\sigma/d\Omega(\gamma p \to p\eta)$	680 (CB-ELSA), 100 (TAPS)
$\Sigma(\gamma p \to p\eta)$	51 (GRAAL 98), 100 (GRAAL 07)
$T(\gamma p \to p\eta)$	50 (Phoenics)
$d\sigma/d\Omega(\gamma p \to \Lambda K^+)$	1320 (CLAS 09)
$P(\gamma p \to \Lambda K^+)$	1270 (CLAS 09), 84 (GRAAL)
$C_x(\gamma p \to \Lambda K^+)$	160 (CLAS)
$C_z(\gamma p \to \Lambda K^+)$	160 (CLAS)
$\Sigma(\gamma p \to \Lambda K^+)$	66 (GRAAL), 45 (LEP)
$T(\gamma p \to \Lambda K^+)$	66 (GRAAL 09)
$O_x(\gamma p \to \Lambda K^+)$	66 (GRAAL 09)
$O_z(\gamma p \to \Lambda K^+)$	66 (GRAAL 09)
$d\sigma/d\Omega(\gamma p \to \Sigma^0 K^+)$	1590 (CLAS)
$P(\gamma p \to \Sigma^0 K^+)$	344 (CLAS)
$C_x(\gamma p \to \Sigma^0 K^+)$	94 (CLAS)
$C_z(\gamma p \to \Sigma^0 K^+)$	94 (CLAS)
$\Sigma(\gamma p \to \Sigma^0 K^+)$	42 (GRAAL), 45 (LEP)
$d\sigma/d\Omega(\gamma p \to \Sigma^+ K^0)$	48 (CLAS), 72 (CB-ELSA 10)
$P(\gamma p \to \Sigma^+ K^0)$	24 (CB-ELSA 10)
$\Sigma(\gamma p \to \Sigma^+ K^0)$	15 (CB-ELSA 10)
$d\sigma/d\Omega(\gamma p \to p\pi^0\pi^0)$	1.4 GeV, 3.2 GeV (CB-ELSA)
$E(\gamma p \to p\pi^0\pi^0)$	16 (MAMI)
$\Sigma(\gamma p \to p\pi^0\pi^0)$	128 (GRAAL)
$d\sigma/d\Omega(\gamma p \to p\pi^0\eta)$	3.2 GeV (CB-ELSA)
$\Sigma(\gamma p \to p\pi^0\eta)$	180 (GRAAL)
$I_c, I_s(\gamma p \to p\pi^0\eta)$	3.2 GeV (CB-ELSA)

Table 1.3: Polarization observables in the photo-production of mesons used in Bonn-Gatchina PWA model. Image Source: [26]

Chapter 2

Experiment Setup: CEBAF, Hall B and HD-ice Target

The data in this study were taken in the G14 run period from Nov. 19, 2011 to May. 17, 2012 at the Thomas Jefferson National Accelerator Facility (Figure 2.1), also called Jefferson Lab in Newport News, Virginia. This experiment used a tagged photon beam to hit an HD-ice target, and the final state particles were detected by the Hall B CLAS(CEBAF Large Acceptance Spectrometer) detector. The photon beam was produced by bremsstrahlung from polarized electrons from the CEBAF accelerator using a radiator with the Hall B photon tagging system. Either circularly or linearly photon beams could be produced by using different radiators. The HD-ice target was composed of solid hydrogen deuteride, with one hydrogen atom and one deuterium atom in each molecule. The HD was polarized longitudinally along the beam direction. The CLAS has quasi 4π solid angle coverage($\sim 3\pi$), and was optimized to study exclusive channels with multiple final state particles.

Figure 2.1: Jefferson Lab: The racetrack shape is the CEBAF accelerator, and the three mounds on the right are the three experiemntal halls A, B and C. Image Source: [27]

2.1 CEBAF: Continuous Electron Beam Accelerator Facility
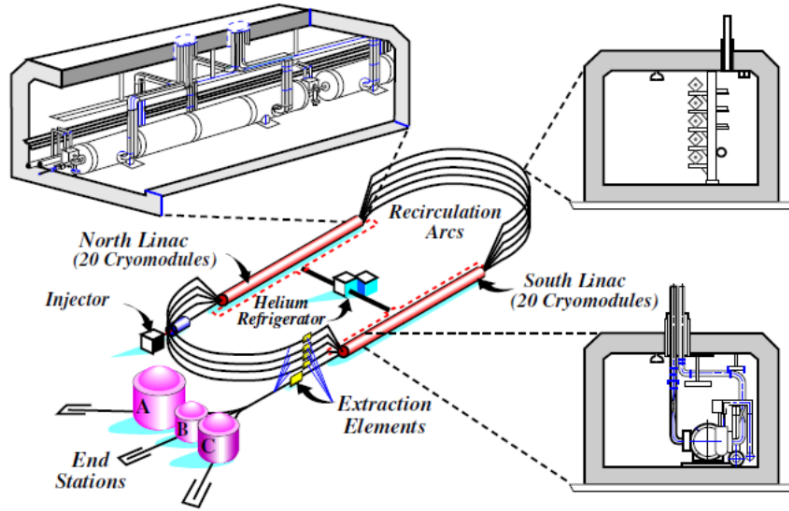
Figure 2.2: The Continuous Electron Beam Accelerator Facility (CEBAF): The polarized electron beam is generated in the Injector, it gains 1.2 GeV in the two LINACs in each pass, and reaches 6 GeV after 5 passes. Image Source: [28]

CEBAF is an electron accelerator that is able to deliver up to 6 GeV electron beams to the three experimental halls simultaneously. Superconducting radio frequency(SRF) cavities are used for electron acceleration. The SRF cavities allow the accelerator to reach a full-time duty factor without down-time for cooling the conduction elements of the accelerator. The nearly zero energy lost of the SRF cavities provides three times higher efficiency in terms of RF power than non-superconducting RF cavities . As shown in Figure 2.2, the accelerator consists of an injector and a pair of superconducting RF linear accelerators (LINACs). The two LINACs are connected by two arc sections, which have four circulating arcs at the west end and five at the east end. The electrons gain 1.2 GeV for each pass. After five successive passes, their energy reaches 6 GeV. Beams from different passes can be extracted for different experimental halls, which gives each hall the ability to choose different beam energies.

2.1.1 Injector

The injector has a polarized photo-emission electron gun with three pulsed lasers. The three lasers, one for each experimental hall, are pulsed independently and differ by 120° in phase. The three lasers are synchronized and combined to strike a strained GaAs photocathode at the third subharmonic (499 MHz) of the accelerating cavity frequency (1497 MHz) [30]. The electron gun produces a polarized 100 KeV electron beam. This beam then passes through three-hole chopper to cleanly separate the bunches for the different halls. Electrons are then accelerated to 67 MeV in 2 1/4 cryomodules(18 SRF cavities) before sending them to the CEBAF recirculating LINACs. This arrangement

allows each hall to receive electron bunches every 2 ns and to control its current and beam polarization independently.
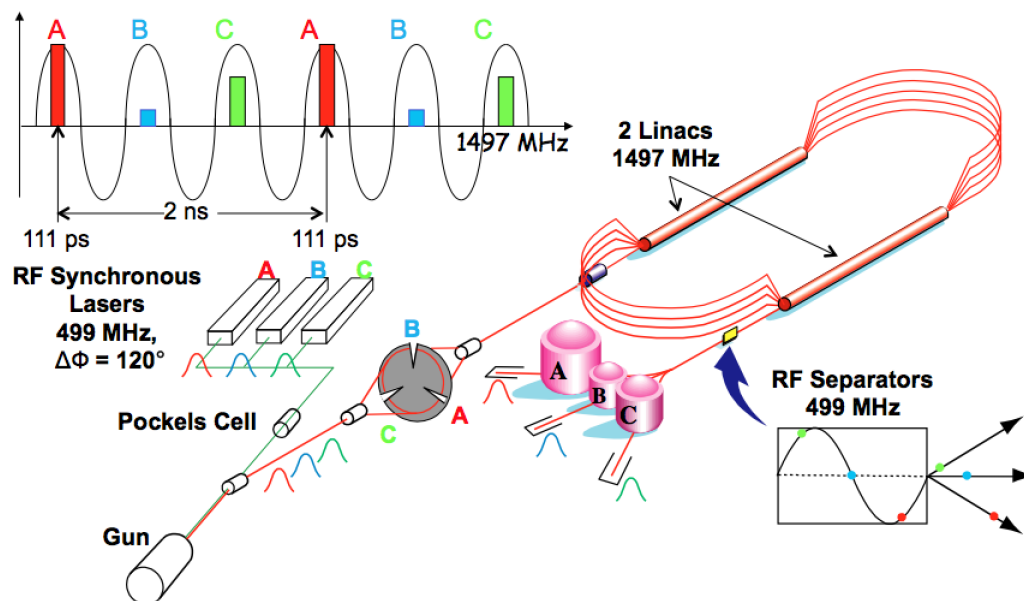
Figure 2.3: Injector. Image Source: [31]

2.1.2   Linear accelerators(LINACs)

Each of the two LINACs contains 20 cryomodules (Figure 2.4). Inside each cryomodule, there are eight SRF cavities. Figure 2.5 shows a pair of 5 cell SRF cavities. During the run, these SRF cavities are cooled down to 2K with liquid Helium to become super-conducting. An RF standing wave in the cavities is locked in phase with the electron bunches, as shown in Figure 2.6, so that the electrons always experience an accelerating electrical field. Each LINAC can increase the electron energy up to 600 MeV. After five passes, the energy of the electron beam can reach up to 6 GeV.

Figure 2.4: Cryomodules. Image Source: [28]

Figure 2.5: A pair of CEBAF's 5 cell SRF cavities. Image Source: [28]
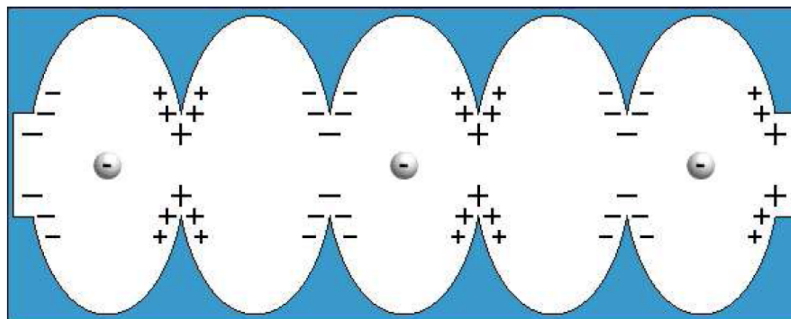
Figure 2.6: Accelerating RF field inside the SRF cavities. Image Source: [28]

2.1.3 Recirculation Arcs and RF Separators
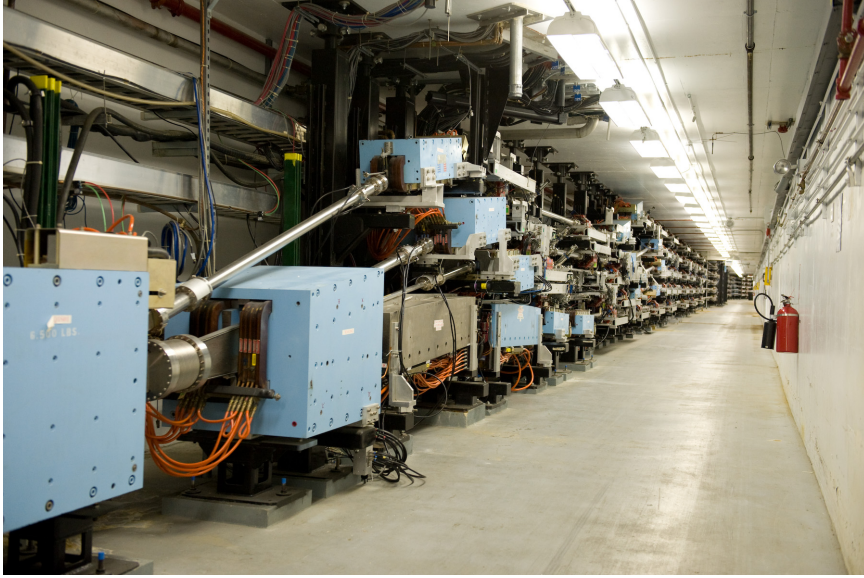
Figure 2.7: Eastern recirculation arc. Image Source: [28]

Since the electron beams need to recirculate in the accelerator and pass the two LINACs 5 times in order to reach the maximum energy of 6 GeV, electron beams from different passes coexist in the accelerator. In order to bend them around to recirculate in the LINACs, a configuration as shown in Figure 2.7 is used. Figure 2.7 is a photo of the eastern recirculation area, where electron beams with five different energies enter from the north LINAC, and are separated by a group of dipole magnets. The beams pass through the five arcs with different magnetic fields to be bent to the south LINAC. In the western recirculation area, a similar arrangement is used, but only four arcs are needed for the first four pass beams, since the fifth pass will go to the RF separators and be directed to the halls.

The RF separators are used to extract the electron beams for different halls. As shown in Figure 2.8, there are two working modes for the separator, a 2-way and a 3-way beam split. For the 2-way beam split, the phase of RF wave is tuned with the electron bunches so that a transverse force is applied to the electron bunch to deflect the beam to the experiment hall. Meanwhile, another transverse force in the opposite direction is applied to the other two electron bunches, forcing them back to the recirculating loops. The 2-way beam split is used for the pass 1-4 beams. For the pass 5 beam, the RF wave exerts a transverse force on the first electron bunch, leaves the second electron bunch alone, and exerts an opposite transverse force on the third electron bunch. The 3-way beam split separates the electron beam into three beams. From the description above, we notice that the pass 1-4 beams can be used in one experimental hall at a time, while the pass 5 beam can be used in all three experimental halls simultaneously as needed.
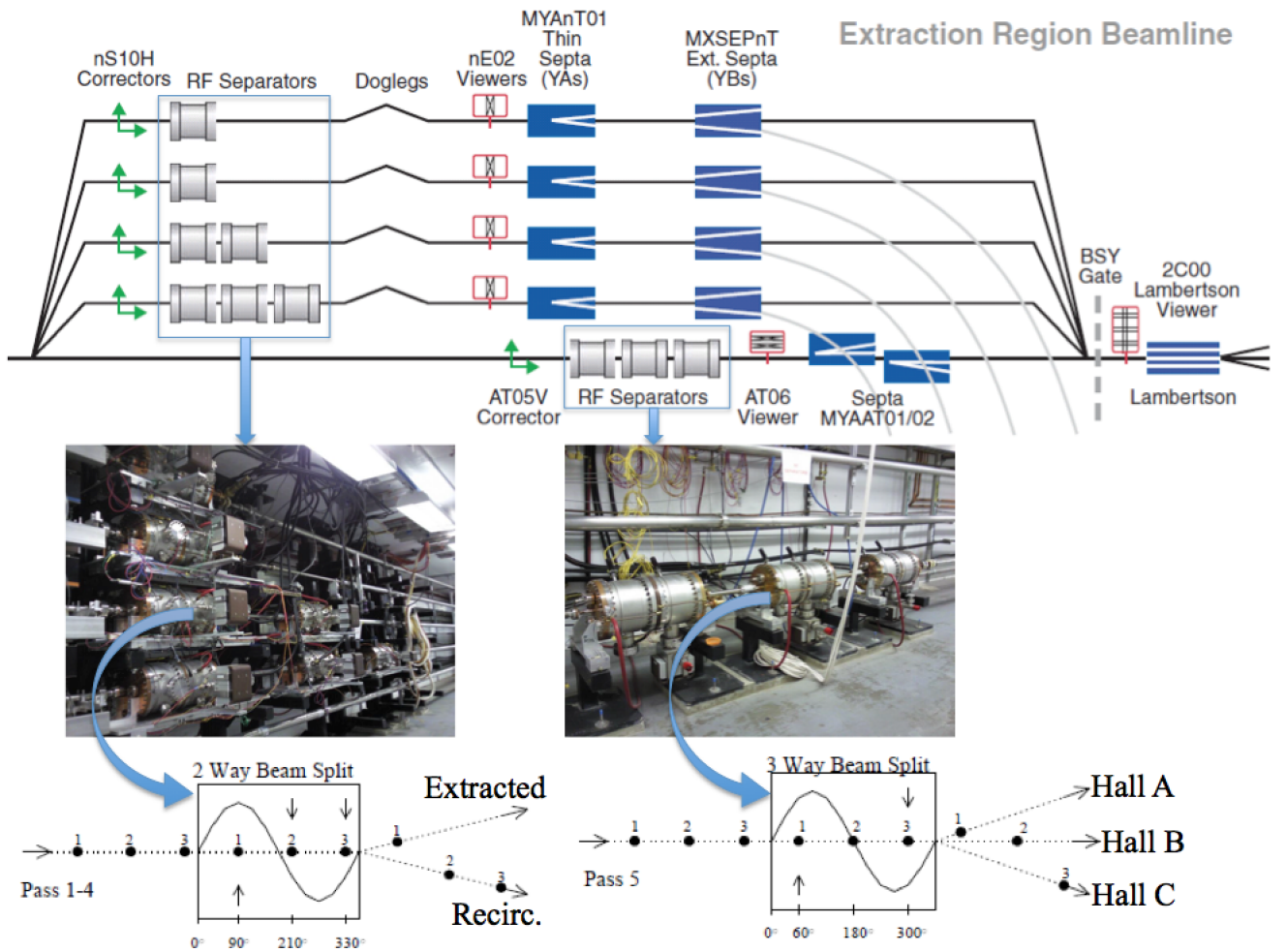
Figure 2.8: RF Separators. Image Source: [32]

2.2 Hall B

Hall B in Jefferson Lab can run experiments using either electron or photon beams. This hall uses a nearly 4π detector, the CEBAF Large Acceptance Spectrometer(CLAS), which is ideal for the study of exclusive reactions with multiple particles in the final state detected. Figure 2.9 shows the beam-line layout in Hall B, which includes the photon tagging system, the CLAS detector, and some beam-line devices for diagnostic studies.

2.2.1 Photon Tagging System

Photon beams are produced by the electron bremsstrahlung reaction, where an electron with energy E_0 is scattered by the electromagnetic field of a nucleus, and emits a photon with energy E_γ. By detecting the energy of the scattered electron $E_{e'}$, the photon energy E_γ is "tagged" by energy conservation: $E_\gamma = E_0 - E_{e'}$. The Hall B system can tag photon energies ranging from 20% to 95 % of the incident electron energy. As shown in Figure 2.10, the tagging system has five main parts: the radiator, the tagger magnet, the hodoscope, the readout, and the collimation system. Three modes of photon beams can be generated: a non-polarized mode, a circularly polarized mode, and a linearly polarized mode, as determined by the polarization of the electron beam and the type of photon radiator in use[33].

The Radiator

There are two kinds of photon radiators used in Hall B: amorphous or diamond crystals. The amorphous radiator is a thin Gold/Carbon foil, which is 5×10^{-5} to 3×10^{-4} radiation lengths of gold plated on a thin carbon support foil. The bremsstrahlung process for the amorphous radiator is incoherent and the generated photon beam has a $1/E_\gamma$ energy spectrum. Non-polarized or circularly polarized photon beams are generated with this radiator depending on the electron beam polarization. The circular polarization of the photon beam comes from polarization transfer from the longitudinally polarized electron beam. The polarization transfer relation is given by Eq. 2.1[34].

$$P_{circ} = P_{el}\frac{4x - x^2}{4 - 4x + 3x^2} \tag{2.1}$$

where $x = E_\gamma/E_0$ is the ratio of the photon energy (E_γ) over the electron energy (E_0), P_{circ} and P_{el} are the degree of polarization for the circularly polarized photon beam and the longitudinally polarized electron beam. For high energy photons, $x \approx 1$, $P_{circ} \approx P_{el}$, the polarization transfer is almost 100%. For low energy photons, such as $x = 0.5$, $P_{circ} \approx 0.6P_{el}$.

The other kind of radiator is a thin diamond crystal, which is 20-50 μm thick. Linearly polarized photon beams are produced via coherent bremsstrahlung from the well-ordered crystal lattice. The photon beam produced by the diamond crystal radiator contains both the coherent linearly polarized photons and the incoherent background, in which the incoherent part is due to the lattice vibrations. The angular cone of incoherent bremsstrahlung varies slowly with photon energy, while the emission angle of coherent bremsstrahlung is sharply peaked[35]. By passing the photon beam through a tight collimator, the relative contribution of coherent bremsstrahlung can be enhanced. Figure
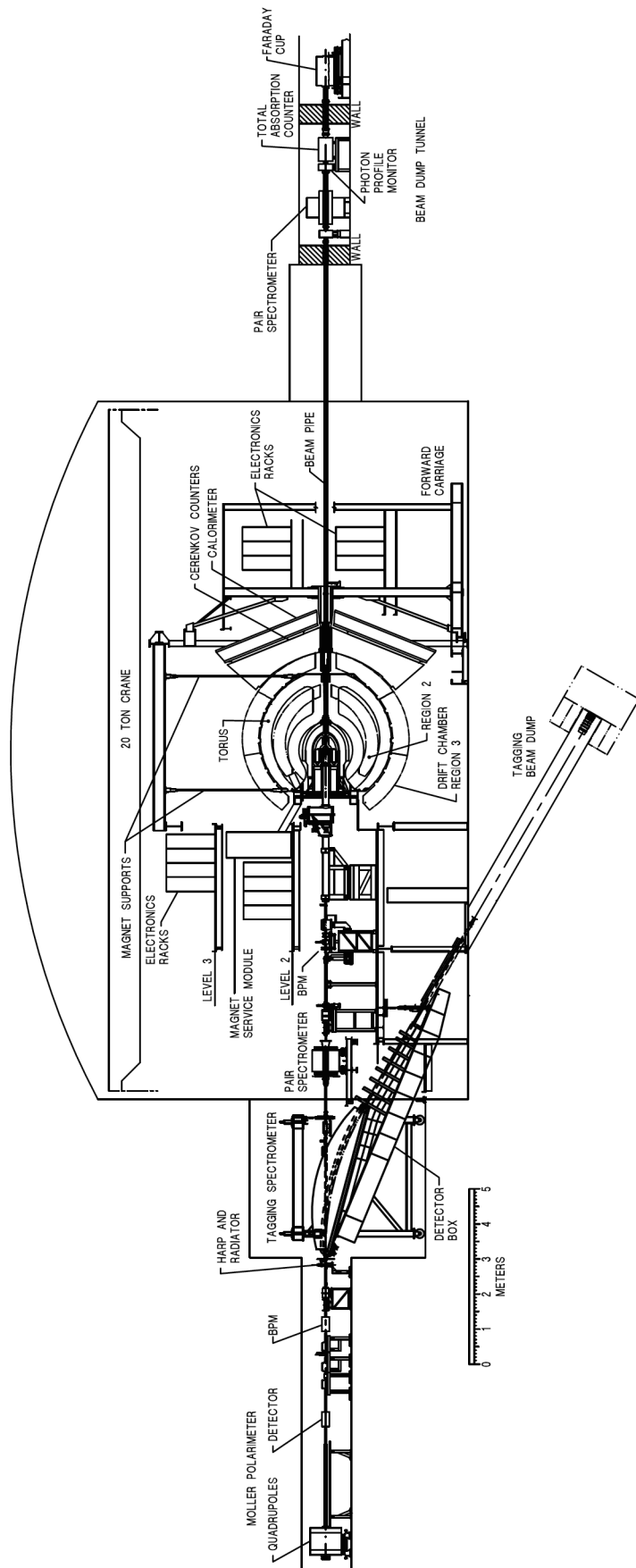
Figure 2.9: Hall B beamline. Image Source: [29]
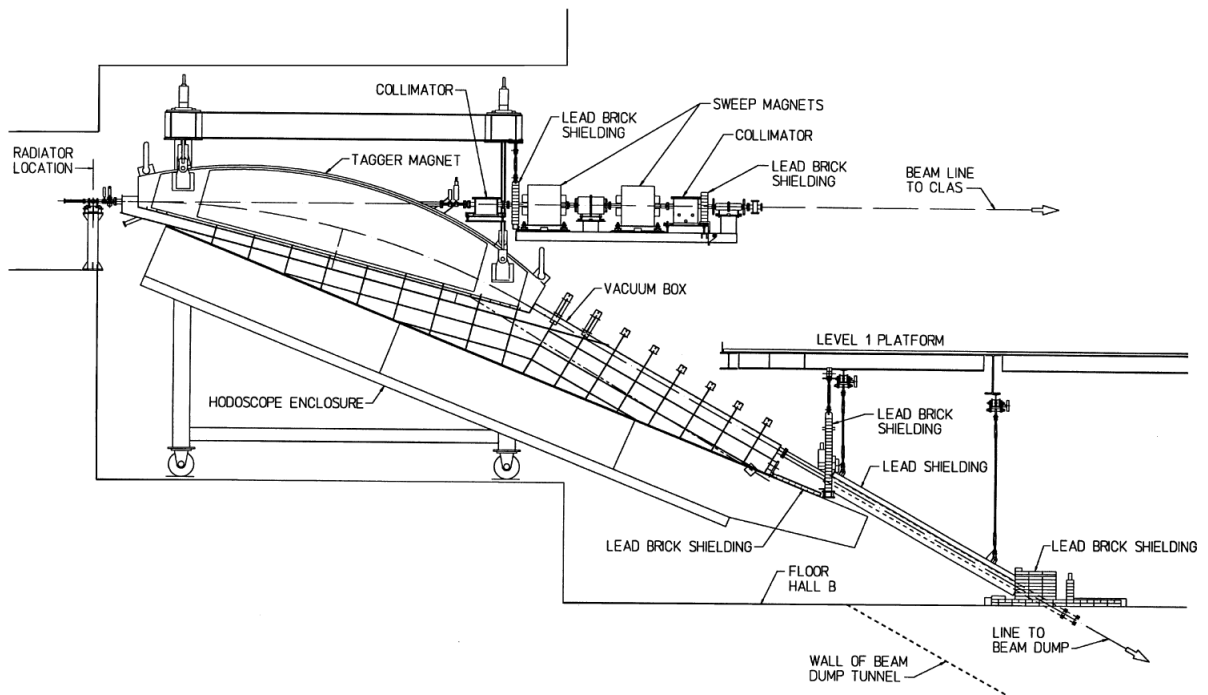
Figure 2.10: Hall B photon tagging system. Image Source: [33]
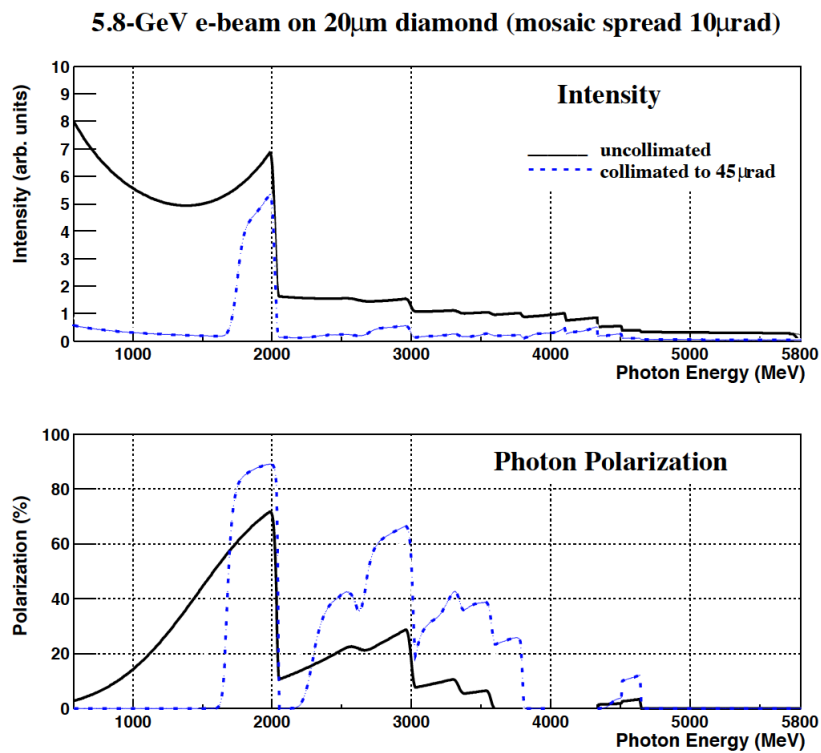
Figure 2.11: Calculated photon spectrum and polarization for a photon beam produced by an incident electron beam of 5.8 GeV on a 20 μm diamond crystal. Image Source: [35]

2.11 shows simulated results for the photon spectrum and its polarization before and after using a collimator. The blue dashed lines show that by using a collimator, the polarization of the photon beam is enhanced in a window of 200 MeV near 2.0 GeV. (We refer to this window as the coherent peak.) Since the energy of the coherent bremsstrahlung is related to the crystal orientation, by rotating the crystal, the position of the coherent peak can be changed gradually to cover all of the desired energy region. The polarization of the linearly polarized beam is determined by fitting the photon spectrum from the diamond radiator with respect to the photon spectrum from an amorphous radiator to a model that takes into account all known contributions of coherent and incoherent bremsstrahlung, multiple scattering, mosaic spread and beam divergence[36].

The Tagger Magnet

The tagger magnet is a single uniform dipole. It has a full-energy radius of curvature of 11.80 meters and deflection angle of 30°. It's length is 6.06 m along the open chord, and there is a gap of 5.7 cm wide in the middle for the electron beam to pass through (Figure 2.12). The magnet bends the electron beam out of the beamline, which bends the energy-degraded electrons to the hodoscope, and the full-energy electrons to the beam dump. The requirement of $10^{-3}E_0$ in energy resolution requires good field uniformity. For the original upper limit of the CEBAF beam of 4 GeV, the required magnetic filed of 1.13T has good uniformity. For the upgraded 6 GeV beam, the tagger magnet needs to provide a magnetic field of 1.75T to bend the full-energy beam to the beam dump. This high field has some degraded field uniformity, but by modifying the shape of the return yoke, the field could achieve a satisfactory uniformity.
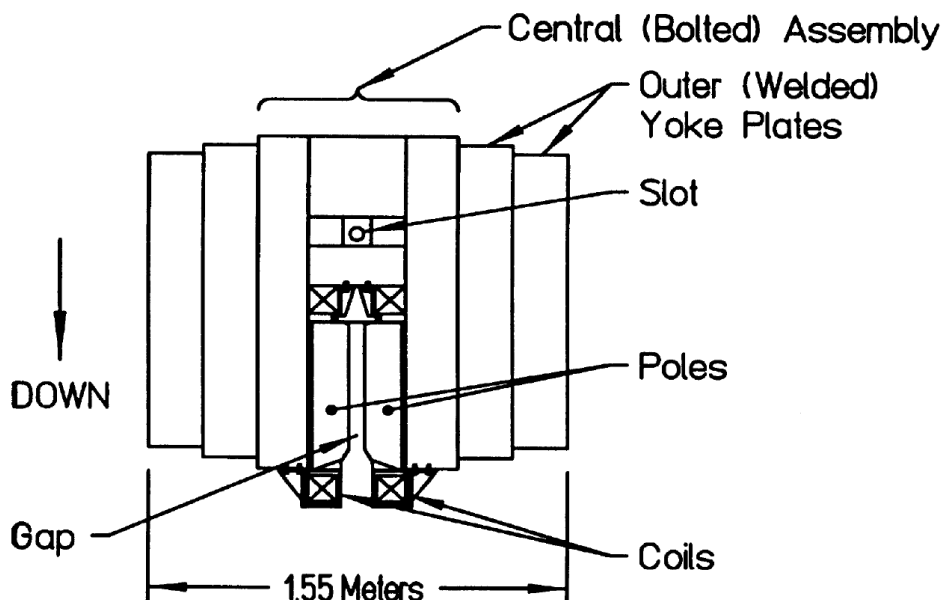
Figure 2.12: The transverse section of the tagger magnet. The laminar structure of the yoke is completely open in the middle for the electron beam passage. Image Source: [33]

The Hodoscope

The focal-plane hodoscope is used to measure the momentum and timing of the recoiling electrons. It consists of two separate planes of scintillator detectors, the E-plane and T-plane. Since electron trajectories cross the focal plane at different angles ranging from 9.5° for high momentum electrons to 25° for low momentum electrons, each detector needs to be arranged with its working surface normal to the electron trajectory(Figure 2.13),
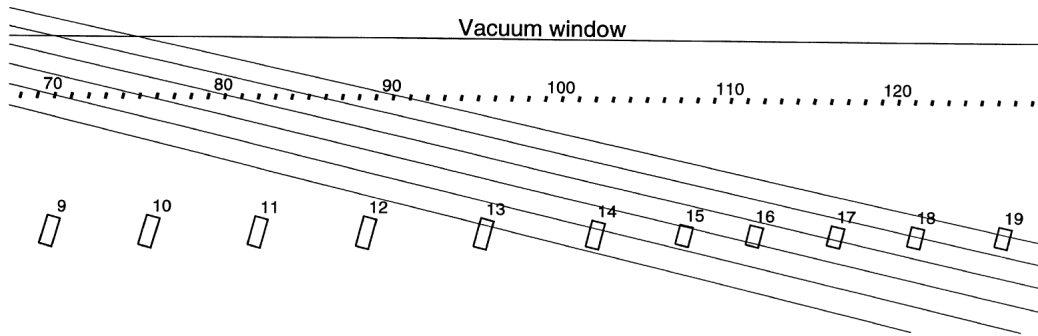
Figure 2.13: A section of the hodoscope showing the arrangement of the scintillator detectors in E-plane and T-plane. The parallel lines indicate the direction of the electron trajectories. Image Source: [33]
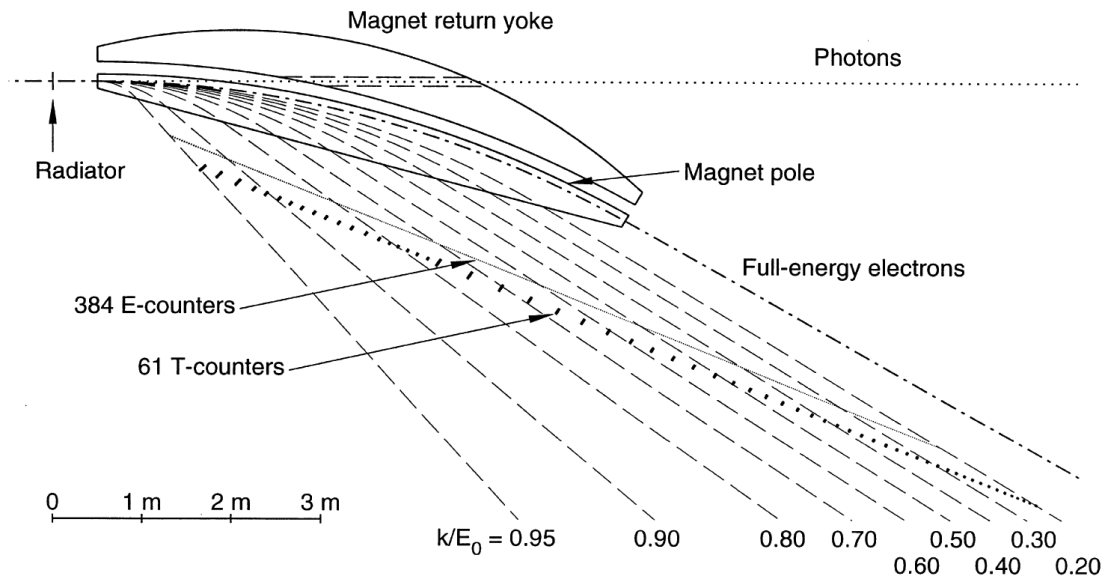
Figure 2.14: The relative positons for the E-plane and T-plane. Image Source: [33]

The E-plane lies on the optical focal plane of the magnet(Figure 2.15). This plane is used for the momentum definition of the recoiling electrons. The momentum of the recoiling electron is then used to determine the energy of the bremsstrahlung photon. The requirement of an energy resolution of $10^{-3}E_0$ results in a plane with a high degree of segmentation. For a focal plane of around 9 m in length, there are 384 scintillators. These scintillators are 20 cm long and 4 mm thick. Their widths (along the dispersion

direction) vary from 6 to 18 mm, which covers approximately equal size momentum intervals of 0.003 E_0. The scintillators are arranged to optically overlaps their neighbors by one-third of their width, this arrangement increases the effective number of photon energy bins to 767 and gives an energy resolution of 0.001 E_0.

The T-plane lies 20 cm downstream of the E-plane. This plane is used to make accurate timing measurements for the recoiling electrons. It contains 61 counters, each counter is 2 cm thick, and can provide a timing resolution of 110 ps. The T-counters are separated into two groups. The first group has 19 narrower counters, and covers the photon energy from 75% to 95% of the incident electron energy. The second group of 42 counters covers the range from 20% to 75%. The widths of the T-counters vary to compensate for the $1/E_\gamma$ distribution of the bremsstrahlung cross section, and make the counting rate approximately the same within each group. Because the widths of the counters in first group are narrower, the counting rate in the first group is about 1/3 of the second group. (This design is for the experiments that are only interested in high energy photons, the relatively low counting rate allows for operation at higher tagged-photon rates for the high energy photons.) The lengths of the T-counters also vary from 20 cm at the high-momentum end to 9 cm at the low-momentum end in order to compensate for the the bremsstrahlung characteristic angle distribution. The timing information extracted from the T-counter is used to associate photons with events in the CLAS detectors.

The Readout
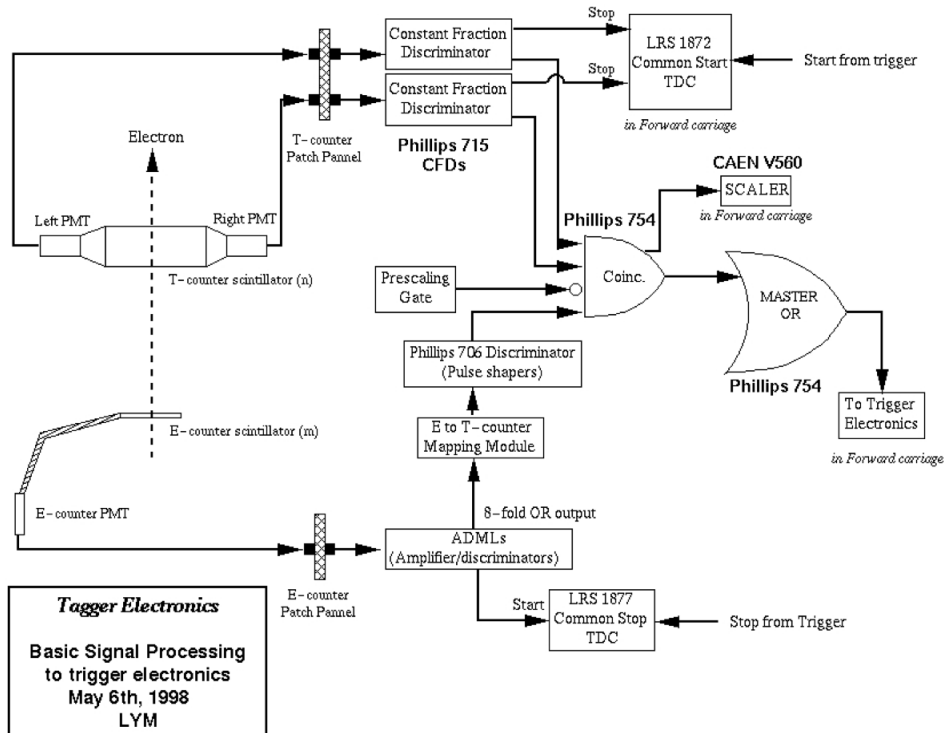
Figure 2.15: Schematic of the tagger readout setup. Image Source: [33]

The signals produced by the scintillators are read out by photomultiplier tubes (PMTs).

Each E-counter has one phototube attached at one end by an optical fiber light guide, each T-counter has two phototubes attached by solid light guides at both ends. T-counter signals are fed to constant-fraction discriminators(CFDs) first, and are then used in two ways. First, the signals from the discriminator are sent to the FASTBUS TDCs (LRS 1872), operating in the common-start mode with a timing resolution of 50 ps/channel. The TDCs are used to extract the timing information from the T-counters and to count the total number of hits recorded in the tagger. The other CFD output establishes a coincidence with a fast AND logic unit between the two PMTs from the same T-counter. Then the output of the AND gate is sent to a Master OR, which sets the trigger for CLAS events. The output of each E-counter PMT is sent to a signal-amplifier, discriminator, multiplexer and logic module (ADML). The outputs from the ADMLs are fed to the FASTBUS TDCs (LRS 1877), running in the common-stop mode with a timing resolution of 500 ps/channel. The TDCs are used to determine which of the E-counters were hit during the time bucket of the trigger. The rest of the signals from the discriminator are used to establish a hardware coincidence between each T-counter and the group of E-counters. The output of the E-T logic unit is fed to one of the inputs of the AND gate for each T-counter for the MASTER OR trigger. However, the output gate width of the E-T logic unit is set to be much longer than the outputs from the T-counter discriminators, so the timing of the event is still determined by the T-counter signal.

During the offline analysis, the timing information from both the E- and T- counters is used to establish the hit pattern and to make tight timing coincidences between the counters to remove background events. The timing information is also used to determine the event start time. The time resolution of the tagger is sufficient to identify the RF beam bucket associated with each photon. By calculating the propagating time of the photon from the radiator to the event interaction vertex, the event vertex time can be determined.

The Collimation System

The collimator downstream the tagger magnet is used to remove the halos of the photon beam, and restricts the size of the photon beam on target. A magnet is placed just downstream from the collimator(a 25 cm long nickel block) to clean up any charged particles created in the collimator walls. The collimator is placed about 14 m downstream the radiator, and trims the diameter of the photon beam so that it is entirely within the target. In the G14 experiment, for the circularly polarized beam, a collimator with a 2.6 mm diameter hole was used. For the linearly polarized beam, a 2.0 mm diameter collimator was used.

2.2.2 The CLAS Detectors

The CEBAF Large Acceptance Spectrometer (CLAS) is used to detect the final state particles in the G14 experiment. It is composed of a toroidal magnet and several layers of sub-detectors. The main CLAS subsystems are the start counter for event triggering and start time measurement for time-of-flight measurement, drift chambers to track the trajectories of charged particles, Cherenkov counters for electron identification, TOF scintillators for time-of-flight measurement, and electromagnetic calorimeters for neutral

particle detection. The Cherenkov counters are only used in electro-production experiments for recoil electron triggering and identification, and will not be discussed here. The polar angle coverage of CLAS for charged particles is $8° < \theta < 142°$, and for neutral particles, it is $8° < \theta < 45°$. The azimuthal angles are mostly covered except for the 6 gaps where the torus magnets are. Figure 2.16 is a schematic diagram showing all the sub-detectors of CLAS, and a photo of it in real life.
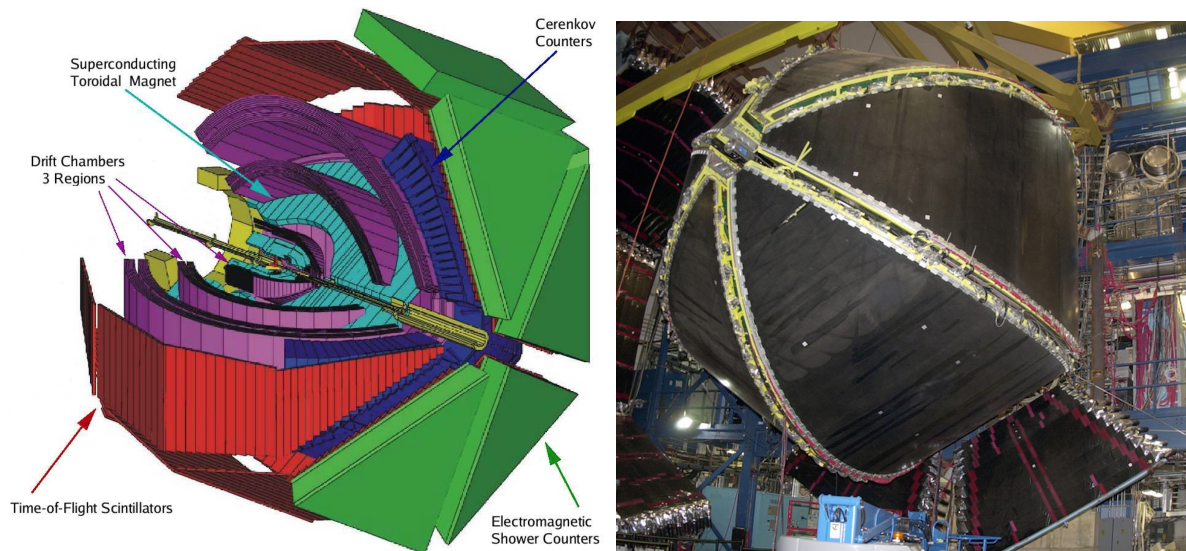
Figure 2.16: Left plot is a schematic diagram for the CLAS detector, right plot is a photo of the CLAS in Hall B during a maintenance period. Image Source: [28]

Torus Magnet

The Torus Magnet is the heart of the CLAS detectors. Its magnetic field gives good momentum resolution for charged particles, provides large angle coverage, and keeps the target region magnetic field free for the use of polarized targets. It consists of six kidney-shaped superconducting coils arranged in a toroidal way around the beam-line, each separated in the azimuthal direction by 60°. This arrangement generates a field mainly pointing in the ϕ direction around the beam-line. Figure 2.17 shows the magnetic field in the middle plane between two coils, and in a plane transverse to the beam and centered on the target. The maximum design current of the torus coils is 3860A. During G14 runs, two torus currents were used, +1918A and -1495A.

Start Counter

The Start Counter is a six sector scintillator detector (Figure 2.18) [37]. Each sector has four scintillator paddles. Each paddle is a single piece scintillator with a straight section 502 mm long, 29 mm wide and 2.15 mm thick with a bend at each end. The upstream bend couples to an acrylic light guide and then to the PMTs; the downstream bend couples to a tapered end to form the "nose".

The Start Counter is used for two purposes. One is for particle identification, this is done by measuring the time-of-flight of the scattered particles from the interaction vertex
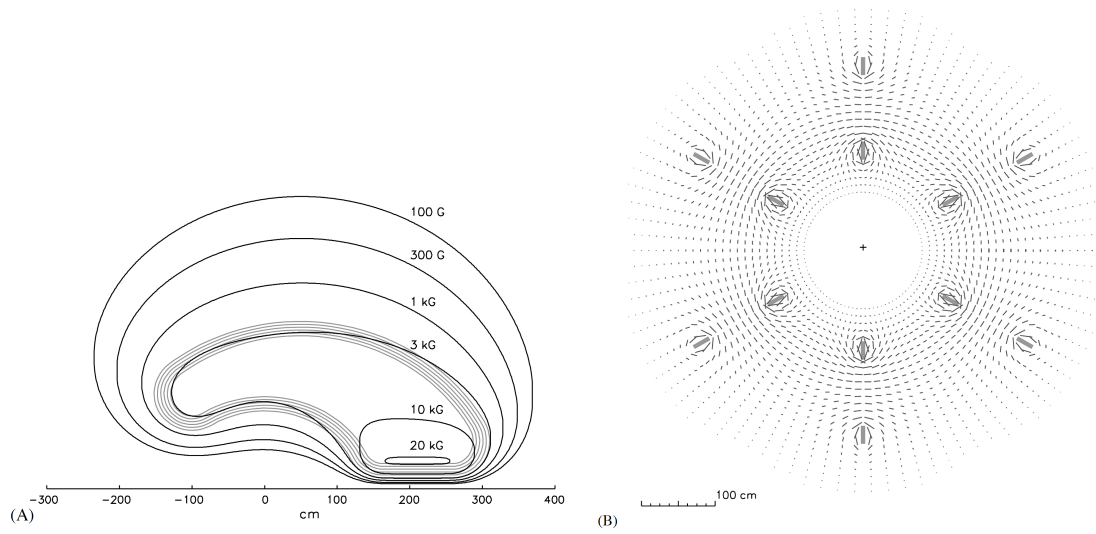
Figure 2.17: (A) Magetic field of the CLAS torus magnet in the middle plane between two coils; (B) Magnetic field vectors of the CLAS torus magnet in the plane transverse to the beam and centered on the target. Image Source: [29]
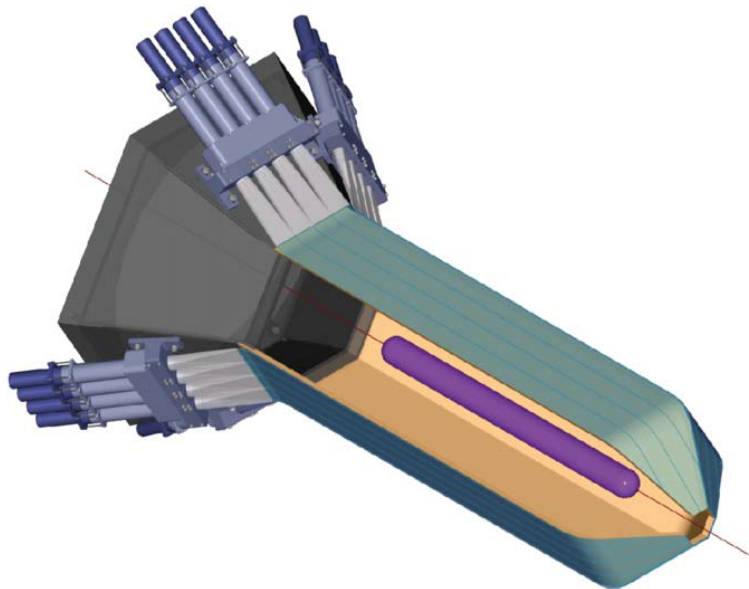
Figure 2.18: Start Counter. Image source: [37]

to the TOF or EC. The interaction time is determined from identification of the photon beam bucket that produced the hadronic interaction. Since the photon beam buckets have 2 ns intervals, a sub-nanosecond coincidence of the Start Counter with the Tagger T-counter is required for this purpose. For a confidence interval of 99% and a Gaussian time distribution, the Start Counter needs to have resolution less than 388 ps. With good identification of the photon bucket, the RF time gives the start time of the scattering particle trajectory with a resolution of less than 25 ps.

The other use of the Start Counter is to define the trigger for photon runs. As shown in Figure 2.19, the Start Counter signals are used in two parts of the Level 1 trigger: the synchronous leg, and the asynchronous leg. In the synchronous leg, for each of the six sectors, 4 discriminated PMT signals and the corresponding TOF, EC PMT signals are fed into a synchronous memory lookup unit. If the required topology is found, a trigger signal is generated. In the asynchronous leg, the 24 Start Counter signals from the CAMAC C207 discriminators are combined in an OR circuit, the output of the OR circuit and the MOR signal from the tagger are ANDed to form the fast asynchronous (ASYNC) signals. The trigger signals from the synchronous leg and the ASYNC signals from the asynchronous leg are fed into a final memory lookup unit. If the desired logic is met, the trigger supervisor will generate a signal to initiate the digitization and readout of the event.
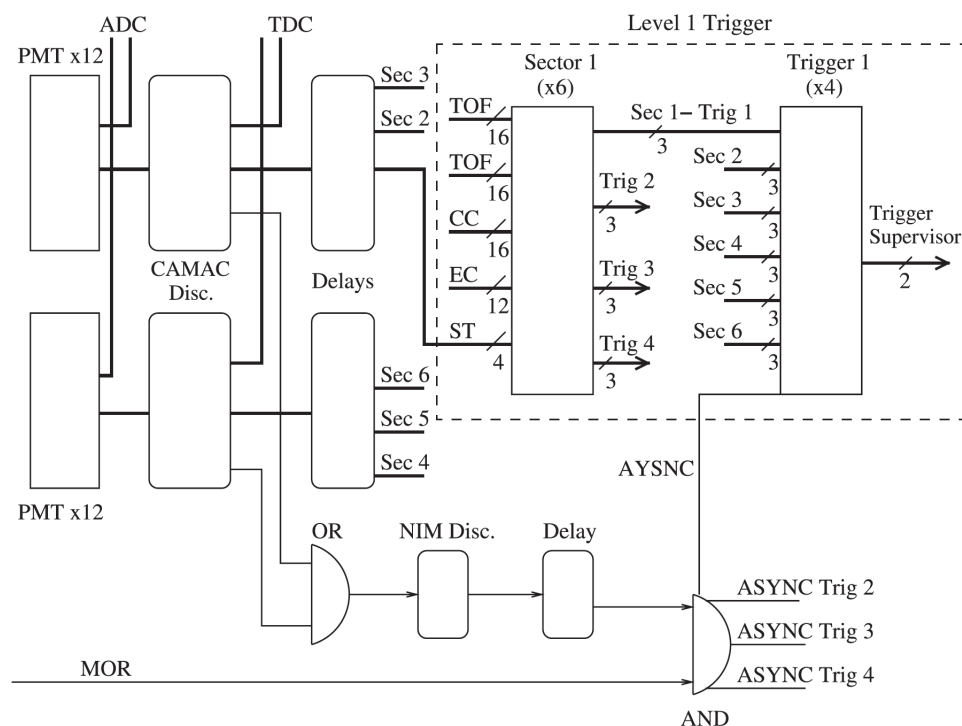
Figure 2.19: Start Counter trigger logic.

Drift Chambers

The Drift Chambers are used to reconstruct the trajectories of the charged particles emerging from the target with momenta greater than 200 MeV/c. When the charged

particles pass through the gas inside the drift chamber, they ionize the gas and produce free electrons and ions, the static electric field in the detector drifts the electron cloud to the anode, and produces a signal. The goals for the track resolution for 1 GeV/c charged particles are $\delta p/p \leq 0.5\%$, and $\delta\theta, \delta\phi \leq 2$ mrad. In order to achieve these goals, the tracks are measured at three locations in the three "Regions" (R1, R2, R3) of the Drift Chambers. Since the Torus Magnet coils separate the detector into six independent sectors, in total there are 18 separate drift chambers located at three radial locations in the six sectors. The six "Region One" chambers are inside the torus coils, where the magnetic fields are low. The six "Regions Two" chambers are placed between the torus coils in an area of high magnetic field, where the maximal curvature of the particle's trajectory is. The six "Region Three" chambers are situated outside the torus coils. This setup provides a polar angle coverage from 8° to 142°, and an azimuthal angle coverage up to 80%. A schematic view of the three regions of the Drift Chambers is shown in Figure 2.20.
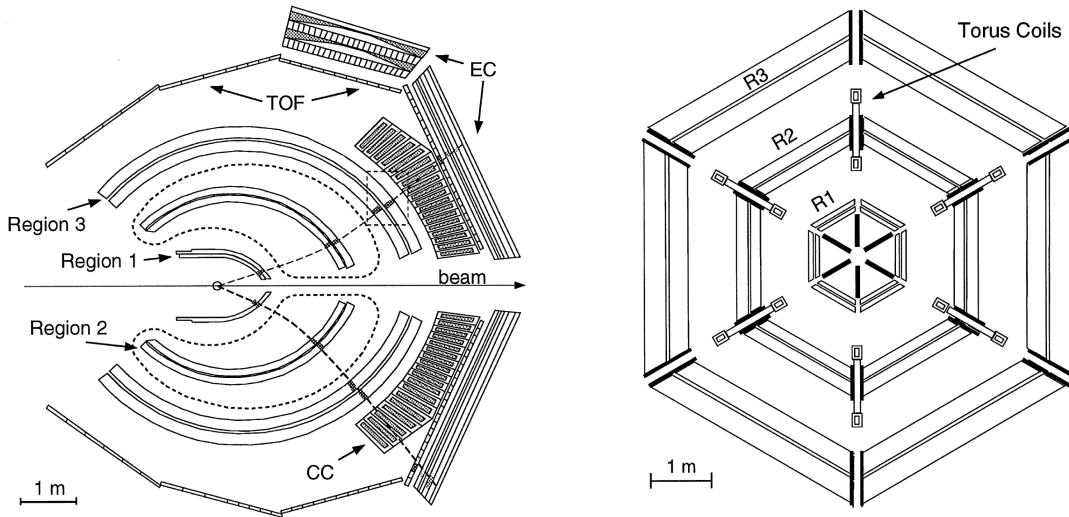
Figure 2.20: Horizontal cut and Vertical cut of the Drift Chambers. Image Source: [29]

In each of the 18 Drifter Chambers, the wire layers are grouped into two "super-layers". In one group, the wires are aligned along the magnetic field, and in the other group, the wires are tilted at a 6° stereo angle around the radius to provide azimuthal information. Inside each super-layer, the wire positions are shifted by half the nominal spacing in successive layers with the repeating pattern of two field-wire layers and one sense-wire layer. This arrangement results in a quasi-hexagonal cell as shown in Figure 2.21. Each cell has one sense wire in the middle, surrounded by six field wires. The distance between the field and sense wires increases uniformly with increasing distance from the target. The average distance between the field and sense wires is 0.7 cm in R1, 1.5 cm in R2, and 2.0 cm in R3. Each R2 and R3 sector consists of 12 layers of sense wires; the 6 axial layers are at smaller radius, and 6 stereo layers are at larger radius. For R1 sectors, there are only 10 layers because of the limited space, and the arrangement of stereo and axial layers is opposite to R2 and R3, with the 4 stereo layers at smaller radius and 6 axial layers at larger radius. A 88% argon and 10% CO_2 mixture gas was chosen for the chamber gas. This mixture is non-flammable, and has reasonably low multiple

33

scattering, good efficiency, and short collection times. To keep constant pressure in the chamber, an active feedback system is used to make small adjustments to the out-flow.
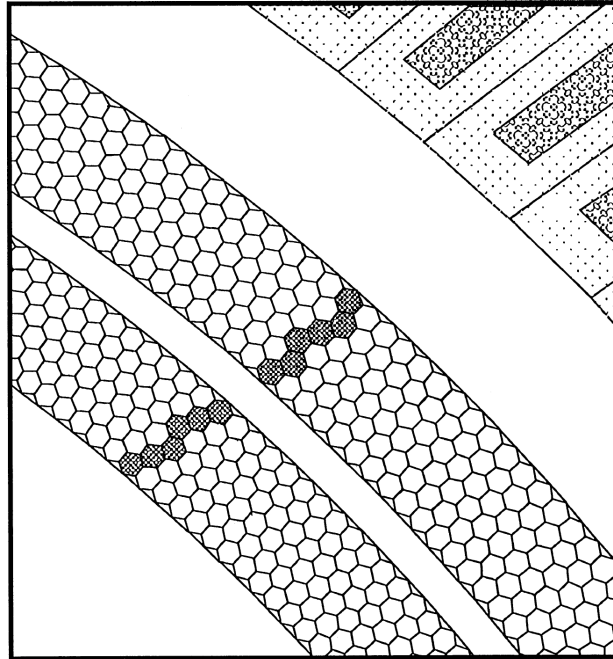
Figure 2.21: Schematic representation of portion of an R3 drift chamber. There are two superlayers with 6 layer of drift cell in each superlayer. The sense wires are at the center of each hexagon and the field wires are at the vertices. Image Source: [29]

Time-of-flight counters

The TOF system is used for particle identification, CLAS Level 1 trigger, and energy-loss measurements. It covers an area of 206 m^2, which fills all 6 sectors of the CLAS in the azimuthal direction, and from 8° to 142° in the polar direction. The scintillators are positioned between the Cherenkov detectors and the forward electromagnetic calorimeter, as shown in Figure 2.16. The system is composed of 342 scintillation counters with nominal thickness of 2 in. (5.08 cm), the forward-angle system has 15-cm wide and 32 to 376 cm long scintillators, the large-angle system has 22-cm wide and 371 to 445 cm long scintillators. As shown in Figure 2.22, the 57 scintillators are grouped in four panels in each of the six CLAS sectors. Counters 1-22 in panel 1 are called the forward-angle system, they cover the polar angle up to 45°. Counters 23-57 in panel 2,3,4 are refereed as large-angle system. The high segmentation of the TOF system is for achieving excellent timing resolution, the time resolution of the system determined by cosmic-rays is shown in Figure 2.23.

Forward Electromagnetic Calorimeter

The forward electromagnetic calorimeter (EC) is used in G14 experiment for detection of photons with energies above 0.2 GeV and neutrons. The detected photons are used to reconstruct π° and η from the 2γ decays. The discrimination between photons and
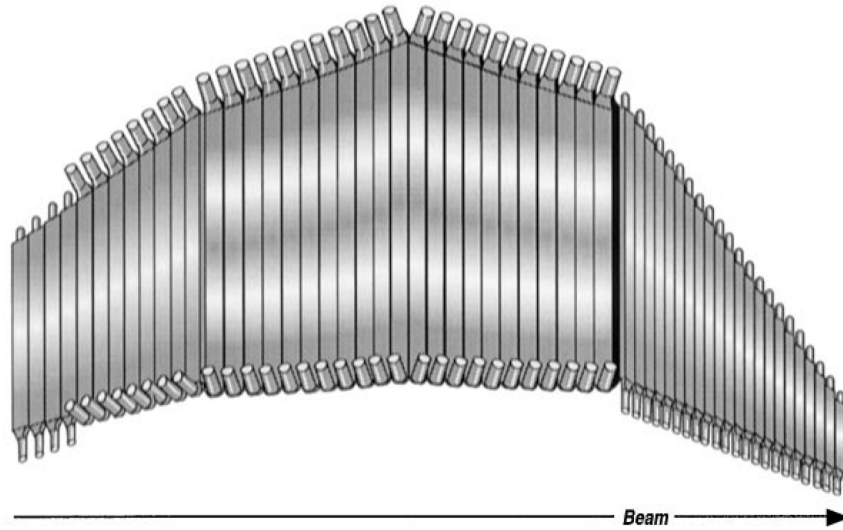
Figure 2.22: Four panels of the TOF scintillatros in one CLAS sector. The forward-angle scintillators have short stubby light guides and 2 inch PMTs. The large-angle scintillators, except for the last four, have bent light guides and 3 inch PMTs. Image Source: [38]
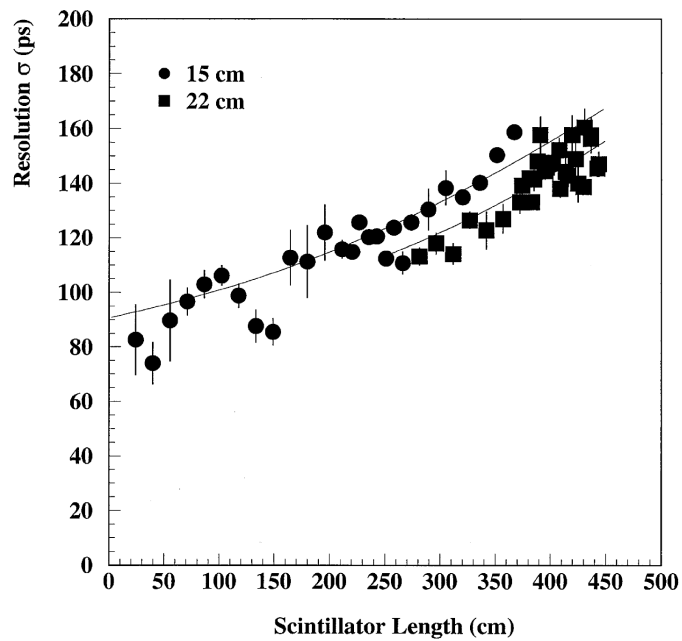
Figure 2.23: The timing resolution as determined from cosmic-ray tests for all counters. Image Source: [38]

35

neutrons is from the β value from the time of flight measurement. The mass separation of π° and η requires the detection of photons has an energy resolution $\sigma/E \leq 0.1/\sqrt{E(GeV)}$ and a position resolution $\delta r \approx 2$ cm at 1 GeV. To distinguish photons from neutrons requires the time resolution ≈ 1 ns.

The EC covers the θ range up to $45°$. This system uses a sampling calorimeter made of alternating layers of scintillator strips and lead sheets. The ratio of the thickness of the lead to scintillator is 0.24, with 39 cm thickness of scintillator and 8.4 cm thickness of lead.

There are six EC modules to match the hexagonal shape of the CLAS. Each module is contained in a volume with the shape of an equilateral triangle. There are 39 layers in each module, which consist of a 10 mm thick scintillator followed by a 2.2 mm thick lead sheet. Along the direction pointing away from the CLAS target, the area of each successive layer increases, this "projective" geometry minimizes the shower leakage at the edges of the active volume. Each scintillator layer is made of 36 strips parallel to one side of the triangle, with the orientation of the strips rotated by $120°$ in each successive layer as shown in Figure 2.24. This arrangement results in three views (labeled U, V and W), and provides stereo information of the location of energy deposition. Each stereo view contains 13 layers, which are further subdivided into an inner (5 layers) and outer (8 layers) set. Each set is connected to an PMT as shown in Figure 2.25. Thus, each module needs 36 (strips) $\times$ 3 (views) $\times$ 2 (sets) $=216$ PMTs, and all six modules need 1296 PMTs.
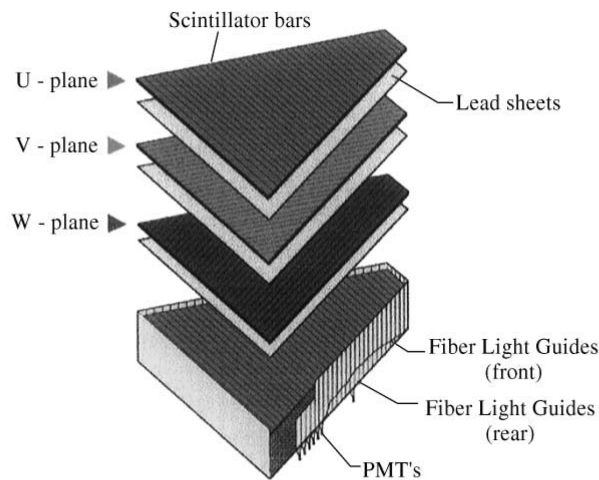
Figure 2.24: The U-, V- and W-plane of the electromagnetic calorimeter. Image Source: [39]

The reconstruction of an EM shower event requires a peak in all three views U, V and W. An algorithm is used to check the peak position, and the peak energy to confirm a hit of a particle in the EC. A reconstructed EM shower event is shown in Figure 2.26.
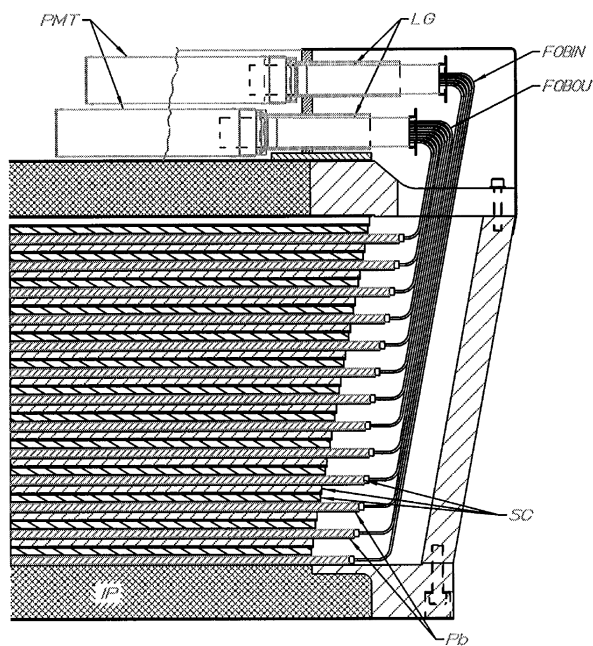
Figure 2.25: EC light readout system. PMT-photomultiplier, LG-light guide, FOBIN-fiber optic bundle inner, FOBOU-fiber optic bundle outer, SC-scintillators, Pb-2.2 mm lead sheets, IP -inner plate(closest to target). Image Source: [39]
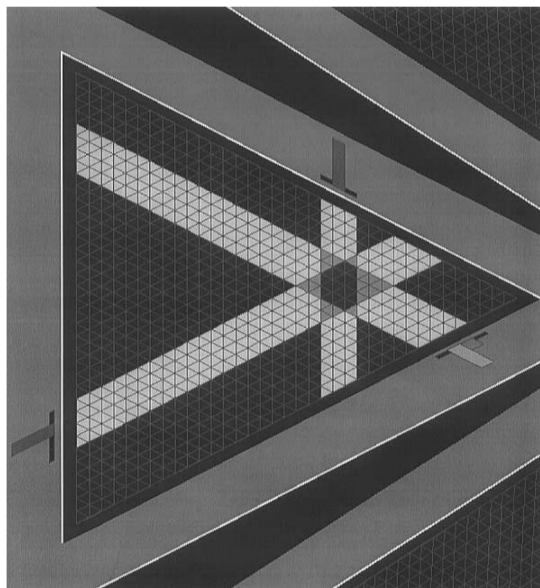
Figure 2.26: The diagram of an event reconstruction in EC. Image Source: [39]

2.2.3 Beam-line Devices

Beam Position Monitors: BPMs

The Beam Position Monitors (BPMs) are used to measure continuously the position of the electron beam entering Hall B. The BPM is composed of three RF cavities. For the G14 experiment, two BPMs were used at two different positions. The 2C21A BPM is placed 36 m upstream of the target, the 2C24C is placed 24.6 m upstream of the target. The BPMs provide the electron beam position (x,y) and intensity, this information is used continuously in the feedback loops to keep the electron beam centered, and the position and current information is also written in the data stream every 20 seconds.

Beam Profile Monitors: Harps

The Beam Profile Monitors measure the electron beam profile by moving thin wires through the beam. As the crossed wires (horizontal and vertical) move across the beam-line along the 45° angle with respect to the horizontal axis, the scattered electrons are measured by the Cherenkov light in the glass windows of the PMTs. Figure 2.27 shows the results of a harp scan during the G14 experiment. The harp scan intercepts the beam, so this procedure occurs when CLAS is not taking data and is performed after any major change to the electron beam.
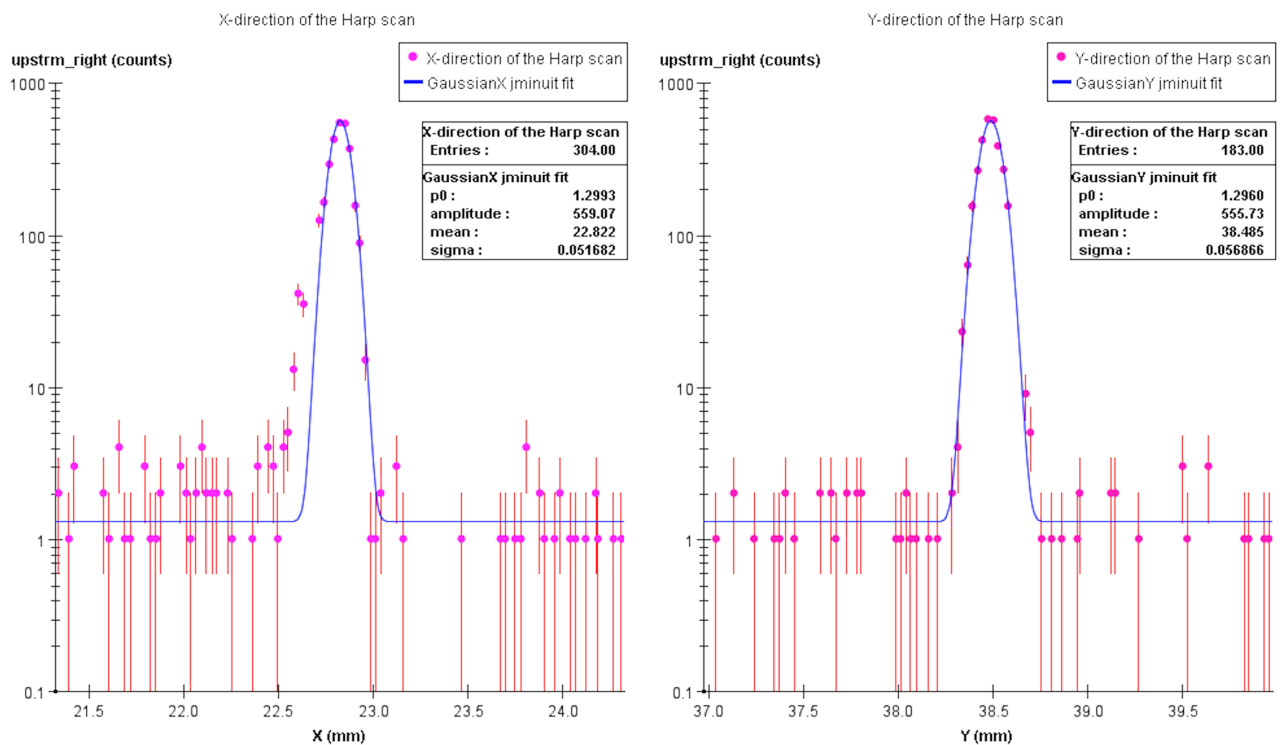
Figure 2.27: The electron beam profile from a harp scan during the G14 experiment.

Beam Polarization: Møller polarimeter

The polarization of the electron beam used in Hall B is measured by a Møller polarimeter. The polarimeter is located in the beam-line upstream of the bremsstrahlung tagging system (Figure 2.9). The schematic diagram of the system is shown in Figure 2.28. The asymmetry in the elastic electron-electron (Møller) scattering is measured by the two detectors, which gives the polarization of the electron beam.
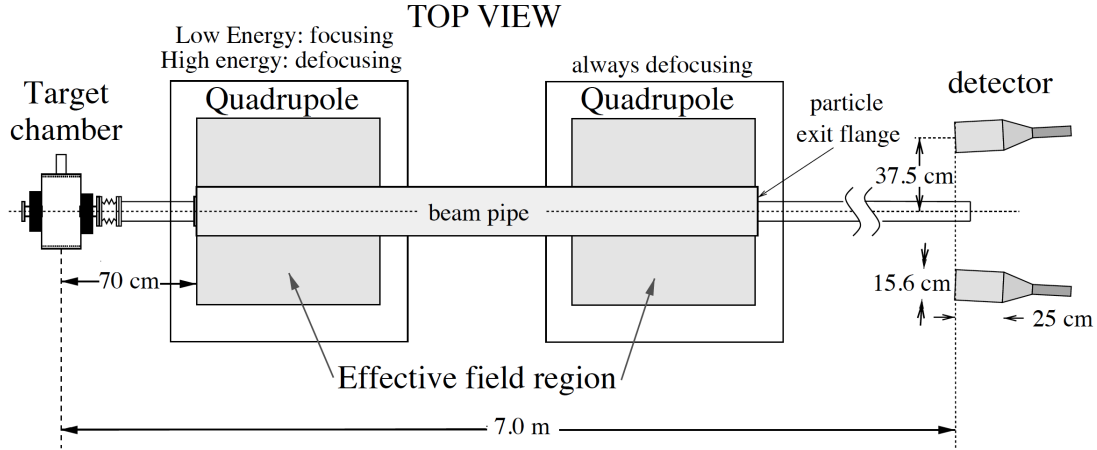
Figure 2.28: The schematic diagram of the Hall B Møller polarimeter. Image Source: [33]

Photon Flux: Total Absorption Shower Counter and Pair Spectrometer

The Total Absorption Shower Counter (TASC) at the end of the beam-line is used for measuring the photon flux. The TASC is a lead glass scintillator array, with close to 100% photon detection efficiency at low photon flux. The reason the TASC is placed at the end of the beam-line is that not all the tagged photons arrive at the target; some of them are lost due to the collimation and dispersion. The tagging ratio $\epsilon = \frac{N^T \bigotimes TASC}{N^T}$ is used to calculate the number of photons reaching the target, in which $N^T \bigotimes TASC$ is the number of "good" hits in the tagger in coincidence with the photons measured by the TASC, and N^T is the total number of "good" hits in the tagger. The tagging ratio is only calculated in the normalization runs, which have very low fluxes (beam currents up to 100 pA).

The TASC must be retracted from the beam-line during the production runs. Thus, secondary monitors, with absolute efficiency of only a few percent but linear in flux over a wide range, are cross-calibrated against the TASC at low rates and used to determine the flux at higher rates. Two devices are used as the secondary monitors, the Pair Spectrometer(PS) and the Pair Counter(PC). They are placed in front of the TASC as shown in Figure 2.29. The Pair Spectrometer consists of a thin conversion foil, a large aperture dipole magnet and eight scintillator counters. A photon hitting the thin converter produces e^+e^- pairs, which are dispersed by the magnetic field and then detected in the eight scintillator counters. The pair counter is a much simpler device, and is used as a backup intensity monitor.
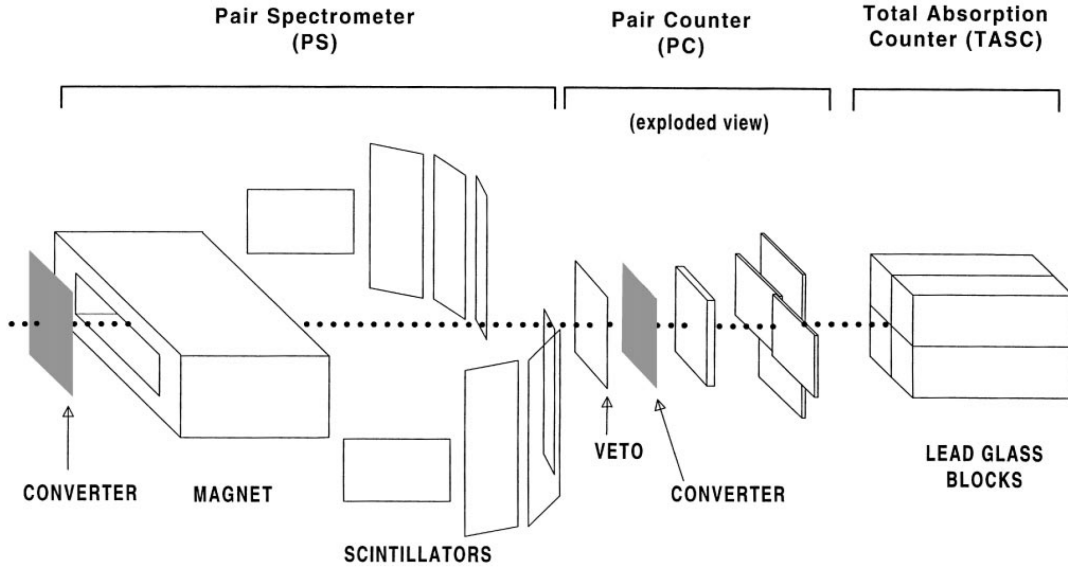
Figure 2.29: Layout of the flux monitoring devices. Image Source: [29]

2.2.4 Trigger and Data Acquisition System

Trigger System

Each of the CLAS subsystems is actively run and generates signals, but not all signals are worth recording. Background signals such as the signals from cosmic rays or electronic noise should be rejected. The CLAS uses a two-level hierarchical trigger system to acquire events of interest. This system consists of three parts: Level 1 trigger, Level 2 trigger and Trigger supervisor.

The Level 1 trigger is deadtime-less, and uses any or all available information from PMT channels to select the desired events. The information used in the Level 1 trigger includes the signals from the Start Counters, the TOF Counters and the tagger Master OR output. Preloaded trigger definitions are programmed in the hardware memory, and the signals are processed through a 3-stage memory lookup to generate an event trigger.

The Level 2 trigger uses the track information from the Drift Chambers. It is designed to reject events from cosmic-rays that can set the Level 1 trigger but lack matching tracks in the Drift Chambers. If no track candidates are found, a fast-clear signal is issued.

The Trigger supervisor (TS) takes the Level 1 and Level 2 triggers as inputs and produces the common signals, busy gates, and resets for the detector electronics. The TS can be programmed in two configurations. The first configuration (CLASS 1) requires that the event passes only the Level 1 trigger, the second configuration (CLASS 2) requires both Level 1 and Level 2 confirmations. After the event passes the TS requirement, it is placed on the readout queue for asynchronous readout.

Data Acquisition System

The Data Acquisition System (DAQ) is used to manipulate and record data from various CLAS subsystems. The data flow is shown in Figure 2.30. Firstly the data are digitized in 24 FASTBUS and VME crates in the experiment hall and collected by the Readout

Controllers (ROC1 to ROC24). Then the data arrays are buffered and transferred to the CLAS online acquisition computer (CLON10) in the control room via fast Ethernet cables. The CLON10 computer carries out three primary processes, the Event Builder(EB), Event Transport (ET), and Event Recorder (ER). The EB assembles the data arrays, or event fragments, into complete events, which are labeled by a run and event number, and event type, and trigger bits that are all contained in a header bank. The completed events from the EB is then passed to shared memory (ET1). ET1 can be accessed by several processes, the ER takes all events for permanent storage, part of the events from ET1 are transferred to remote ET systems (ET2 and ET3) for raw data checks and online reconstruction. The ER writes the data in a single stream to an array of local magnetic media (RAID disks), the data files are then transferred to the remote tape silo by a fiber link from the local RAID in the control room to the computer center a kilometer away.
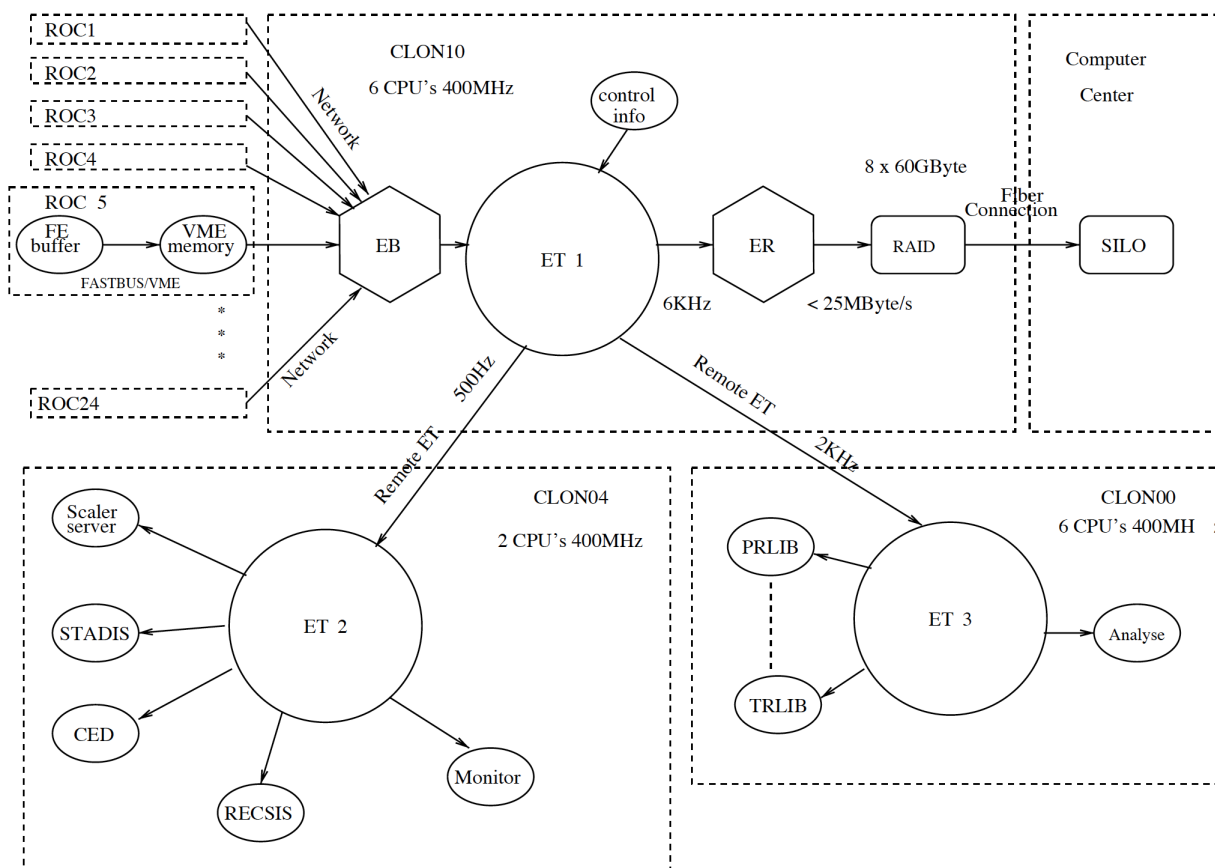
Figure 2.30: The data flow diagram for CLAS DAQ. Image Source: [29]

2.3 HD-ice Target

HD-ice is a frozen spin target of solid hydrogen deuteride. It has many attractive features, such as low Z, high dilution factor (all protons and neutrons in HD are polarizable), long spin-relaxation time, and freedom of transferring polarization between H and D. Figure 2.31 shows what the target looks like. The cell walls are made from C_2ClF_3(poly-

chloro-tri-fluor-enthylene), which is a hydrogen-free polymer that minimizes the NMR backgrounds for H. Aluminum wires are put in the target to extract the heat from HD. The aluminum wires are soldered to a copper ring, which is thermally anchored to a cold bath. The target has 0.4 moles of HD, which at 1K occupies a cylindrical volume 1.5cm in diameter and 5.0cm in length. The composition of a standard HD target is: 77% HD, 17% Al($750 \times 50\mu$ Al wires) and 6% C_2ClF3.

Figure 2.31: HD-ice target cell used in G14 experiment. Image source: [41].

2.3.1 Basic HD physics

Polarized targets are essential in nuclear physics, since they can provide access to the spin structure of the nucleon. One often measured observable is the double spin asymmetry:

$$A^{exp} = \frac{N(\rightarrow\Rightarrow) - N(\leftarrow\Rightarrow)}{N(\rightarrow\Rightarrow) + N(\leftarrow\Rightarrow)} = P_B P_T f A^{phys}$$

$$\frac{\delta A^{exp}}{A^{exp}} = \frac{1}{\sqrt{2N} P_B P_T f A^{phys}},$$

(2.2)

where $\rightarrow$ is the direction of beam polarization, $\Rightarrow$ is the direction of target polarization, P_B is beam polarization, P_T is target polarization, f is dilution factor, N is number of events. In order to get big signal for A^{exp} and small $\frac{\delta A^{exp}}{A^{exp}}$, we need big P_B, P_T and f. HD has the highest content of polarizable nucleons(f), compared with other solid polarized targets such as the butanol(C_4H_9OH), ammonia(NH_3, ND_3), and Lithium deuteride(^6LiD). The HD molecule has no limitation of symmetry, both its proton and deuteron can be polarized by aligning their spins with a magnetic field.

At its lowest energy state with no phonon coupling in solid HD crystal, it's spin-relaxation time is very long(years). But it also means that to polarize pure HD would need a long time. This problem can be solved by adding a small amount of H_2 and $D_2(\sim 10^{-4})$ in the target. The H_2 and D_2 molecules have two spin isomers with spins

either parallel (ortho-H_2, para-D_2) with total molecular nuclear spin $I_{molecular} = 1$ or antiparallel (para-H_2, ortho-D_2) with total molecular nuclear spin $I_{molecule} = 0, 2$. The name para or ortho is determined by spin degeneracy(g_I) of the species, the one with larger spin degeneracy is named ortho as in Table 2.1.

Molecule(I_N)	$I_{mol}(\Phi(I_{mol}))$	$J(\Phi(J))$	$\Phi(r)$	Φ_{total}	g_I	Isomer
Hydrogen (1/2)	0 (AS)	Even (S)	S	AS	1	para
	1 (S)	J=Odd (AS)	S	AS	3	ortho
Deuterium (1)	1 (AS)	Odd (AS)	S	S	3	para
	0, 2 (S)	Even (S)	S	S	6	ortho

Table 2.1: Nuclear spin states and rotational states for hydrogen and deuterium. I_N is spin of nucleon, I_{mol} is molecular nuclear spin, J is rotational state, g_I is nuclear weight. AS(S) is abbreviation for antisymmetric (symmetric). $\Phi(r), \Phi(J), \Phi(I_{mol})$ are the vibrational, rotational and nuclear wave functions. Φ_{total} is the total wave function, which is a product of vibrational, rotational and nuclear wave functions. Since the nucleons inside H_2 (D_2) are identical particles, their wave functions are restricted by special symmetries. Since the proton(deuteron) is a fermion (boson), the total wave function of $H_2(D_2)$ is AS(S). Table source [44].

The polarization of H in HD uses both species of H_2. At room temperature, the normal-H_2 has both para and ortho species. The thermal equilibrium between para- and ortho-H_2 is governed by Boltzmann's law. From Table 2.1, we know that para-H_2 has even and ortho-H_2 has odd rotational quantum numbers, the ratio (β) can be expressed by Equation 2.3 [45].

$$\beta = \frac{[p - H_2]}{[o - H_2]} = \frac{\sum\limits_{J=even} (2J + 1)e^{-E_J/kT}}{3 \sum\limits_{J=odd} (2J + 1)e^{-E_J/kT}} \tag{2.3}$$

At high temperatures limit ($E_J << kT$), $\beta = 1/3$. Since the transition from the ortho state to the para state is forbidden, if the H_2 is cooled down to the solid state, almost all the para-H_2 falls into the $J = 0$ state and the ortho-H_2 falls into the $J = 1$ state, and these two rotational states have an energy gap of 172 K ($\frac{E_{J=1} - E_{J=0}}{k_B}$) in the temperature units. In the solid state (T = 4 K), the interactions between molecules can cause conversion from ortho-H_2 to para-H_2 with a decay constant of 151 hours.

The process of polarization can be described in four steps as in the Figure 2.32.

1. HD is cooled down to the solid state (T = 4 K), almost all H_2 falls to the molecular states $I = 1, J = 1$(ortho-H_2, 75%) and $I = 0, J = 0$(para-H_2, 25%), in which ortho-H_2 has a very short T_1 and can be polarized by an external field very fast.

2. The protons in the ortho-H_2 are cross-relaxed with the protons in the HD. The H polarization in ortho-H_2 is transferred to the HD through spin-exchange [40].

3. Since HD is a quantum solid, the wave function of adjacent HD molecules overlap each other, spin of H will diffuse inside HD. In this way, the HD molecules far away from the ortho-H_2 also get polarized.

43
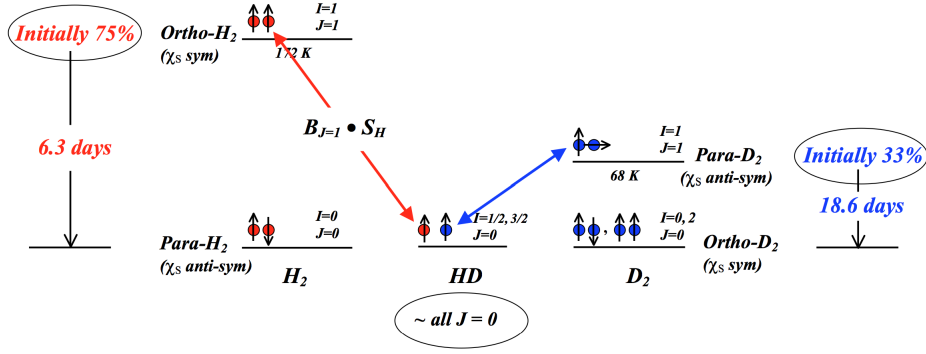
Figure 2.32: Polarization mechanism for HD-ice target. Image source: [41].

4. Since the nuclear spin interaction between the nucleons in two different atoms is weak, the decay of ortho-H_2 to para-H_2 is forbidden, which provide enough time for ortho-H_2 to polarize the HD. After several half times, most ortho-H_2 molecules decay to para-H_2. Para-H_2 is $J = 0$ state, which is symmetric and generates no external field. There is no dipole interaction between para-H_2 and HD, leaving the HD target in a frozen-spin state.

The H_2 impurity plays a role of "switch" for the frozen spin state of HD. Ortho-H_2 shortens T_1^H for HD, which speeds up ("turns on") the polarization of H in HD. As ortho-H_2 decays to para-H_2, T_1^H grows longer for HD, which slows down ("stops") the polarization process, and HD becomes a frozen spin state. In practice, the commercial HD gas already contains about 1.5% of H_2 and 0.5% of D_2, the HD gas must be purified to the desired level of 10^{-4}.

The D in HD can be polarized in a similar way. The equilibrium H and vector-D polarization is described by the Brillouin function (Eq. 2.4):

$$P_{TE}(x, I) = \frac{2I+1}{2I} \coth(\frac{2I+1}{2I}x) - \frac{1}{2I} \coth(\frac{x}{2J}), \qquad (2.4)$$

where $x = \frac{\mu B}{k_B T}$, I is nuclear spin(1/2 for H, 1 for D). Since $I_D = 1$, deuteron has both vector polarization ($P_V(D)$) and tensor polarization ($P_T(D)$) (Eq. 2.5):

$$\begin{aligned}
P_V(D) &= \frac{N(I_z = 1) - N(I_z = -1)}{N(I_z = 1) + N(I_z = -1) + N(I_z = 0)}, \\
P_T(D) &= \frac{N(I_z = 1) + N(I_z = -1) - 2N(I_z = 0)}{N(I_z = 1) + N(I_z = -1) + N(I_z = 0)}.
\end{aligned} \qquad (2.5)$$

In thermal equilibrium, the population of $I_z = 0$ is the geometric mean of ± 1 states, which gives $P_T(D) = 2 - \sqrt{(4 - 3(P_V(D))^2)}$. The current setup can reach $B = 15T$ and $T = 12mK$, which can produce $\sim 90\%$ polarized H and $\sim 30\%$ polarized vector D. However, the decay of ortho-H_2 to para-H_2 generates heat, which makes temperature higher than $12mK$ during polarization, and T_1^H becomes very long as most of ortho-H_2 decay, ideal thermal equilibrium will not be achieved, so the final polarizations of H and D are lower than the above values. Polarization of $\sim 60\%$ for H and $\sim 15\%$ for D) have been achieved in HD-ice lab as shown in Figure 2.33.

44
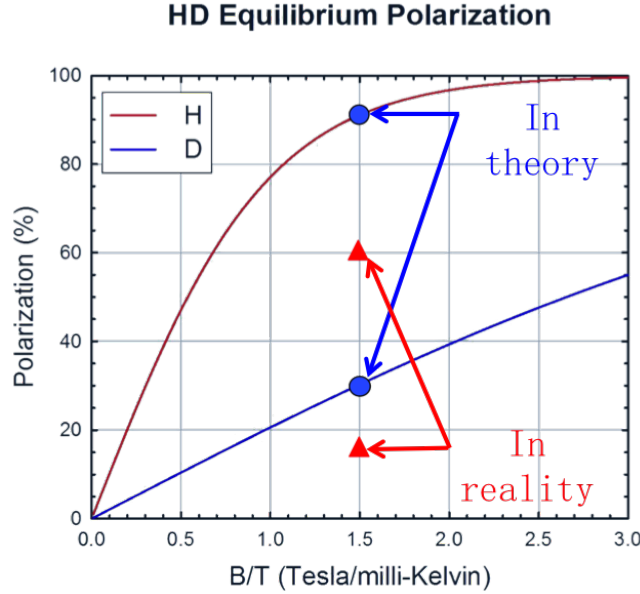
Figure 2.33: HD polarization in theory and in reality. For a magnetic field of 15 T and temperature of 12 mK, polarizations of $\sim 90\%$ for H and $\sim 30\%$ for D are expected in theory; $\sim 60\%$ for H and $\sim 15\%$ for D are achieved in reality.

The polarization of D can be further increased by transferring polarization from H to D via RF transition [46, 47]. The transferring mechanism is shown in Figure 2.34. The transitions between the mixed state $|m_H, m_D >$ are referred as Forbidden Adiabatic Fast Passage (FAFP). It is "Forbidden", because the transitions move polarization from H in one molecule to D in a neighboring molecule via the inter-molecular dipole-dipole coupling, and it is a two-photon process with RF frequency equal to the difference of the H and D Larmor frequencies ν(H-D) = 36.0416 MHz/Tesla. The intra-molecular dipolar coupling of H and D in the same HD molecule averages to zero, because at this low temperature, almost all HD molecules are in the J=0 rotational state. The term "Adiabatic" refers to the fact that the time scale for the process is relative long with respect to the Larmor frequencies, and "Fast" is with respect to the spin-relaxation times. The "Forbidden" transitions require very high power to flip the spins. This would raise the temperature of the dewar and result in a loss of frozen-spin polarization. The method the HD-ice group uses is to saturate the RF transition over a long period of time (~ 15 min) with low-power RF, which equalizes, instead of reverses, the populations of the $m_H = +1/2; m_D = -1, 0$ and $m_H = -1/2; m_D = 0, 1$ states. This method has boosted the deuteron vector polarization ($P_V(D)$) from 15% to 27%.

2.3.2 Cryostats for HD target

The production and use of the polarized HD target is more complicated than that of the conventional polarized nuclear targets. In the lifetime of a HD target, it goes through 5 different cryogenic systems: production dewar (PD), transfer cryostat (TC), dilution refrigerator (DF), storage dewar (SD), in-beam cryostat (IBC).
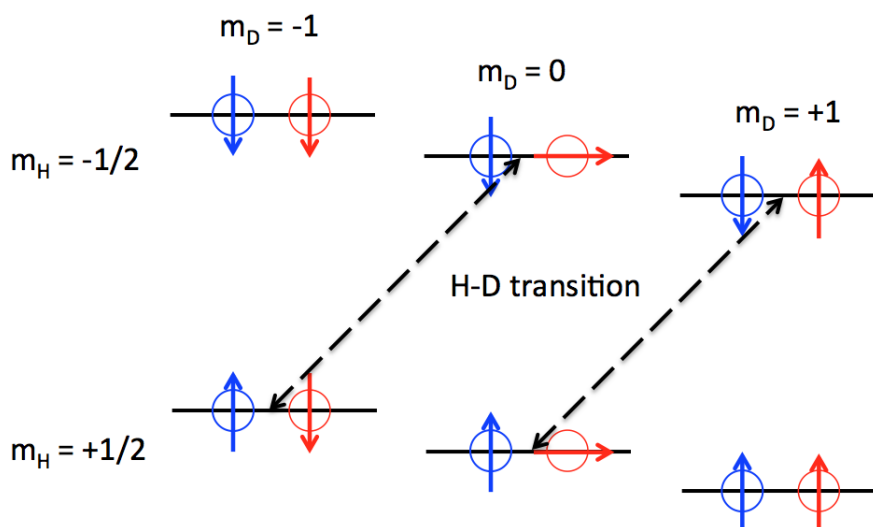
Figure 2.34: Magnetic energy levels for dipole-dipople coupled mixed state $|m_H, m_D >$ between neighboring HD molecules. The two photon transitions with the difference of the H and D Larmor frequencies are shown as dashed lines.

Production dewar

The PD (production dewar) is a stock Janis cryostat, which has a pumpable vari-temp system in a liquid helium bath with a liquid nitrogen space and shield (Figure 2.38). Within the varitemp space is a custom-built insert holding the HD target and NMR coils. The PD is used as the crystat for condensing the HD and calibrating the NMR signals for polarization calculations. It has a 2 T magnet and the varitemp space can be cooled below 2 K. After the condensation and NMR calibration, the HD target is moved to the dilution refrigerator using the transfer cryostat.

Transter cryostat

The TC (transfer cryostat) is a tool to relocate the target from one cryostat to another. It has a left-hand threaded coldhead on the end of a liquid helium tube, which can be extended into the cryostat, and be used to capture the HD target with the matching threads between the TC and the target cell (Figure 2.36). The liquid helium volume of the TC can be pumped to cool the coldhead below 2 K. The cylindrical LHe tube is separated by vacuum from the surrounding LN_2 toroidal volume, and then surrounded by an insulating vacuum space formed from highly compressible bellows (Figure 2.37). A cylindrical permanent magnet array (Halbach magnet) produces a magnetic field of 0.1 T to keep the target polarization. Since the HD target has the shortest T_1 in the TC compared with the other 4 cyrostats (the smallest B/T), minimizing the time for the target inside TC is preferred. With the failure rate of less that 5% per transfer, the overall success rate exceeds 75% for using the HD target, which requires 5 transfers.
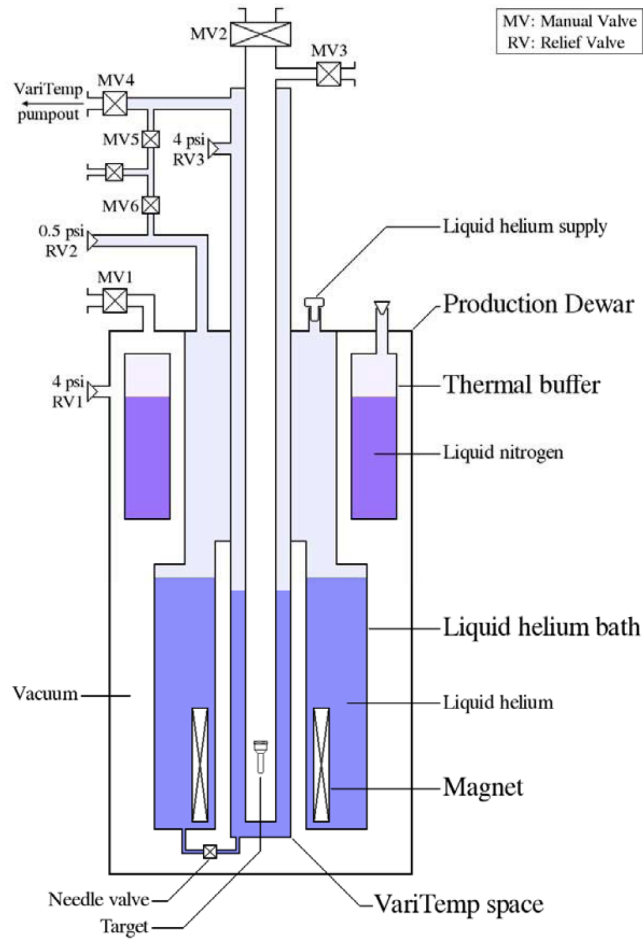
Figure 2.35: Schematic plot of the production dewar. Image source: [49].
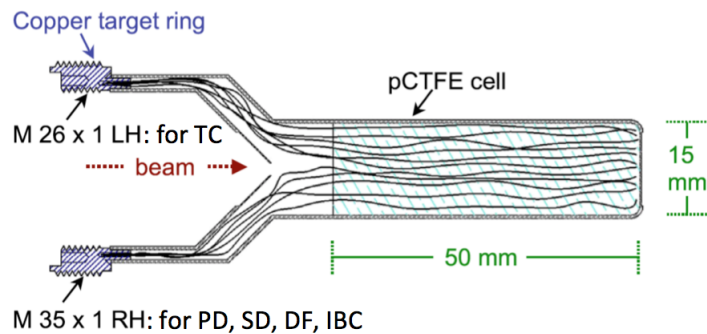
Figure 2.36: Threads on the copper target ring for relocating the target. The interior lef-handed threads match the threads on coldhead of the TC, the exterior right-handed threads match the theads of the cryostats, such as PD, DF, SD, IBC. Image source: [48].
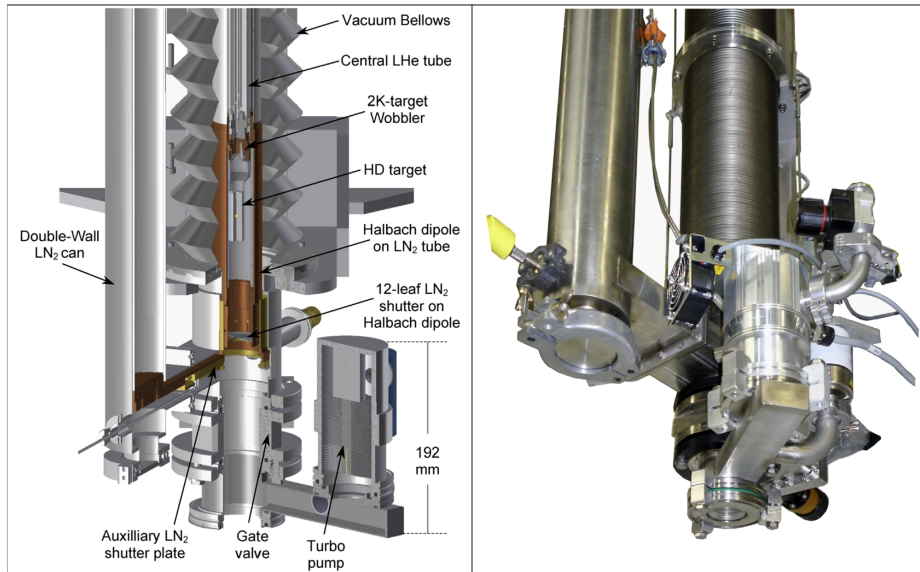
Figure 2.37: A schematic plot (left) and a photo (right) of the TC (transfer cryostat). Image source: [48].

Dilution refrigerator

The DF system consists of an Oxford Instruments dilution refrigerator and a large magnet system. The dilution refrigerator has a base temperature of about 8 mK without energizing the magnet, and a base temperature below 10 mK with the magnetic field energized up to 15 T. The DF is able to polarize up to 3 targets at the same time.

Storage dewar

The SD (storage dewar) is also a stock Janis cryostat, which has a bigger magnetic field (7 T), and lower temperature (1.6 K) than the PD. The sample space has thread positions for holding up to 3 targets. The SD has a longer liquid helium holding time and is portable, to allow moving the polarized target from the HD-ice lab to the experiment hall.

In-beam cryostat

The IBC (In-beam cryostat) is a dilution refrigerator and magnet system for holding the polarized HD target during the experiment. The base temperature of the dilution refrigerator is 50 mK. It has two magnet systems. The solenoid magnet creates a field of 1 T along the beamline, which is also the polarization direction of the longitudinally polarized target. The saddle coil magnet creates a field of 0.075 T perpendicular to the beamline, which is used during the spin rotation to change the polarization direction of the longitudinally polarized HD target. A backup coil with a field of 0.01 T is used during the run, in case there is a quench of the main solenoid magnet.
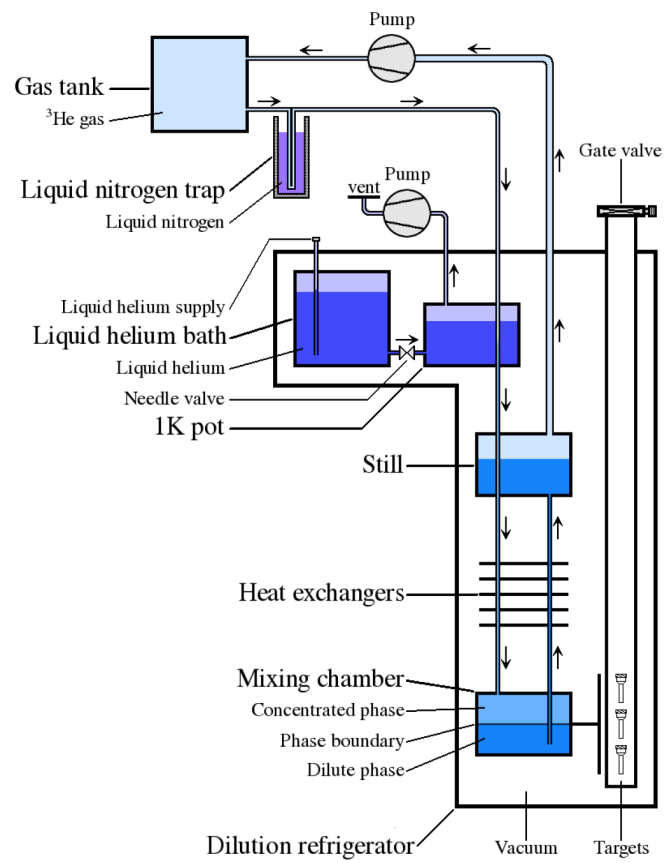
Figure 2.38: Schematic plot of the dilution refrigerator. Image source: [49].

The HD target life cycle

The life of the HD target starts with the condensation of HD gas into the PD, where an NMR measurement is done for calibrating the thermal equilibrium polarization of the target. Then the solid HD target is transferred to the DF for polarization. After 3-6 months of polarizing and aging of the target, it is relocated from the DF to the PD for another NMR measurement to determine the polarization of the target. This step can be bypassed if a good cross-calibration between the PD and the IBC NMR systems is known. After the NMR measurement, the HD is transferred from the PD to the SD for storage and then it is transported to the experiment hall. In the experiment hall, the HD is transferred from the SD to the IBC for the experiment. Inside the IBC, periodic NMR measurements are performed to monitor the target polarization during the experiment. Moreover, several spin manipulations for H and D are conducted, which includes using SFP (saturated forbidden adiabatic fast passage) to transfer polarization from H to D, reversing the z-direction of the polarization of H or D. After the experiment is finished, the HD is transferred from the IBC to the PD for another NMR measurement in the PD for cross-calibration between the PD and the IBC NMR circuits. Then the HD is warmed up to be collected for gas chromatography measurements and Raman scattering measurements to determine the H_2 and D_2 levels in the HD gas. Figure 2.39 is a schematic plot of the life cycle of an HD target. Figure 2.40 is a schematic plot of the HD target transfer process.
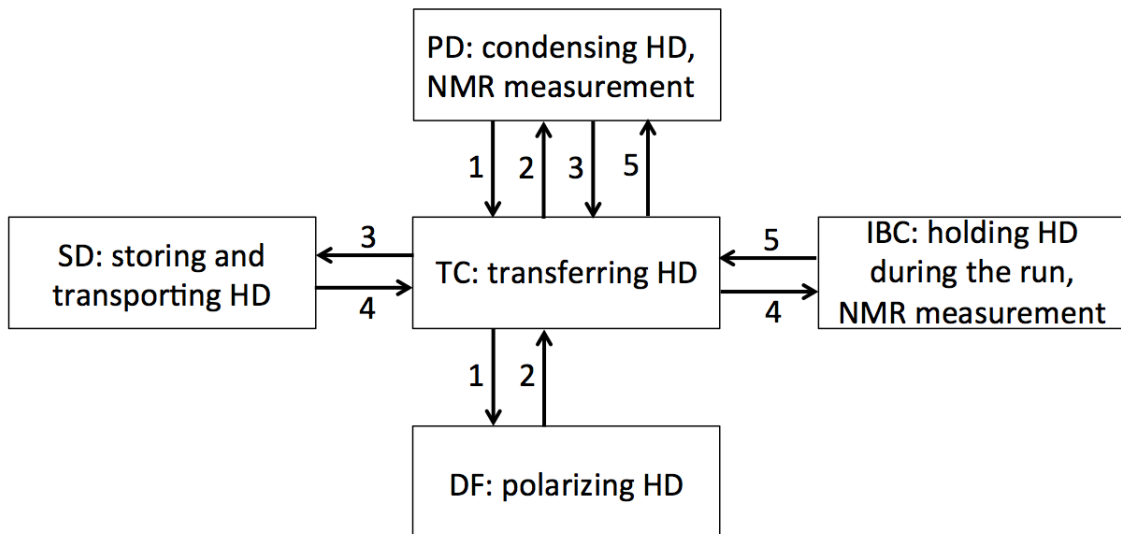
Figure 2.39: Schematic plot of the life cycle of an HD target. The labels from 1 to 5 for the arrows represents the 5 times use of the TC is used for transferring the HD target.

2.3.3 NMR analysis for target polarization

Definition of target polarization

A nuclus with non-zero spin I has $2I+1$ spin states for its ground state. These states are degenerate in the absence of a magnetic field, but will be separated into different energy
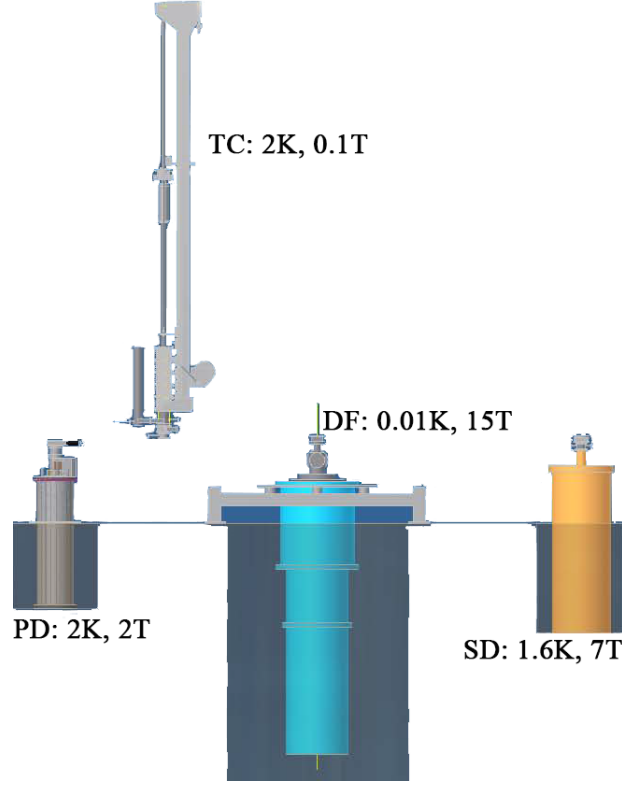
Figure 2.40: The schematic plot of the HD target transfer process. Image source: [41].

levels in a magnetic field (Zeeman effect). The energy levels for the spin states relative to the ground state are: $E = -\mu \cdot B = -\gamma I_z B = -\gamma (m\hbar)B$, where m = -I, ... I, $\mu = \gamma I$ is the magnetic moment for the nucleon, $\gamma = gq/2m$ is the gyromagnetic ratio, g is the g-factor.

The vector polarization of a target is the normalized difference between the number of spins parallel to the magnetic filed and those anti-parallel to the magnetic field, as in Equation 2.6.

$$P = \frac{N_{m=I} - N_{m=-I}}{\sum\limits_{m=-I}^{I} N_m} \tag{2.6}$$

In thermal equilibrium, the spin state population follows the Boltzmann distribution. The thermal equilibrium polarization for spin $I = 1/2$ (proton) and spin $I = 1$ (deuteron) is shown in Equations 2.7 and 2.8. These two equations are equivalent to Equation 2.4 in the previous section.

$$P_{TE}(H) = \frac{e^{\frac{\gamma\hbar B}{2kT}} - e^{-\frac{\gamma\hbar B}{2kT}}}{e^{\frac{\gamma\hbar B}{2kT}} + e^{-\frac{\gamma\hbar B}{2kT}}} = \tanh(\frac{\gamma\hbar B}{2kT}), \tag{2.7}$$

$$P_{TE}(D) = \frac{e^{\frac{\gamma\hbar B}{kT}} - e^{-\frac{\gamma\hbar B}{kT}}}{e^{\frac{\gamma\hbar B}{kT}} + 1 + e^{-\frac{\gamma\hbar B}{kT}}} = \frac{4\tanh(\frac{\gamma\hbar B}{2kT})}{3 + \tanh^2(\frac{\gamma\hbar B}{2kT})}, \tag{2.8}$$

Principles for NMR measurement

The polarizations of H and D in the target are measured by NMR polarimetry. Figure 2.41 is a cartoon of a NMR setup. In the figure, the main static magnetic field B_0 is along the z-axis, the transmitter (RF drive coils) generates an oscillating magnetic field B_1 along the x-axis, the receiver (pick-up coils) measures the induced oscillation of the target magnetism along the y-axis. The induced RF signals in the receiver is proportional to the polarization of the target.
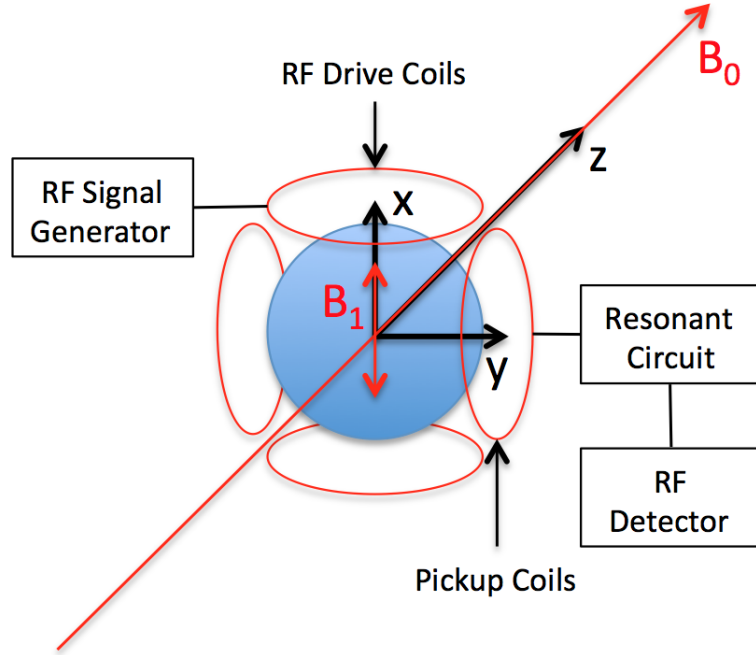
Figure 2.41: A cartoon for the NMR setup [42].

The principle of the NMR measurement can be described in the following way. Take the spin half proton ($I = \hbar/2$) as an example. In an external magnetic field B_0, the nucleons' spin states are separated into different energy levels, which follow the Boltzmann distribution. More spins are aligned parallel to B_0 ($I_z = -\hbar/2$) than anti-parallel ($I_z = +\hbar/2$), resulting a net magnetization M_0 along B_0 (z-axis). The RF drive coils produce an oscillating RF field B_1 along the x-axis. When the frequency of RF satisfies the resonance condition: $\hbar\omega = \Delta E = \gamma\hbar B_0$, the magnetization M_0 will be tipped away from the z-axis and obtains a component in the x-y plane. The oscillation of M_y will induce a current in the pick-up coils, which is the NMR signal. ΔE is the difference of the energy levels for the two spin states of the proton in a magnetic field, $\omega = \gamma B_0$ is referred as Larmor frequency. There is a proportional relationship between the NMR signal S_{NMR} and the polarization of the target P_t as in Equation 2.9, in which M_y and S_{NMR} are the magnitude of the oscillating signals.

$$P_t \propto M_0 \propto M_y \propto S_{NMR}. \tag{2.9}$$

There are two methods to reach the resonance condition $\omega = \gamma B_0$. One is to vary the RF frequency with fixed magnetic field B_0, another is to vary B_0 with fixed RF frequency.

The G14 experiment uses the second method. Figure 2.42 shows the down-sweep and up-sweep of the magnetic field to search for the NMR resonance peak for the deuteron. The sweep range of the magnetic field is 300 Gauss, which is from 3004 G to 2704 G in 31 seconds, then staying at the low field for 1 second, back to 3004 G in 31 seconds, then waiting in the high field for 1 second. The RF frequency is fixed to 1774.00 kHz. The finite width of the peak is caused by the fact that nucleons experience slightly different magnetic field in solid state environment.
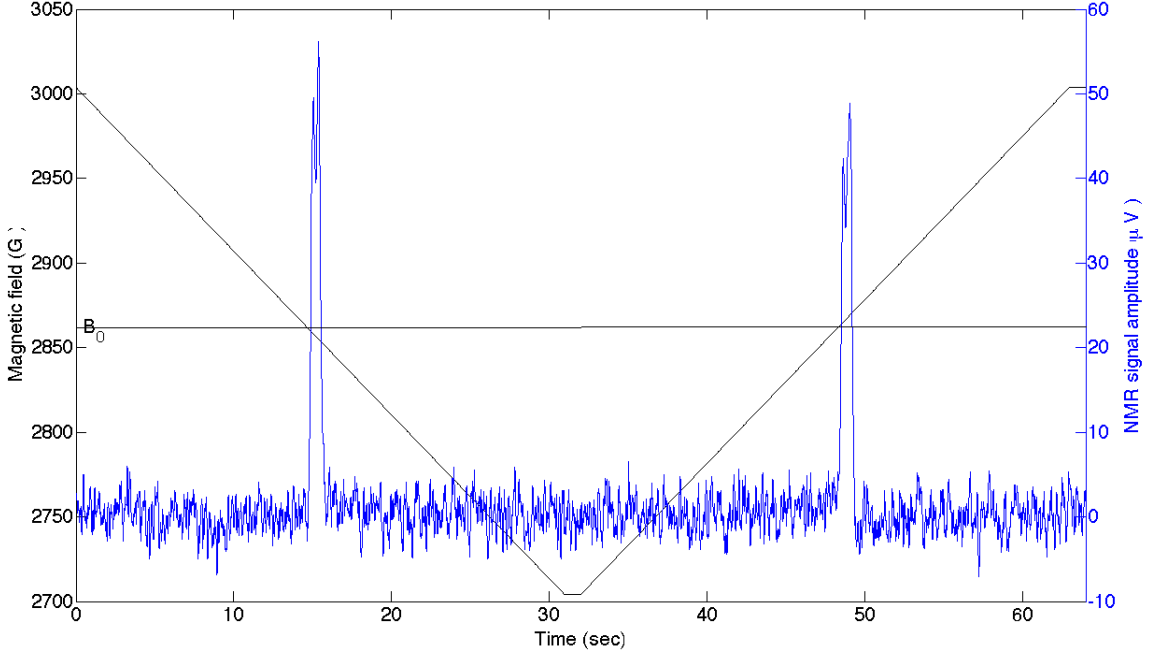
Figure 2.42: Magnetic field sweeps (black line) through B_0 twice searching for the NMR resonance (blue line) for deuteron.

The polarization of the target is proportional to the integrated area under the NMR peak: $P_t = c\, I_{NMR}$, where I_{NMR} is the integration of S_{NMR} over time. It is noted that there is a linear relationship between the magnetic field and time, thus the integration has more physical meaning if it is integrated over the changing magnetic field: $I_{NMR} = \int S_{NMR} dB$. The determination of the constant overall factor(c) is done by a cross calibration between the target in frozen spin mode (FS) and in thermal equilibrium (TE). In these two conditions, we have $P_{FS} = c_{FS}\, I_{FS}$, $P_{TE} = c_{TE}\, I_{TE}$, combining the two equations gives

$$P_{FS} = \frac{c_{FS}}{c_{TE}} \frac{P_{TE}}{I_{TE}} I_{FS} = c_{overall} I_{FS}, \tag{2.10}$$

in which P_{TE} can be calculated using the Equation 2.4. The ratio $\frac{c_{FS}}{c_{TE}}$ relates to the conditions of NMR measurements as in Equation 2.11.

$$\frac{c_{FS}}{c_{TE}} = \frac{f_{TE}}{f_{FS}} \frac{10^{\frac{pwr_{TE}}{20dBm}}}{10^{\frac{pwr_{FS}}{20dBm}}} \frac{Gain_{TE}}{Gain_{FS}}, \tag{2.11}$$

53

in which f_{TE}, f_{FS} are the RF frequencies used in the two measurements, pwr_{TE}, pwr_{FS} are the RF power in the units of dBm, Gain_{TE}, Gain_{FS} are the gains of the RF circuit. Table 2.2 gives the overall factor $c_{overall}$ for different frozen spin HD targets used in G14 experiment.

Target	21a	19b	22b
$c_{overall}(\text{H})$ $[\%/(\mu V \cdot Gauss)]$	14.9/240	29.61/230	46.45/230
$c_{overall}(\text{D})$ $[\%/(\mu V \cdot Gauss)]$	27.7/267	14.97/152	5.994/152

Table 2.2: Overall factors for different frozen spin HD target in G14 experiment. Values are from Alexdrander Deur [43].

NMR signal analysis

During the G14 experiment, periodic NMR measurements were conducted to monitor the target polarization. For each NMR measurement, four independent signals were collected for the NMR peaks, as in Figure 2.43, two signals from the X-channel for sweeping up and down of the magnetic field, another two from the Y-channel. The dispersion signals from Y-channel can be transformed to absorption signals using the Kramers-Kronig relations.
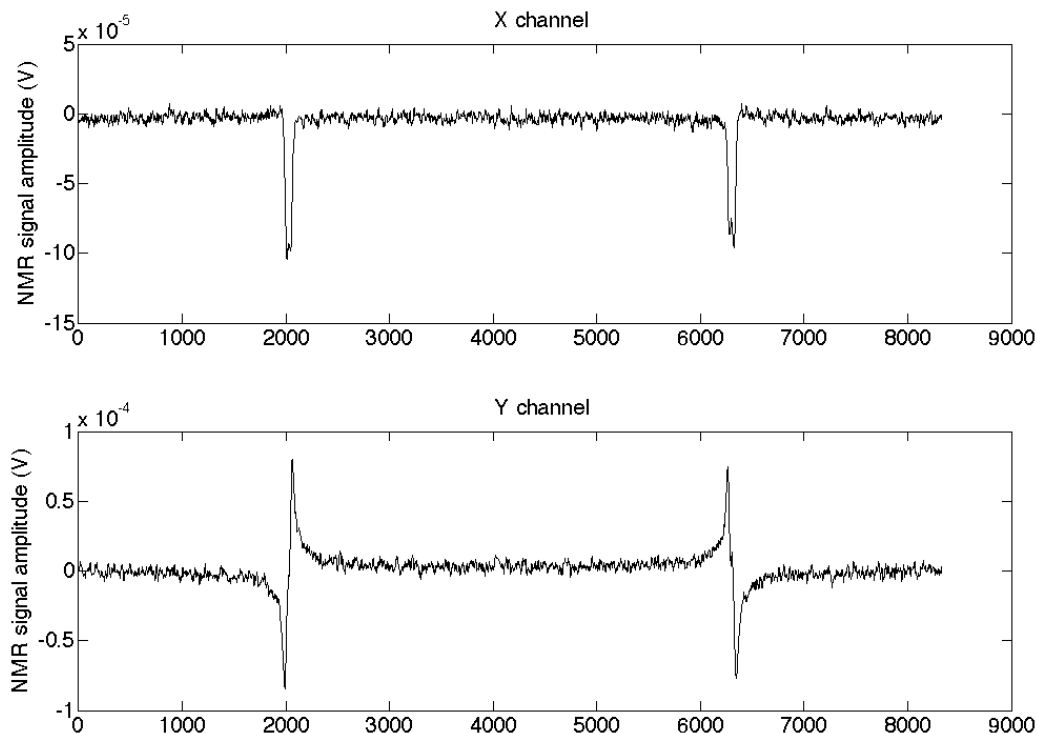
Figure 2.43: X-channel and Y-channel for the NMR resonance for deuteron.

We know from the previous discussion that the NMR signal is proportional to the magnetization of the material M_0, which is proportional to the magnetic susceptibility

$\chi(\omega)$, $S_{NMR} \propto M_0 \propto \chi(\omega)$. The magnetic susceptibility has both real and imaginary parts: $\chi(\omega) = \chi_1(\omega) + i\chi_2(\omega)$, which are measured by the X-channel and Y-channel respectively. $\chi_1(\omega), \chi_2(\omega)$ are related by the Kramers-Kronig relations as in Equation 2.12.

$$\chi_1(\omega) = \frac{1}{\pi} P \int_{-\infty}^{\infty} \frac{\chi_2(\omega')}{\omega' - \omega} d\omega',$$
$$\chi_2(\omega) = -\frac{1}{\pi} P \int_{-\infty}^{\infty} \frac{\chi_1(\omega')}{\omega' - \omega} d\omega', \tag{2.12}$$

where P is the Cauchy principal integral. These relations convert the two dispersion signals from the Y-channel to absorption signals, and give two more measurements for the polarization. Before applying the Kramers-Kronig transformation, a phase rotation may be needed for some measurements. As in Figure 2.43, the X-channel signal is not flat around the absorption peaks. This is caused by the mix of the absorption signal and the dispersion signal. A phase rotation (Eq. 2.13) can be used to solve this problem.

$$x' = \cos(\theta)x + \sin(\theta)y,$$
$$y' = -\sin(\theta)x + \cos(\theta)y. \tag{2.13}$$
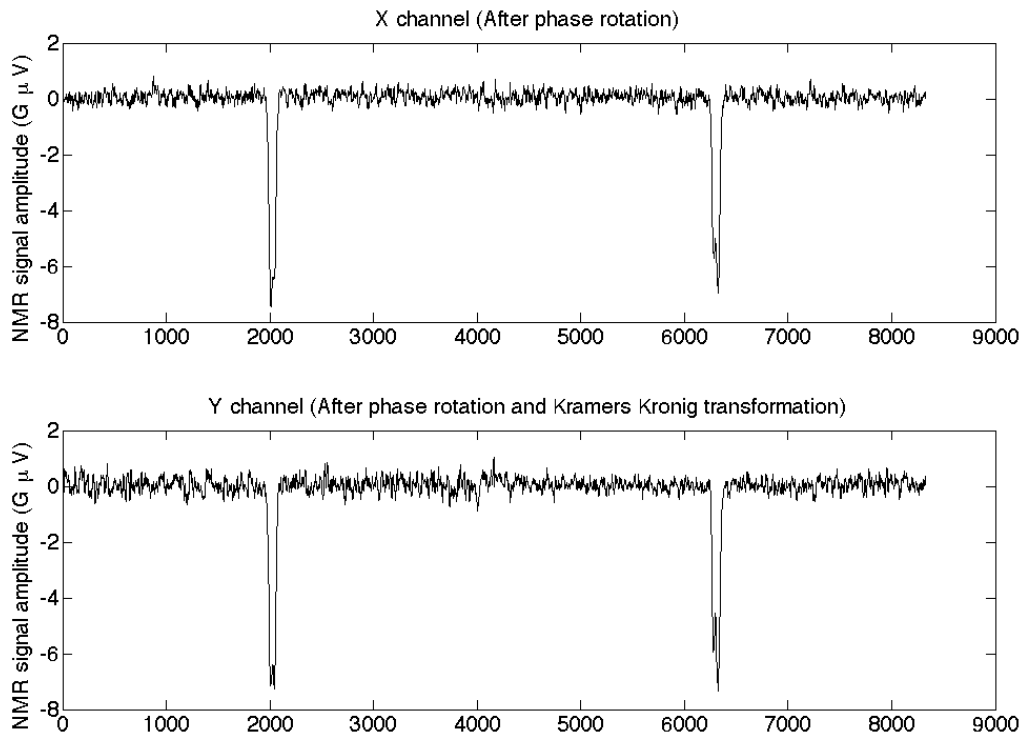
Figure 2.44: X-channel and Y-channel after phase rotation and Kramers Kroning transformation for the NMR resonance for deuteron.

Figure 2.44 gives the transformed signals for the same NMR measurement, both the X and Y channel signals have had the phase rotation applied. Afterwards the Y-channel

signal also had the Kramers Kronig transformation applied. Finally, if the background noise level is not at zero, a background level adjustment has to be applied.

Figures 2.43 and 2.44 have different y values. They are different by the multiplier $10^6 \times 300/(31 \times 128)$. The reason for this conversion is that the x-axis does not have the unit of Gauss for magnetic field. The x values are the data points stored in the register, and the DAQ rate is 128 Hz, the sweeping rate for the magnetic field is 300 G/31 seconds. To convert the x value from data point number to Gauss, we need to multiply it by $300/(31 \times 128)$. On the other hand, the y values are multiplied by 10^6 to convert from volts to micro-volts. Furthermore, the area under the peak is the integration of $y\Delta x$, so the multiplier applied to the x-value can be transferred to the y-value without changing the result for $y\Delta x$. This gives the final adjustment for the y-value of $10^6 \times 300/(31 \times 128)$ with the x-value staying unchanged. After the conversion of the y values, the unit for the integrated peak area is $Gauss \cdot \mu V$.

Since the background around the NMR peak is fluctuating, a technique referred to as "scanning window" is used. Figure 2.45 shows how this technique works. Firstly, a window
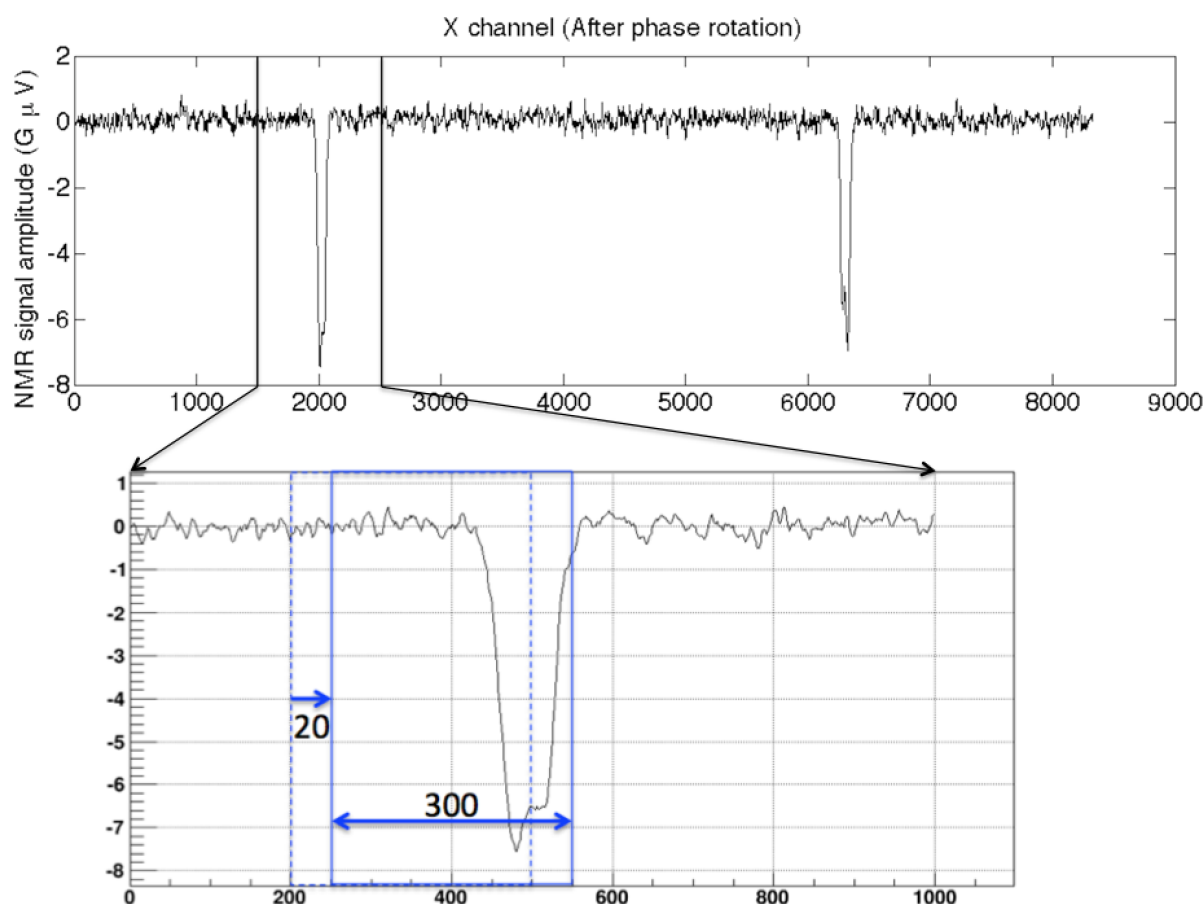
Figure 2.45: "Scanning window" is used for the calculation of NMR peak area. 1000 data points around the first NMR peak in the top plot is zoomed into the bottom plot.

of 300 data point is chosen in order to include the entire NMR peak for integration. Secondly, 36 integrations are conducted with an integration window that scans through the NMR peak with a step of 20 data points. Finally, the results for the integrations are

plotted vs the integration starting point as in Figure 2.46. The plateau in Figure 2.46 is the region where the scanning window covers the whole NMR peak. The weighted mean is used to estimate the average of the peak area, and the error is the sample standard deviation of the 10 points.

$$I = \frac{\sum_{i=1}^{10} \frac{I_i}{\sigma_i^2}}{\sum_{i=1}^{10} \frac{1}{\sigma_i^2}},$$

$$\sigma = \sqrt{\frac{1}{9} \cdot \sum_{i=1}^{10} (I_i - \bar{I})^2}$$

(2.14)
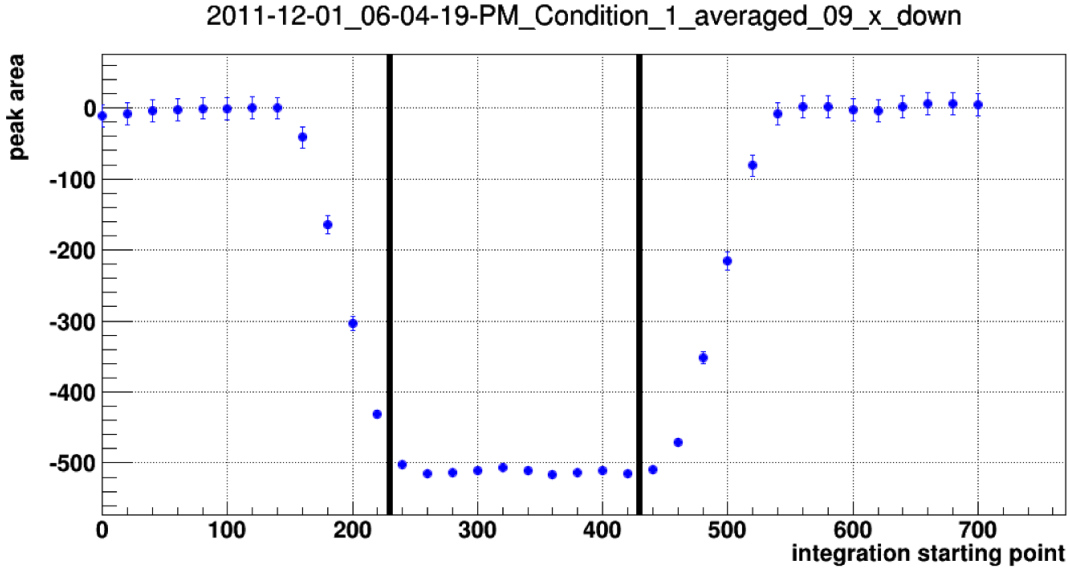
Figure 2.46: Results for integration with the range of a window scanning through the NMR peak.

In [49], the error is estimated using the flat noisy background and is related to the size of the integration range. The uncertainty on one data point in the background region can be computed as:

$$\sigma = \sqrt{\frac{1}{N-1} \cdot \sum_{i=1}^{N} (x_i - \bar{x})^2},$$

(2.15)

where N is the number of sweeps for this background data point. With the assumption that the error on each points is the same, the statistical error on the peak integral can be computed by summing in quadrature: $\epsilon = \sqrt{n} \cdot \sigma$, where n is the number of points in the integration range. It is noted that a larger integration range(larger $\sqrt{n}$) gives a bigger error ϵ. The error estimation used in the "scanning window" procedure does not have this problem.

The same procedure is then applied to the other 3 peaks for the same NMR measurement. Then the 4 values are averaged using a weighted mean, and their standard deviation is the error for the peak area.

57

To convert the integral of the peak area to the polarization value, an overall factor from Table 2.2 is used. These values are obtained from comparing the results from an NMR measurement of the HD target in thermal equilibrium state and an NMR measurement of the target in frozen spin state, in which the frozen spin target NMR measurement is referred as a reference measurement. Because the NMR measurements of the frozen spin target have been taken with different settings (RF power, RF frequency, Gain), the signals need to be normalized to the reference measurement in order to be compared to each other. The normalization is shown in Equation 2.16, since S_{NMR} is proportional to RF power, RF frequency and the circuit gain, all the signals should be normalized back to values with the reference settings.

$$I' = \frac{f_{ref}}{f} 10^{\frac{P_{ref} - P}{20}} \frac{Gain_{ref}}{Gain} I. \tag{2.16}$$

The polarization of target is equal to the overall factor ($c_{overall}$) times the normalized peak area integral (I').

$$P_t = c_{overall} I' = c_{overall} \frac{f_{ref}}{f} 10^{\frac{P_{ref} - P}{20}} \frac{Gain_{ref}}{Gain} I. \tag{2.17}$$

The results of the polarization for the three HD targets used in the G14 experiment are shown in the following figures.
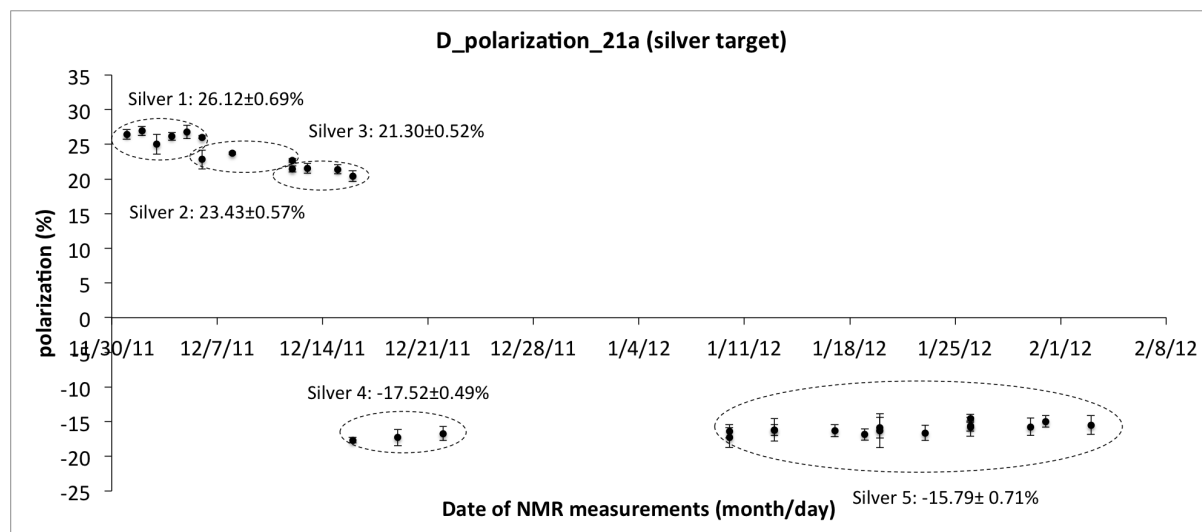
Figure 2.47: Deuteron polarization for the 21a target (silver runs).

The target polarization for each run period and its statistical uncertainty are shown in Table 2.3, the weighted mean of the NMR polarization values during the period gives the average value, and the sample standard deviation is used as its statistical error. The systematic errors associated with the target polarization are summarized in Section 4.3.4, Table 4.8.
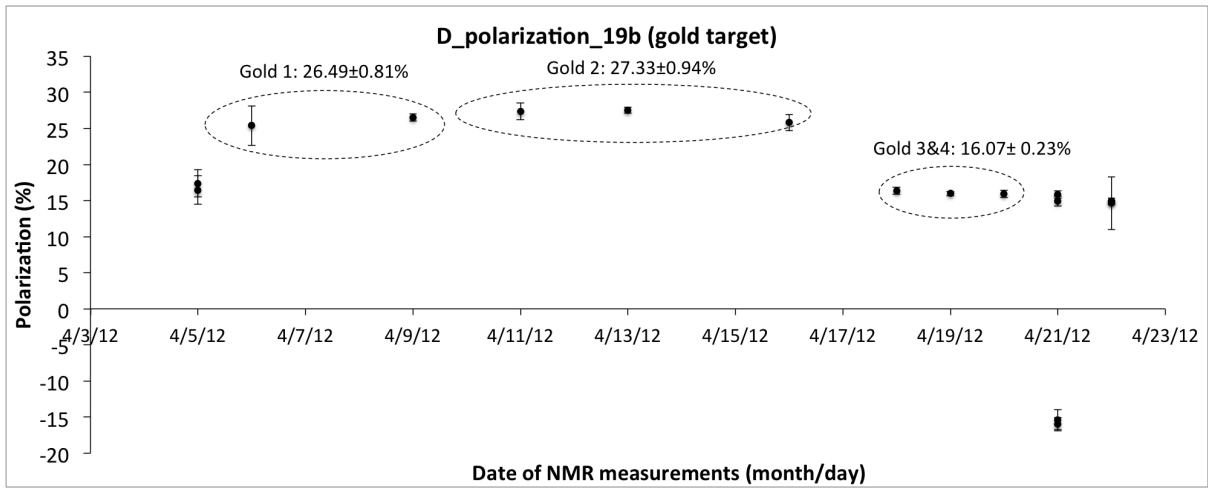
Figure 2.48: Deuteron polarization for the 19b target (gold runs).
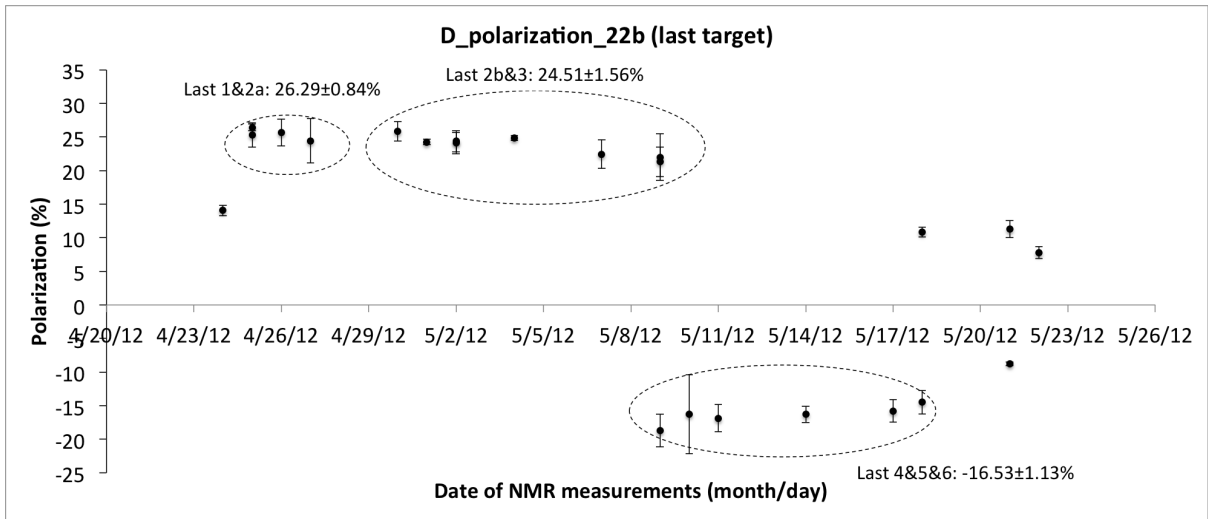
Figure 2.49: Deuteron polarization for the 22b target (last target runs).
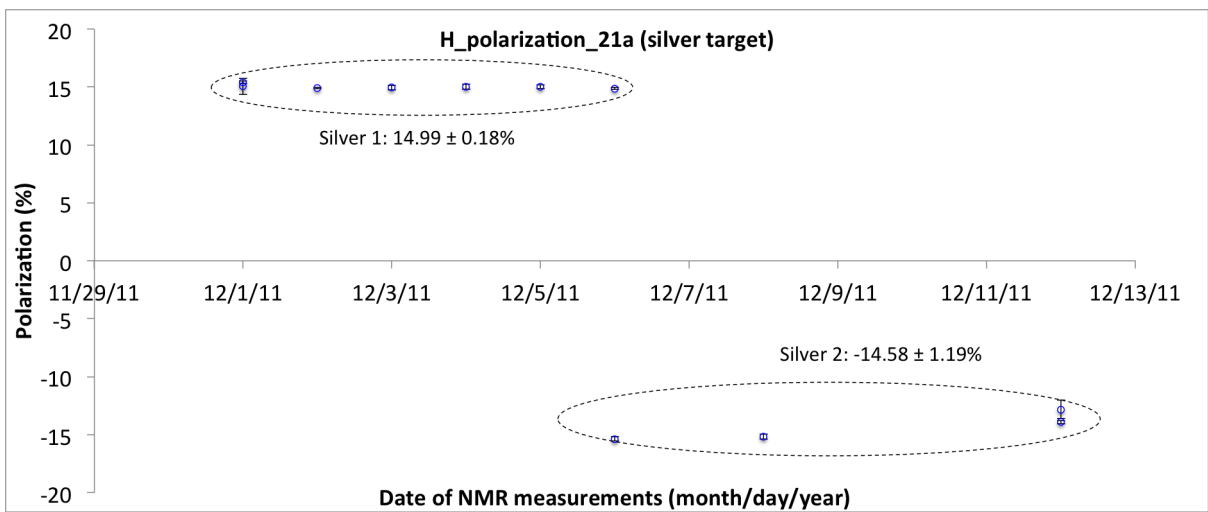
Figure 2.50: Hydrogen polarization for the 21a target (silver runs).
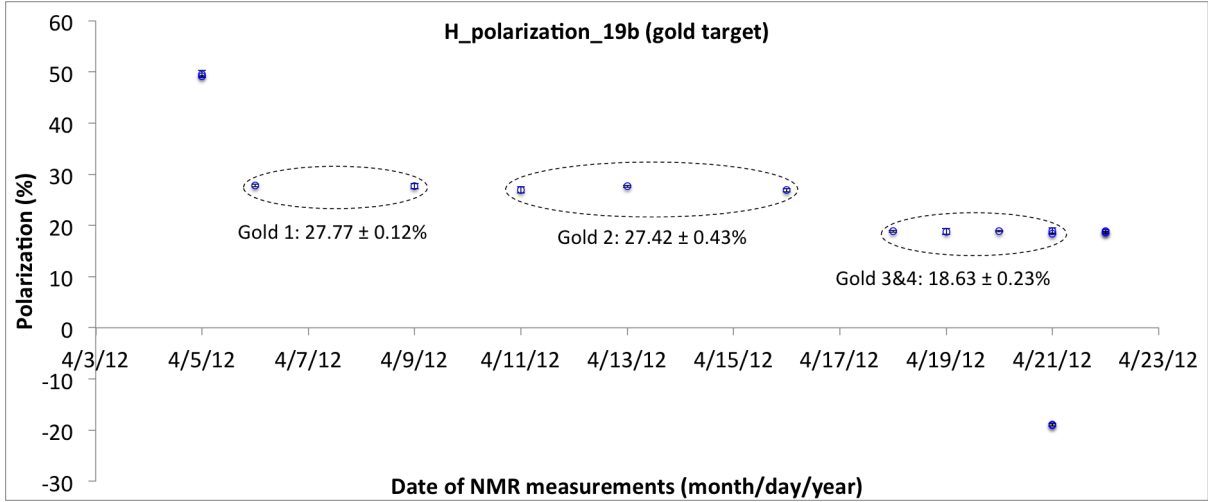
Figure 2.51: Hydrogen polarization for the 19b target (gold runs).
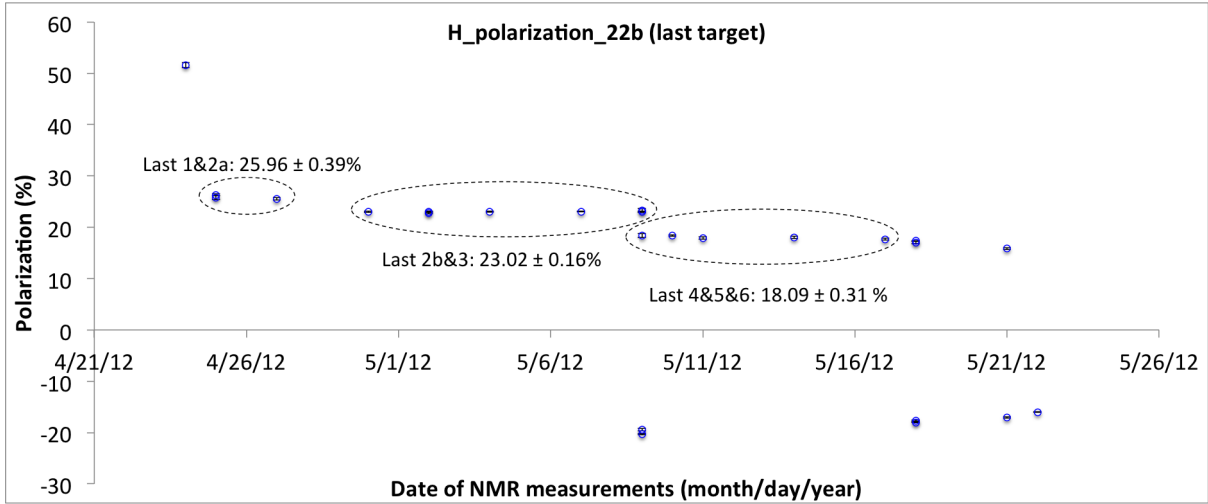
Figure 2.52: Hydrogen polarization for the 22b target (last target runs).

Run period	D polarization (stat. error)	H polarization (stat. error)
Silver 1	$+25.6(\pm0.7)\%$	$+14.7(\pm0.2)\%$
Silver 2	$+23.0(\pm0.6)\%$	$-14.3(\pm1.2)\%$
Silver 3	$+20.9(\pm0.5)\%$	
Silver 4	$-17.2(\pm0.5)\%$	
Silver 5	$-15.5(\pm0.7)\%$	
Gold 1	$+26.0(\pm0.8)\%$	$+27.2(\pm0.1)\%$
Gold 2	$+26.8(\pm0.9)\%$	$+26.9(\pm0.4)\%$
Gold 3&4	$+15.8(\pm0.2)\%$	$+18.3(\pm0.2)\%$
Last 1&2a	$+25.8(\pm0.8)\%$	$+25.5(\pm0.4)\%$
Last 2b&3	$+24.0(\pm1.5)\%$	$+22.6(\pm0.2)\%$
Last 4&5&6	$-16.2(\pm1.1)\%$	$+17.7(\pm0.3)\%$

Table 2.3: Polarization of the HD target from NMR signal analysis. Compared with the figures above, a 2% TC transfer loss has been applied to the values in the table.

60

Chapter 3

Event Selection

Three channels are studied: $\gamma n \to p\pi^-$, $\gamma p \to p\pi^+\pi^-$ and $\gamma n \to n\pi^+\pi^-$. The charged particles are detected using the CLAS drift chambers, start counters and time-of-flight counters. The drift chambers measure the particle tracks, which are used to determine the particle momentum (p) and flight path, while the start counters and time-of-flight counters give the particle TOF, which, when combined with the flight path, gives the particle velocity (β). The momentum and velocity are combined to give the particle mass: $m = p/\beta\gamma$.

The neutrons are detected by the forward electromagnetic calorimeter. The run conditions and procedures for selecting events for the three channels are described in the following sections.

3.1 Run Conditions

According to different targets and photon beam conditions, the G14 data is divided into different run periods. Table 3.1 shows the run periods with a circularly polarized photon beam, table 3.2 shows the run periods with a linearly polarized photon beam.

3.2 CLAS Banks

The reconstructed particle information is stored in the CLAS banks [50]. For historical reasons, there are two systems of banks: the "PID" banks and "SEB" banks. These two systems use different algorithms to reconstruct events. The "PID" banks include HEAD, TGBI, GPID, TBID, ECHB, SCRC, STRE, TAGR, MVRT, VERT, TBER, EPIC. The "SEB" banks include HEVT, EVNT, DCPB, TRPB, ECPB, SCPB, STPB, TGPB. The banks used in this study are the "PID" banks. GPID is the main bank used in the G14 analysis. It contains all the information for the charged particles, and the information for the tagger photons. The GPID bank is a combination of the PART and TBID banks. MVRT gives the vertex information for an event. The ECHB bank contains the information from the forward electromagnetic calorimeter, and gives the information for neutral particles. The HEAD bank contains the helicity information when a electron polarized beam was used. The TAGR bank stores the tagger information, which gives the energy, time, T counter ID, and E counter ID for the tagged photons. The TBER bank

Period	E_{beam} (MeV)	Beam Polarization	Events	Torus Curr.	Target	Target Pol.
Silver1	2280.96	-81.7%	830 M	+1920 A	21a	+D(25.6%) +H(14.7%)
Silver2a	2280.96	-81.7%	300 M	+1920 A	21a	+D(23.0%) -H(14.3%)
Silver2b	2280.96	-76.2%	870 M	+1920 A	21a	+D(23.0%) -H(14.3%)
Silver3	2280.96	-76.2%	250 M	-1500 A	21a	+D(20.9%) -H(N/A)
Silver4	2280.96	-76.2%	820 M	-1500 A	21a	-D(17.2%) -H(N/A)
Silver5	2257.75	88.8%	5210 M	-1500 A	21a	-D(15.5%) -H(N/A)
Gold2a	2541.31	88.2%	440 M	-1500 A	19b	+D(26.8%) +H(26.9%)
Gold2b	2541.31	-83.4%	1660 M	-1500 A	19b	+D(26.8%) +H(26.9%)

Table 3.1: Run periods for runs with a circularly polarized photon beam. The first column is the name of the period, silver runs use the "21a" target, gold runs use the "19b" target. The second column is the energy of the electron beam. The third column is the electron beam polarization, which has an error of $1.4\%(stat.) \pm 3.0\%(sys.)$. The fourth column is the number of events. The fifth column is the Torus Current, which determines the direction of the torus magnetic field. The sixth column is the target used. The seventh column is the degree of polarization for the HD target, where "$\pm$" indicate the direction of deuterons polarization along "z" direction in lab coordinate. A 2% transfer loss of polarization from TC has been applied to the numbers in the table.

Period	Coherent Edge	Perp Events	Para Events	Amo. Events	Target	Target Pol.
Last tgt3	1800 MeV	506.6 M	483.0 M	86.0 M	22b	+D(24.0%), +H(22.6%)
Last tgt4	1800 MeV	307.6 M	304.2 M	52.4 M	22b	-D(16.2%), +H(17.7%)
Last tgt2a Last tgt2b	2000 MeV	461.3 M	464.9 M	106.7 M	22b	+D(25.77%), +H(25.5%) +D(24.0%), +H(22.6%)
Last tgt5	2000 MeV	184.7 M	208.8 M	40.8 M	22b	-D(16.2%), +H(17.7%)
gold1	2200 MeV	220.5 M	181.1 M	109.3 M	19b	+D(26.0%), +H(27.2%)
gold4	2200 MeV	20 M	20 M	0 M	19b	+D(15.8%), +H(18.3%)
last tgt1	2200 MeV	110.2 M	93.6 M	54.7 M	22b	+D(25.8%), +H(25.5%)
last tgt6	2200 MeV	93.6 M	148.3 M	10.2 M	22b	-D(16.2%), +H(17.7%)

Table 3.2: Run periods for runs with a linearly polarized photon beam, a 30 μm diamond is used as the radiator, the electron beam energy for all these runs is 5551.77 MeV, the Torus field setting is -1500 A. The first column is the name of the period. The second column is the coherent edge energy. The third column is the number of events with the E-plane of the linearly polarized photon beam perpendicular to the lab floor. The fourth column is the number of events with the E-plane of the linearly polarized photon beam parallel to the lab floor. The fifth column is the number of events for runs with an amorphous radiator. The sixth column is the target name. The seventh column is the target polarization. A 2% transfer loss of polarization from TC has been applied to the numbers in the table.

gives the covariance matrix for the CLAS detectors. SCRC bank contains information from the TOF counters.

3.3 Channel selection

The G14 experiment is designed to study several pseudo-scalar meson channels as listed in Table 3.3. To select the channel of interest, several particle ID filters, geometric cuts, and kinematic cuts are applied to the data.

Reaction	Observables
$\gamma + n \rightarrow \pi^- p$	σ_0, Σ, E, G
$\gamma + n \rightarrow \pi^+ \pi^- n$	$\sigma_0, I^c(\Sigma), I^s, I^\odot, P_z, P_z^\odot(E), P_z^s(G), P_z^c$
$\gamma + p \rightarrow \pi^+ \pi^- p$	$\sigma_0, I^c(\Sigma), I^s, I^\odot, P_z, P_z^\odot(E), P_z^s(G), P_z^c$
$\gamma + n \rightarrow K^0 \Lambda$	σ_0, Σ, E, G $O_{x'}, O_{z'}, C_{x'}, C_{z'}, P, T(-O_{y'})$ $L_{x'}, L_{z'}, T_{x'}, T_{z'}$
$\gamma + n \rightarrow K^0 \Sigma^0$	$\sigma_0, \Sigma, P, E, G$
$\gamma + n \rightarrow K^+ \Sigma^-$	σ_0, Σ, E, G

Table 3.3: Pseudoscalar meson reactions and observables measured in the G14 experiment.

3.3.1 Particle ID Filters

The first filter requires the event to have the right number of final state particles. In the GPID bank, each event has a list of the final state particles, which contains each particle's PID number: proton(14), neutron(no PID in GPID bank, need ECPB bank for neutron identification), π^+(8), π^-(9). The numbers in the parenthesis are the PID number in the GPID bank. For the reaction $\gamma n \rightarrow p\pi^-$, the first filter requires the final state to have one proton and one π^-.

The second filter requires the proton and π^- to have the same "targid", which indicates that the proton and π^- are from the event caused by the same tagged photon.

The third filter is "ngrf ==1", which requires the number of photons in an RF bucket to be one, this remove the ambiguity for events that relate to several tagged photons.

The fourth filter is the "$\Delta\beta$" filter. This filter compares the β value of the particle from two methods to remove mis-identified particles. The first β value is calculated from the timing information(δt) from the start counter and the TOF counter, and the distance(δl) from the start counter to the TOF counter, $\beta_1 = \frac{v}{c} = \frac{\delta l}{c\delta t}$. The second β value comes from the momentum of the particle, which is calculated from the track information measured by the drift chamber. Using the definition for relativistic momentum $p = m_0 v/\sqrt{1 - v^2/c^2} = m_0\beta c/\sqrt{1 - \beta^2}$, we get $\beta_2 = \frac{p}{\sqrt{p^2+m_0^2 c^2}}$, where m_0 is the PDG mass for the particle. The definition of this filter is $\Delta\beta = \beta_1 - \beta_2$. A filter with abs($\Delta\beta$)<0.06 for protons and abs($\Delta\beta$)<0.03 for pions is used, as shown in Figure 6.4. Figure 3.2 shows the effect of this filter on the event selection.

(a) Proton: abs($\Delta\beta$)<0.06.

(b) π^+: abs($\Delta\beta$)<0.03.

(c) π^-: abs($\Delta\beta$)<0.03.
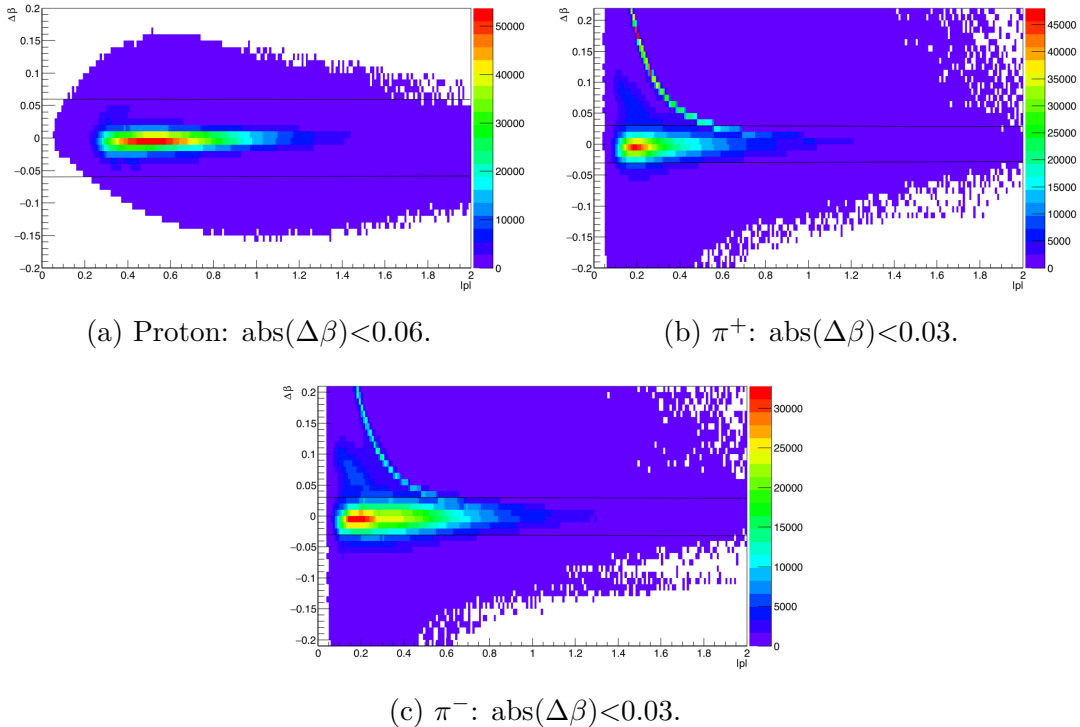
Figure 3.1: $\Delta\beta$ filter for proton, π^+ and π^-, the x-axis is |p| (particle momentum).

After the four filters, the selected channel is ready for next step analysis.
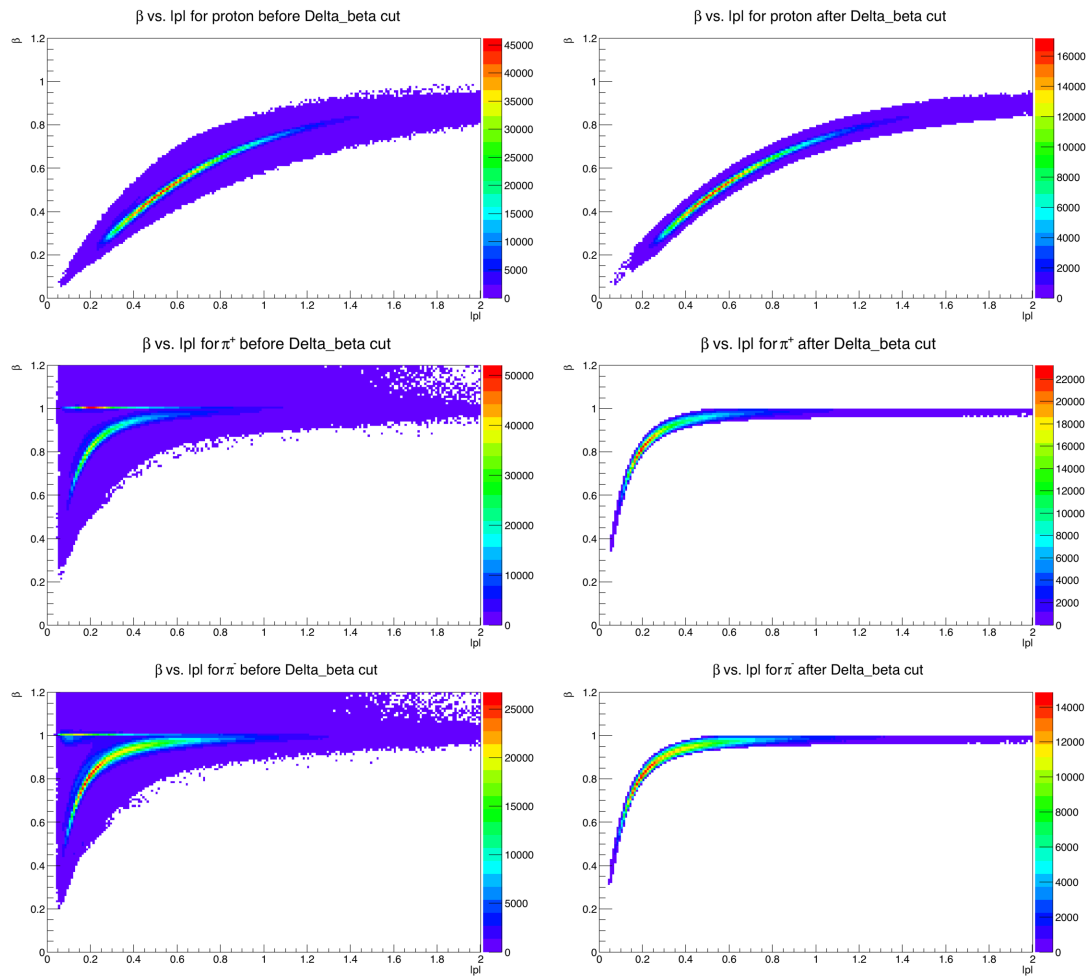
Figure 3.2: The β vs mometum plots for proton, π^+ and π^- before(left plots) and after(right plots) the $\Delta\beta$ cut. Most mis-identified particles are removed with this filter.

3.3.2 Geometric Cuts

There are two geometric cuts used in this study: the fiducial cut and the vertex cut. The fiducial cut takes into account the acceptance of the CLAS detectors, and the vertex cut removes events from regions outside the HD target.

Fiducial Cut

The fiducial cut removes the angular region where there are known obstructions to the acceptance of the detectors and near the torus coils where the torus field is not well known for good track reconstruction. The fiducial cut can be defined by a relation between the polar angle θ and azimuthal angle ϕ as in Equation 3.1 [53].

$$\theta > 4.0 + \frac{510.58}{(30 - \phi)^{1.5518}} \tag{3.1}$$

The resulting plot of θ vs. ϕ is shown in Figure 3.3.
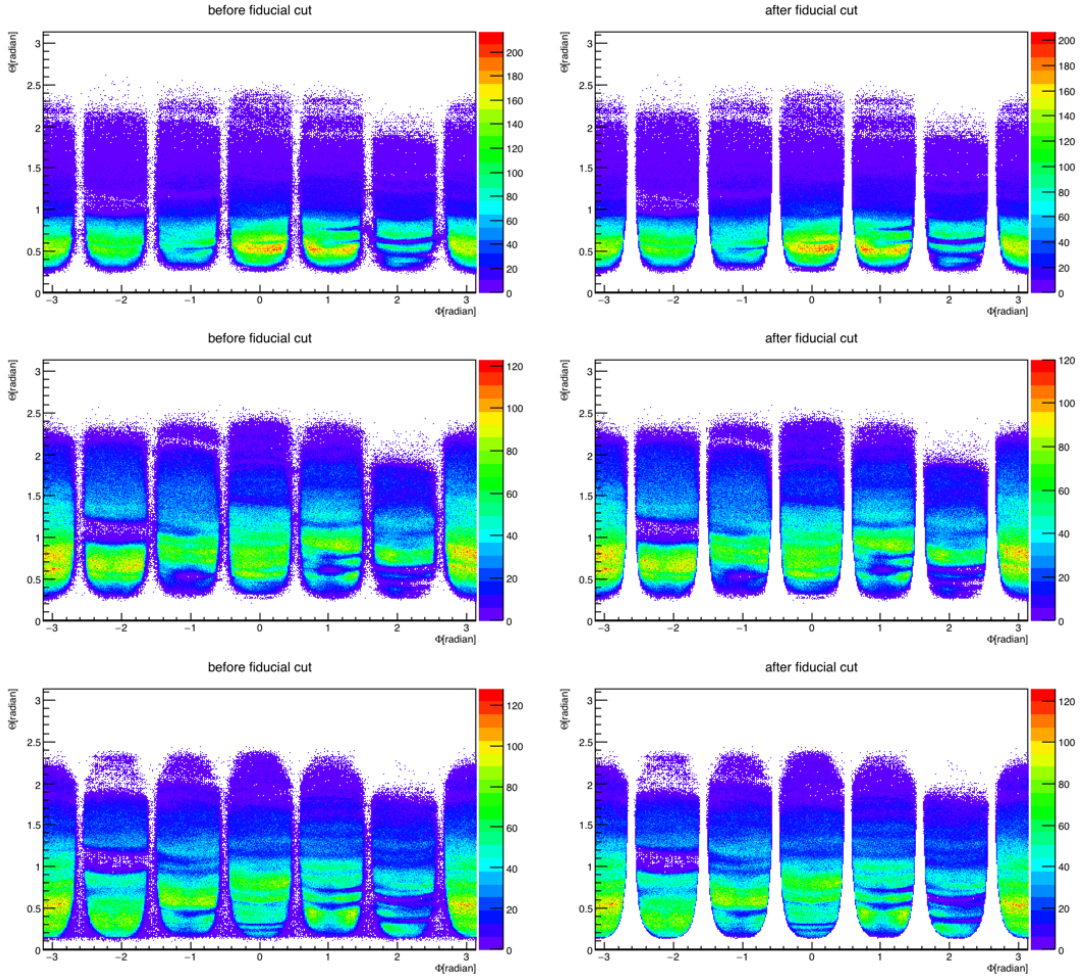
Figure 3.3: Fiducial cuts for proton, π^+ and π^-.

Vertex Cut

The HD target has a cylindrical shape with dimensions 5 cm in length and 1.5 cm in diameter. The reconstruction code can determine where the event happens in the target region (the vertex information: x, y, z). This information can be used to remove the events that do not come from the HD target. Two cuts are applied to the data, one is along the z direction: -10.5 cm < z < -5.5 cm (Figure 3.4), the other is along the radial direction: $r = \sqrt{x^2 + y^2} < 1$ cm (Figure 3.5).
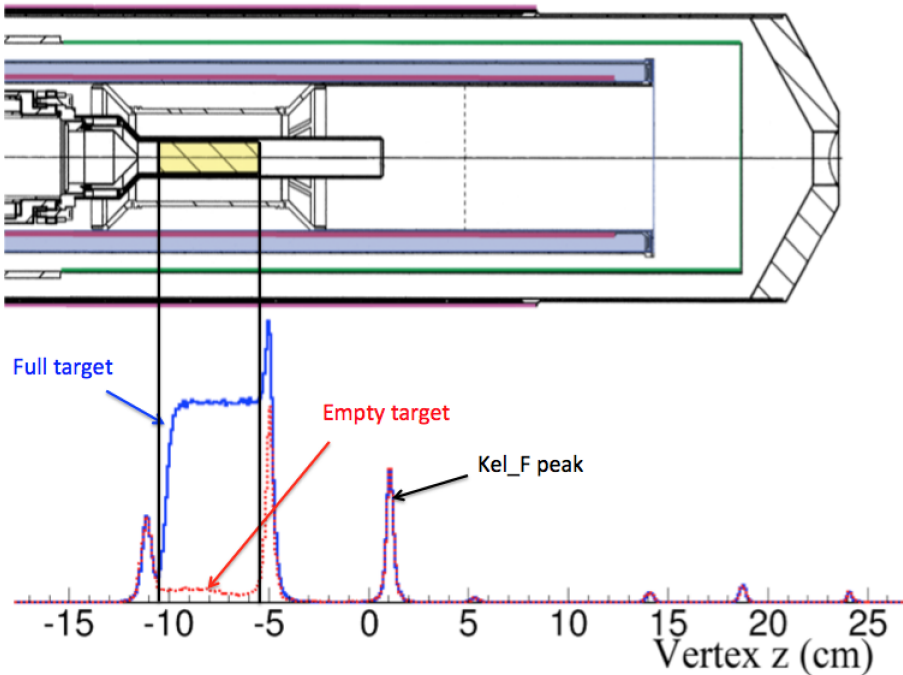
Figure 3.4: Vertex z cut: -10.5 cm < z < -5.5 cm. The top plot is a schematic diagram of the HD target in the IBC (In-Beam-Cryostat). The bottom plot is the vertex plot using the z coordinate from the MVRT bank. The blue line is for a HD target run, the red line is for an empty cell target run, the red curve is scaled to match the downstream Kel-F peak.

3.3.3   Kinematic Cuts

Kinematic cuts use the conservation of 4 momentum in the reaction to make cuts on the missing mass, missing momentum, and reaction angles to select the channel of interest. For example, the reaction of a photon scattering on a neutron target resulting in a recoiling proton and a recoiling π^- can be written in this form: $\gamma + (n) \rightarrow p + \pi^-$. The neutron (n) is in parenthese, because the neutron is in the deuteron with unknown initial momentum, and we view neutron as a missing particle in this reaction. The missing mass and missing momentum for the neutron target can be calculated using the 4 momentum of the detected proton, π^-, and incoming photon. Three kinematic cuts are used to remove background events: missing mass cut, missing momentum cut, and coplanarity cut (Figure 3.6). The coplanarity cut uses the fact that there are only two final state particles, the recoiling
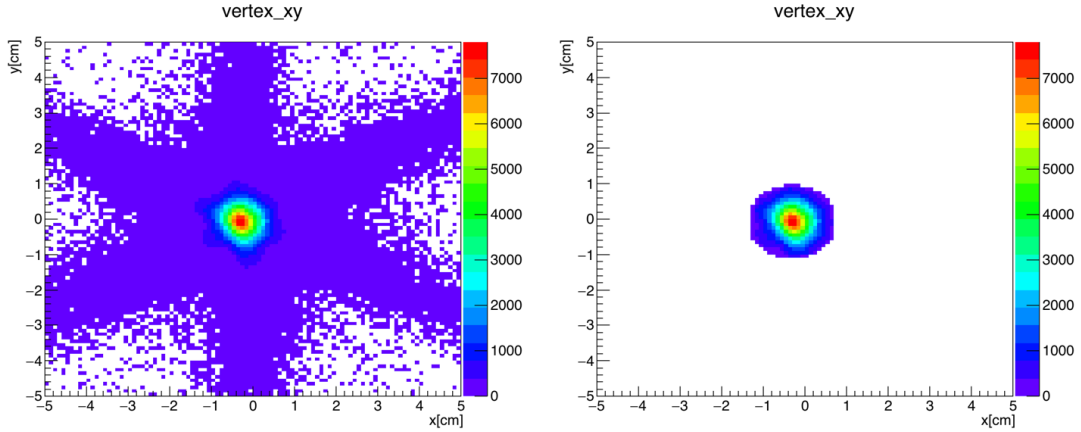
Figure 3.5: Vertex xy cut: r < 1 cm. The left plot is vertex xy before the cut, the six bands correspond to the gaps in CLAS detector. The right plot is vertex xy after the cut.

proton and the π^-. In the center of momentum frame, the difference of the ϕ angles for these two particles should be 180°.

A problem with the cuts in Figure 3.6 is that some background events under the main peak cannot be removed.

A procedure using kinematic fitting to remove background events has been applied in this study. The results for the same reaction $\gamma + (n) \rightarrow p + \pi^-$ are shown in Figure 3.7. From the plots we can see that the blue curves, which represent the events passing the cut, are restricted automatically to the kinematic cuts used in Figure 3.6, and the background events are mostly removed. In the next section, this kinematic fitting procedure will be described in detail.

After all the filters and cuts have been applied to the data, the desired channel is selected, and it is now ready to extract the cross section and polarization observables for this channel.

3.4   Kinematic Fitting

Kinematic Fitting is a technique that uses the least squares fit with physical constraints to improve measured quantities and to estimate unmeasured quantities.[51]. Take the reaction $\gamma + (n) \rightarrow p + \pi^-$ as an example. The kinematic fitting procedure can improve the measured tagged photon energy and the 4 momentum for the recoiling proton and π^-, and can estimate the 4 momentum for the bound neutron target. The constraints used in this procedure are the conservation of the 4 momentum before and after the reaction.

An iterative procedure is used to minimize $\chi^2 = (\mathbf{y} - \hat{\eta})^T \mathbf{V_y}^{-1} (\mathbf{y} - \hat{\eta}) + 2\lambda^{\mathbf{T}} \mathbf{f}(\hat{\eta}, \hat{\xi})$, where y are measured quantities, η are fitted value for the measured quantities, ξ are the unmeasured values, $\mathbf{V_y}^{-1}$ is the covariance matrix. The minimized χ^2_{min} follows a chi-square distribution with (K-J) degree of freedom, where K is the number of constraint functions, J is the number of unmeasured variables. Based on this chi-square distribution, the confidence level and pull distributions will be calculated to measure the goodness-of-fit and to evaluate the error estimation.

Previous studies[52, 54] have shown that the correct error estimation is crucial for
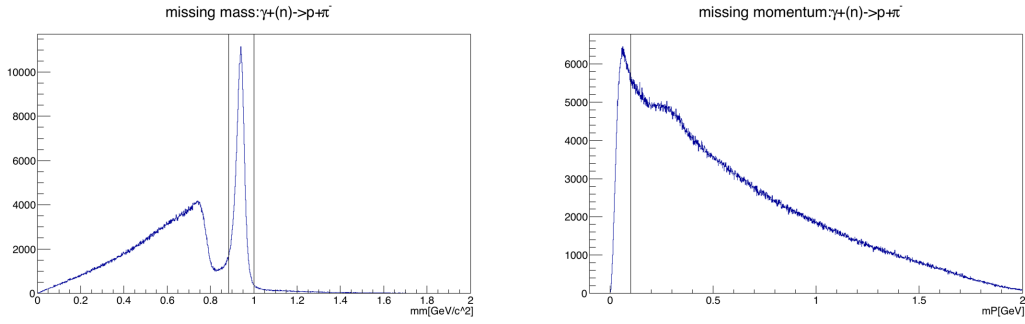
(a) Missing mass cut: 940±60 MeV.

(b) Missing momentum cut: < 100 MeV.
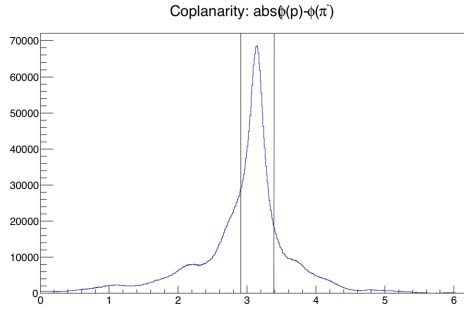
(c) Coplanarity cut: 3.14 ± 0.24.

Figure 3.6: Kinematic Cuts for the missing neutron in the reaction: $\gamma + (n) \rightarrow p + \pi^-$.

kinematic fitting. In CLAS, the covariance matrix is stored in the TBER bank, in which the diagonal and off-diagonal elements give the resolution errors and correlation coefficients of the tracking parameters for each track respectively. Before the kinematic fitting, the covariance matrix needs to be corrected for energy loss, multiple scattering effects and different experiment settings. The confidence level and pull distributions can also help to fine tune the covariance matrix.

The results of the kinematic fitting can be used in two ways, one is to use the confidence level to remove the background events, the other is to use the fitted values to construct the new four momentum for the particles.

3.4.1 Least Squares Fitting

Suppose we have N independent experimental values $y_1, y_2, ..., y_N$ at the points $x_1, x_2, ..., x_N$. The true values of y_i are unknown, but we assume there are some theoretical functions that will predict the true value at each x_i, $f_i = f_i(\theta_1, \theta_2, ..., \theta_L; x_i)$, where $\theta_1, \theta_2, ..., \theta_L$ is a set of parameters, $L \leq N$.

Since each y_i has measurement error σ_i, the equations $f_i = f_i(\theta_1, \theta_2, ..., \theta_L; x_i)$ cannot all be satisfied if $L < N$. For example, if we have three points not in the same line, a linear fitting function with only two parameters cannot go though all three points. But, we can require that the equation be satisfied "as closely as possible" if we define a statistic $X^2 = \sum_{i=1}^{N}((y_i - f_i)/\sigma_i)^2$, and demand that the values of θ_i be chosen so as to minimize X^2. Here we have assumed the measurement y_i is independent, X^2 can be written in
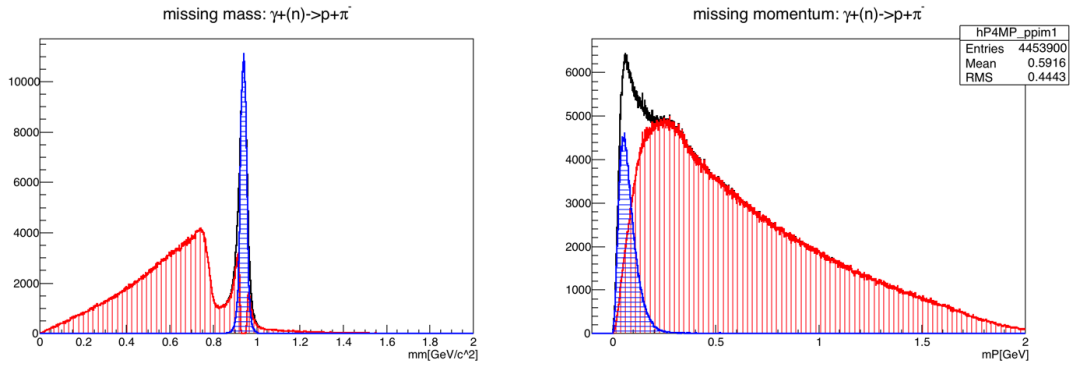
(a) Missing mass.

(b) Missing momentum.
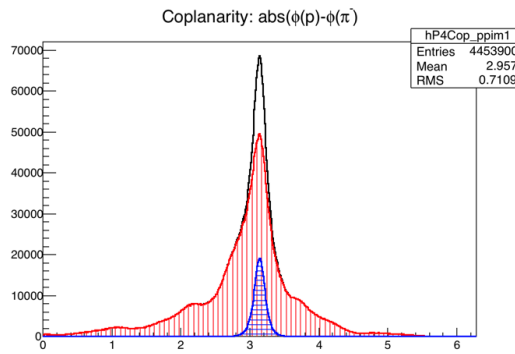
(c) Coplanarity relation.

Figure 3.7: Kinematic fitting procedure for selectiong the channel: $\gamma + (n) \rightarrow p + \pi^-$. In each subplot, the black line is for all the events before using kinematic fitting, the blue line is for the good events that pass the cut, and the red line is for the background events that don't pass the cut.

matrix form:

$$X^2 = (\mathbf{y} - \mathbf{f})^T \mathbf{V_y}^{-1} (\mathbf{y} - \mathbf{f}), \tag{3.2}$$

where $\mathbf{y} = \begin{pmatrix} y_1 \\ y_2 \\ \cdot \\ \cdot \\ \cdot \\ y_N \end{pmatrix}$, $\mathbf{f} = \begin{pmatrix} f_1 \\ f_2 \\ \cdot \\ \cdot \\ \cdot \\ f_N \end{pmatrix}$, $\mathbf{V_y} = \begin{pmatrix} \sigma_1^2 & 0 & . & . & . & 0 \\ 0 & \sigma_2^2 & . & . & . & 0 \\ . & . & . & . & . & . \\ . & . & . & . & . & . \\ . & . & . & . & . & . \\ 0 & 0 & . & . & . & \sigma_N^2 \end{pmatrix}$.

The Linear Least Square Model

If the functions f_i are linear functions of the parameters θ_i, then an exact solution for the parameters can be solved.

$$f_i = f_i(\theta_1, \theta_2, ..., \theta_L; x_i) = \sum_{l=1}^{L} a_{il}\theta_l, \qquad i = 1, 2, ..., N; \quad L < N \tag{3.3}$$

In matrix notation $\mathbf{f} = \mathbf{A}\theta$, $\mathbf{A} = \begin{pmatrix} a_{11} & a_{12} & . & . & . & a_{1L} \\ a_{21} & a_{22} & . & . & . & a_{2L} \\ . & . & . & . & . & . \\ . & . & . & . & . & . \\ . & . & . & . & . & . \\ a_{N1} & a_{N2} & . & . & . & a_{NL} \end{pmatrix}$, $\theta = \begin{pmatrix} \theta_1 \\ \theta_2 \\ \cdot \\ \cdot \\ \cdot \\ \theta_L \end{pmatrix}$.

$$X^2 = (\mathbf{y} - \mathbf{A}\theta)^T \mathbf{V_y}^{-1} (\mathbf{y} - \mathbf{A}\theta) \tag{3.4}$$

Minimizing X^2 by taking the derivatives of X^2 with respect to θ, we have,

$$\nabla_\theta X^2 = -2(\mathbf{A}^T \mathbf{V_y}^{-1} \mathbf{y} - \mathbf{A}^T \mathbf{V_y}^{-1} \mathbf{A}\theta) = 0 \tag{3.5}$$

If the matrix $(\mathbf{A}^T \mathbf{V_y}^{-1} \mathbf{A})$ is non-singular and can be inverted, the solution for θ is:

$$\hat{\theta} = (\mathbf{A}^T \mathbf{V_y}^{-1} \mathbf{A})^{-1} \mathbf{A}^T \mathbf{V_y}^{-1} \mathbf{y}. \tag{3.6}$$

Substitute $\hat{\theta}$ back to Eq. (3.4), we get the minimized X^2_{min}:

$$X^2_{min} = (\mathbf{y} - \mathbf{A}\hat{\theta})^T \mathbf{V_y}^{-1} (\mathbf{y} - \mathbf{A}\hat{\theta}) \tag{3.7}$$

The uncertainties for θ can also be solved by using the formula for error propagation,

$$\begin{aligned} \mathbf{V}(\hat{\theta}) &= \left((\mathbf{A}^T \mathbf{V_y}^{-1} \mathbf{A})^{-1} \mathbf{A}^T \mathbf{V_y}^{-1} \right) \mathbf{y} \left((\mathbf{A}^T \mathbf{V_y}^{-1} \mathbf{A})^{-1} \mathbf{A}^T \mathbf{V_y}^{-1} \right)^T. \\ &= (\mathbf{A}^T \mathbf{V_y}^{-1} \mathbf{A})^{-1} \end{aligned} \tag{3.8}$$

From some algebra calculations we have:

$$X^2 = X^2_{min} + (\theta - \hat{\theta})^T \mathbf{A}^T \mathbf{V_y}^{-1} \mathbf{A}(\theta - \hat{\theta}) = X^2_{min} + (\theta - \hat{\theta})^T \mathbf{V}^{-1}(\hat{\theta})(\theta - \hat{\theta}) \tag{3.9}$$

If the N measurements y_i are normally distributed, by definition X^2 would be a chi-square distribution with N degree of freedom. Since $\hat{\theta}$ is linearly related to y_i, it is also normally distributed. All the three terms in Eq.(3.9) will be chi-square distributed, in which X^2 has N degree of freedom, X^2_{min} has (N-L) degree of freedom, $(\theta - \hat{\theta})^{\mathbf{T}}\mathbf{V}^{-1}(\hat{\theta})(\theta - \hat{\theta})$ has L degree of freedom.

Eq.(3.6) and (3.8) give the solution to the linear LS problem for unknown parameters θ. This result also holds when V_y is a matrix with non-zero covariance terms. In this case, the N measurements y_i are not independent.

The Nonlinear Least Squares Model

If f_i are nonlinear functions of the parameters θ_i, there are no exact solutions for θ_i as in the linear case. We need to use an iterative procedure to perform the minimization.

As discussed earlier, we want to minimize the quantity $X^2 = (\mathbf{y} - \mathbf{f})^T \mathbf{V_y}^{-1}(\mathbf{y} - \mathbf{f})$, where $\mathbf{y}$ is the vector of measurements with covariance matrix $\mathbf{V_y}$, and $\mathbf{f} = \mathbf{f}(\theta; \mathbf{x})$ is the vector of predicted values, which is nonlinear function of θ. Suppose we have found of a set of approximate parameters $\theta^\nu = \{\theta_1^\nu, \theta_2^\nu, ..., \theta_L^\nu\}$ in the ν-th iteration. To make the calculation simple, we assume independent measurements, $V_{yii} = \sigma_i^2$, the derivative of X^2 with respect to θ at $\theta = \theta^\nu$ is,

$$g_l(\theta^\nu) = g_l^\nu = \frac{\partial X^2}{\partial \theta_l} = \sum_{i=1}^{N}\left(-\frac{2}{\sigma_i^2}\right)(y_i - f_i^\nu)\left[\frac{\partial f_i}{\partial \theta_l}\right]_{\theta^\nu}, \qquad l = 1, 2, ..., L \qquad (3.10)$$

We want to find an increment $\Delta\theta^\nu$ to θ^ν which make $g(\theta^\nu + \Delta\theta^\nu) = 0$. To find $\Delta\theta^\nu$, we expand g_l around θ^ν to first order,

$$g_l^\nu + \frac{\partial g_l^\nu}{\partial \theta_1}\Delta\theta_1^\nu + \frac{\partial g_l^\nu}{\partial \theta_2}\Delta\theta_2^\nu + ... + \frac{\partial g_l^\nu}{\partial \theta_L}\Delta\theta_L^\nu = 0, \qquad l = 1, 2, ..., L \qquad (3.11)$$

Write

$$G_{kl}^\nu = \frac{\partial g_l^\nu}{\partial \theta_k} = \frac{\partial^2 X^2}{\partial \theta_k \partial \theta_l} = \sum_{i=1}^{N}\left(-\frac{2}{\sigma_i^2}\right)\left[-\frac{\partial f_i}{\partial \theta_k}\frac{\partial f_i}{\partial \theta_l} + (y_i - f_i^\nu)\frac{\partial^2 f_i^2}{\partial \theta_k \partial \theta_l}\right] \qquad (3.12)$$

Eq.(3.11) can be written in matrix form $\mathbf{g}^\nu + \mathbf{G}^\nu\mathbf{\Delta\theta}^\nu = 0$,

$$\text{where } \mathbf{g}^\nu = \begin{pmatrix} g_1^\nu \\ g_2^\nu \\ . \\ . \\ . \\ g_L^\nu \end{pmatrix}, \mathbf{\Delta\theta}^\nu = \begin{pmatrix} \Delta\theta_1^\nu \\ \Delta\theta_2^\nu \\ . \\ . \\ . \\ \Delta\theta_L^\nu \end{pmatrix}, \mathbf{G}^\nu = \begin{pmatrix} \frac{\partial g_1}{\partial \theta_1} & \frac{\partial g_1}{\partial \theta_2} & . & . & . & \frac{\partial g_1}{\partial \theta_L} \\ \frac{\partial g_2}{\partial \theta_1} & \frac{\partial g_2}{\partial \theta_2} & . & . & . & \frac{\partial g_2}{\partial \theta_L} \\ . & . & . & . & . & . \\ . & . & . & . & . & . \\ . & . & . & . & . & . \\ \frac{\partial g_L}{\partial \theta_1} & \frac{\partial g_L}{\partial \theta_2} & . & . & . & \frac{\partial g_L}{\partial \theta_L} \end{pmatrix}_{\theta = \theta^\nu} . \text{ Then}$$

$\mathbf{\Delta\theta}^\nu = -(\mathbf{G}^\nu)^{-1}\mathbf{g}^\nu$. The new parameters $\theta^{\nu+1} = \theta^\nu + \Delta\theta^\nu$ are used to find $(X^2)^{\nu+1}$, if $(X^2)^{\nu+1} < (X^2)^\nu$, the new parameters are a better estimation, and the procedure is repeated until the improvement between two consecutive iterations is smaller than the preset value. If it is found that one iteration gives $(X^2)^{\nu+1} > (X^2)^\nu$, one can redefine the ν-th step by taking a smaller value, such as $\Delta\theta^\nu = \frac{1}{2}\Delta\theta^\nu$ to do the procedure.

Improved Measurements

In the previous sections, the least squares method is used to find the best values for the unknown parameters θ, which are used in some theoretical functions $f(\theta; x)$ to predict the true observable η. However, in many situations, the unknowns are the observables η themselves, such as in the kinematic fitting. In this case, we will use the observations $\mathbf{y}$ and the covariance matrix $\mathbf{V_y}$ as the initial estimates and use the principle of least squares to find the best estimates of η which will minimize the quantity $X^2 = \epsilon^{\mathbf{T}} \mathbf{V_y^{-1}} \epsilon$, where $\epsilon = \mathbf{y} - \eta$. The final estimates $\hat{\eta}$ of the true value η are called the "improved measurements".

Least Squares Model with Constraints

As before, we first consider the linear LS problem with linear constraint functions:

$$X^2 = (\mathbf{y} - \mathbf{A}\theta)^T \mathbf{V_y}^{-1}(\mathbf{y} - \mathbf{A}\theta),$$
$$\mathbf{B}\theta - \mathbf{b} = 0, \tag{3.13}$$

where the L parameters θ are related through K constraint functions, $\mathbf{B}$ is a matrix with dimension $K \times L$, $\mathbf{b}$ is a component vector. We introduce a K-component Lagrangian multiplier λ and rewrite the problem in the unconstrained form with L+K unknowns.

$$X^2 = (\mathbf{y} - \mathbf{A}\theta)^T \mathbf{V_y}^{-1}(\mathbf{y} - \mathbf{A}\theta) + 2\lambda^{\mathbf{T}}(\mathbf{B}\theta - \mathbf{b}). \tag{3.14}$$

Eq.(3.14) can be solved exactly if we equate to zero the derivatives of X^2 with respect to θ_l and λ_k[51]. In the most general situation, both the f_i and the constraint functions are nonlinear of θ, the iterative procedure using the method of Lagrangian multipliers will be used to minimize X^2. In the following, we give an example to show how to use least squares estimation with constraints to "improve measurements" and estimate unmeasured quantities.

Suppose we have a process $\gamma + p \rightarrow p + \pi^+ + \pi^-$, where the momenta and angles of the two pions are measured, but the recoiling proton is not measured, the momentum and energy conservation give four constraint functions. For convenience, we use a vector $\eta = \{\eta_1, \eta_2, ...\eta_N\}$ to represent the true values for the N measured quantities $\mathbf{y} = \{y_1, y_2, ...y_N\}$, the vector $\xi = \{\xi_1, \xi_2, ...\xi_J\}$ to represent the true values for the J unmeasured quantities. The total unknowns are N+J for η and ξ, there are K constraint equations which relate the unknowns:

$$f_k(\eta_1, \eta_2, ...\eta_N, \xi_1, \xi_2, ...\xi_J) = 0, \qquad k = 1, 2, ..., K. \tag{3.15}$$

The Least Squares Principle requires that the best estimates of the unknowns η and ξ are the values making the following equations true:

$$X^2 = (\mathbf{y} - \hat{\eta})^T \mathbf{V_y}^{-1}(\mathbf{y} - \hat{\eta}) = minimum,$$
$$\mathbf{f}(\hat{\eta}, \hat{\xi}) = 0, \tag{3.16}$$

As before, we introduce K additional unknowns $\lambda = \{\lambda_1, \lambda_2, ...\lambda_K\}$, and rewrite the problem by requiring:

$$X^2 = (\mathbf{y} - \hat{\eta})^T \mathbf{V_y}^{-1}(\mathbf{y} - \hat{\eta}) + 2\lambda^{\mathbf{T}} \mathbf{f}(\hat{\eta}, \hat{\xi}) = minimum, \tag{3.17}$$

Equating the derivatives of X^2 with respect to all N+J+K unknowns to zero gives N+J+K equations:

$$\nabla_\eta X^2 = -2\mathbf{V_y}^{-1}(\mathbf{y} - \eta) + 2F_\eta^T \lambda = 0,$$
$$\nabla_\xi X^2 = 2F_\xi^T \lambda = 0, \tag{3.18}$$
$$\nabla_\lambda X^2 = 2\mathbf{f}(\eta, \xi) = 0,$$

where the matrices $F_\eta (dimension : K \times N)$ and $F_\xi (dimension : K \times J)$ are:

$$(F_\eta)_{ki} = \frac{\partial f_k}{\partial \eta_i}, \qquad (F_\xi)_{kj} = \frac{\partial f_k}{\partial \xi_j}. \tag{3.19}$$

Since $f(\eta, \xi)$ are nonlinear functions of η, ξ, the N+J+K functions cannot solve the N+J+K unknowns exactly, the solution must be found by iteration.

Let us suppose that solution $\eta^\nu, \xi^\nu, \lambda^\nu$ are found in the ν-th iteration, which gives $(X^2)^\nu$. We want to find the next $\eta^{\nu+1}, \xi^{\nu+1}, \lambda^{\nu+1}$, which gives $(X^2)^{\nu+1}$ smaller than $(X^2)^\nu$. Equations in (3.18) are used to relate the values in two iteration steps. First, we make a Taylor expansion of the third equation in (3.18) around η^ν, ξ^ν and neglect the second and higher orders,

$$f_k^\nu + \sum_{i=1}^N (F_\eta^\nu)_{ki}(\eta_i^{\nu+1} - \eta^\nu) + \sum_{j=1}^J (F_\xi^\nu)_{kj}(\xi_i^{\nu+1} - \xi^\nu) = 0. \tag{3.20}$$

Then we write the other two equations in (3.18) at the $(\nu + 1)$-th iteration values:

$$\eta^{\nu+1} = y - \mathbf{V_y}(F_\eta^T)^\nu \lambda^{\nu+1},$$
$$(F_\xi^T)^\nu \lambda^{\nu+1} = 0, \tag{3.21}$$

Substituting $\eta^{\nu+1}$ in Eq.(3.21) to Eq.(3.20), and introducing $\mathbf{r} = \mathbf{f}^\nu + \mathbf{F}_\eta^\nu(\mathbf{y} - \eta^\nu), \mathbf{S} = \mathbf{F}_\eta^\nu \mathbf{V_y}(\mathbf{F}_\eta^\mathbf{T})^\nu$, yields:

$$\mathbf{f}^\nu + \mathbf{F}_\eta^\nu \left[(\mathbf{y} - \mathbf{V_y}(\mathbf{F}_\eta^\mathbf{T})^\nu \lambda^{\nu+1}) - \eta^\nu \right] + (\mathbf{F}_\xi^\nu)(\xi^{\nu+1} - \xi^\nu) = \mathbf{0}$$
$$\Rightarrow \mathbf{r} + (\mathbf{F}_\xi^\nu)(\xi^{\nu+1} - \xi^\nu) = \mathbf{S}\lambda^{\nu+1} \tag{3.22}$$
$$\Rightarrow \lambda^{\nu+1} = \mathbf{S}^{-1} \left[\mathbf{r} + (\mathbf{F}_\xi^\nu)(\xi^{\nu+1} - \xi^\nu) \right].$$

Using $\lambda^{\nu+1}$ from Eq.(3.22) in the first equation in Eq.(3.21), we can solve $\xi^{\nu+1}, \lambda^{\nu+1}, \eta^{\nu+1}$:

$$\xi^{\nu+1} = \xi^\nu - \left[(\mathbf{F}_\xi^\mathbf{T})^\nu \mathbf{S}^{-1} \mathbf{F}_\xi^\nu \right]^{-1} (\mathbf{F}_\xi^\mathbf{T})^\nu \mathbf{S}^{-1} \mathbf{r}$$
$$\lambda^{\nu+1} = \mathbf{S}^{-1} \left[\mathbf{r} + (\mathbf{F}_\xi^\nu)(\xi^{\nu+1} - \xi^\nu) \right] \tag{3.23}$$
$$\eta^{\nu+1} = y - \mathbf{V_y}(F_\eta^T)^\nu \lambda^{\nu+1}.$$

By keeping the Taylor expansion of $\mathbf{f}(\eta, \xi)$ to first order, we linearize the equation set, and the completely unknown $\xi^{\nu+1}$ are solved at first, next the Lagrangian multipliers $\lambda^{\nu+1}$ and lastly the improved measurements $\eta^{\nu+1}$ are solved. These new values will be used to calculate the new $(X^2)^{\nu+1}$, which will be compared with $(X^2)^\nu$ to decide when to stop the iteration process. The convergence of $\mathbf{\Delta}\eta, \mathbf{\Delta}\xi$ may also need to be checked. For the starting values, we can choose $\eta^\mathbf{0} = \mathbf{y}$, the measured value, and $\xi^\mathbf{0}$ can be calculated from the constraint equations by inserting $\eta^\mathbf{0}$. The covariance matrix for η, ξ can also be calculated[51].

Confidence Level and Pull Distributions

From section 2.1, we know that the residuals X^2_{min}, which are obtained from the minimization process, have a chi-square distribution. This distribution can be used to define a measure for the goodness-of-fit, which is,

$$P_{\chi^2} = \int_{\chi^2_{min}}^{\infty} f(\chi^2;\nu)d\chi^2 = 1 - F(\chi^2_{min};\nu), \tag{3.24}$$

where $f(\chi^2;\nu)$ is the PDF (probability distribution function), and $F(\chi^2_{min};\nu)$ is the CDF (cumulative distribution function) for the chi-square distribution with ν degrees of freedom. In Root, P_{χ^2} is calculated using the function TMath::Prob(chisq,ndf), which denotes the probability that an observed chi-square exceeds the value "chisq". Since CDF is uniformly distributed within [0,1](see Figure 3.8), P_{χ^2}(often called p-value) is also uniformly distributed. If the minimization process gives P_{χ^2} non-uniform, this means either the hypothesis is not satisfied or the measurements are bad. An example is when P_{χ^2} is strongly peaked near zero, this indicates a contamination of the data from the background events, since background events gives bigger χ^2, which means fatter tail in the PDF $f(\chi^2;\nu)$, and a peak in P_{χ^2} at low probabilities. By cutting the small P_{χ^2}, we can remove the background events, as shown in Figure 3.9.
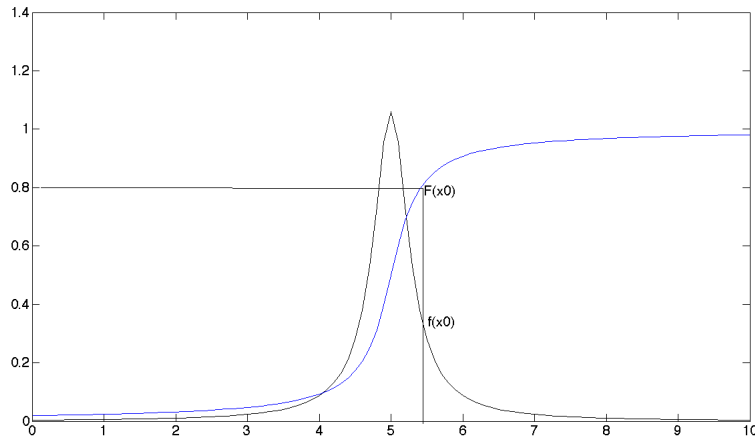
Figure 3.8: f(x) is PDF, F(x) is CDF for a lorentz distribution, the pobability for x<x0 is P(f(x<x0))=P(F(x)<F(x0))=F(x0). The distribution which has the property P(r<r0)=r0 is the uniform distribution over the region [0,1].

Quite often, a big χ^2_{min} is not due to the wrong hypothesis or background events, but because either the measured values are altered by Energy loss or multi-scattering, or a wrong error estimate is used. It is helpful to define the Pull Distribution to look at each measured value,

$$z_i = \frac{\epsilon_i}{\sigma(\epsilon_i)} = \frac{y_i - \hat{\eta}_i}{\sqrt{\sigma^2(y_i) - \sigma^2(\hat{\eta}_i)}}, \qquad i = 1, 2, ..., N, \tag{3.25}$$

where $\epsilon_i = y_i - \hat{\eta}_i$ measures the deviations between the observations and the fitted values, ϵ_i is normalized relative to its uncertainty $\sigma(\epsilon_i)$ to allow for comparison of different
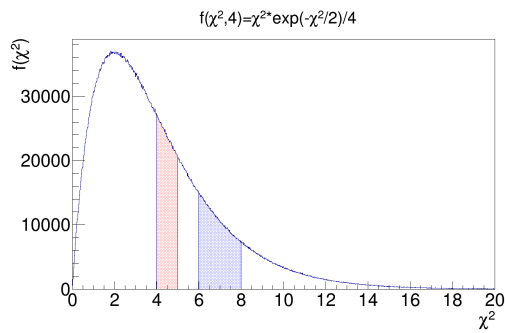
(a) monte carlo $\chi^2(4)$
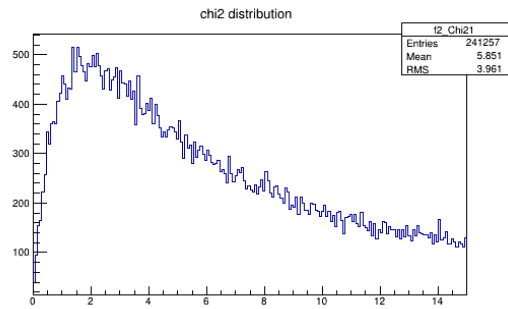
(b) real data $\chi^2(4)$
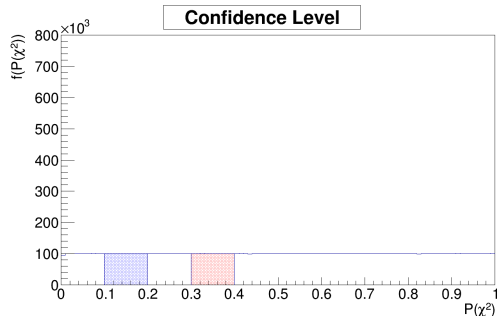
(c) monte carlo cofident level
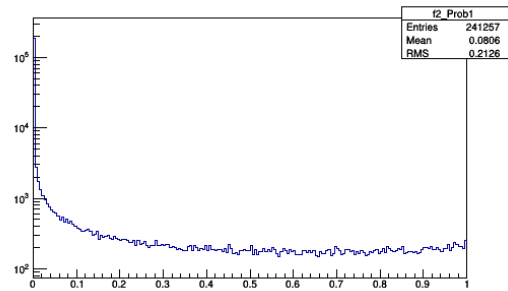
(d) real data cofident level

Figure 3.9: χ^2 distribution with degrees of freedom $n = 4$ and its confidence level from monte carlo and real data. Right two plots are those from real data, background events give a fatter tail for $f(\chi^2; \nu)$ at large χ^2 and sharp peak for P_{χ^2} around 0.

measurements. The minus sign in the calculation for $\sigma(\epsilon_i)$ comes from the fact that $y_i, \hat{\eta}_i$ are completely correlated,

$$\sigma^2(\epsilon_i) = V_{ii}(y - \hat{\eta}) = V_{ii}(y) - 2cov(y, \hat{\eta})_{ii} + V_{ii}(\hat{\eta}) = V_{ii}(y) - V_{ii}(\hat{\eta}). \qquad (3.26)$$

The pull should be normally distributed about zero with $\sigma = 1$. If z_i is shifted away from zero, this indicates a systematic error in the i-th observation. If the observed z_i is too broad(narrow) compared to the normal distribution N(0,1), the error in the i-th observation is consistently too small(large). Before the kinematic fitting, the effect of Energy loss, multi-scattering and other factors should be corrected for the observations and the covariance matrix. The pull distribution provides a way to test how well the corrections work.

Degrees of Freedom

The function TMath::Prob(chisq,ndf) for the calculation of the confidence level requires the degree of freedom for the distribution χ^2_{min}. From Eq.(3.9) in section 2.1, we know that if we have N measured values and L unknown fitted values, χ^2_{min} has (N-L) degree of freedom. If there are K constraint functions relating the L unknowns, only (L-K) of them are independent, giving (N-(L-K)) independent terms in χ^2_{min}, so χ^2_{min} is distributed as $\chi^2(N - L + K)$.

For the process $\gamma + p \rightarrow (p) + \pi^+ + \pi^-$, with recoiling proton not measured. N = 7, in which 1 is for incoming photon energy, 6 are for 2 sets of pion tracking variables. L = N+J =10, where J=3 is for the fitting values for the missing proton. K = 4 from the 4 constraint equations of the conservation of energy and momentum. This is a (N-L+K)=1C fit. If all the initial and final states are known, then it is a 4C fit.

3.4.2 Covariance Matrix in CLAS

From section 2.4.1, we know that an accurate covariance matrix is important for good kinematic fitting. Instead of using the 4-vector momentum to describe the status of a particle, CLAS uses the tracking parameters $q/p, \lambda, \phi$. This section will introduce how the tracking parameters are defined, the covariance matrix for these parameters, and corrections need to be done for the covariance matrix to make it more accurate.

Track Reconstruction

The track reconstruction for charged particles in the drift chambers in CLAS is done in a sector dependent system. As shown in Figure 3.10, the x_{track}-axis is along the z_{lab} direction, the y_{track}-axis goes through the center of the sector, and the z_{axis} is along the average magnetic field in the given sector. The relations between the tracking coordinates and lab coordinates are:

$$\begin{pmatrix} x_{track} \\ y_{track} \\ z_{track} \end{pmatrix} = \begin{pmatrix} z_{lab} \\ \cos(\alpha)x_{lab} + \sin(\alpha)y_{lab} \\ -\sin(\alpha)x_{lab} + \cos(\alpha)y_{lab} \end{pmatrix} \qquad (3.27)$$

where $\alpha = \frac{\pi}{3}(N_{sector} - 1)$ is sector dependent.
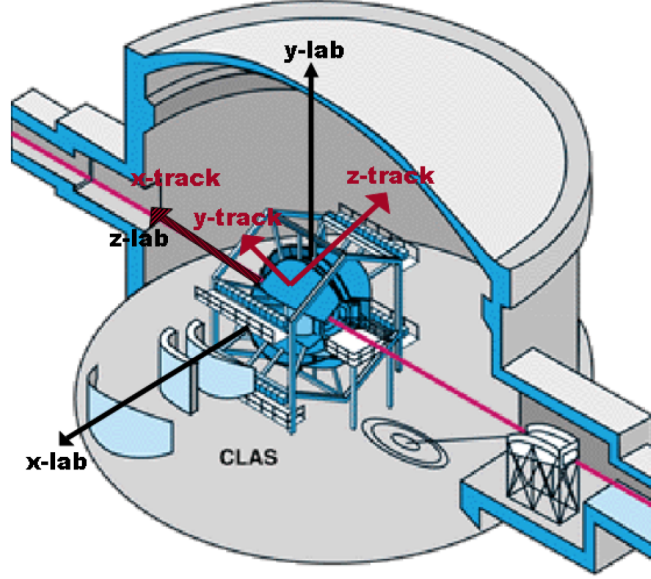
Figure 3.10: Scheme for tracking coordinates and lab coordinates

The tracking parameters for the particles in the TBER bank include: $q/p, \lambda, \phi, d_0, z_0$, in which d_0 and z_0 are used in vertex reconstruction; we only discuss the first three parameters here. q is the charge of the particle, p is its momentum in the lab frame, $\lambda \in (-\pi/6, \pi/6)$ is the angle between the track and the (x_{track}, y_{track}) plane, ϕ is the angle in the (x_{track}, y_{track}) plane relative to x_{track}-axis. Using the tracking parameters, we can write the momentum of the particles in the lab frame as:

$$\begin{pmatrix} p_{x_{lab}} \\ p_{y_{lab}} \\ p_{z_{lab}} \end{pmatrix} = \begin{pmatrix} p(\cos(\lambda)\sin(\phi)\cos(\alpha) - \sin(\lambda)\sin(\alpha)) \\ p(\cos(\lambda)\sin(\phi)\sin(\alpha) + \sin(\lambda)\cos(\alpha)) \\ p\cos(\lambda)\cos(\phi) \end{pmatrix}, \qquad (3.28)$$

The covariance matrix for the tracking parameters are also given in the TBER bank:

$$\begin{pmatrix} cov(\frac{q}{p}, \frac{q}{p}) = c_{11} & cov(\frac{q}{p}, \lambda) = c_{12} & cov(\frac{q}{p}, \phi) = c_{13} \\ cov(\lambda, \frac{q}{p}) = c_{12} & cov(\lambda, \lambda) = c_{22} & cov(\lambda, \phi) = c_{23} \\ cov(\phi, \frac{q}{p}) = c_{13} & cov(\phi, \lambda) = c_{23} & cov(\phi, \phi) = c_{33} \end{pmatrix}. \qquad (3.29)$$

These covariance matrix elements are determined from the tracking information only without any corrections. The resolution error for ϕ is approximately $\sigma_{\phi_{res}} \approx \sigma_s/R$, where $\sigma_s \approx 200\mu m$ is the resolution of detector in the plane of ϕ. $R \approx 75cm$ is the distance from the vertex to the drift chamber, so $\sigma_{\phi_{res}}$ is about 0.27 mrad. The resolution of the detector in the plane of λ is one order of magnitude worse than that for ϕ, $\sigma_{\lambda_{res}}$ is about 2.7 mrad. These two errors can be calculated from the TBER bank, $\sigma_{\phi_{res}} = \sqrt{c_{33}}$ and $\sigma_{\lambda_{res}} = \sqrt{c_{22}}$. Figure 3.11 gives the errors for the two tracking angles for proton, π^+ and π^-, respectively. The correlation coefficients between the tracking parameters are defined as $\rho_{ij} = c_{ij}/\sqrt{c_{ii}c_{jj}}$. From Figure 3.12, we see a strong correlation between q/p and ϕ. This is because $q/p = 1/(Br\sin\theta)$, where B is the magnetic field, r is the radius of curvature of the track; on the other hand, the CLAS toroidal filed B has a strong ϕ(which is the polar angle θ in lab coordinates) dependence, B is smaller for bigger ϕ as

shown in Fig.5 in [29], so the two tracking parameters q/p and ϕ are strongly correlated.

(a) $\sigma_{\lambda_{res}}$ for proton

(b) $\sigma_{\lambda_{res}}$ for π^+

(c) $\sigma_{\lambda_{res}}$ for π^-

(d) $\sigma_{\phi_{res}}$ for proton
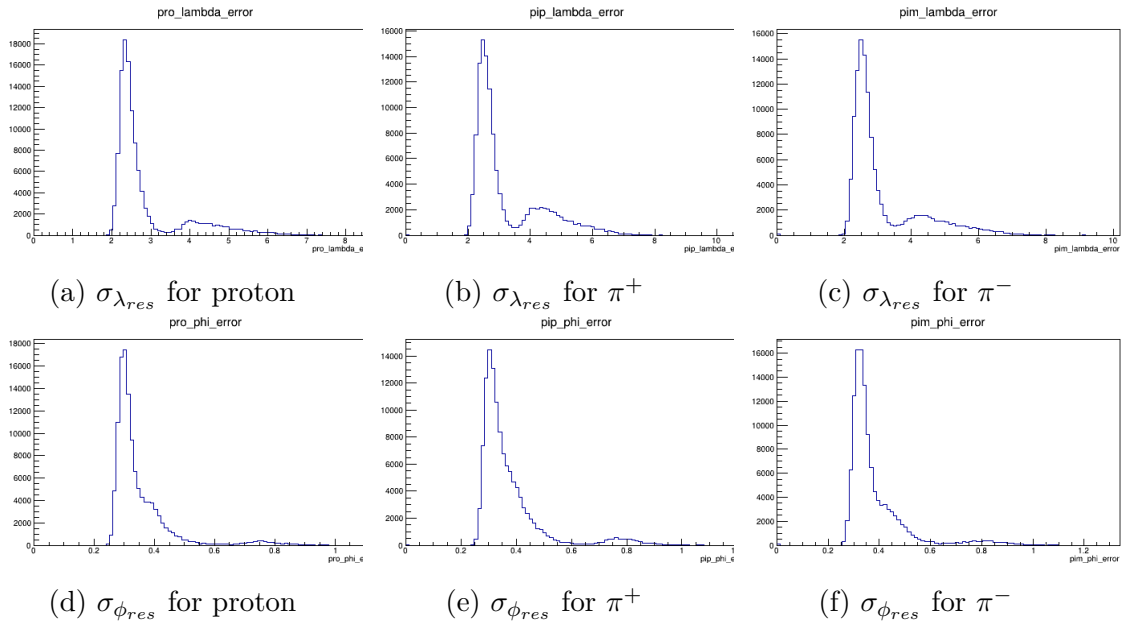
(e) $\sigma_{\phi_{res}}$ for π^+

(f) $\sigma_{\phi_{res}}$ for π^-

Figure 3.11: $\sigma_{\lambda_{res}}$ and $\sigma_{\phi_{res}}$ for proton, π^+ and π^-
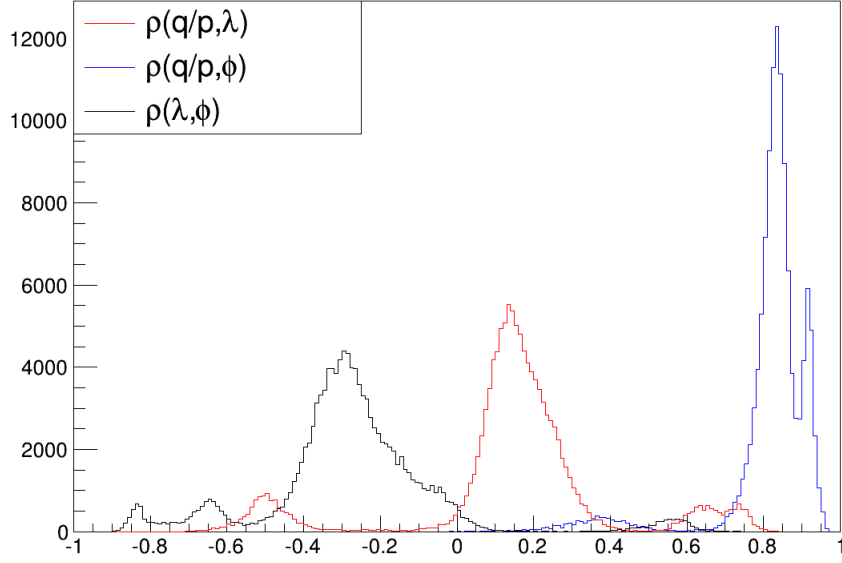
Figure 3.12: Correlation coefficiences between tracking parameters. $\rho(q/p, \phi) \approx 0.85$, $\rho(q/p, \lambda) \approx 0.15$, $\rho(\lambda, \phi) \approx -0.27$.

Effect of Energy Loss and Multiple Scattering on Covariance Matrix

It's easier to study the energy loss effect using the parameter p instead of q/p, so we write the new covariance matrix in terms of p as:

$$
\begin{aligned}
C^{pp} &= \left(\frac{\partial p}{\partial (q/p)} \right)^2 C^{\frac{q}{p}\frac{q}{p}} = \frac{p^4}{q^2} C^{\frac{q}{p}\frac{q}{p}}, \\
C^{p\phi} &= \left(\frac{\partial p}{\partial (q/p)} \right) \left(\frac{\partial \phi}{\partial \phi} \right) C^{\frac{q}{p}\phi} = -\frac{p^2}{q} C^{\frac{q}{p}\phi}, \\
C^{p\lambda} &= \left(\frac{\partial p}{\partial (q/p)} \right) \left(\frac{\partial \lambda}{\partial \lambda} \right) C^{\frac{q}{p}\lambda} = -\frac{p^2}{q} C^{\frac{q}{p}\lambda},
\end{aligned}
\tag{3.30}
$$

It was found in previous studies that some corrections for the covariance matrix need to be done before the energy loss and multiple scattering corrections. For the two angle parameters, the values were found to be off by a factor of 1.5:

$$
\begin{aligned}
\sigma_{\phi_{res}} &= 1.5 \sigma_{\phi_{TBER}}, \\
\sigma_{\lambda_{res}} &= 1.5 \sigma_{\lambda_{TBER}}.
\end{aligned}
\tag{3.31}
$$

For the momentum, the TBER bank does not account for the torus current, which makes the value off by a factor of I_{max}/I:

$$
\sigma_{p_{res}} = \frac{I_{max}}{I} \sigma_p = \frac{I_{max}}{I} \frac{p^2}{q} \sigma_{(q/p)_{TBER}},
\tag{3.32}
$$

During the experiment, before reaching the detectors, the final state particles need to pass through some material first, such as the target, the in-beam cryostat and the start

80

counter. This material will change both the values of the tracking parameters and its covariance matrix. These corrections are not included in the TBER bank, and need to be added separately.

The corrections for energy loss and multiple scattering to the tracking errors are as follows:

$$
\begin{aligned}
\sigma_p^2 &= \sigma_{p_{res}}^2 + \sigma_{el}^2, \\
\sigma_\phi^2 &= \sigma_{\phi_{res}}^2 + \sigma_{ms}^2, \\
\sigma_\lambda^2 &= \sigma_{\lambda_{res}}^2 + \sigma_{ms}^2.
\end{aligned}
\tag{3.33}
$$

where $\sigma_{p_{res}}$, $\sigma_{\phi_{res}}$ and $\sigma_{\lambda_{res}}$ are resolution errors before the correction, σ_{el} is the energy loss correction to the momentum error, σ_{ms} is the multiple scattering correction to the tracking angle errors. The method to calculate σ_{el} and σ_{ms} can be found in section 3.1 of [54].

The Corrected Covariance Matrix

We can now write down the corrected covariance matrix for the kinematic fitting taking into account all the corrections in the previous section. Consider a reaction with L charged particles in the final state. There are (3L+1) fit parameters,

$$
C_\eta =
\begin{pmatrix}
\sigma_{E_\gamma}^2 \\
p_1 \\
\lambda_1 \\
\phi_1 \\
\cdot \\
\cdot \\
\cdot \\
p_L \\
\lambda_L \\
\phi_L
\end{pmatrix},
\tag{3.34}
$$

where E_γ is the incident photon energy and p_i, λ_i, ϕ_i are the tracking parameters for the ith charged particle.

Since the measurements of different particles are uncorrelated, the covariance between different particles is zero. The covariance matrix is,

$$
\eta =
\begin{pmatrix}
\sigma_{E_\gamma}^2 & 0 & 0 & 0 & \cdots & 0 & 0 & 0 \\
0 & C_1^{pp} & C_1^{p\lambda} & C_1^{p\phi} & \cdots & 0 & 0 & 0 \\
0 & C_1^{\lambda p} & C_1^{\lambda\lambda} & C_1^{\lambda\phi} & \cdots & 0 & 0 & 0 \\
0 & C_1^{\phi p} & C_1^{\phi\lambda} & C_1^{\phi\phi} & \cdots & 0 & 0 & 0 \\
\vdots & \vdots & \vdots & \vdots & \ddots & \vdots & \vdots & \vdots \\
0 & 0 & 0 & 0 & \cdots & C_L^{pp} & C_L^{p\lambda} & C_L^{p\phi} \\
0 & 0 & 0 & 0 & \cdots & C_L^{\lambda p} & C_L^{\lambda\lambda} & C_L^{\lambda\phi} \\
0 & 0 & 0 & 0 & \cdots & C_L^{\phi p} & C_L^{\phi\lambda} & C_L^{\phi\phi}
\end{pmatrix},
\tag{3.35}
$$

where $\sigma_{E_\gamma}^2$ is the error of measuring the tagged photon. $\sigma_{E_\gamma}^2$ is calculated using the energy resolution of E-plane paddles in the tagger, which is $0.001E_0$, E_0 is the electron beam

81

energy. For a photon with energy $\bar{E}$, the energy of the photon is uniformly distributed within $[\bar{E} - 0.001E_0, \bar{E} + 0.001E_0]$ because of the resolution of the detector. The error of $\bar{E}$ is,

$$\sigma^2_{E_\gamma} = \int_{\bar{E}-0.001E_0}^{\bar{E}+0.001E_0} \frac{(E-\bar{E})^2}{0.002E_0} dE = \int_{-0.001E_0}^{0.001E_0} \frac{E'^2}{0.002E_0} dE' = \frac{(0.001E_0)^2}{3}. \tag{3.36}$$

Other covariance matrix elements are calculated using the information from the TBER bank:

$$
\begin{aligned}
C_i^{pp} &= \left(\frac{I_{max}p_i^2}{Iq_i}\right)^2 C_{TBER}^{\frac{q_i}{p_i}\frac{q_i}{p_i}} + \sigma^2_{p_{eloss}}, \\
C_i^{\lambda\lambda} &= 2.25 C_{TBER}^{\lambda_i\lambda_i} + \sigma^2_{ms}, \\
C_i^{\phi\phi} &= 2.25 C_{TBER}^{\phi_i\phi_i} + \sigma^2_{ms}, \\
C_i^{p\lambda} &= -\left(\frac{1.5I_{max}p_i^2}{Iq_i}\right) C_{TBER}^{\frac{q_i}{p_i}\lambda}, \\
C_i^{p\phi} &= -\left(\frac{1.5I_{max}p_i^2}{Iq_i}\right) C_{TBER}^{\frac{q_i}{p_i}\phi}, \\
C_i^{\lambda\phi} &= 2.25 C_{TBER}^{\lambda\phi}.
\end{aligned}
\tag{3.37}
$$

To check if the covariance matrix has been corrected, we can look at the pull distribution of the tracking parameters, an iterative process will help determine the best estimation for the error correction.

3.4.3 Preparation for Kinematic Fitting

Before the kinematic fitting, we should do the following three corrections to get the four momentum of the particles as accurate as possible: energy loss correction, momentum correction and tagger sag correction. The kinematic fitting can be used to test how good the correction is by looking at the pull distributions.

Energy Loss Correction

As the charged particles pass through the material in the CLAS detector, they will lose some of their energy, thus a systematic adjustment to the particles' energy is required. The ELOSS package [55] is used for the corrections. This package uses a first principle method to calculate the energy loss by considering all the material that the particles go through. The differences $\Delta E = E_{after} - E_{before}$ for proton, π^+, π^- are shown in Figure 3.13. As seen in the plots, the high momentum protons have small energy loss of around 15 MeV, and for low momentum protons, the correction is about 50 MeV. This is reasonable from the relation $dE/dx \sim 1/\beta^2$. The lighter particles π^+, π^- lose less energy than the heavier particles such as the proton.

In order to check if the Eloss correction package works, we can plot the pull distributions before and after Eloss correction. Figure 3.14 gives this comparison for the pull distribution for P_{pro} (proton's momentum). We can see that after the Eloss correction, the pull distribution becomes more like a standard normal distribution, except that the mean value is still not zero, the reason will be explained in the next section.
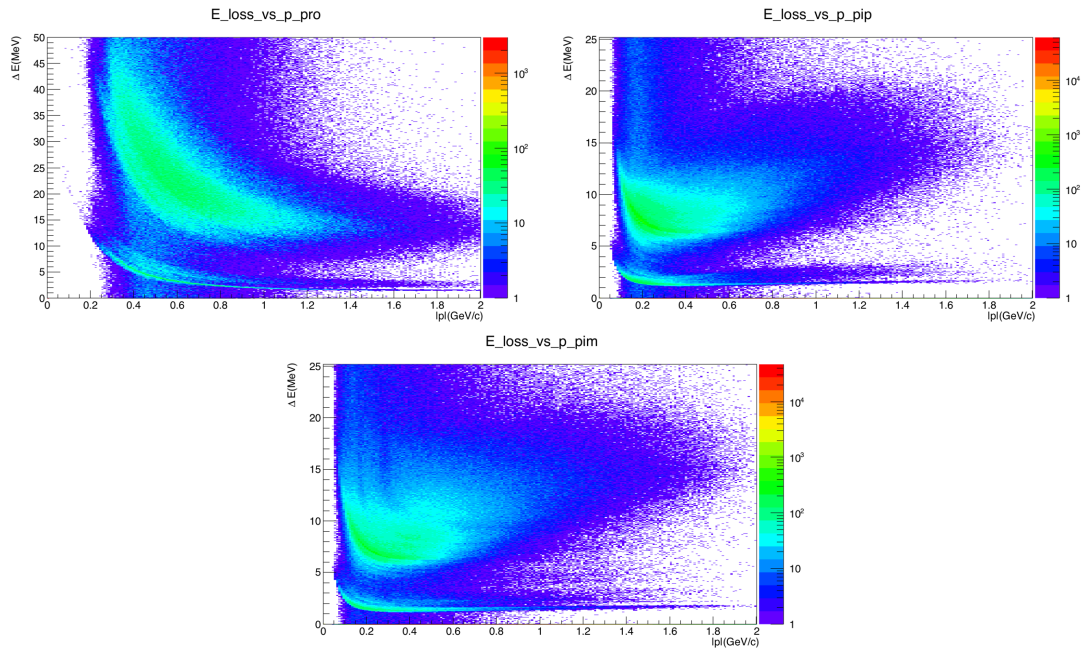
Figure 3.13: Eloss correction vs. momentum for proton (top left), π^+ (top right), π^- (bottom)
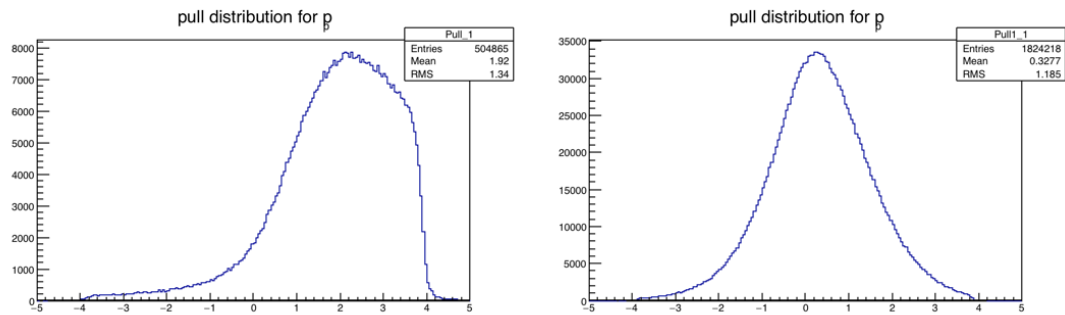
Figure 3.14: Pull distribution before(left plots) and after(right plots) the energy loss correction for proton momentum.

Momentum Correction and Photon Energy Correction

After the energy loss correction, the pull distributions have improved a lot, but their means are still not close to zero. The reason for this problem can be seen in Figure 3.15. We can see that the missing mass for the missing particle depends on the ϕ angle of
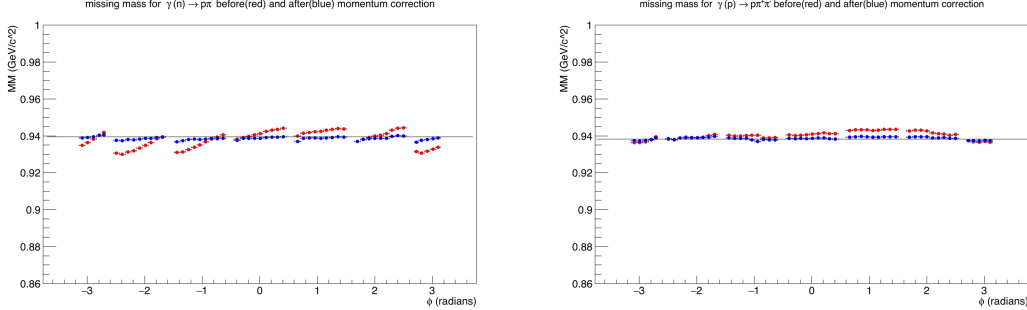
Figure 3.15: Missing Mass vs. ϕ_{pro} for the reaction $\gamma(n) \rightarrow p\pi^-$ (left plot) and $\gamma(p) \rightarrow p\pi^+\pi^-$ (right plot), the particle in the parenthesis is the missing particle. The red points are before momentum and photon energy correction, the blue points are after momentum and photon energy correction.

the recoiling proton. This is caused by the misalignment of the drift chamber with the magnetic field. Thus we need to correct the momentum of the final state particles for each θ and ϕ bin, and to correct the incoming photon energy in terms of the tagger's 767 energy bins. The way to do these two corrections is to use kinematic fitting to get the fitted value for the particles' momenta for each θ and ϕ bin and photon energy for each E-counter energy bin, then take the difference between the fitted values and the measured values to get the correction equations, $\Delta p = p^{kfit} - p^{meas}$, $\Delta E_\gamma = E_\gamma^{kfit} - E_\gamma^{meas}$.

The momentum correction is done for 9 (θ) × 36 (ϕ) bins. θ and ϕ are for angles in the lab frame for recoiled protons. The nine θ bins are $0° < \theta \leq 20°$, $20° < \theta \leq 30°$, $30° < \theta \leq 40°$, $40° < \theta \leq 50°$, $50° < \theta \leq 60°$, $60° < \theta \leq 70°$, $70° < \theta \leq 80°$, $80° < \theta \leq 100°$, $100° < \theta \leq 180°$. The 36 bins come from binning each of the six CLAS sectors into six bins. The schematic plots for θ and ϕ bins can be seen in Figure 3.16. The use of both the single pion channel and double pion channel extends the dynamic range of applicability of these corrections, since pion momentum is relatively high in the single pion channel, and pion momenta in the double pion channel are relatively low.

The momentum correction is done for protons, π^+, π^- respectively. The correction for the bin $20° < \theta \leq 30°$, $-164° < \phi \leq -152°$ for protons is shown in Figure 3.17. For protons and π^-, the correction combines the kinematic fitted values from both the two pion channel $\gamma(p) \rightarrow p\pi^+\pi^-$ and the one pion channel $\gamma(n) \rightarrow p\pi^-$. For π^+, the correction only uses the two pion channel $\gamma(p) \rightarrow p\pi^+\pi^-$. The corrections for π^+ and π^- for the bin $20° < \theta \leq 30°$, $-164° < \phi \leq -152°$ are shown in Figure 3.18.

Photon energy correction $\Delta E_\gamma = E_\gamma^{kfit} - E_\gamma^{meas}$ is calculated in terms of the 767 E-counter energy bins, and the result is also a combination of the correction from both channels: $\gamma(p) \rightarrow p\pi^+\pi^-$ and $\gamma(n) \rightarrow p\pi^-$. Figure 3.19 gives the result for the photon energy correction.

After the momentum and photon energy corrections, the same pull distribution as in Figure 3.14 is plotted again in Figure 3.20. From the figure, we can see that the mean of
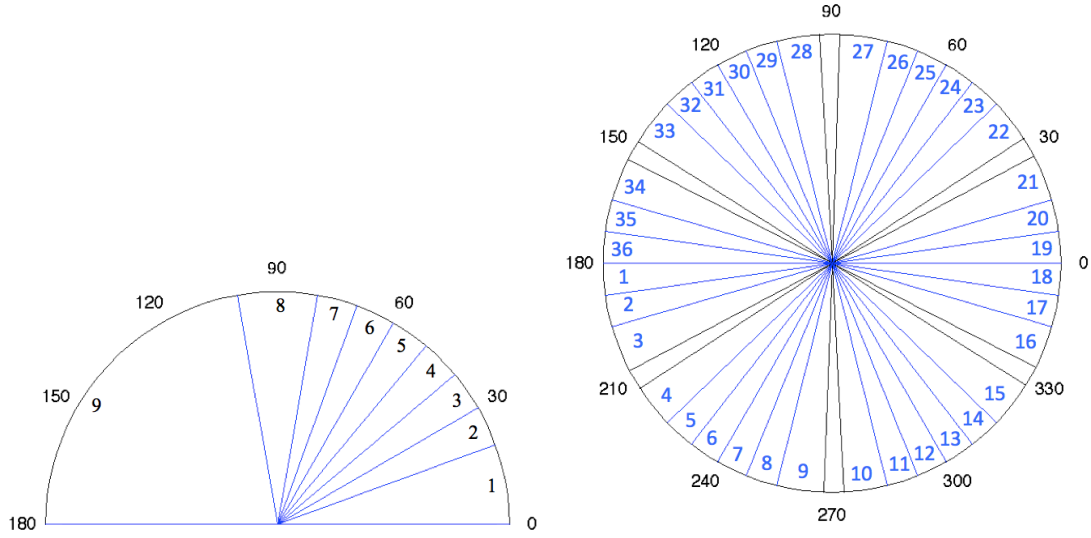
Figure 3.16: θ bins (left plot) and ϕ bins (right plot) for momentum correction. The different sizes of the θ bins are chosen by considering that the CLAS acceptance is small in the forward angle and backward angle. In the plot for ϕ bins, the gaps enclosed by black lines correspond to the gaps between the six CLAS sectors. The bin size near the gap is bigger because of a smaller acceptance in this region.
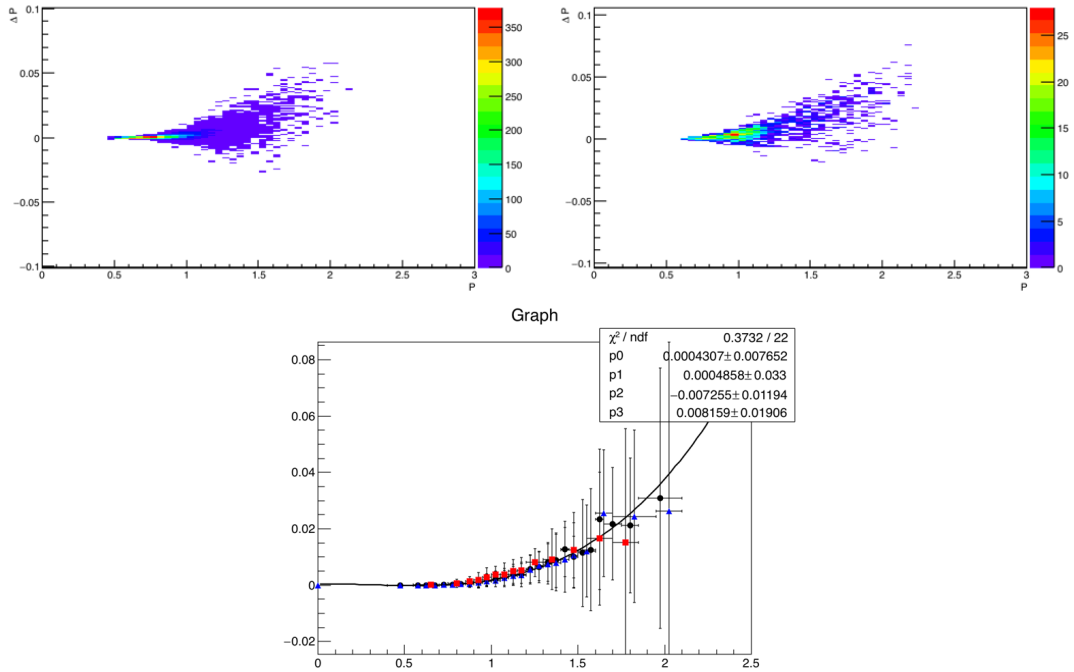
Figure 3.17: Momentum correction Δp vs p for protons in the bin $20° < \theta \leq 30°$, $-164° < \phi \leq -152°$. Top left: Δp vs p for the reaction $\gamma(p) \rightarrow p\pi^+\pi^-$. Top right: Δp vs p for the reaction $\gamma(n) \rightarrow p\pi^-$. Bottom: The Gaussian fit for Δp by binning p, blue triangle markers are for the two pion channel, red square markers are for the single pion channel, black circle markers are the combination of the two channel.

85
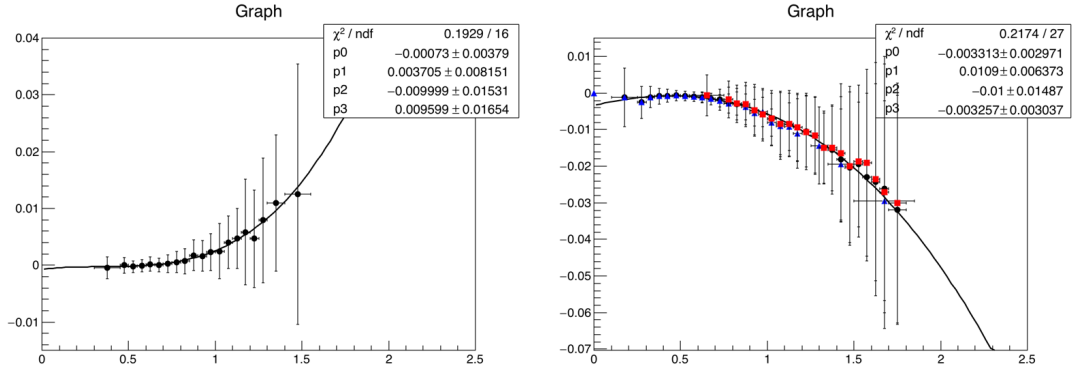
Figure 3.18: Momentum correction Δp vs p for π^+ and π^- in the bin $20° < \theta \leq 30°$, $-164° < \phi \leq -152°$. Left: correction for π^+ using the channel $\gamma(p) \to p\pi^+\pi^-$. Right: correction for π^- using both $\gamma(p) \to p\pi^+\pi^-$ and $\gamma(n) \to p\pi^-$, blue triangle markers are for the two pion channel, red square markers are for the single pion channel, black circle markers are for the combination of the two channels.
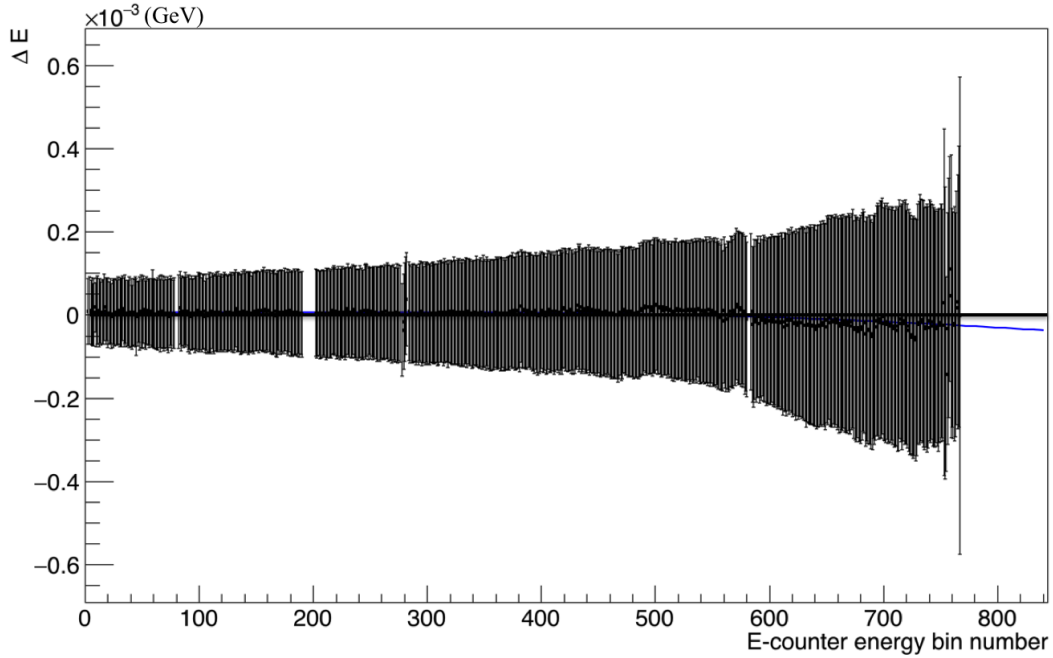
Figure 3.19: Photon energy correction $\Delta E_\gamma = E_\gamma^{kfit} - E_\gamma^{meas}$ vs. Tagger E-counter bins.

86

the pull distribution moves from 0.3079 to -0.01356, and the sigma changes from 1.043 to 1.007. The momentum and photon energy corrections makes the pull distribution more like the standard gaussian distribution.
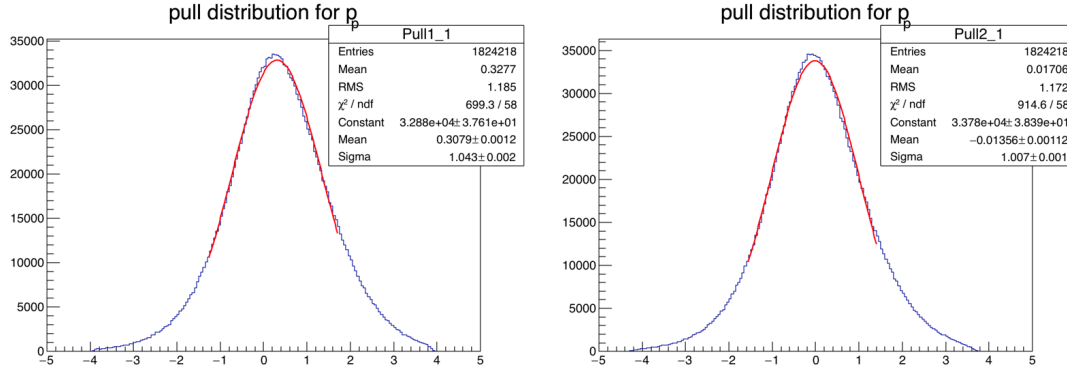
Figure 3.20: Pull distribution before(left plots) and after(right plots) Momentum and Photon Energy corrections for proton momentum. The mean value has moved from 0.31 to -0.01

It should be noted that the G14 experiment uses different targets and different Torus currents. The data collected is divided into different periods as shown in Table 3.1. The momentum and photon energy corrections are done for 4 different run periods: Silver 1 and 2, Silver 3 and 4, Silver 5, Gold 2.

3.4.4 Kinematic Fitting for $\gamma n \to p\pi^-$

In order to select the channel of interest, the kinematic fitting is used again. The four momenta of the final state particles have had the energy loss correction, momentum correction, and photon energy correction applied. For this channel, we could apply two equivalent hypothese. One is $\gamma(n) \to p\pi^-$, which assumes an unknown moving neutron target, the other is $\gamma D \to p(p)\pi^-$, which assumes a deuteron target and a missing spectator proton in the final state. We choose the first hypothesis, since this method removes the events from the high momentum neutron in the deuteron target automatically, and the polarization observables in this study require a target with minimal initial momentum (ideally zero momentum). The confidence level cut is used to remove the background events, and the quality of the selected channel will be checked with the missing mass plot, missing momentum plot, coplanarity plot, and the pull distributions for all the final state particles' tracking parameters. These results will be shown for the gold2a period at first (Figure 3.21 and Figure 3.22). Then the confidence level plots (Figure 3.23), missing mass vs. ϕ plots (Figure 3.24), and the mean and sigma values of the pull distributions (Table 3.4) will be shown for all the run periods with circularly polarized beam.

Since the neutron used in this channel is a quasi-free particle, in the kinematic fitting, an effective mass for the neutron is used in the procedure, and the value is estimated as following. For a free particle, the invariant mass of the particle relates to its energy and momentum as $E^2 - p^2 = m^2$. For a quasi-free particle, this relation becomes $(E - V)^2 = k^2 + m^2$, with an extra potential term V. If the potential term is much smaller than the mass of the particle, we can still view the particle as a free particle but with an off-shell
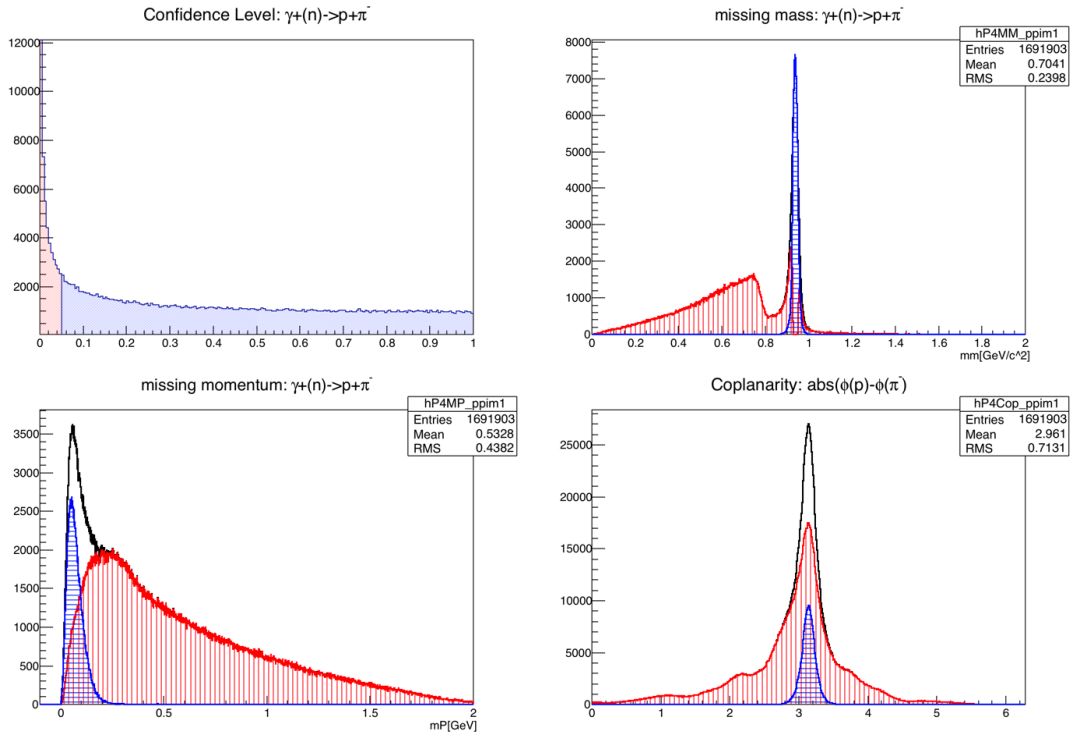
Figure 3.21: Effect of the kinematic fitting's confidence level cut on event selection for the channel $\gamma(n) \to p\pi^-$ using the data from gold2a. Top left: confidence cut at 5%. top right: missing mass plot, bottom left: missing momentum, bottom right: coplanarity. For all the plots, the blue region is for good events that pass the cut, the red region is the background events that are removed by the cut.
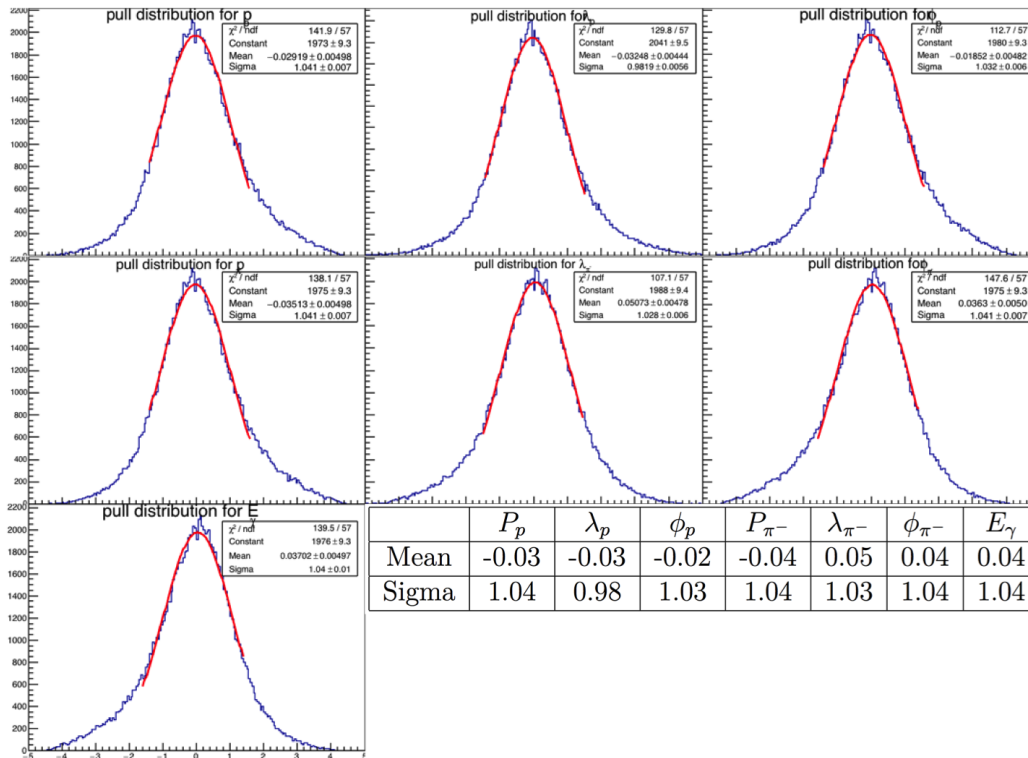
Figure 3.22: Pull distribution for gold2a data for channel $\gamma(n) \rightarrow p\pi^-$. The mean and sigma values for the gaussian fit of the pull distribution are inserted at the bottom right corner, the values are very close to a standard gaussian distribution.

	P_p	λ_p	ϕ_p	P_{π^-}	λ_{π^-}	ϕ_{π^-}	E_γ
Mean	-0.03	-0.03	-0.02	-0.04	0.05	0.04	0.04
Sigma	1.04	0.98	1.03	1.04	1.03	1.04	1.04
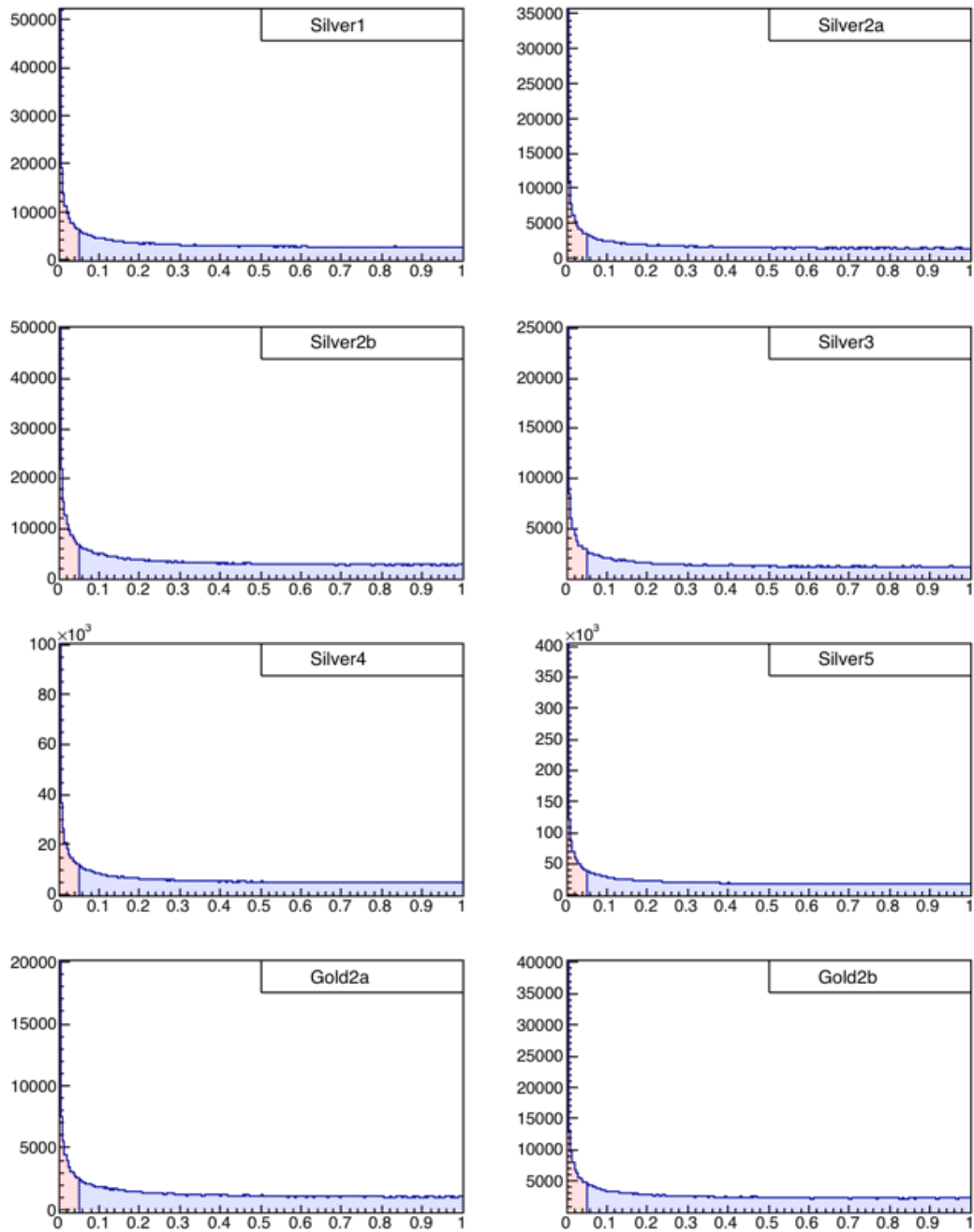
Figure 3.23: 5% confidence level cut for all circular photon polarization periods for the reaction $\gamma(n) \to p\pi^-$.
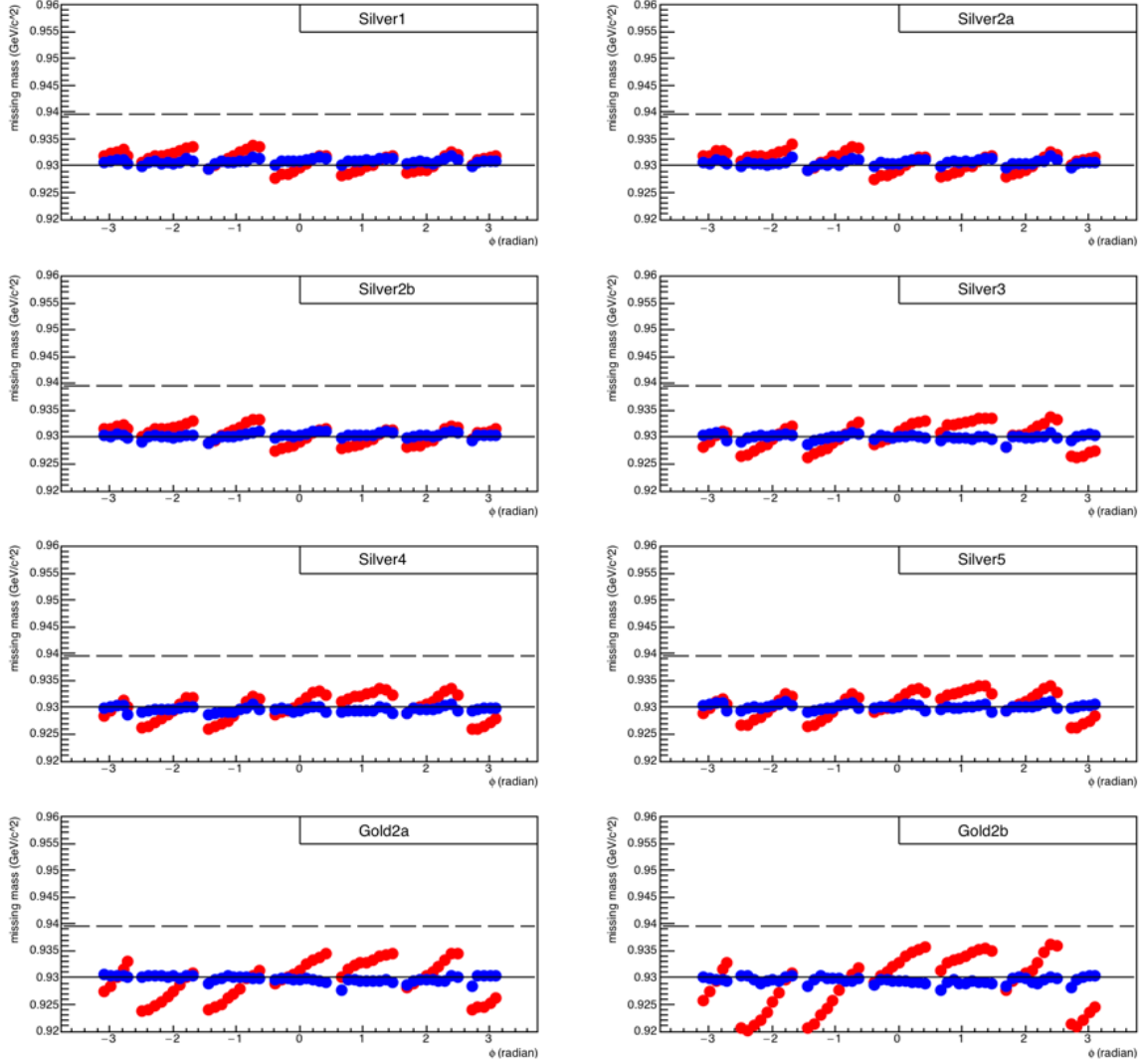
Figure 3.24: Missing Mass vs. ϕ_{pro} for the reaction $\gamma(n) \rightarrow p\pi^-$ for all circular photon polarization periods.

effective mass m^* : $E^2 - k^2 = (m^*)^2 = m^2 + 2EV - V^2$. Since $V << m$, $m^* \approx m + V$. For deuteron, the binding energy is 0.00223 GeV, $m^* \approx m - C \times 0.00223$, where C is a constant, which is estimated to be 4.3 as studied in Appendix. This gives $m^* \approx 0.930$ GeV.

Period	Pull Dist.	P_p	λ_p	ϕ_p	P_{π^-}	λ_{π^-}	ϕ_{π^-}	E_γ
Silver1	Mean	0.02	0.06	-0.01	0.01	-0.03	0.02	-0.01
	Sigma	1.11	1.04	1.11	1.12	1.07	1.11	1.11
Silver2a	Mean	0.02	0.06	-0.02	0.02	-0.04	0.03	-0.02
	Sigma	1.10	1.02	1.10	1.10	1.05	1.10	1.10
Silver2b	Mean	0.05	0.04	-0.05	0.05	-0.01	0.06	-0.04
	Sigma	1.12	1.03	1.11	1.12	1.07	1.12	1.12
Silver3	Mean	0.04	-0.03	0.06	0.03	0.02	-0.03	-0.03
	Sigma	1.03	0.94	1.02	1.04	1.00	1.04	1.04
Silver4	Mean	0.09	-0.02	0.10	0.09	-0.03	-0.08	-0.08
	Sigma	1.02	0.95	1.02	1.03	1.00	1.03	1.03
Silver5	Mean	0.01	-0.08	0.02	-0.00	0.02	0.00	0.00
	Sigma	0.97	0.91	0.97	0.98	0.95	0.98	0.98
Gold2a	Mean	-0.03	-0.03	-0.02	-0.04	0.05	0.04	0.04
	Sigma	1.04	0.98	1.03	1.04	1.03	1.04	1.04
Gold2b	Mean	-0.02	-0.03	-0.01	-0.03	0.04	0.03	0.03
	Sigma	1.05	0.98	1.04	1.04	1.03	1.05	1.04

Table 3.4: Mean and sigma values of the pull distributions for all the circular photon polarization periods for channel $\gamma(n) \to p\pi^-$.

3.4.5 Kinematic Fitting for $\gamma p \to p\pi^+\pi^-$

For the reaction of two charged pion photo-production from a proton target, since the HD molecule has one free proton and one bound proton in the deuteron, we cannot separate the events in these two cases. Thus it's not proper to assume either H or D as the target in the kinematic fitting. The only hypothesis for the kinematic fitting we can make is to assume the proton target's momentum is unknown, and all the final state particles are detected. This makes the kinematic fitting a 1-C fit. The same set of plots as the single pion channel are shown in the following. Figure 3.25 shows the confidence cut of 5% for the gold2a period, and the effect of this cut on the missing mass, missing momentum, and coplanarity plots. Figure 3.26 shows the pull distributions for all 10 kinematic variables after energy loss correction, photon energy correction and momentum correction for gold2a period. The results are very close to the standard normal distribution as expected. Figure 3.27 shows the confidence level distribution for all circular photon polarization runs, and figure 3.28 shows their missing mass vs ϕ plots.
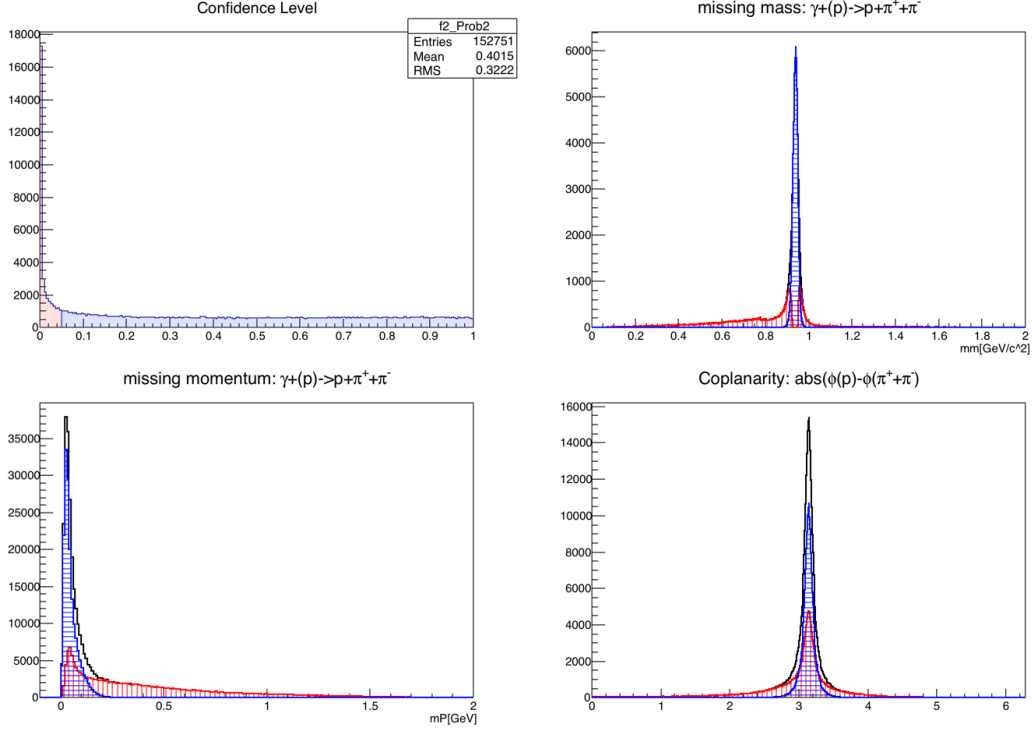
Figure 3.25: Effect of the kinematic fitting's confidence level cut on event selection for channel $\gamma(p) \to p\pi^+\pi^-$ using the data from gold2a. Top left: confidence cut at 5%. top right: missing mass plot, bottom left: missing momentum, bottom right: coplanarity. For all the plots, the blue region is for good events that pass the cut, the red region is the background events that are removed by the cut.

Period	Pull Dist.	P_p	λ_p	ϕ_p	P_{π^+}	λ_{π^+}	ϕ_{π^+}	P_{π^-}	λ_{π^-}	ϕ_{π^-}	E_γ
Silver1	Mean	-0.02	0.07	0.03	-0.01	-0.04	-0.00	-0.01	-0.03	0.00	0.01
	Sigma	1.04	0.98	1.04	1.04	0.97	1.04	1.04	0.99	1.04	1.04
Silver2a	Mean	-0.03	0.07	0.06	-0.03	-0.06	-0.01	-0.02	-0.07	-0.02	0.03
	Sigma	1.03	0.98	1.02	1.03	0.96	1.04	1.03	0.99	1.03	1.03
Silver2b	Mean	-0.01	0.06	0.02	-0.00	-0.07	0.01	-0.00	-0.03	0.01	0.00
	Sigma	1.06	0.99	1.06	1.06	0.96	1.06	1.06	1.01	1.06	1.06
Silver3	Mean	0.02	-0.05	0.04	0.02	0.01	-0.01	0.02	0.03	-0.02	-0.02
	Sigma	1.06	0.97	1.06	1.06	1.01	1.06	1.06	1.01	1.06	1.06
Silver4	Mean	0.07	-0.01	0.09	0.08	-0.01	-0.07	0.08	-0.02	-0.07	0.07
	Sigma	1.05	0.99	1.05	1.05	1.01	1.05	1.05	1.03	1.05	1.06
Silver5	Mean	0.02	-0.04	0.04	0.03	0.01	-0.01	0.02	0.01	-0.01	-0.02
	Sigma	1.03	0.96	1.04	1.03	0.99	1.03	1.03	1.00	1.02	1.03
Gold2a	Mean	0.02	-0.02	0.03	0.02	0.02	-0.01	0.02	0.04	-0.01	-0.01
	Sigma	1.06	0.94	1.06	1.06	1.00	1.05	1.05	0.98	1.05	1.05
Gold2b	Mean	0.02	-0.02	0.04	0.03	0.01	-0.02	0.02	0.02	-0.02	-0.02
	Sigma	1.04	0.94	1.04	1.04	1.00	1.04	1.04	0.98	1.04	1.04

Table 3.5: Mean and sigma values of the pull distributions for all the circularly run periods for channel $\gamma(p) \to p\pi^+\pi^-$.
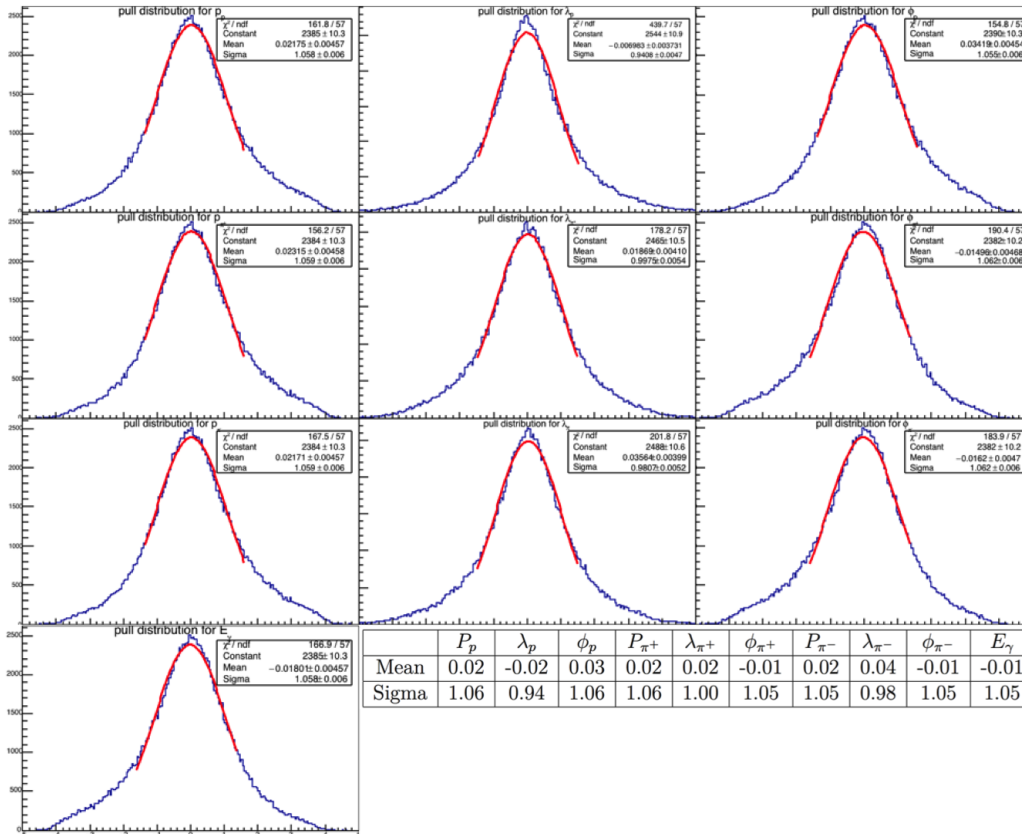
Figure 3.26: Pull distribution for gold2a for channel $\gamma(p) \to p\pi^+\pi^-$. The mean and sigma values for the gaussian fit of the pull distribution are inserted at the bottom right corner. The values are very close to a standard gaussian distribution.

	P_p	λ_p	ϕ_p	P_{π^+}	λ_{π^+}	ϕ_{π^+}	P_{π^-}	λ_{π^-}	ϕ_{π^-}	E_γ
Mean	0.02	-0.02	0.03	0.02	0.02	-0.01	0.02	0.04	-0.01	-0.01
Sigma	1.06	0.94	1.06	1.06	1.00	1.05	1.05	0.98	1.05	1.05
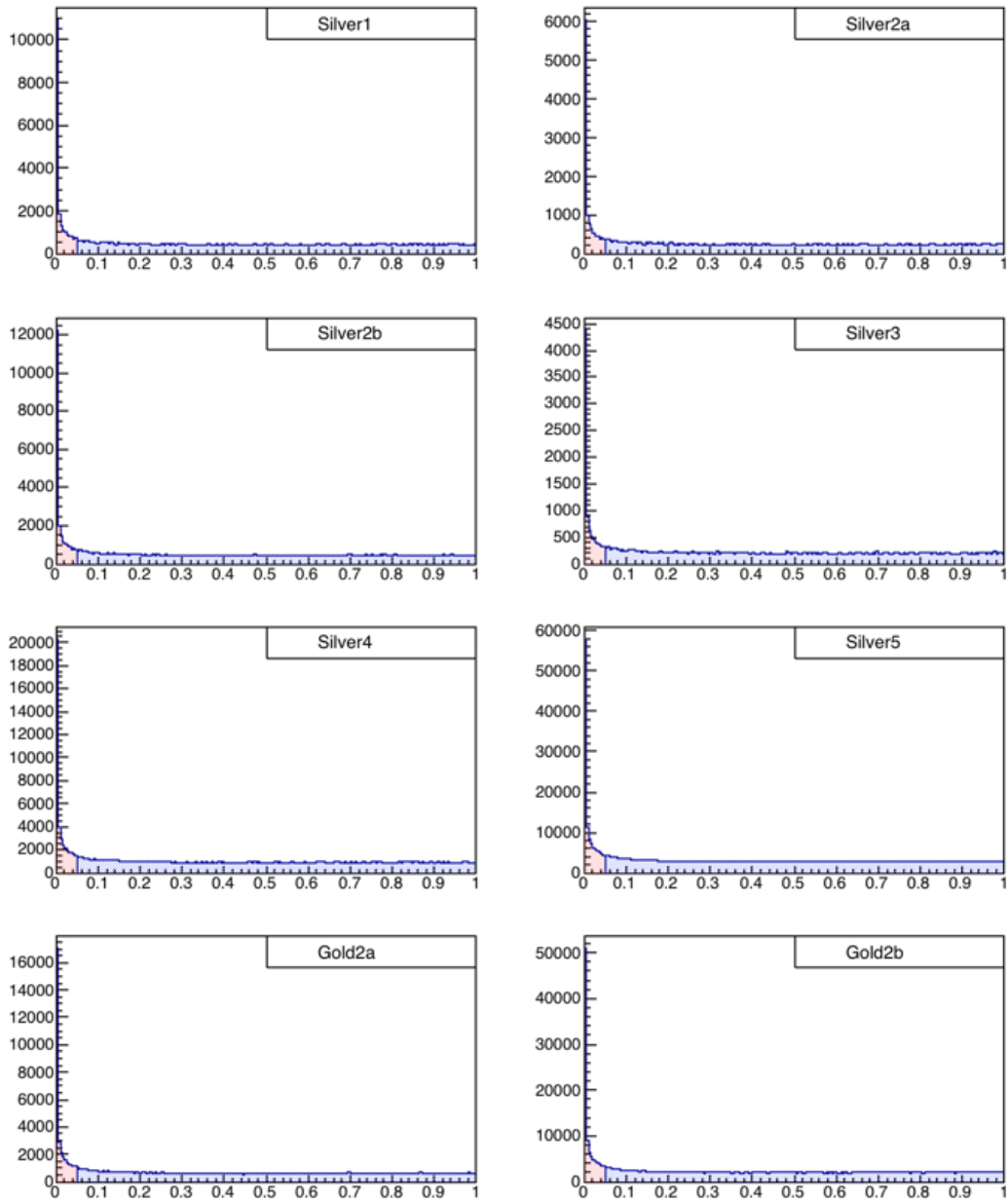
Figure 3.27: 5% confidence level cut for all circular photon polarization periods for the reaction $\gamma(p) \rightarrow p\pi^+\pi^-$.
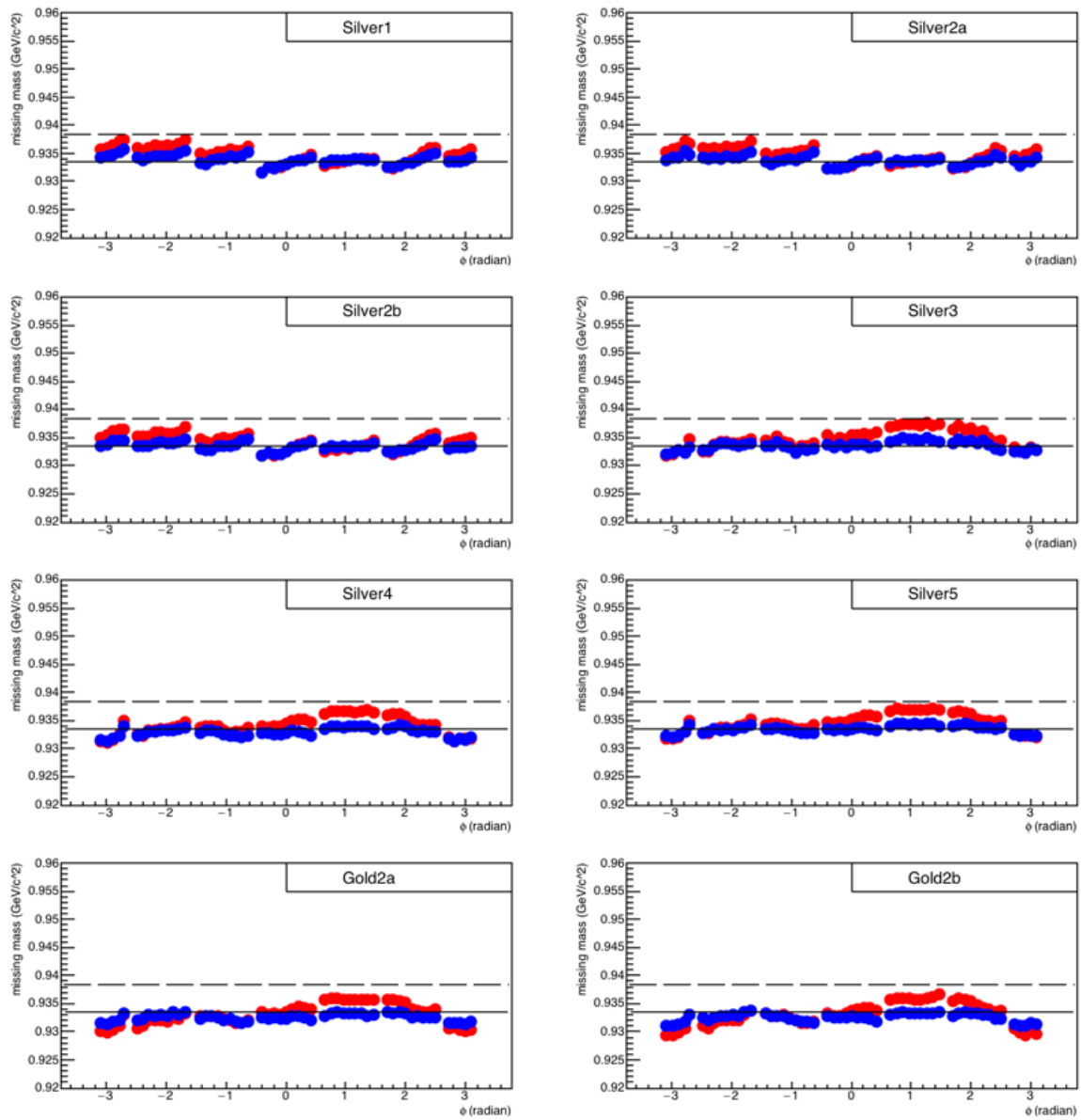
Figure 3.28: Missing Mass vs. ϕ_{pro} for the reaction $\gamma(p) \to p\pi^+\pi^-$ for all circular photon polarization periods.

Chapter 4

E asymmetry for $\gamma n \to p\pi^-$

An accurate evaluation of the electromagnetic couplings in meson photo-production remains unknown due to the lack of experiment data on the neutron targets. Moreover, the existing data on neutron target are mainly differential cross sections, only 15% are from polarization observable measurements [16]. Our measurement of the E asymmetry for $\gamma n \to p\pi^-$ is the first for this polarization observable on the neutron target.

4.1   Formalism
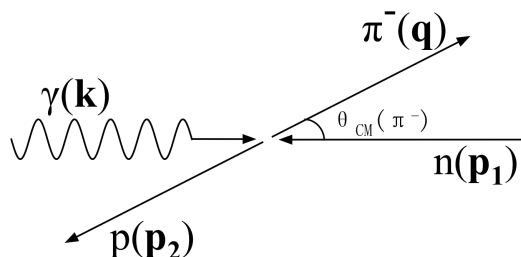
Figure 4.1: Kinematics diagram for π^- photoproduction off a neutron target in the center of momentum frame. $\boldsymbol{k}$, $\boldsymbol{p_1}$, $\boldsymbol{q}$, $\boldsymbol{p_2}$ are the momenta for the incident photon, target neutron, and final state π^- and recoiling proton, $\theta_{CM}(\pi^-)$ is the polar angle of the π^- in center of momentum frame.

For the reaction of a photon scattering off a nucleon, the four-momenta of the incident photon, the outgoing pion, the initial nucleon and final nucleon are denoted by $k = (\mathbf{k}, k), q = (\mathbf{q}, \omega), p_1 = (\mathbf{p_1}, E_1), p_2 = (\mathbf{p_2}, E_2)$. The photo-production amplitude A relates to the S matrix by the following equation:

$$S = 1 + (2\pi)^4 i\delta^4(P_f - P_i)(8\pi W N)A, \tag{4.1}$$

where $P_i = k+p_1, P_f = q+p_2, W^2 = s = (k+p_1)^2, N = (16k\omega E_1 E_2)^{1/2}$ is a normalization factor.

Since the electromagnetic interaction violates isospin conservation, the transition operator can be decomposed into an isoscalar part $\hat{S}$ and an isovector part $\hat{V}$, the pion

97

photo-production amplitude A has three independent matrix elements with the notation $< I_f, I_{f3}|\hat{A}|I_i, I_{i3} >$[10, 17]:

$$
\begin{aligned}
A^{IS} &=< \frac{1}{2}, \pm\frac{1}{2}|\hat{S}|\frac{1}{2}, \pm\frac{1}{2} >, \\
\mp A^{IV} &=< \frac{1}{2}, \pm\frac{1}{2}|\hat{V}|\frac{1}{2}, \pm\frac{1}{2} >, \\
A^{V3} &=< \frac{3}{2}, \pm\frac{1}{2}|\hat{V}|\frac{1}{2}, \pm\frac{1}{2} > .
\end{aligned}
\tag{4.2}
$$

The determination of the three isospin amplitudes can be obtained from the following four photoproduction reactions.

$$
\begin{aligned}
A(\gamma p \to \pi^+ n) &= -\sqrt{\frac{1}{3}}A^{V3} + \sqrt{\frac{2}{3}}(A^{IV} - A^{IS}), \\
A(\gamma p \to \pi^0 p) &= +\sqrt{\frac{2}{3}}A^{V3} + \sqrt{\frac{1}{3}}(A^{IV} - A^{IS}), \\
A(\gamma n \to \pi^- p) &= +\sqrt{\frac{1}{3}}A^{V3} - \sqrt{\frac{2}{3}}(A^{IV} + A^{IS}), \\
A(\gamma n \to \pi^0 n) &= +\sqrt{\frac{2}{3}}A^{V3} + \sqrt{\frac{1}{3}}(A^{IV} + A^{IS}),
\end{aligned}
\tag{4.3}
$$

The way to get the above expressions can be found in [10], an example for $\gamma n \to \pi^- p$ is shown in the following. The isospin part of the wave function for the nucleon and pion could be written as:

$$
\begin{aligned}
|p> &= |\frac{1}{2}, +\frac{1}{2} >, |n> = |\frac{1}{2}, -\frac{1}{2} >, \\
|\pi^+> &= -|1, +1 >, |\pi^0> = |1, 0 >, |\pi^-> = |1, -1 >
\end{aligned}
\tag{4.4}
$$

For the reaction $\gamma n \to \pi^- p$, the initial state isospin wave function is $|\gamma n> = |\frac{1}{2}, -\frac{1}{2} >$. The final state isospin wave function is $|\pi^- p> = |1, -1 > |\frac{1}{2}, +\frac{1}{2} > = \sqrt{\frac{1}{3}}|\frac{3}{2}, -\frac{1}{2} > -\sqrt{\frac{2}{3}}|\frac{1}{2}, -\frac{1}{2} >$. The transition amplitude A for this reaction is:

$$
\begin{aligned}
A(\gamma n \to \pi^- p) &=< \pi^- p|\hat{A}|\gamma n > \\
&= (\sqrt{\frac{1}{3}} < \frac{3}{2}, -\frac{1}{2}| - \sqrt{\frac{2}{3}} < \frac{1}{2}, -\frac{1}{2}|)\hat{S} + \hat{V}|\frac{1}{2}, -\frac{1}{2} > \\
&= +\sqrt{\frac{1}{3}}A^{V3} - \sqrt{\frac{2}{3}}(A^{IV} + A^{IS}).
\end{aligned}
\tag{4.5}
$$

Equation 4.3 shows that A^{V3} can be obtained from only the reaction using a proton target, the other two component can only be separated using both the proton data and the neutron data. For each reaction in Equation 4.3, the amplitude can be decomposed into helicity amplitudes or CGLN amplitudes. Helicity is the projection of spin onto the direction of momentum: $\lambda_k = \pm 1$ for incident photon, $\lambda_1 = \pm 1/2$ for initial nucleon, $\lambda_2 = \pm 1/2$ for final nucleon, $\lambda_k = 0$ for pion. The initial and final state helicities

$\lambda = \lambda_k - \lambda_1 = \pm 1/2, \pm 3/2$ and $\mu = \lambda_q - \lambda_2 = \pm 1/2$ give eight helicity amplitudes $A_{\mu\lambda}$. The eight helicity amplitudes are not independent, parity conservation relates the four amplitudes with $\lambda_k = 1$ to $\lambda_k = -1$ by $A_{-\mu,-\lambda}(\theta, \phi) = -e^{i(\lambda-\mu)(\pi-2\phi)} A_{\mu,\lambda}(\theta, \phi)$ [18].

The four independent amplitudes are all complex numbers, and eight independent measurements are required to determine the production amplitude A without ambiguities.

There are 16 nonzero observables for single pseudo-scalar meson photo-production as below [19]:

$$
\begin{aligned}
\frac{d\sigma}{d\Omega} & (\vec{P}^\gamma, \vec{P}^T, \vec{P}^R) \\
= \frac{1}{2} \Big\{ & d\sigma_0 [1 - P_L^\gamma P_y^T P_{y'}^R \cos(2\phi_\gamma)] + \hat{\Sigma}[-P_L^\gamma \cos(2\phi_\gamma) + P_y^T P_{y'}^R] \\
& + \hat{T}[P_y^T - P_L^\gamma P_{y'}^R \cos(2\phi_\gamma)] + \hat{P}[P_{y'}^R - P_L^\gamma P_y^T \cos(2\phi_\gamma)] \\
& + \hat{E}[-P_c^\gamma P_z^T + P_L^\gamma P_x^T P_{y'}^R \sin(2\phi_\gamma)] + \hat{G}[P_L^\gamma P_z^T \sin(2\phi_\gamma) + P_c^\gamma P_x^T P_{y'}^R] \\
& + \hat{F}[P_c^\gamma P_x^T + P_L^\gamma P_z^T P_{y'}^R \sin(2\phi_\gamma)] + \hat{H}[P_L^\gamma P_x^T \sin(2\phi_\gamma) - P_c^\gamma P_z^T P_{y'}^R] \\
& + \hat{C}_{x'}[P_c^\gamma P_{x'}^R - P_L^\gamma P_y^T P_{z'}^R \sin(2\phi_\gamma)] + \hat{C}_{z'}[P_c^\gamma P_{z'}^R + P_L^\gamma P_y^T P_{x'}^R \sin(2\phi_\gamma)] \\
& + \hat{O}_{x'}[P_L^\gamma P_{x'}^R \sin(2\phi_\gamma) + P_c^\gamma P_y^T P_{z'}^R] + \hat{O}_{z'}[P_L^\gamma P_{z'}^R \sin(2\phi_\gamma) - P_c^\gamma P_y^T P_{x'}^R] \\
& + \hat{L}_{x'}[P_z^T P_{x'}^R + P_L^\gamma P_x^T P_{z'}^R \cos(2\phi_\gamma)] + \hat{L}_{z'}[P_z^T P_{z'}^R - P_L^\gamma P_x^T P_{x'}^R \cos(2\phi_\gamma)] \\
& + \hat{T}_{x'}[P_x^T P_{x'}^R - P_L^\gamma P_z^T P_{z'}^R \cos(2\phi_\gamma)] + \hat{T}_{z'}[P_x^T P_{z'}^R + P_L^\gamma P_z^T P_{x'}^R \cos(2\phi_\gamma)] \Big\}
\end{aligned}
\tag{4.6}
$$

In Eq. 4.6, P_L^γ and P_c^γ are the degrees of polarization for circular and linear polarized photon beams. P_i^T and $P_{i'}^R$ are the degrees of polarization of target and recoil nucleons. $d\sigma_0$ is the unpolarized differential cross section. Three asymmetries which to leading order scale by a single polarization of either beam, target or recoil(Σ, T, P) are single polarization asymmetries. Three sets of four asymmetries whose leading polarization dependence involves two polarizations of either beam–target (E, F, G, H), beam–recoil ($C_{x'}$, $C_{z'}$, $O_{x'}$, $O_{z'}$), or target–recoil ($L_{x'}$, $L_{z'}$, $T_{x'}$, $T_{z'}$) are double polarization asymmetries. Each of the double polarization asymmetries has two ways to be measured in experiment. Take the beam-target asymmetry E as an example, $2\hat{E} = \sigma(+1, -z, 0) - \sigma(+1, +z, 0)$ (target polarization is flipped) or $2\hat{E} = \sigma(+1, -z, 0) - \sigma(-1, -z, 0)$ (beam polarization is flipped). The 16 observables are not independent, their are 37 relations between them as shown in appendix C of [19].

Figure 4.2 shows the list of observables that can be measured for single pseudo-scalar meson photo-production. The cross section σ_0 is an un-polarization measurement; Σ, T, P are single-polarization asymmetries; and $E, F, G, H, Cx, Cz, Ox, Oz, Lx, Lz, Tx, Tz$ are double polarization asymmetries. The complete experiment that eliminates ambiguities requires a minimum of eight observables, which can be chosen to be σ_0, Σ, T, P and four double-polarization asymmetries with at least one involving recoil polarization. For the channel $\gamma n \to p\pi^-$, there are 1381 cross section points between 0.4 and 2.0 GeV, only 326 single-polarization(Σ, T, P) points, and none for the double polarization asymmetries. The G14 experiment has measured two more new asymmetries for this reaction: E with circular polarized beam, and G with linear polarized beam. This Chapter will show the result for the E asymmetry.

This reaction needs two independent variables to determine the kinematics, which can be chosen to be the total energy W and the polar angle of the π^-, $\theta_{CM}(\pi^-)$ in the c.m

Photon beam	Target			Recoil			Target + Recoil								
				x'	y'	z'	x'	x'	x'	y'	y'	y'	z'	z'	z'
	x	y	z				x	y	z	x	y	z	x	y	z
Unpolarized	σ₀	T			P		$T_{x'}$		$L_{x'}$		Σ		$T_{z'}$		$L_{z'}$
$P_l^\gamma \sin(2\varphi_\gamma)$		H	G	$O_{x'}$		$O_{z'}$		$C_{z'}$		E		F		$-C_{x'}$	
$P_l^\gamma \cos(2\varphi_\gamma)$	-Σ	-P			-T		$-L_{z'}$		$T_{z'}$		-σ₀		$L_{x'}$		$-T_{x'}$
Circular P_c^γ		F	-E	$C_{x'}$		$C_{z'}$		$-O_{z'}$		G		-H		$O_{x'}$	

Figure 4.2: Polarization observables in the reaction of pseudoscalar meson photo-production. Each observalve can be measured in two different methods as shown in the table. The observables in blue cells were measured in previous experiments, the ones in yellow cells are new observables that are measured in G14 experiment. Image source: [19]

frame. W is divided into 21 bins from 1500 MeV to 2300 MeV with the bin size of 40 MeV. $\theta_{CM}(\pi^-)$ is divided into 13 bins from $\cos(\theta_{CM}(\pi^-)) = -0.975$ to $\cos(\theta_{CM}(\pi^-)) = 0.975$ with the bin size of 0.15. The E asymmetry will be calculated for each 21×13 bins.

4.2   Extraction of E asymmetry

The E asymmetry is a beam target double polarization asymmetry as shown in Figure 4.2. The normalized E is defined as:

$$E = \frac{\sigma(+1, -z, 0) - \sigma(-1, -z, 0)}{\sigma(+1, -z, 0) + \sigma(-1, -z, 0)}, \tag{4.7}$$

where the first value in the parenthesis represents the helicity of the circularly polarized photon beam, the second value represents the direction of polarization for the longitudinally polarized target, and the third value represents the recoil nucleon polarization. Taking into account of the degree of polarization for the photon beam and target, and relating the cross section to the yields of events, we can write the beam target asymmetry E and its statistical error as:

$$E = \frac{1}{P_\gamma P_t} \frac{N_{1/2} - N_{3/2}}{N_{1/2} + N_{3/2}}$$
$$\sigma_E = \frac{1}{P_\gamma P_t} \frac{2(N_{1/2} N_{3/2})^{1/2}}{(N_{1/2} + N_{3/2})^{3/2}} \tag{4.8}$$

where P_γ, P_t are degrees of polarization when the photon beam and target. $N_{1/2}$ is the total number of events for beam polarization and target polarization are anti parallel and $N_{3/2}$ is the total number of events when the beam polarization and target polarization are parallel.

Since the HD target has aluminum wires and KelF in the target region. We need to make corrections to the E asymmetry caused by the aluminum background.

$$E^{raw} = \frac{1}{P_\gamma P_t} \frac{N_{1/2} - N_{3/2}}{N_{1/2} + N_{3/2} + N_{empty}} = \frac{1}{P_\gamma P_t} \frac{N_{1/2} - N_{3/2}}{(N_{1/2} + N_{3/2})(1 + \frac{N_{empty}}{N_{1/2} + N_{3/2}})}, \tag{4.9}$$

100

$$E = (1 + \frac{N_{empty}}{N_{1/2} + N_{3/2}})E^{raw}, \tag{4.10}$$

where N_{empty} is the scaled total number of events from the empty target run, E^{raw} is the E asymmetry before empty target correction, E is the E asymmetry after empty target correction.

For the 8 data sets in circular photon polarization runs, corrections for E asymmetry from background are done for each data set separately. Figure 4.3 shows two examples from Gold2b and Silver 1 for the comparison of z vertex between full target and empty target runs. Since the empty target run and the full target run have different beam times, the empty run events have to be scaled by a constant number. This number is calculated by comparing the events from the KelF peak between z = 0 cm to z = 2 cm as in Figure 4.3. This scale constant is 0.80 for Gold2a and 0.91 for Silver1. Moreover, the empty run and all the Silver runs use the same target cell (21a), the Gold2 runs used a different target cell (19b). The amount of aluminum wires is different in these two cells, the 19b target only has 70% of the aluminum wires used in 21a. Within the target region: -10.5
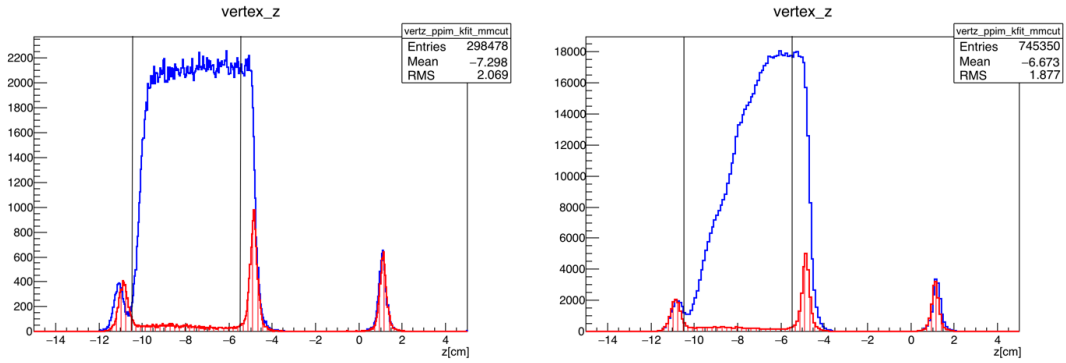
(a) Comparison of z vertex between Gold2b(blue line) and Empty-a(red line) periods.

(b) Comparison of z vertex between Silver1(blue line) and Empty-a(red line) periods.

Figure 4.3: Empty target correction for E asymmetry.

cm < z < -5.5 cm, the ratio of events between the empty target run and the full target run can be calculated using the above information. For the Gold 2a run period, the ratio is (10978*0.80*0.70)/251974 = 0.024, where 0.80 is the scale factor for the empty run, 0.70 is the ratio of aluminum wires between the Gold2a target cell and Empty-a target cell. For the Silver 1 run period, the ratio is (16796*0.91)/428213 = 0.036.

The correction values of the E asymmetry for these two periods are given as: $E = 1.024E^{raw}$ for Gold2a period and $E = 1.036E^{raw}$ for Silver1 period. It is found that the correction values depend on the c.m. energy W; a detailed study of this dependence is shown in Appendix C.

The results for the E asymmetry for each run period (Silver1, Silver2a, Silver2b, Gold2a, Gold2b) are shown in Figure 4.4-4.8. The comparison of the E asymmetry for different run periods is shown in Figure 4.9. The results combining all periods with the method of weighted mean are shown in Figure 4.10. In each figure, the two blue

lines are from Bonn-Gatchina 2011-2 predictions for the E asymmetry [13], the two lines correspond to the upper and lower energy boundary for each energy bin. The two red lines are from SAID CM12 predictions [15].
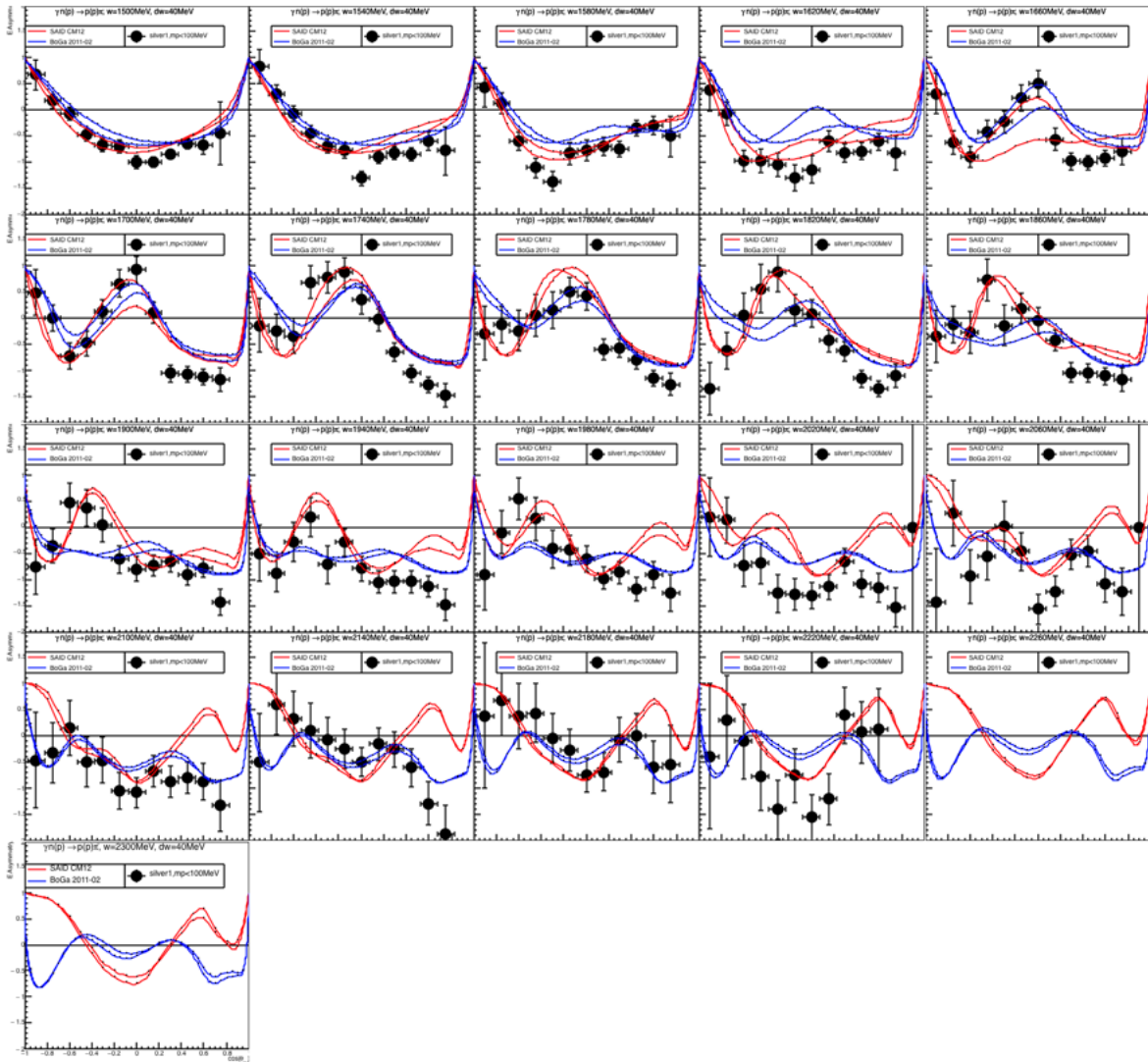
Figure 4.4: Silver 1 run period: E asymmetry vs $\cos(\theta_{CM})$ for different center of momentum energy W.
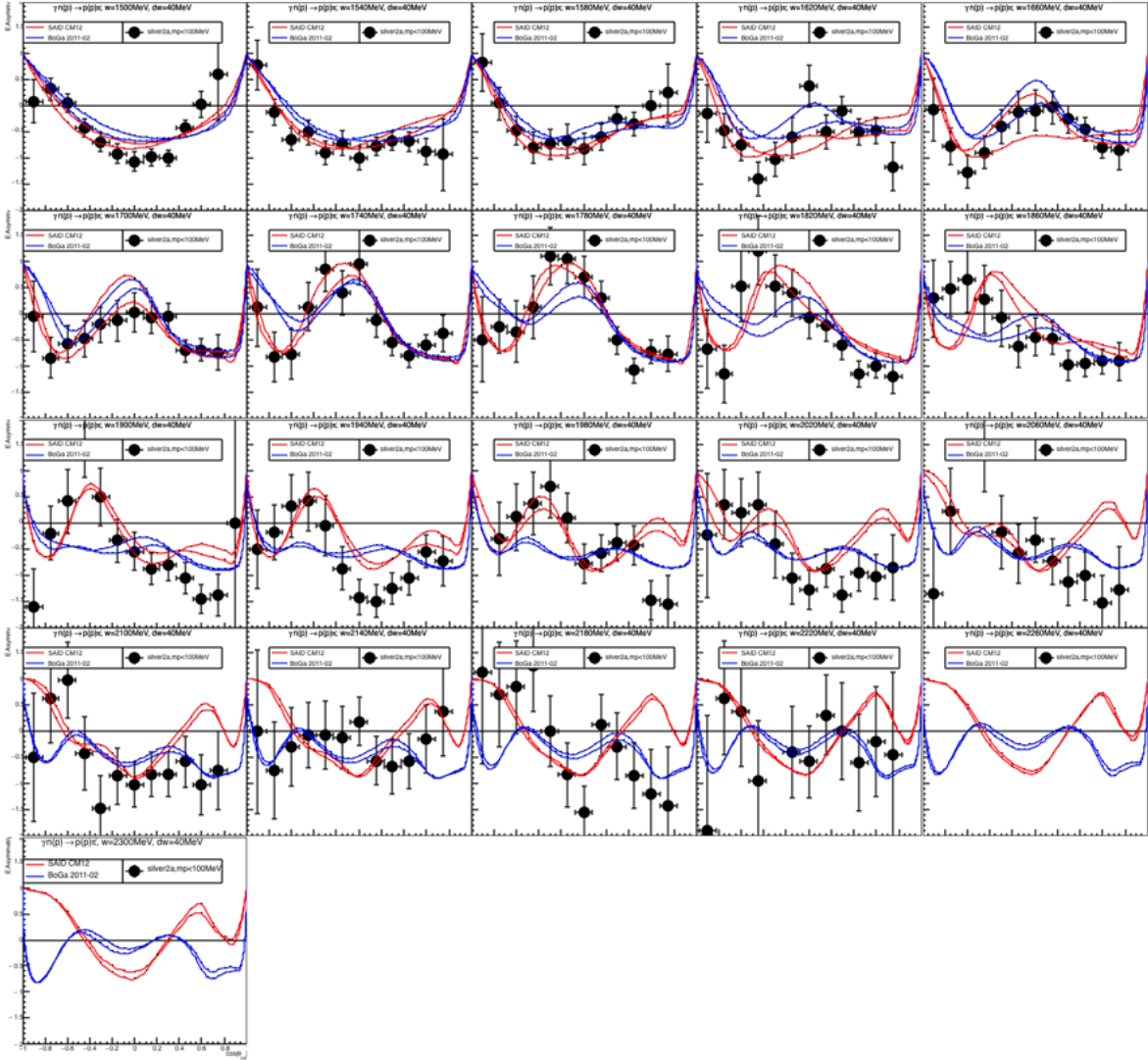
Figure 4.5: Silver 2a run period: E asymmetry vs $\cos(\theta_{CM})$ for different center of momentum energy W.
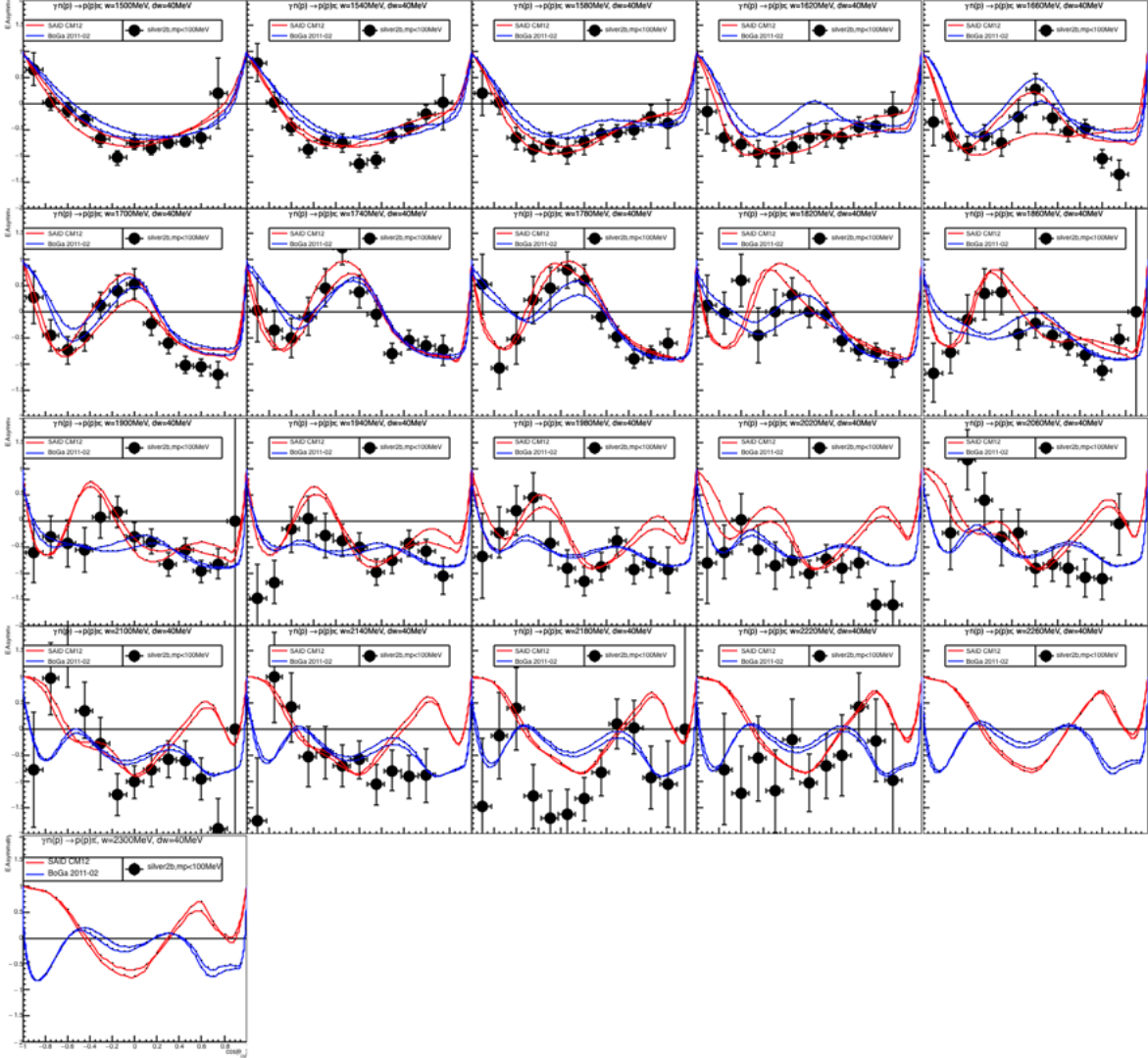
Figure 4.6: Silver 2b run period: E asymmetry vs $\cos(\theta_{CM})$ for different center of momentum energy W.
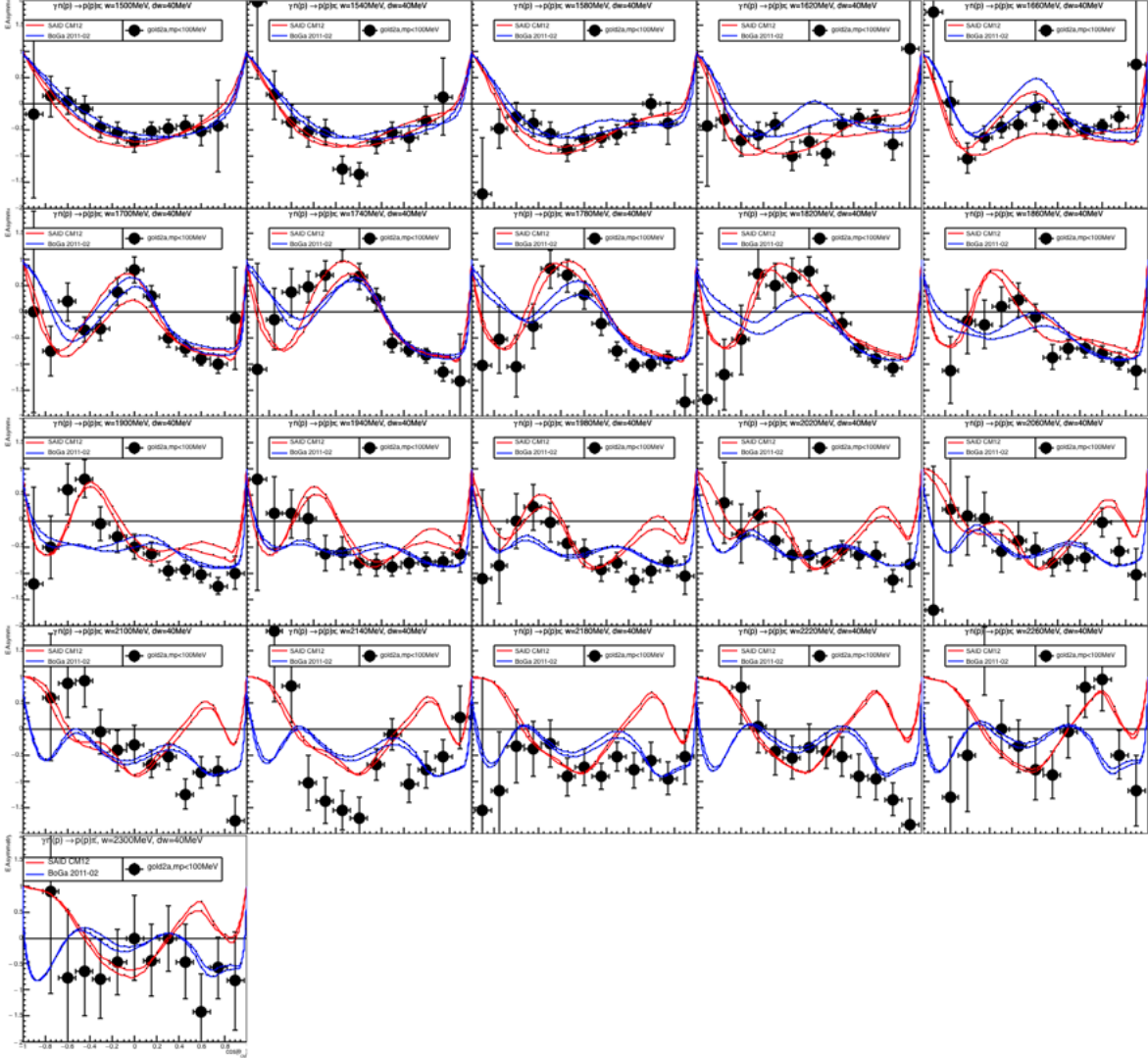
Figure 4.7: Gold 2a run period: E asymmetry vs $\cos(\theta_{CM})$ for different center of momentum energy W.
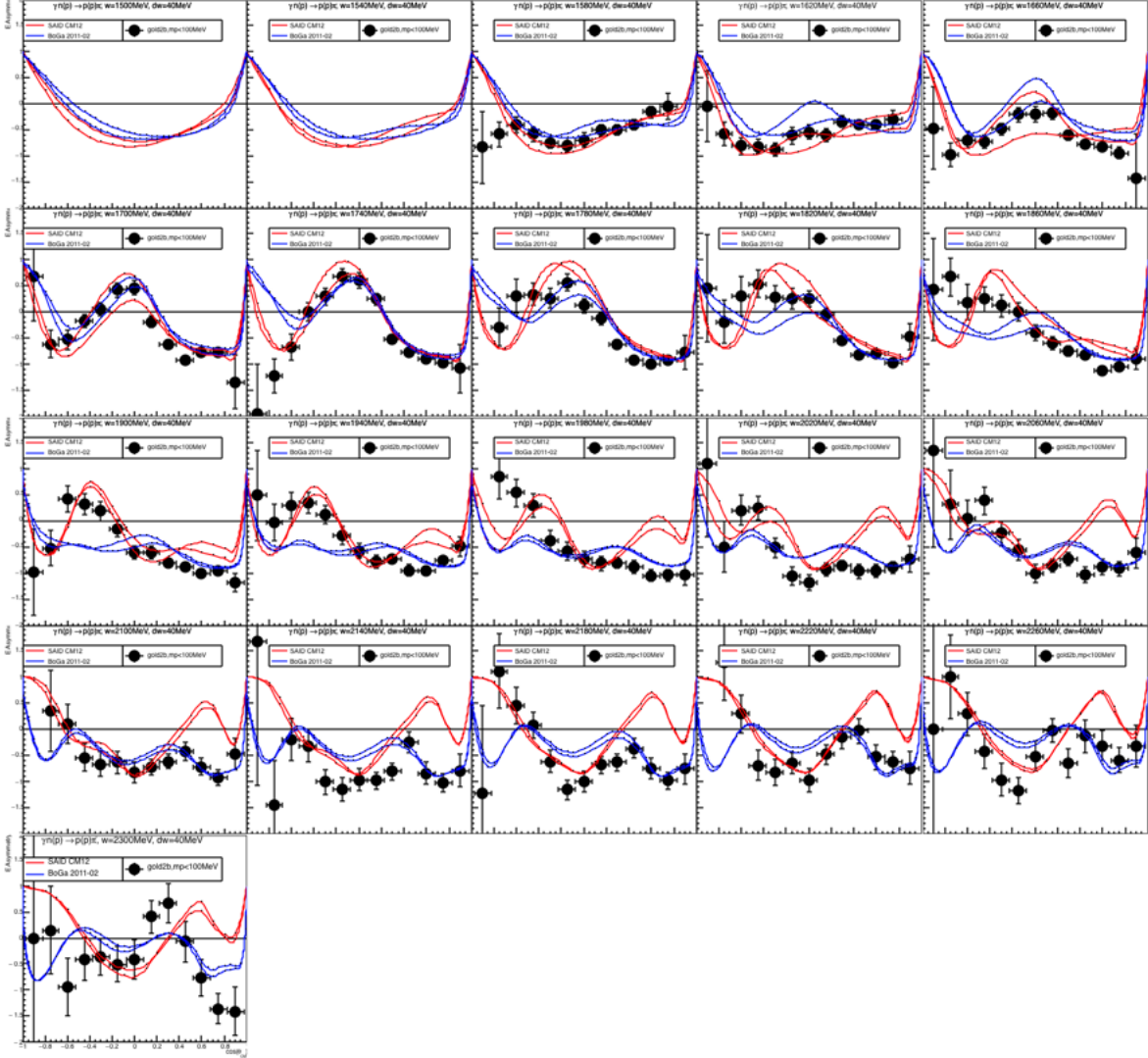
Figure 4.8: Gold 2b run period: E asymmetry vs $\cos(\theta_{CM})$ for different center of momentum energy W.
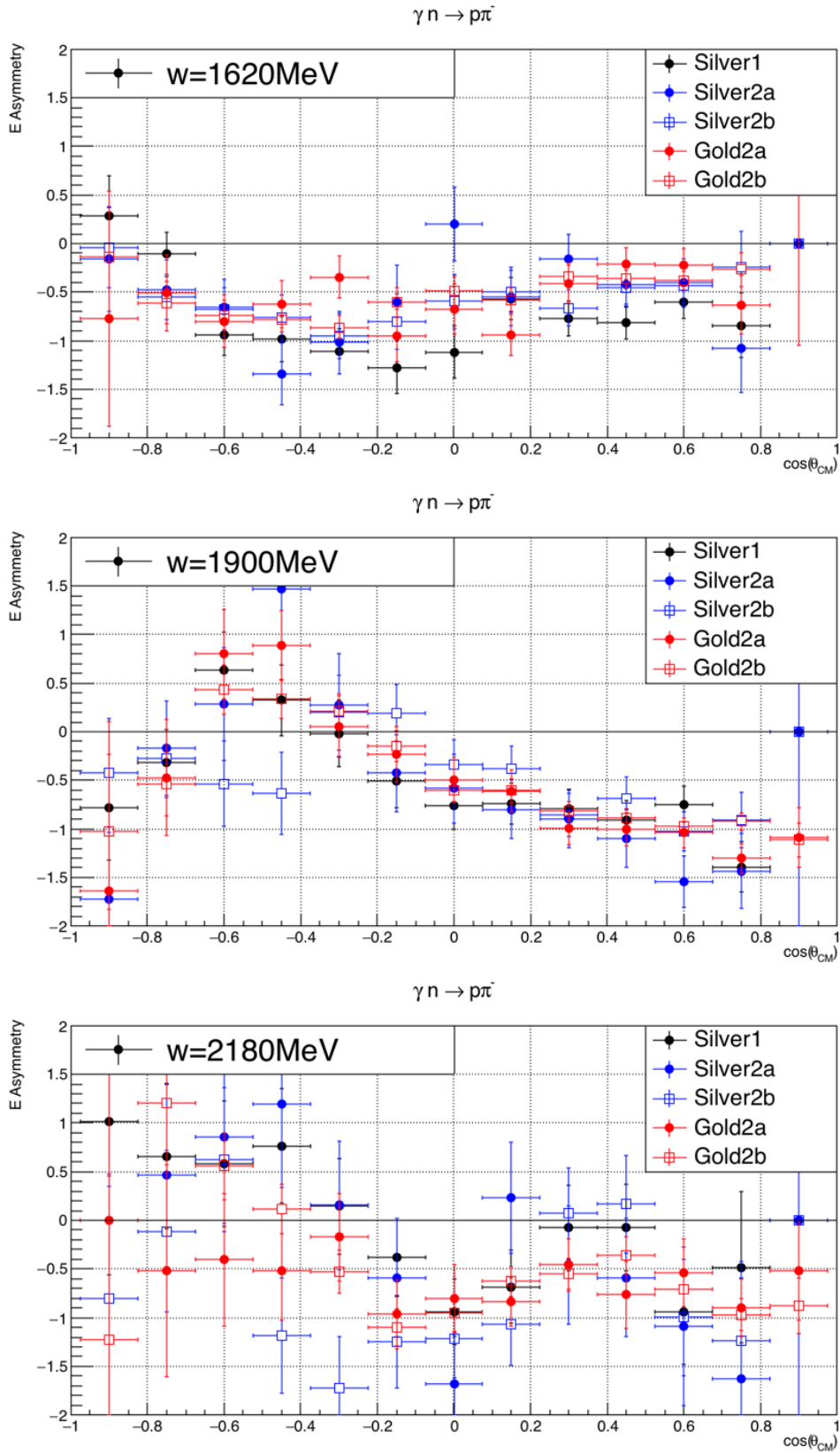
Figure 4.9: Comparison of E asymmetry from 5 different run periods for 3 different center of momentum energies.
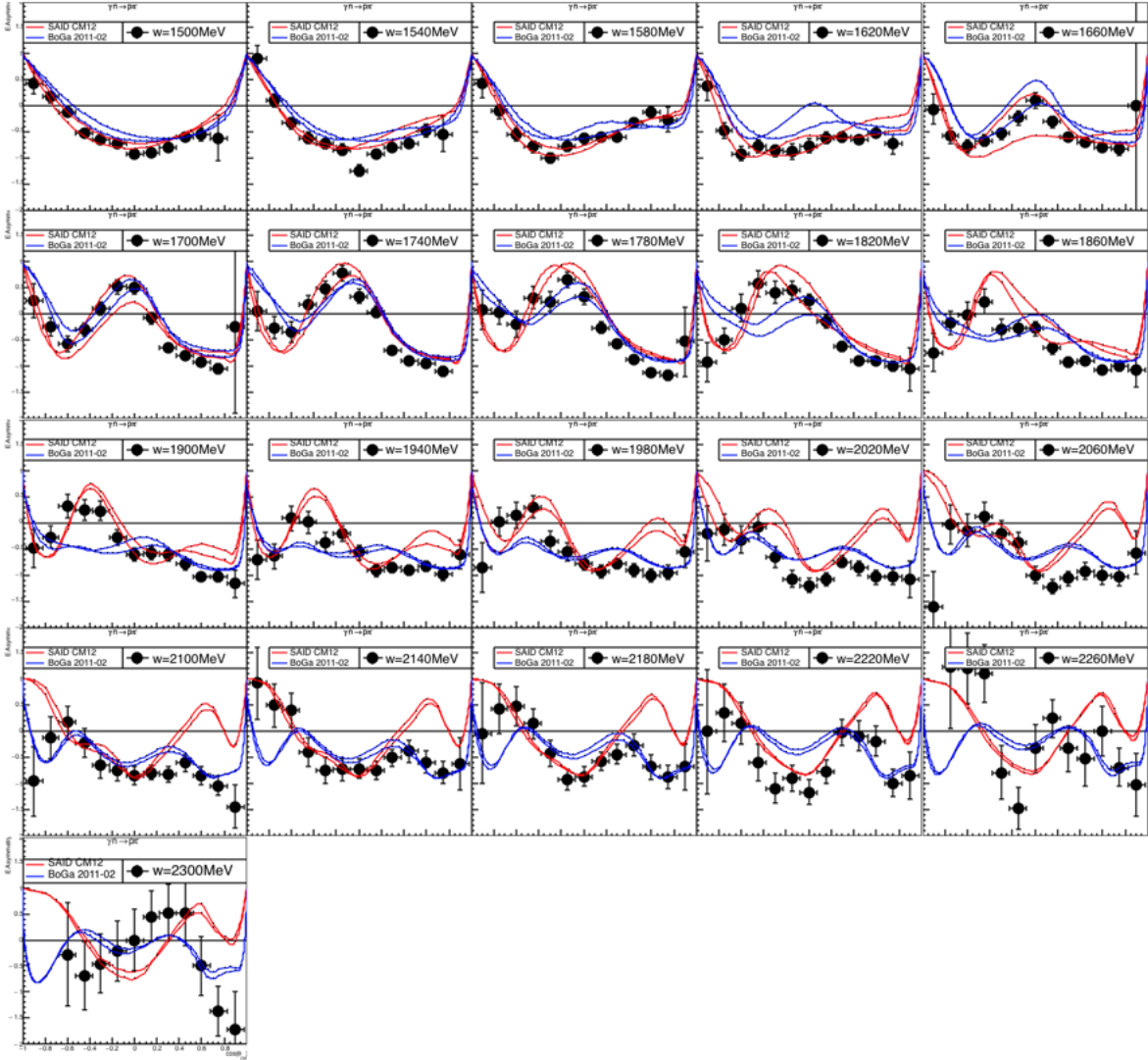
Figure 4.10: Combined result: E asymmetry vs $\cos(\theta_{CM})$ for different center of momentum energy W.

4.3 Systematic Studies

Different values of the cuts used in the channel selection procedure will affect the final results for the E asymmetry. This section studies the systematic errors induced by using different "vertex z" cuts, "confidence level" cuts, and "missing momentum" cuts. The systematic error is defined in the following way:

1. The E asymmetry is calculated for each $\cos(\theta_{CM})$ and energy W bin for cut 1 and cut 2, respectively. There are 13 $\cos(\theta_{CM})$ bins and 21 W bins, which give a total of $13 \times 21 = 273$ bins.

2. The relative difference of the E asymmetry is calculated using the two different cuts: $\delta E/E_{cut2} = (E_{cut1} - E_{cut2})/E_{cut2}$ (a condition of $|E_{cut2}| > 0.2$ is imposed to avoid the case of zero denominator), and the results are used to fill a 1-D histogram, which will be fitted with a Gaussian distribution. The mean (μ_δ) of the Gaussian is the relative systematic error caused by using these two different cuts.

3. Calculate the mean (μ_δ) and width (σ_δ) of the Gaussian distribution of $\delta E/E_{cut2}$ for all the circularly polarized beam run periods, and use the weighted mean to obtain the overall systematic error.

$$\sigma_{systematic} = \frac{\sqrt{\frac{\mu_{Silver1}^2}{\sigma_{\mu Silver1}^2} + \frac{\mu_{Silver2a}^2}{\sigma_{\mu Silver2a}^2} + \frac{\mu_{Silver2b}^2}{\sigma_{\mu Silver2b}^2} + \frac{\mu_{Gold2a}^2}{\sigma_{\mu Gold2a}^2} + \frac{\mu_{Gold2b}^2}{\sigma_{\mu Gold2b}^2}}}{\sqrt{\frac{1}{\sigma_{\mu Silver1}^2} + \frac{1}{\sigma_{\mu Silver2a}^2} + \frac{1}{\sigma_{\mu Silver2b}^2} + \frac{1}{\sigma_{\mu Gold2a}^2} + \frac{1}{\sigma_{\mu Gold2b}^2}}}, \quad (4.11)$$

where $\sigma_\mu = \sigma_\delta/\sqrt{N}$ is the standard error of the mean value, N is the size of the sample.

4.3.1 Systematic Study of Vertex Z cuts

As shown in Chapter 3, section 3.3.2, there is a cut along the z-axis of the target: -10.5cm < z < -5.5 cm. This cut removes most of the events from the KelF target cell that enclose the HD target. A variation of ±0.2 cm of the vertex z cut is used to study the systematic effect of vertex z cut on the E asymmetry.

Tightening the vertex z cut by 0.2 cm: -10.3 cm < z < -5.7 cm, the 1-D histogram of the difference between the E asymmetry calculated from the new vertex cut and standard vertex cut (-10.5 cm < z < -5.5 cm) for circular runs silver1, silver 2, and gold2 are shown in Figure 4.11. The systematic error caused by the change of vertex z cut is calculated using Equation 4.11, and result is shown in Table 4.1. The results for loosening the vertex z cut by 0.2 cm: -10.7cm < z < -5.3 cm are shown in Figure 4.12 and Table 4.2. The total systematic error caused by tightening and loosening the vertex z cut is the quadrature sum of the two errors, which is: $\sigma_{systematic}(\text{vertex z}) = \sqrt{0.006^2 + 0.010^2} = 1.2\%$

4.3.2 Systematic Study of Confidence level cuts

To separate the events for a channel of interest from the background events, a confidence level cut of "CL > 5%" is used. The systematic effect of this cut can be studied by varying the value for the cut. The E asymmetry will be calculated with the confidence level cuts of 2% and 10%, and the results will be compared with the E asymmetry with the 5% confidence level cut. The difference between the two E asymmetry values for all bins (21
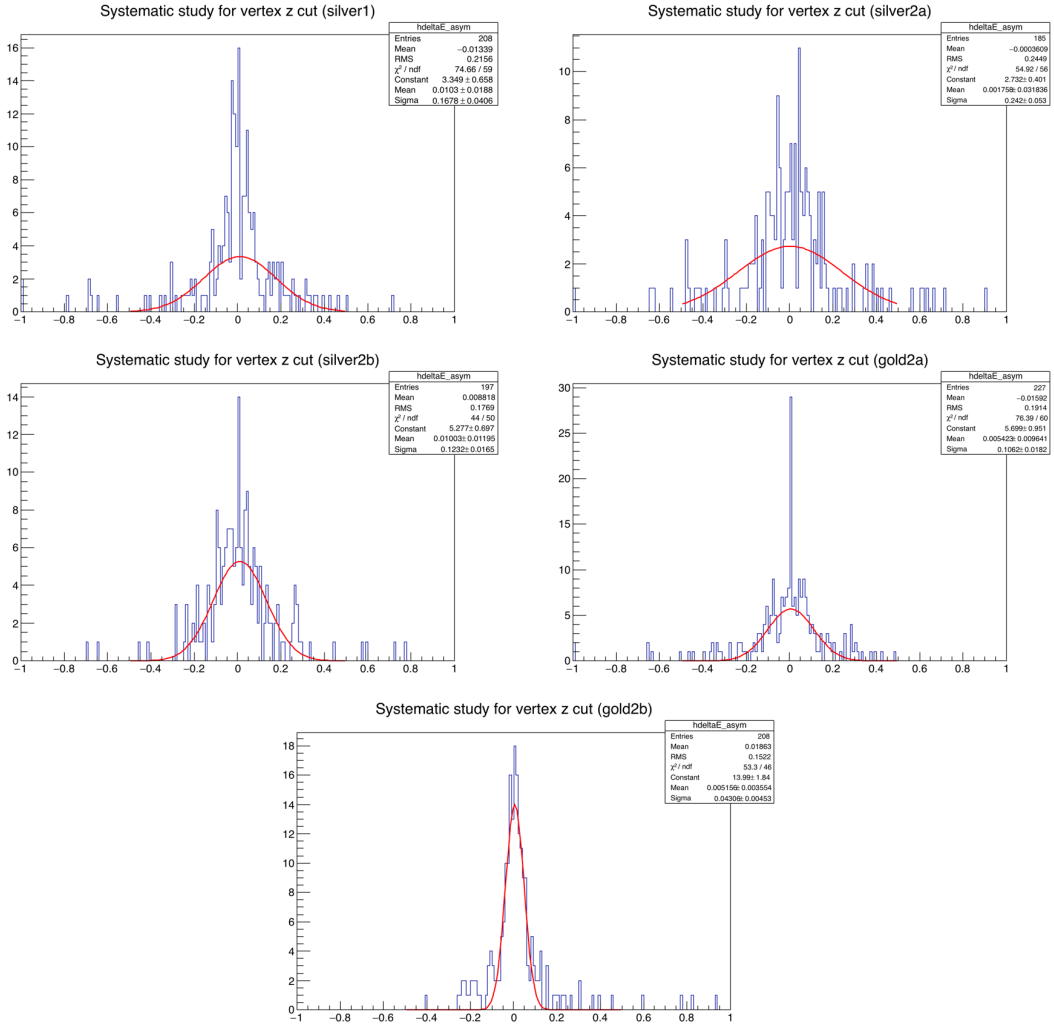
Figure 4.11: Difference between the E asymmetry calculated from the tight vertex cut (-10.3 cm < z < -5.7 cm) and standard vertex cut (-10.5 cm < z < -5.5 cm).

Period	μ_δ	σ_δ	N	σ_μ
Silver1	1.0 %	16.8%	208	1.2 %
Silver2a	0.2%	24.2%	185	1.8%
Silver2b	1.0%	12.3%	197	0.9%
Gold2a	0.5%	10.6%	227	0.7%
Gold2b	0.5%	4.3%	208	0.3%
$\sigma_{systematic}$	0.6%			

Table 4.1: Mean and error for the Gaussian distribution in Figure 4.11. Equation 4.11 is used to calculate the systematic error between the vertex z cut: -10.3 cm < z < -5.7 cm and -10.5 cm < z < -5.5 cm.
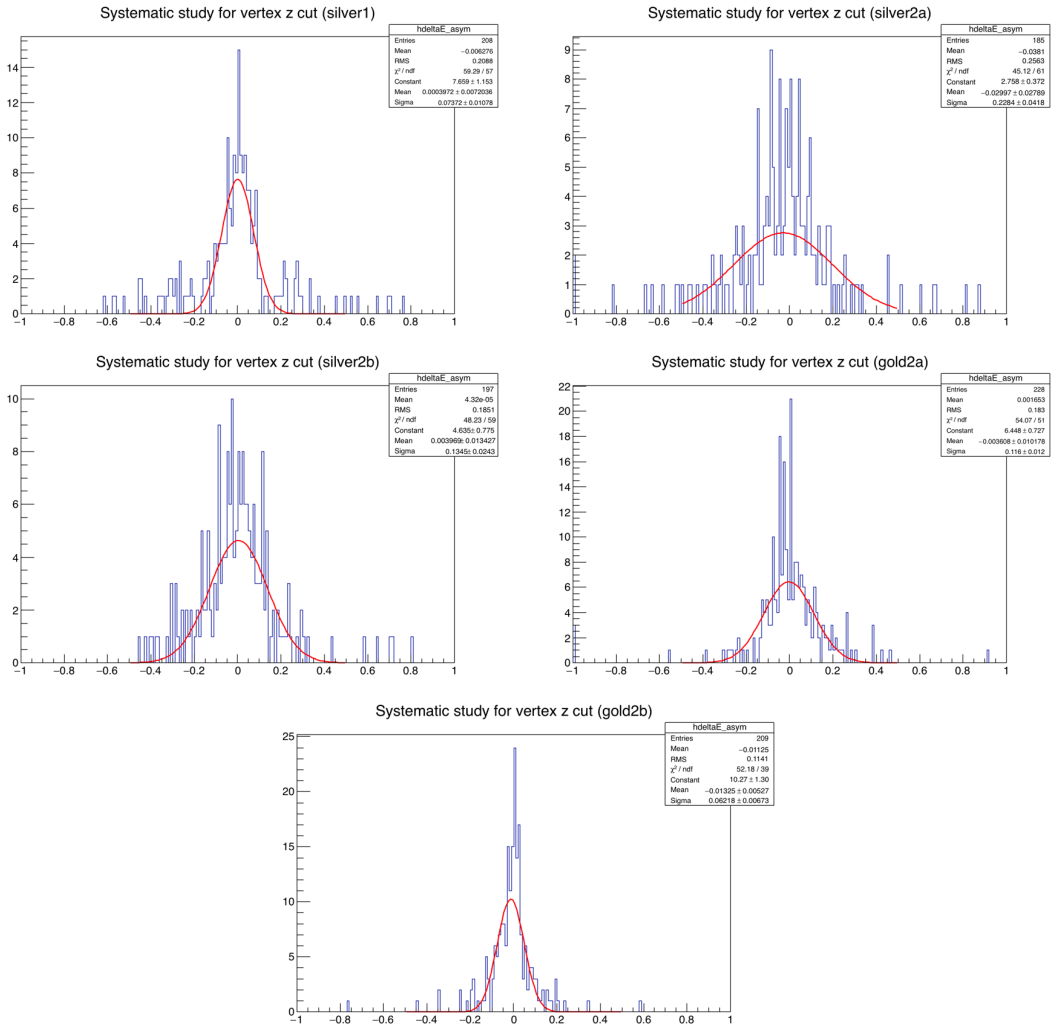
Figure 4.12: Difference between the E asymmetry calculated from the loose vertex cut (-10.7 cm < z < -5.3 cm) and standard vertex cut (-10.5 cm < z < -5.5 cm).

Period	μ_δ	σ_δ	N	σ_μ
Silver1	0.0%	7.4%	208	0.5%
Silver2a	-3.0%	22.8%	185	1.7%
Silver2b	0.4%	13.5%	197	1.0%
Gold2a	-0.4%	11.6%	228	0.8%
Gold2b	-1.3%	6.2%	209	0.4%
$\sigma_{systematic}$	1.0%			

Table 4.2: Mean and error for the Gaussian distribution in Figure 4.12. Equation 4.11 is used to calculate the systematic error between the vertex z cut: -10.7 cm < z < -5.3 cm and -10.5 cm < z < -5.5 cm.

111

energy bins × 13 θ bins) will be used to fill a 1-D histogram, and the mean and error of the fitted Gaussian distribution will be used to estimate the systematic error.

The results of comparing the 2% and 5% confidence level cuts are shown in Figure 4.13 and Table 4.3.
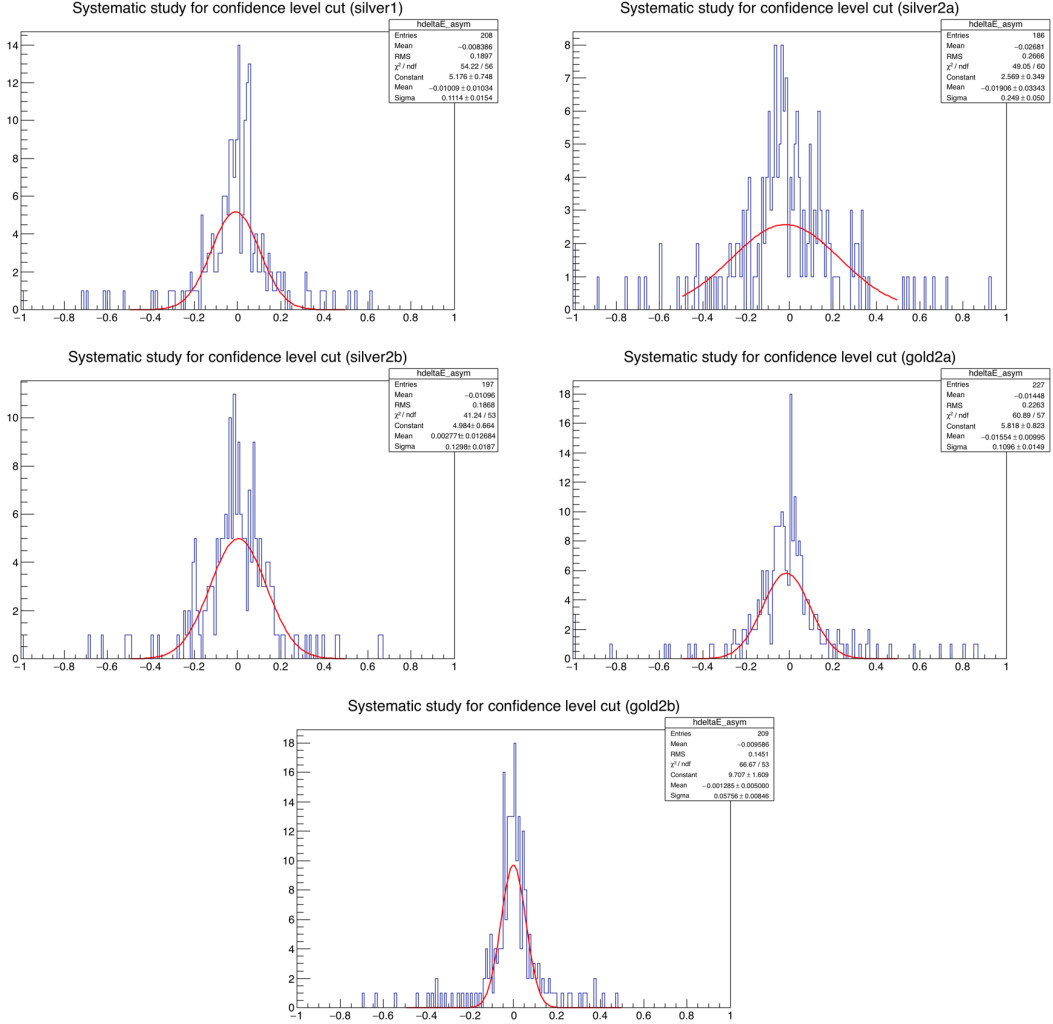
Figure 4.13: Difference between the E asymmetry calculated from confidence level cut (CL > 2%) and standard confidence level cut (CL > 5%).

The results of comparing the 10% and 5% confidence level cuts are shown in Figure 4.14 and Table 4.4. The total systematic error caused by tightening and loosening the confidence level cut is the quadrature sum of the two errors, which is: $\sigma_{systematic}$(confidence level) = $\sqrt{0.008^2 + 0.011^2} = 1.3\%$.

4.3.3 Systematic Study of Missing Momentum cuts

After the vertex z cut of $-10.5 < z < -5.5$ cm and confidence level cut of CL> 5%, most of the events are from the channel of interest: $\gamma + n \rightarrow p + \pi^-$, as shown in the missing momentum plot (Figure 4.15) for gold2a data set. The missing momentum of the target neutron shows the quasi free feature of the neutron target. Figure 4.16 shows

Period	μ_δ	σ_δ	N	σ_μ
Silver1	-1.0%	11.1%	208	0.8%
Silver2a	-1.9%	24.9%	186	1.8%
Silver2b	0.3%	13.0%	197	0.9%
Gold2a	-1.6%	11.0%	227	0.7%
Gold2b	-0.1%	5.8%	209	0.4%
$\sigma_{systematic}$	0.8%			

Table 4.3: Mean and error for the Gaussian distribution in Figure 4.13. Equation 4.11 is used to calculate the systematic error between the confidence level cut: CL > 2% and CL > 5%.
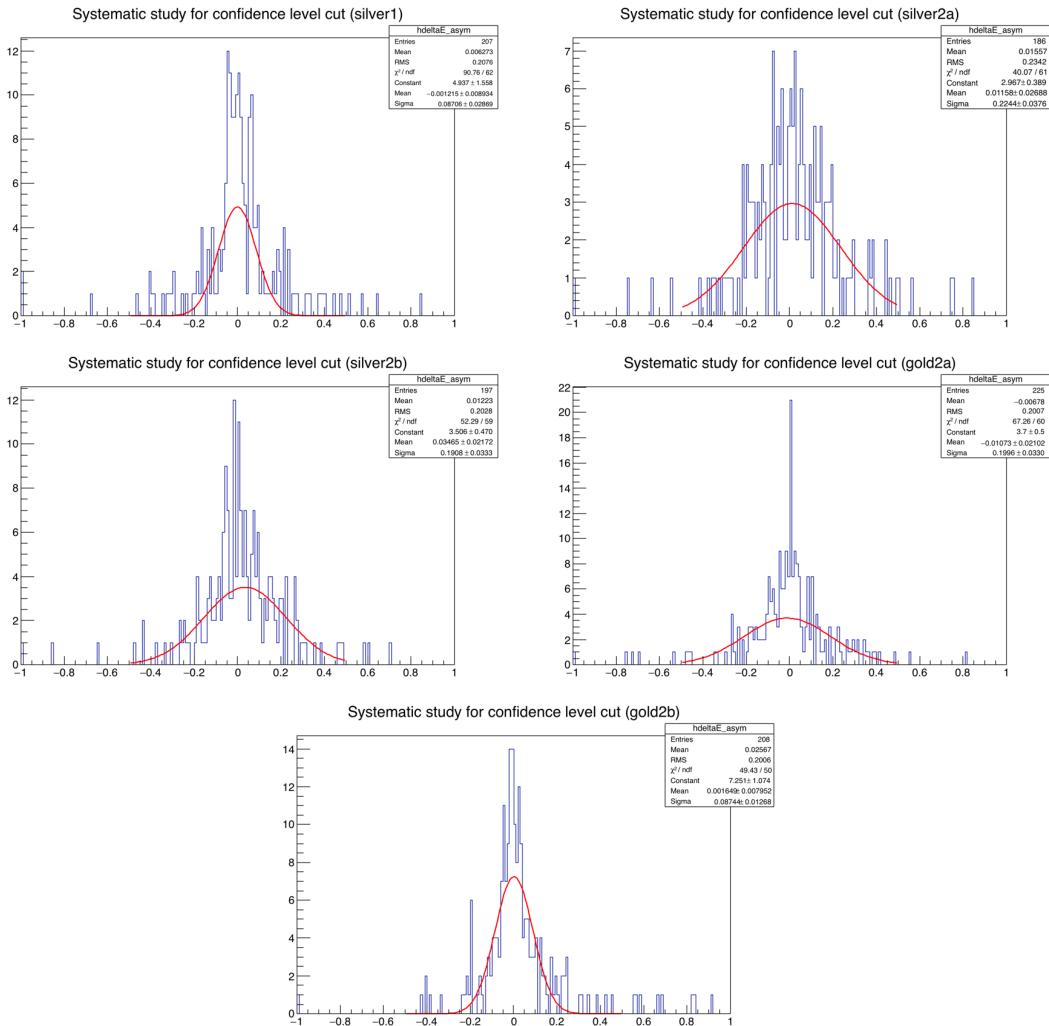
Figure 4.14: Difference between the E asymmetry calculated from confidence level cut (CL > 10%) and standard confidence level cut (CL > 5%).

Period	μ_δ	σ_δ	N	σ_μ
Silver1	-0.1%	8.7%	207	0.6%
Silver2a	1.1%	22.4%	186	1.6%
Silver2b	3.5%	19.1%	197	1.4%
Gold2a	-1.1%	20.0%	225	1.3%
Gold2b	0.2%	8.7%	208	0.6%
$\sigma_{systematic}$	1.1%			

Table 4.4: Mean and error for the Gaussian distribution in Figure 4.14. Equation 4.11 is used to calculate the systematic error between the confidence level cut: CL > 10% and CL > 5%.

that the E asymmetry depends on the missing momentum of the target neutron, the magnitude of the E asymmetry decrease as the missing momentum increases. A cut of missing momentum: mP < 0.1 GeV is chosen for the standard cut, since the E asymmetry is relatively flat for the region: 0 < mP < 0.1 GeV. Another two missing momentum cuts: mP < 0.12 GeV and mP < 0.08 GeV are used for calculating the E asymmetry, which will give the systematic error on the missing momentum cut.
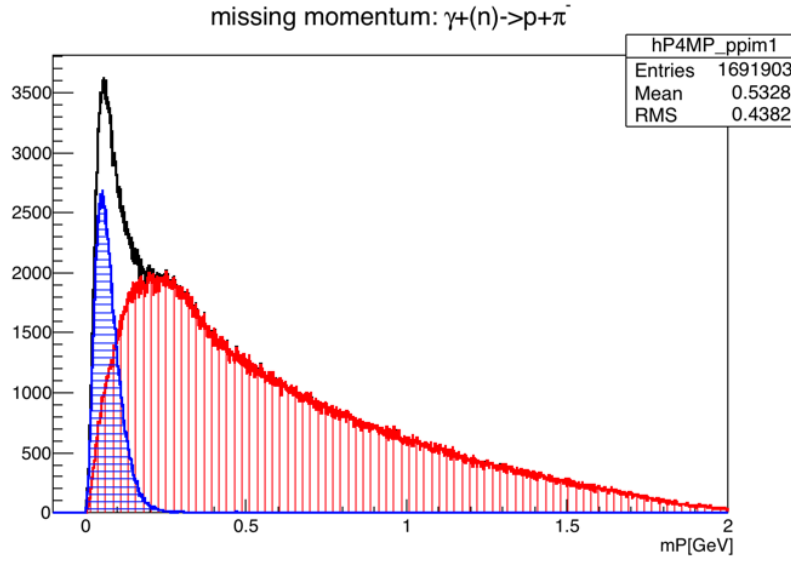
Figure 4.15: Missing momentum plot for the channel: $\gamma(n) \to p\pi^-$. The blue region is for good events that pass the cuts, the red region is the background events that are removed by the cuts.

The results of comparing the mP < 0.12 GeV and mP < 0.1 GeV missing momentum cuts are shown in Figure 4.17 and Table 4.5. The results of comparing the mP < 0.08 GeV and mP < 0.1 GeV missing momentum cuts are shown in Figure 4.18 and Table 4.6. The total systematic error caused by tightening and loosening the missing momentum cut is the quadrature sum of the two errors: $\sigma_{systematic}$(missing momentum) $= \sqrt{0.032^2 + 0.0128^2} = 4.2\%$.
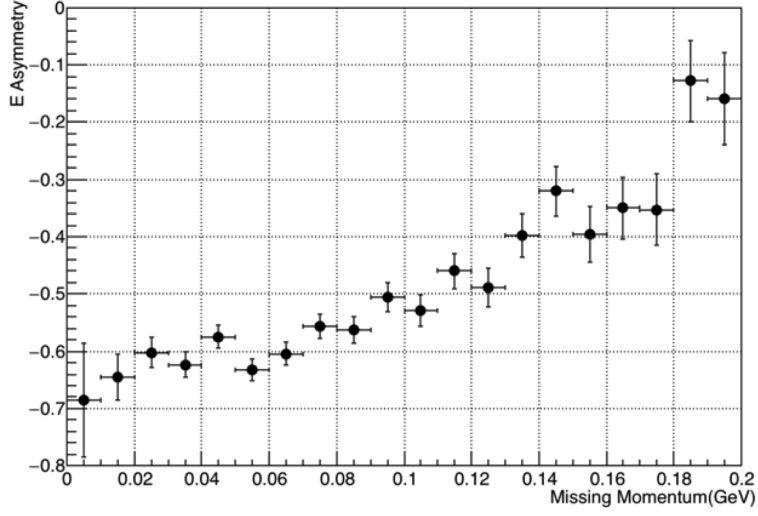
Figure 4.16: E asymmetry vs missing momentum of target neutron for the channel: $\gamma + (n) \rightarrow p + \pi^-$.

Period	μ_δ	σ_δ	N	σ_μ
Silver1	-4.0%	16.5%	207	1.1%
Silver2a	-6.0%	27.0%	185	2.0%
Silver2b	-1.8%	18.3%	196	1.3%
Gold2a	-2.0%	18.2%	225	1.2%
Gold2b	-3.1%	7.6%	208	0.5%
$\sigma_{systematic}$	3.2%			

Table 4.5: Mean and error for the Gaussian distribution in Figure 4.17. Equation 4.11 is used to calculate the systematic error between the missing momentum cut: mP < 0.12 GeV and mP < 0.1 GeV.

Period	μ_δ	σ_δ	N	σ_μ
Silver1	4.7 %	18.3 %	206	1.3 %
Silver2a	-2.2%	36.3 %	184	2.7 %
Silver2b	2.6 %	30.5 %	197	2.2 %
Gold2a	0.1%	28.9%	219	2.0 %
Gold2b	1.1%	14.7%	208	1.0%
$\sigma_{systematic}$	2.8%			

Table 4.6: Mean and error for the Gaussian distribution in Figure 4.18. Equation 4.11 is used to calculate the systematic error between the missing momentum cut: mP < 0.08 GeV and mP < 0.1 GeV.
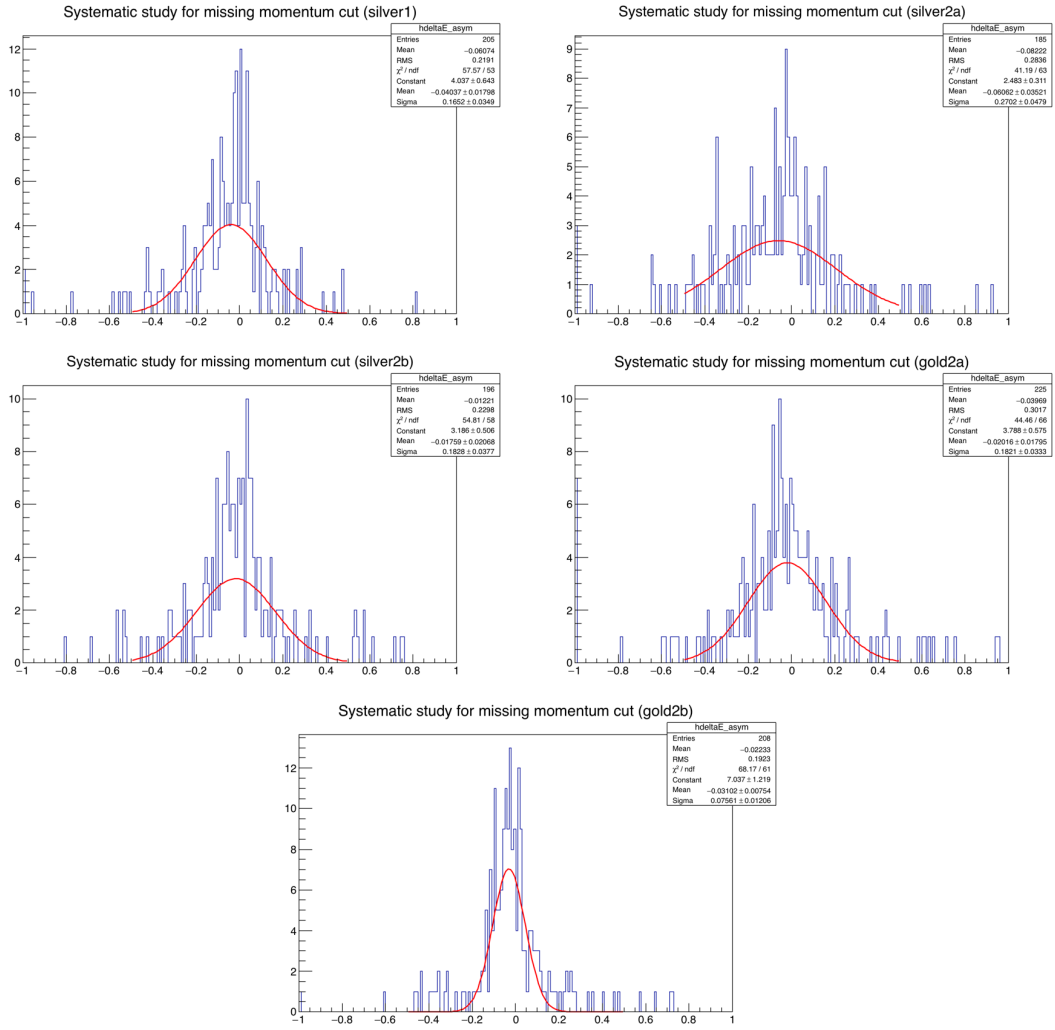
Figure 4.17: Difference between the E asymmetry calculated from missing momentum cut (mP < 0.12 GeV) and standard missing momentum cut (mP < 0.1 GeV).
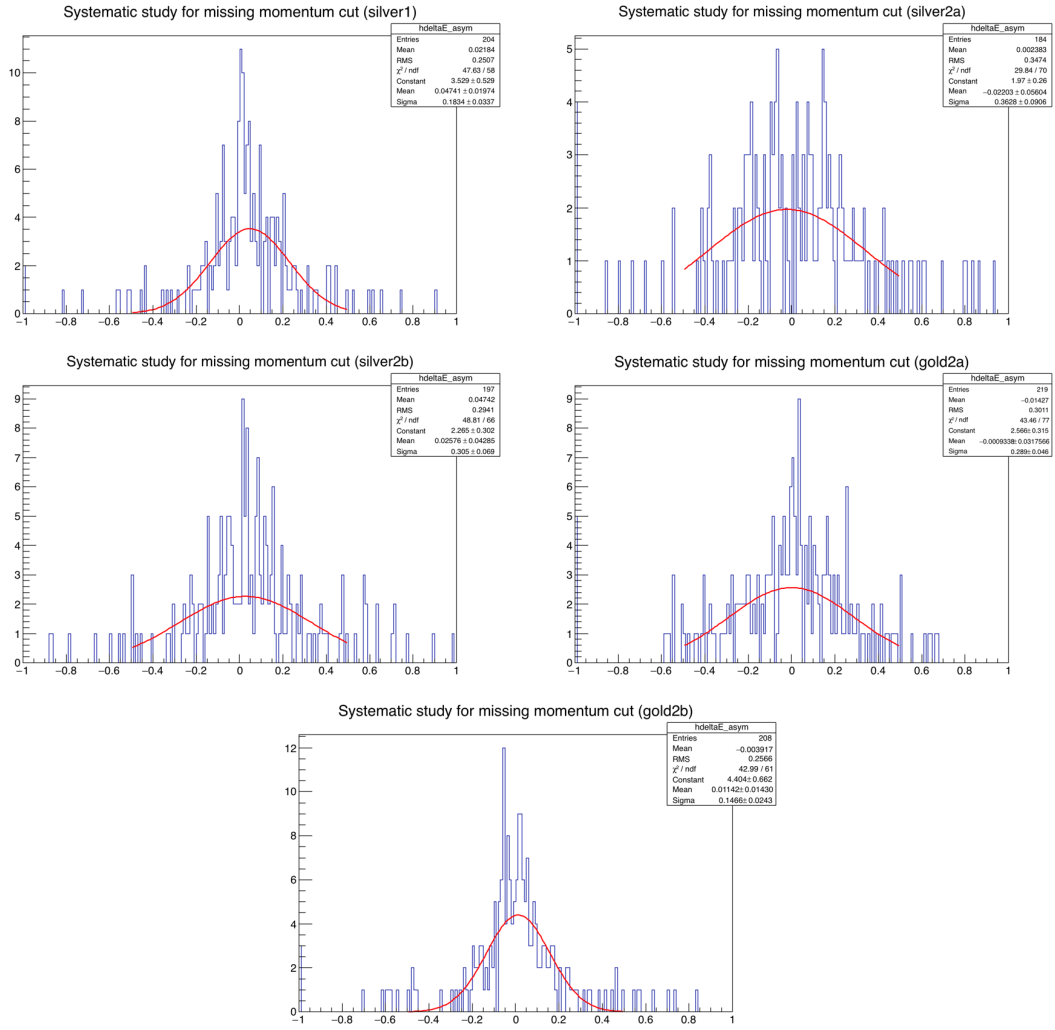
Figure 4.18: Difference between the E asymmetry calculated from missing momentum cut (mP < 0.08 GeV) and standard missing momentum cut (mP < 0.1 GeV).

4.3.4   Other Systematic Errors

Other than the systematic errors caused by the choice of different cut values, the systematic errors of the photon beam polarization and target polarization will also introduce uncertainty in the E asymmetry. Table 4.7 gives the photon beam polarization and its error from the Møller measurement. An estimation of the systematic error for the HD target polarization is shown in table 4.8.

Period	Beam polarization	Error
Silver1	-81.7%	3.5%
Silver2a	-81.7%	3.5%
Silver2b	-76.2%	3.5%
Gold2a	88.2%	3.5%
Gold2b	-83.4%	3.5%

Table 4.7: Photon beam polarization and its error for circular polarized beam run periods.

Uncertainties in reference Thermal Equilibrium (TE) measurement:

PD noise	0.3%	white noise in PD NMR while in HDice Lab
Temperature	0.2%	drift, thermal gradients in HD from radiant heat load
H background	0.4%	H bkg with no target.
Stoichiometry	0.1%	deviation of H:D of 1:1, due to H2 and D2 impurities
Bkg subtraction	0.6%	Err in signal integral from imperfect separation of bkg
Incomplete relaxation	0.5%	T1 for TE measurement can be comparable to sweep time

Uncertainties in measurement of frozen-spin(FS) signal:

IBC noise	0.6%	residual effect of white noise in IBC NMR and PD
Hall-B noise jumps	0.5%	Variations in signal area after correction for signal jumps
Circuit non-linearity	4.0%	From the quadratic dependence of the circuit transducer gain
RF inhomogeneity	1.4%	Field inhomogeneity
RF depolarization	0.1%	Residual uncorrected decrement from repeated rf sweeps

Uncertainties in relating FS signal to TE measurement:

Circuit drift	1.8%	Variation from connecting FS signal to TE reference
Lock-in gain error	2.9%	SRS 844 manufacturer's gain error
Differential ramp-rate	1.0%	Actual ramp rate differs from nominal
TC transfer losses	2.0%	Variation in polarization loss during a TC transfer
Total systematic error	6.0%	For both H and D polarization

Table 4.8: Systematic errors for HD polarization measurement. [57]

From the formula of calculating E asymmetry: $E = \frac{1}{P_\gamma P_t} \frac{N_{1/2} - N_{3/2}}{N_{1/2} + N_{3/2}}$, the relative errors for photon beam polarization (P_γ) and target polarization (P_t) will be propagated to the final result of the E asymmetry. The systematic errors are 3.5% from the photon beam polarization, and 6.30% from the target polarization.

4.3.5 Total Systematic Errors

We have considered two kinds of systematic errors, one is caused by the choice of different cuts in the event selection, another is from the systematic errors in the measurement of the photon beam polarization and HD target polarization. The total error for each kind is combined using a quadratic sum and a summery of the systematic errors is shown in Table 4.9.

Sources	Systematic error for E aysmmetry
Vertex z cut ($\pm$ 0.2 cm)	1.2%
Confidence level cut (+0.05, -0.03)	1.3%
Missing momentum cut ($\pm$0.02 GeV)	4.2%
$\sigma_{sys}(cuts)$	4.6%
Photon beam polarization	3.5%
Target polarization	6.0%
$\sigma_{sys}(polarization)$	6.2%
σ_{total}	7.7%

Table 4.9: Combined systematic error. The main source of systematic error from using different cuts is from the missing momentum cut. The main source of systematic error from polarization measurement is from the target polarization.

4.4 Conclusion

The first measurement of E asymmetry for the reaction of $\gamma + n \to p + \pi^-$ is reported. The E asymmetry is plotted vs. the polar angle of the final state π^- in the center of momentum frame. The c.m. energy ($w_{c.m.}$) ranging from 1500 MeV to 2300 MeV has been divided into 21 bins with the bin size of 40 MeV. The results have been compared with two the predictions from two partial wave analysis group: Bonn-Gatchina and SAID. The agreement between the experiment results and the predictions from partial wave analyse is good for $w_{c.m.} < 1820$ MeV. For $w_{c.m.} > 1820$ MeV, the experiment results are different from the two predictions, and also the two partial wave analysis methods give different predictions. The result of the E asymmetry from this experiment will help the two partial wave analysis to improve their models, and give more accurate predictions for the energy $w_{c.m.} > 1820$ MeV, this energy range is also the place where most of the missing resonances are.

Chapter 5

Polarization Observables for $\gamma p \rightarrow p\pi^+\pi^-$

Double pion photo-production is an important channel for the study of the missing resonance problem, because the cross section for this reaction is much higher than the single pion photo-production for c.m. total energies above 2 GeV, where the missing resonances are predicted to be.

5.1   Formalism
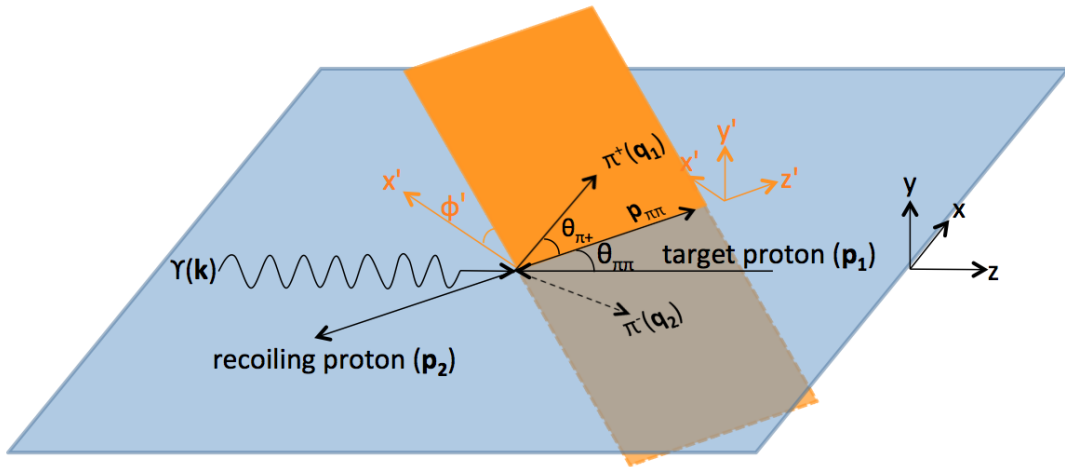
Figure 5.1: Kinematics for the reaction of $\gamma p \rightarrow p\pi^+\pi^-$ in c.m. frame. $\boldsymbol{k}$, $\boldsymbol{p_1}$, $\boldsymbol{p_2}$, $\boldsymbol{q_1}$, $\boldsymbol{q_2}$ are the momenta for the incident photon, proton target, recoiling proton, and the two pions. $\theta_{\pi\pi}$ is the polar angle of the sum vector of the momenta of the two pions in the center of momentum frame. $\theta_{\pi+}$ is the angle between $\boldsymbol{q_1}$ and $\boldsymbol{p_{\pi\pi}}$. ϕ' is the angle between the plane formed by the two pion momenta and the reaction plane.

The kinematics for this process are more complicated than in the single pion process. The differential cross section is described by 5 kinematic variables, which can be chosen as: W, $M_{\pi^+\pi^-}$, $\theta_{\pi\pi}$, $\theta_{\pi+}$ and ϕ', in which W is the c.m. total energy, $M_{\pi^+\pi^-}$ is invariant mass of the two final state pions, $\theta_{\pi\pi}$, $\theta_{\pi+}$, ϕ'; these angles are shown in Figure 5.1. ϕ'

can be obtained in the following equation:

$$\cos \phi' = \frac{(\vec{p}_1 \times \vec{p}_2) \cdot (\vec{q}_1 \times \vec{q}_2)}{|\vec{p}_1 \times \vec{p}_2||\vec{q}_1 \times \vec{q}_2|}. \tag{5.1}$$

If the photon beam and target are polarized, the differential cross section can be written as:

$$\begin{aligned}
\frac{d\sigma}{dx_i} = \sigma_0 \{ & (1 + \vec{\Lambda} \cdot \vec{P}) + \delta_\odot (I^\odot + \vec{\Lambda} \cdot \vec{P}^\odot) \\
& + \delta_l [\sin 2\beta (I^s + \vec{\Lambda} \cdot \vec{P}^s + \cos 2\beta (I^c + \vec{\Lambda} \cdot \vec{P}^c)] \},
\end{aligned} \tag{5.2}$$

where x_i are the kinematic variables, σ_0 is the unpolarized cross section, β is the angle between the direction of the linear polarized photon beam with the x-axis in lab frame, $\delta_\odot$ and δ_l are the degree of polarization for circularly and linearly polarized photon beam. Since there are protons in both hydrogen and deuterium in the HD target, the effective polarization of the proton is $(P_H + P_D)/2$. Λ is the target polarization. $I^\odot$ and $I^{s,c}$ are the beam helicity asymmetries with the use of circularly and linearly polarized photon beams. $\vec{P}$ is the target asymmetry. $\vec{P}^\odot$ is the double asymmetry obtained using a circularly polarized beam and polarized target. $\vec{P}^{s,c}$ are the double asymmetries obtained using a linear polarized beam and polarized target.

For a circularly polarized beam and longitudinal polarized target, the above formula becomes:

$$\frac{d\sigma}{dx_i} = \sigma_0 \{ (1 + \Lambda_z \cdot P_z) + \delta_\odot (I^\odot + \Lambda_z \cdot P_z^\odot) \}. \tag{5.3}$$

The three polarization observables $P_z, I^\odot, P_z^\odot$ can be calculated using the following equations:

$$\begin{aligned}
P_z &= \frac{1}{\Lambda_z} \frac{[N(\rightarrow\Rightarrow) + N(\leftarrow\Rightarrow)] - [N(\rightarrow\Leftarrow) + N(\leftarrow\Leftarrow)]}{[N(\rightarrow\Rightarrow) + N(\leftarrow\Rightarrow)] + [N(\rightarrow\Leftarrow) + N(\leftarrow\Leftarrow)]}, \\
I^\odot &= \frac{1}{\delta_\odot} \frac{[N(\rightarrow\Rightarrow) + N(\rightarrow\Leftarrow)] - [N(\leftarrow\Rightarrow) + N(\leftarrow\Leftarrow)]}{[N(\rightarrow\Rightarrow) + N(\rightarrow\Leftarrow)] + [N(\leftarrow\Rightarrow) + N(\leftarrow\Leftarrow)]}, \\
P_z^\odot &= \frac{1}{\Lambda_z \delta_\odot} \frac{[N(\rightarrow\Rightarrow) + N(\leftarrow\Leftarrow)] - [N(\rightarrow\Leftarrow) + N(\leftarrow\Rightarrow)]}{[N(\rightarrow\Rightarrow) + N(\leftarrow\Leftarrow)] + [N(\rightarrow\Leftarrow) + N(\leftarrow\Rightarrow)]},
\end{aligned} \tag{5.4}$$

where $\rightarrow$ and $\leftarrow$ denote whether the circular beam polarization is parallel or antiparallel to the beam axis, $\Rightarrow$ and $\Leftarrow$ denote whether the direction of the target polarization is parallel or antiparallel to the beam axis. $N(\rightarrow\Rightarrow)$ is the number of events for the photon beam with +1 helicity and target polarization along +z direction. N is related to the differential cross section of the reaction in the following way:

$$\frac{d\sigma}{dx_i} = \frac{N}{A \cdot F \cdot \rho \cdot \Delta x_i}, \tag{5.5}$$

where A is the acceptance, F is the photon flux, ρ is the target density, Δx_i is the size of the kinematic bin. Using this relation, we can relate the experimentally measured event number N to the polarization observable as:

$$N = \sigma_0 (A \cdot F \cdot \rho \cdot \Delta x_i) \{ (1 + \Lambda_z \cdot P_z) + \delta_\odot (I^\odot + \Lambda_z \cdot P_z^\odot) \}. \tag{5.6}$$

The extraction of the three observables requires 4 different sets of measurements with different beam helicity and target polarization: $N(\rightarrow\Rightarrow), N(\leftarrow\Rightarrow), N(\rightarrow\Leftarrow), N(\leftarrow\Leftarrow)$. Moreover the simple form of equation 5.4 uses the assumption that the target polarization(Λ_z), beam polarization ($\delta_\odot$), and photon flux (F) are the same for all run periods. This assumption is not valid in a real experiment. In terms of target polarization, the run periods in the G14 experiment can be divided into two groups. Group 1 has the target polarization along the +z direction of the lab frame, this group includes Silver1, Silver2a, Silver2b, Silver3, Gold2. Group 2 has the target polarization along the -z direction, this group includes Silver4 and Silver5.

In Equation 5.6, we use a single letter C to represent the constant in the equation: $C = \sigma_0 \cdot A \cdot F \cdot \rho \cdot \Delta x_i$. Four equations can be written for the two periods: Silver5 and Gold2 for different beam helicity and target polarization:

$$
\begin{aligned}
N_{g2}^+ &= C_{g2}^+\{(1 + \Lambda_z^{g2} P_z) + \delta_\odot^{g2}(I^\odot + \Lambda_z^{g2} P_z^\odot)\} \\
N_{g2}^- &= C_{g2}^-\{(1 + \Lambda_z^{g2} P_z) - \delta_\odot^{g2}(I^\odot + \Lambda_z^{g2} P_z^\odot)\} \\
N_{s5}^+ &= C_{s5}^+\{(1 + \Lambda_z^{s5} P_z) + \delta_\odot^{s5}(I^\odot + \Lambda_z^{s5} P_z^\odot)\} \\
N_{s5}^- &= C_{s5}^-\{(1 + \Lambda_z^{s5} P_z) - \delta_\odot^{s5}(I^\odot + \Lambda_z^{s5} P_z^\odot)\}
\end{aligned}
\tag{5.7}
$$

where $N^\pm$ is the number of events when the beam helicity equals ± 1. The total events for each run period can be defined as: $N_{g2} = N_{g2}^+ + N_{g2}^-$, $N_{s5} = N_{s5}^+ + N_{s5}^-$. The difference between the events from the two beam helicity states for each run period can be defined as: $\Delta N_{g2} = N_{g2}^+ - N_{g2}^-$, $\Delta N_{s5} = N_{s5}^+ - N_{s5}^-$. In the G14 experiment, the beam helicity flip frequency is 960.015 Hz, thus the flux for the two beam helicity states can be viewed as the same, $C_{g2}^+ = C_{g2}^- = C_{g2}$, $C_{s5}^+ = C_{s5}^- = C_{s5}$. The three polarization observables can be deduced using Eq. 5.7 as follows:

$$
\begin{aligned}
I^\odot &= \frac{\frac{\Delta N_{g2}}{\delta_\odot^{g2}} - \alpha\beta\frac{\Delta N_{s5}}{\delta_\odot^{s5}}}{N_{g2} - \alpha\beta N_{s5}} \\[2mm]
P_z^\odot &= \frac{\frac{\Delta N_{g2}}{\delta_\odot^{g2}\Lambda_z^{s5}} - \alpha\beta\frac{\Delta N_{s5}}{\delta_\odot^{s5}\Lambda_z^{g2}}}{\alpha\beta N_{s5} - N_{g2}} \\[2mm]
P_z &= \frac{\alpha N_{s5} - N_{g2}}{\Lambda_z^{s5}(N_{g2} - \alpha\beta N_{s5})}
\end{aligned}
\tag{5.8}
$$

where $\alpha = \frac{C_{g2}}{C_{s5}}, \beta = \frac{\Lambda_z^{g2}}{\Lambda_z^{s5}}$. If $C_{g2} = C_{s5}$, $\Lambda_z^{s5} = -\Lambda_z^{g2}$, and $\delta_\odot^{g2} = \delta_\odot^{s5}$. Eq. 5.8 goes back to Eq. 5.4. For an asymmetry $A = (N_1 - N_2)/(N_1 + N_2)$, the error is calculated as:

$$
\sigma_A^2 = \left(\frac{\partial A}{\partial N_1}\right)^2 \sigma_{N_1}^2 + \left(\frac{\partial A}{\partial N_2}\right)^2 \sigma_{N_2}^2 + 2\left(\frac{\partial A}{\partial N_1}\right)\left(\frac{\partial A}{\partial N_2}\right) cov(N_1, N_2),
\tag{5.9}
$$

where $\sigma_{N_1}^2 = N_1$, $\sigma_{N_2}^2 = N_2$, and the covariance $cov(N_1, N_2) = 0$ for independent measurement of N_1, N_2. Using this relation, the statistical errors for these three observables

can be calculated to be:

$$\sigma_{I\odot} = \frac{\sqrt{\begin{aligned} & \left(\frac{2N_{g2}^-}{\delta_\odot^{g2}} - \alpha\beta\left(\frac{1}{\delta_\odot^{g2}} - \frac{1}{\delta_\odot^{s5}}\right)N_{s5}^+ - \alpha\beta\left(\frac{1}{\delta_\odot^{g2}} + \frac{1}{\delta_\odot^{s5}}\right)N_{s5}^-\right)^2 N_{g2}^+ \\ & + \left(\frac{2N_{g2}^+}{\delta_\odot^{g2}} - \alpha\beta\left(\frac{1}{\delta_\odot^{g2}} + \frac{1}{\delta_\odot^{s5}}\right)N_{s5}^+ - \alpha\beta\left(\frac{1}{\delta_\odot^{g2}} - \frac{1}{\delta_\odot^{s5}}\right)N_{s5}^-\right)^2 N_{g2}^- \\ & + \left(-2\alpha\beta\frac{N_{s5}^-}{\delta_\odot^{s5}} + \left(\frac{1}{\delta_\odot^{s5}} - \frac{1}{\delta_\odot^{g2}}\right)N_{g2}^+ + \left(\frac{1}{\delta_\odot^{s5}} + \frac{1}{\delta_\odot^{g2}}\right)N_{g2}^-\right)^2 (\alpha\beta)^2 N_{s5}^+ \\ & + \left(-2\alpha\beta\frac{N_{s5}^+}{\delta_\odot^{s5}} + \left(\frac{1}{\delta_\odot^{s5}} + \frac{1}{\delta_\odot^{g2}}\right)N_{g2}^+ + \left(\frac{1}{\delta_\odot^{s5}} - \frac{1}{\delta_\odot^{g2}}\right)N_{g2}^-\right)^2 (\alpha\beta)^2 N_{s5}^- \end{aligned}}}{(N_{g2} - \alpha\beta N_{s5})^2} \tag{5.10}$$

$$\sigma_{P_z\odot} = \frac{\sqrt{\begin{aligned} & \left(-\frac{2N_{g2}^-}{\delta_\odot^{g2}\Lambda_z^{s5}} + \alpha\beta\left(\frac{1}{\delta_\odot^{g2}\Lambda_z^{s5}} + \frac{1}{\delta_\odot^{s5}\Lambda_z^{g2}}\right)N_{s5}^+ - \alpha\beta\left(-\frac{1}{\delta_\odot^{g2}\Lambda_z^{s5}} + \frac{1}{\delta_\odot^{s5}\Lambda_z^{g2}}\right)N_{s5}^-\right)^2 N_{g2}^+ \\ & + \left(-\frac{2N_{g2}^+}{\delta_\odot^{g2}\Lambda_z^{s5}} - \alpha\beta\left(-\frac{1}{\delta_\odot^{g2}\Lambda_z^{s5}} + \frac{1}{\delta_\odot^{s5}\Lambda_z^{g2}}\right)N_{s5}^+ + \alpha\beta\left(\frac{1}{\delta_\odot^{g2}\Lambda_z^{s5}} + \frac{1}{\delta_\odot^{s5}\Lambda_z^{g2}}\right)N_{s5}^-\right)^2 N_{g2}^- \\ & + \left(-2\alpha\beta\frac{N_{s5}^-}{\delta_\odot^{s5}\Lambda_z^{g2}} + \left(\frac{1}{\delta_\odot^{s5}\Lambda_z^{g2}} - \frac{1}{\delta_\odot^{g2}\Lambda_z^{s5}}\right)N_{g2}^+ + \left(\frac{1}{\delta_\odot^{s5}\Lambda_z^{g2}} + \frac{1}{\delta_\odot^{g2}\Lambda_z^{s5}}\right)N_{g2}^-\right)^2 (\alpha\beta)^2 N_{s5}^+ \\ & + \left(-2\alpha\beta\frac{N_{s5}^+}{\delta_\odot^{s5}\Lambda_z^{g2}} + \left(\frac{1}{\delta_\odot^{s5}\Lambda_z^{g2}} + \frac{1}{\delta_\odot^{g2}\Lambda_z^{s5}}\right)N_{g2}^+ + \left(\frac{1}{\delta_\odot^{s5}\Lambda_z^{g2}} - \frac{1}{\delta_\odot^{g2}\Lambda_z^{s5}}\right)N_{g2}^-\right)^2 (\alpha\beta)^2 N_{s5}^- \end{aligned}}}{(N_{g2} - \alpha\beta N_{s5})^2} \tag{5.11}$$

$$\sigma_{P_z} = \frac{\left[\alpha(\Lambda_z^{g2} - \Lambda_z^{s5})\right]\sqrt{N_{g2}N_{s5}(N_{g2} + N_{s5})}}{\left(\Lambda_z^{s5}N_{g2} - \alpha\Lambda_z^{g2}N_{s5}\right)^2} \tag{5.12}$$

The ratio of the constant C between Gold2 and Silver5 period $\alpha = \frac{C_{g2}}{C_{s5}}$ can be obtained from comparing the downstream KelF peak as in Figure 5.2, since the Silver5 target lost some HD in the target region, an overall coefficient of 1.435 (silver target is 70% of the the length of a full target) is multiplied by the ratio: $\alpha = \frac{C_{g2}}{C_{s5}} = 1.435 \times \frac{KelF_{g2}}{KelF_{s5}}$. The ratio of the yields under the KelF peak at 0cm $< z <$ 2cm between Gold2 and Silver5 periods for the six center of momentum total energy bins is shown in Figure 5.3.

5.2 Determination of the target polarization for Silver5 period

From Table 3.1, we see that the polarization for the deuteron in the HD target is 15.79% along the -z direction. However, from the study of the E asymmetry in the single pion channel: $\gamma + n \rightarrow p + \pi^-$, Silver5 data set gives a significant smaller value for E asymmetry if the deuteron polarization is $P_D = -15.79\%$, as shown in Figure 5.4, this result implies that the actual deuteron polarization is much smaller than the value measured by the
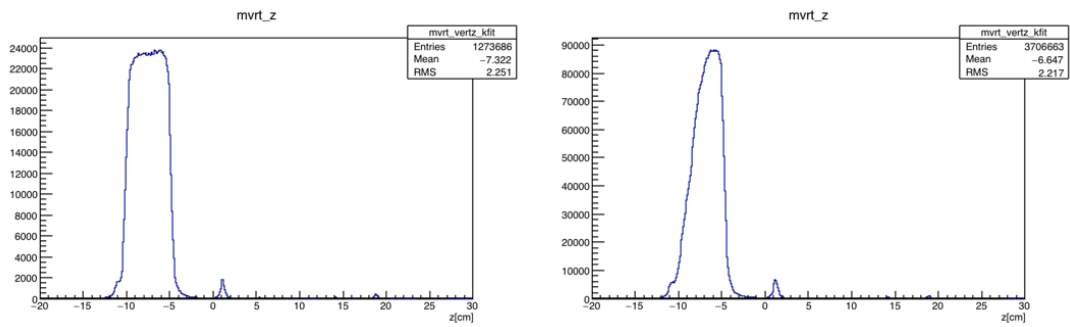
Figure 5.2: Vertex z distribution for the channel $\gamma p \rightarrow p\pi^+\pi^-$ for Gold2 (left) and Silver5(right) periods.
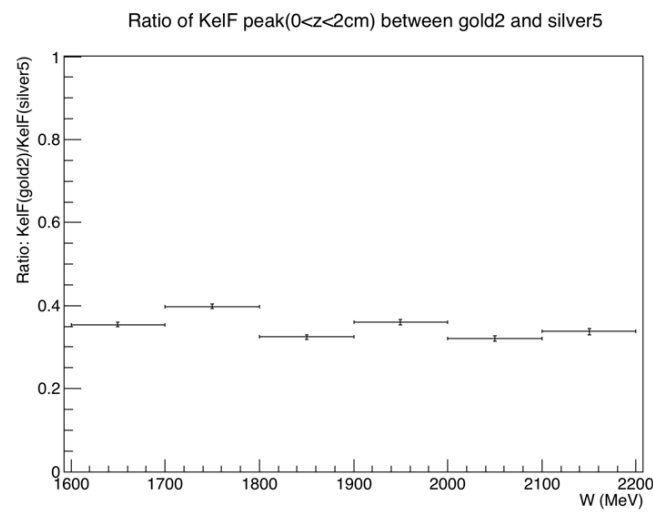

Figure 5.3: The ratio of the yields under the KelF peak at $0cm < z < 2cm$ between Gold2 and Silver5 periods for the six center of momentum energy bins.

NMR. This is the reason why in the previous chapter, the data set of the Silver 5 is not included in the calculation for the E asymmetry. However, in the calculation of
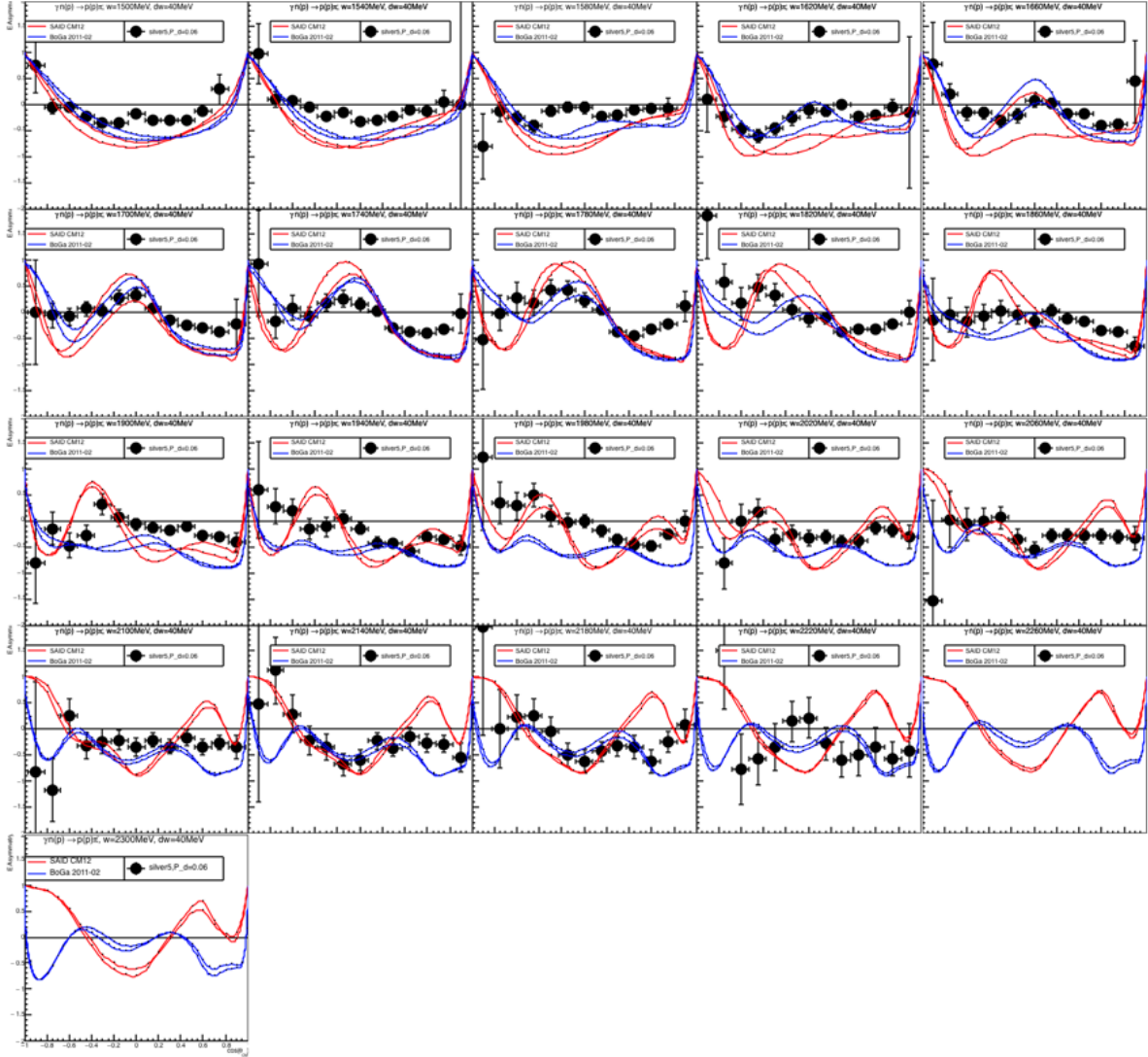

Figure 5.4: E asymmetry vs $\cos(\theta_{CM})$ for different center of momentum energy W for $\gamma + n \rightarrow p + \pi^-$ for the silver5 data set.

$P_z, I^{\odot}, P_z^{\odot}$ for the two pion photo-production, Silver5 data set is required to be used in the calculation, since this data set has the deuteron polarization along the -z direction. Thus we need to get the right value for the deuteron polarization for the Silver5 data set. The method we are using is to vary the value of the deuteron polarization for the Silver5 data set, until we get the closest value for the E asymmetry in the single pion channel between the Silver5 and the combined results from previous chapter. A χ^2 value is defined in the following equation:

$$\sigma_{\chi^2} = \sum_i \frac{(E_{s5} - E_{combine})^2}{\sigma^2(E_{s5} - E_{combine})} \tag{5.13}$$

Figure 5.5 plots the χ^2 vs. the deuteron polarization of Silver5 target. χ^2 is minimized at 5.1%. The error on the polarization was determined to be 0.2% by varying the χ^2 by 1 near its minimal. The result for the deuteron polarization: $D_{pol} = (-5.1 \pm 0.2)\%$ is significantly smaller than the polarization measured by the NMR, which is $(-15.5 \pm 0.7)\%$.
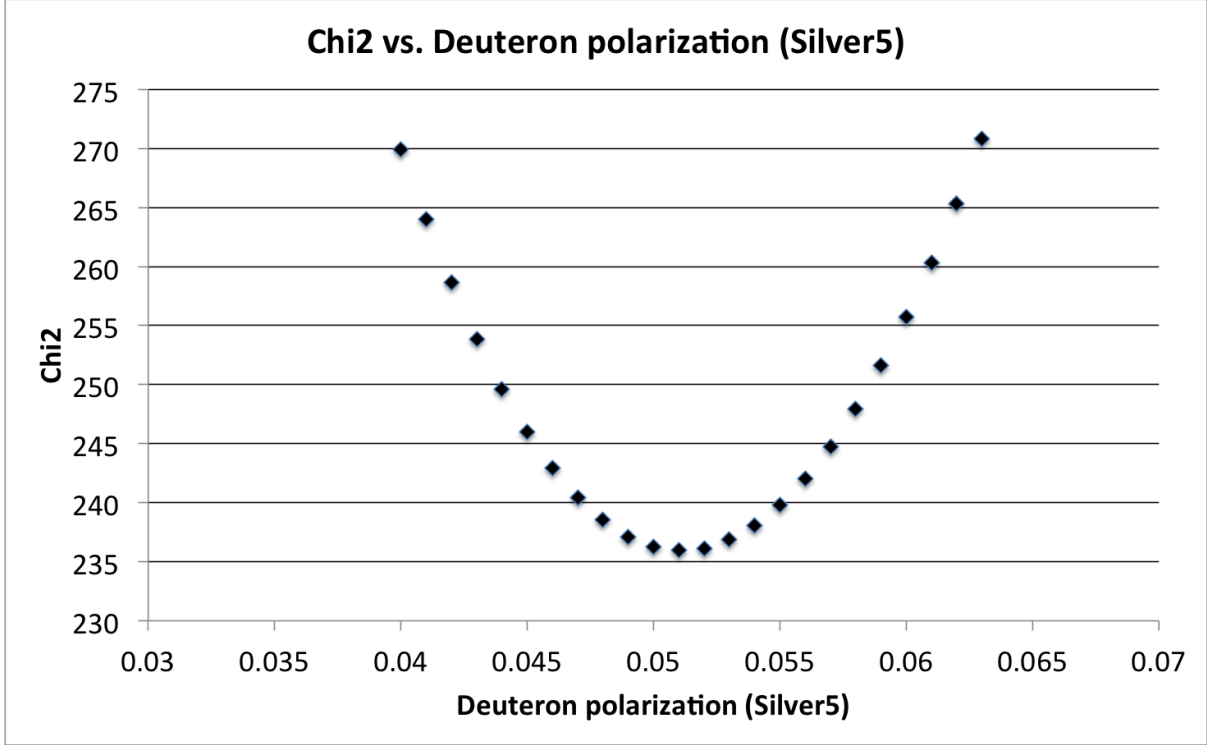

Figure 5.5: χ^2 vs. the deuteron polarization for Silver5 target.

From Eq 5.8, we can see that the small value of deuteron polarization for Silver5 target won't affect the calculation for $I^\odot$, but will affect the other two observables $P_z, P_z^\odot$.

5.3   Beam Helicity Asymmetry $I^\odot$

The results for beam helicity asymmetry are shown in Figure 5.6. The results are compared with previous CLAS experiments g1c [20] and g9a [21], and they are in overall agreement. The prediction of the theory by A.Fix [23] is also shown for the first two energy bins.

We notice that for lower energy bins the amplitudes of the curves from G14 experiment are bigger that the results from G1c and G9a. For higher energy bins the amplitudes of the curves from G14 experiment are smaller than the results from G1c and G9a. These differences are caused by the use of different ways to integrate the polar angle $\theta_{\pi\pi}$. In this study, we integrate $I^\odot$ over $\theta_{\pi\pi}$ by dividing $\cos(\theta_{\pi\pi})$ into 5 bins from -1 to 1, calculate I_c for each $\cos\theta_{\pi\pi}$ bin, and then add them together as:

$$I^\odot(\phi') = \frac{\int_{-1}^{1} I^\odot(\theta_{\pi\pi}, \phi') d(\cos\theta_{\pi\pi})}{\int_{-1}^{1} d(\cos\theta_{\pi\pi})} = \frac{1}{2}\sum I^\odot(\theta_{\pi\pi}, \phi')\Delta(\cos\theta_{\pi\pi}) \qquad (5.14)$$

126
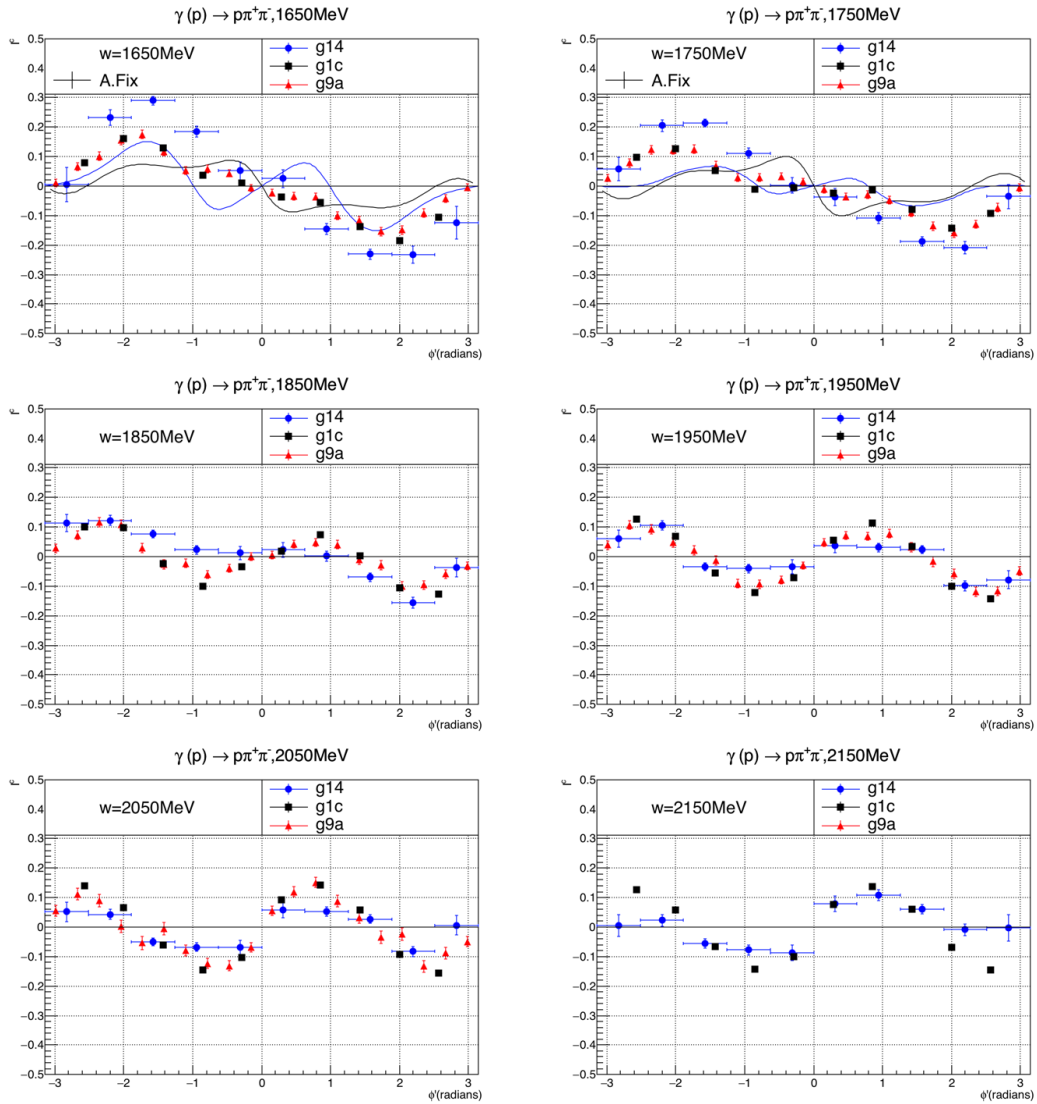
Figure 5.6: Beam helicity asymmetry vs. ϕ' for different center of momentum energy w. The results from previous CLAS measurements g1c [20] and g9a [21], and the prediction from [23] are also shown in the plots.

the 1/2 in the equation is the normalization number from the inverse of the $\cos(\theta_{\pi\pi})$ integration range of 2 from -1 to 1.

On the other hand, the method of integration used in the other experiments views $\cos\theta_{\pi\pi}$ as one bin, and calculates $I^{\odot}(\phi')$ by summing all the events from all $\cos\theta_{\pi\pi}$ bins for each ϕ' bin. We also used the second way of $\cos\theta_{\pi\pi}$ integration, Figure 5.7 shows that the results from three different experiments are very close to each other when the same method for $\cos\theta_{\pi\pi}$ integration is used.
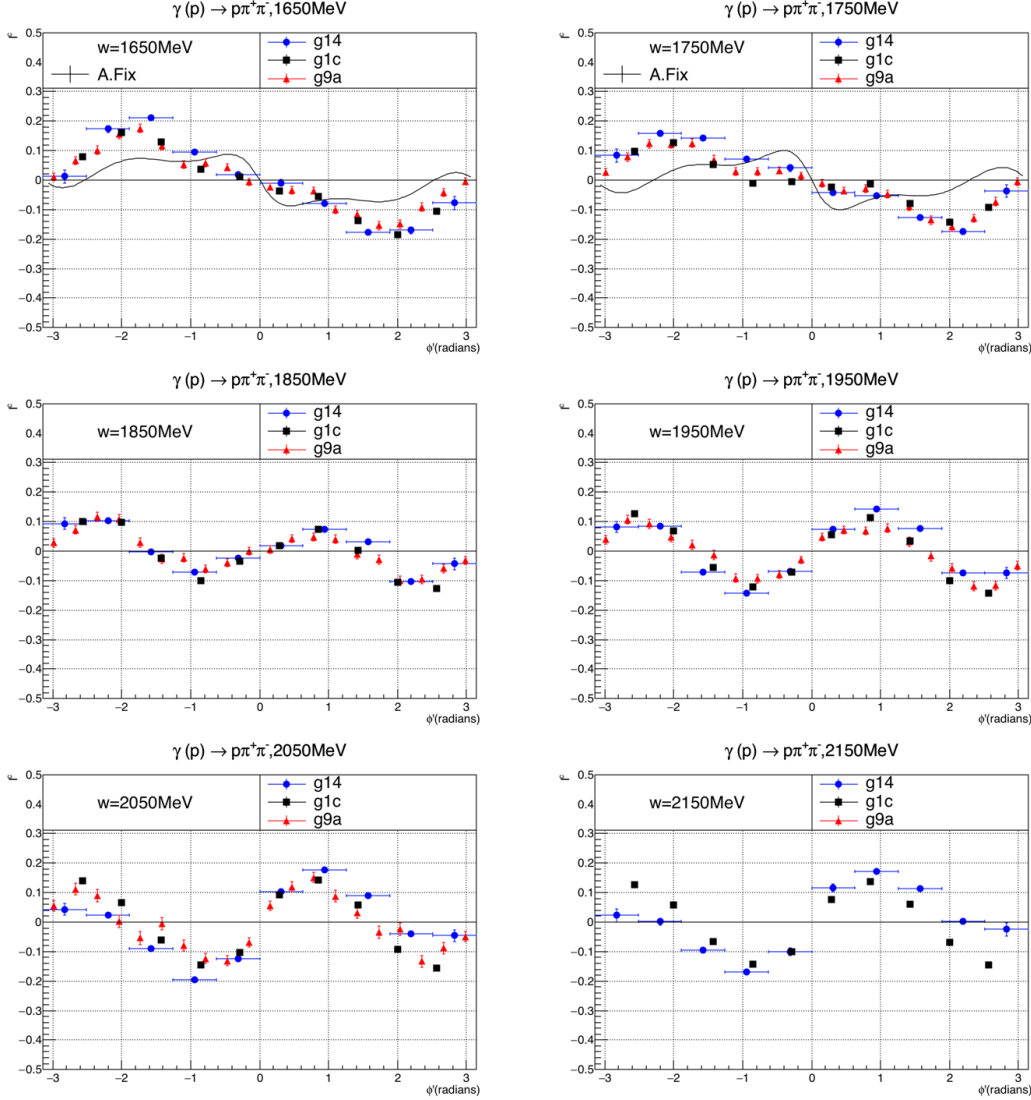

Figure 5.7: Beam helicity asymmetry vs. ϕ' for different center of momentum energy W, calculated under the assuption that $I^{\odot}(\phi')$ is independent of $\theta_{\pi\pi}$. The results from previous CLAS measurements g1c [20] and g9a [21], and the prediction from [23] are also shown in the plots.

However, the second way of integration makes an assumption that the observable $I^{\odot}(\phi')$ is uniformly distributed along $\cos\theta_{\pi\pi}$ for a fixed ϕ' bin. Figure 5.8 shows that this assumption is not true, since $I^{\odot}(\phi')$ fluctuates along $\cos\theta_{\pi\pi}$ direction for fixed ϕ' bins. Based on this observation, we believe that the first method introduced earlier is the right

way for $\cos\theta_{\pi\pi}$ integration. Since these two methods give different values for $I^{\odot}(\phi')$, we suggest the data in g1c and g9b should be replotted using the right way for the $\cos\theta_{\pi\pi}$ integration. While the differences in the approach to $\theta_{\pi\pi}$ integration account for most of the variations between these results and those of g1c and g9a, we note that at the highest energies the present experiment sees significantly less beam helicity asymmetry near the extreme ϕ' angles of $-\pi$ and $+\pi$.
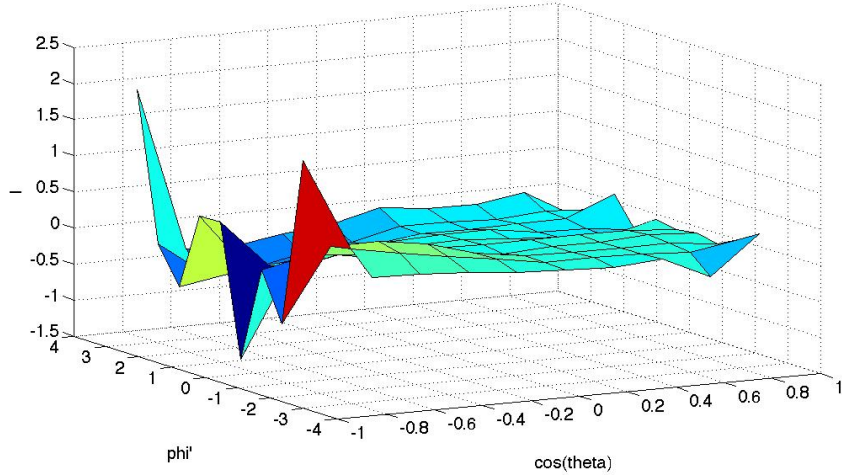

Figure 5.8: Beam helicity asymmetry $I^{\odot}(\phi')$ vs. ϕ' and $\cos\theta_{\pi\pi}$ for center of momentum energy W = 1750 MeV.

5.4 Target Asymmetry P_z

The results for target asymmetry are shown in Figure 5.9, the results using the $\theta_{\pi\pi}$ integration with the assumption that P_z is independent of $\theta_{\pi\pi}$ are shown in Figure 5.10.

5.5 Beam Target Double Asymmetry $P_z^{\odot}$

The results for beam target double asymmetry are shown in Figure 5.11, the results using the $\theta_{\pi\pi}$ integration with the assumption that $P_z^{\odot}$ is independent of $\theta_{\pi\pi}$ are shown in Figure 5.12.

5.6 Conclusion

The three polarization observables for $\gamma p \to p\pi^+\pi^-$ using a circularly polarized photon beam and longitudinally polarized target are compared with previous experiments [20] [21]. $I^{\odot}$ values are in overall agreement between the G14 measurement and the G9a measurement [21], but P_z and $P_z^{\odot}$ have big discrepancies between these two experiments.
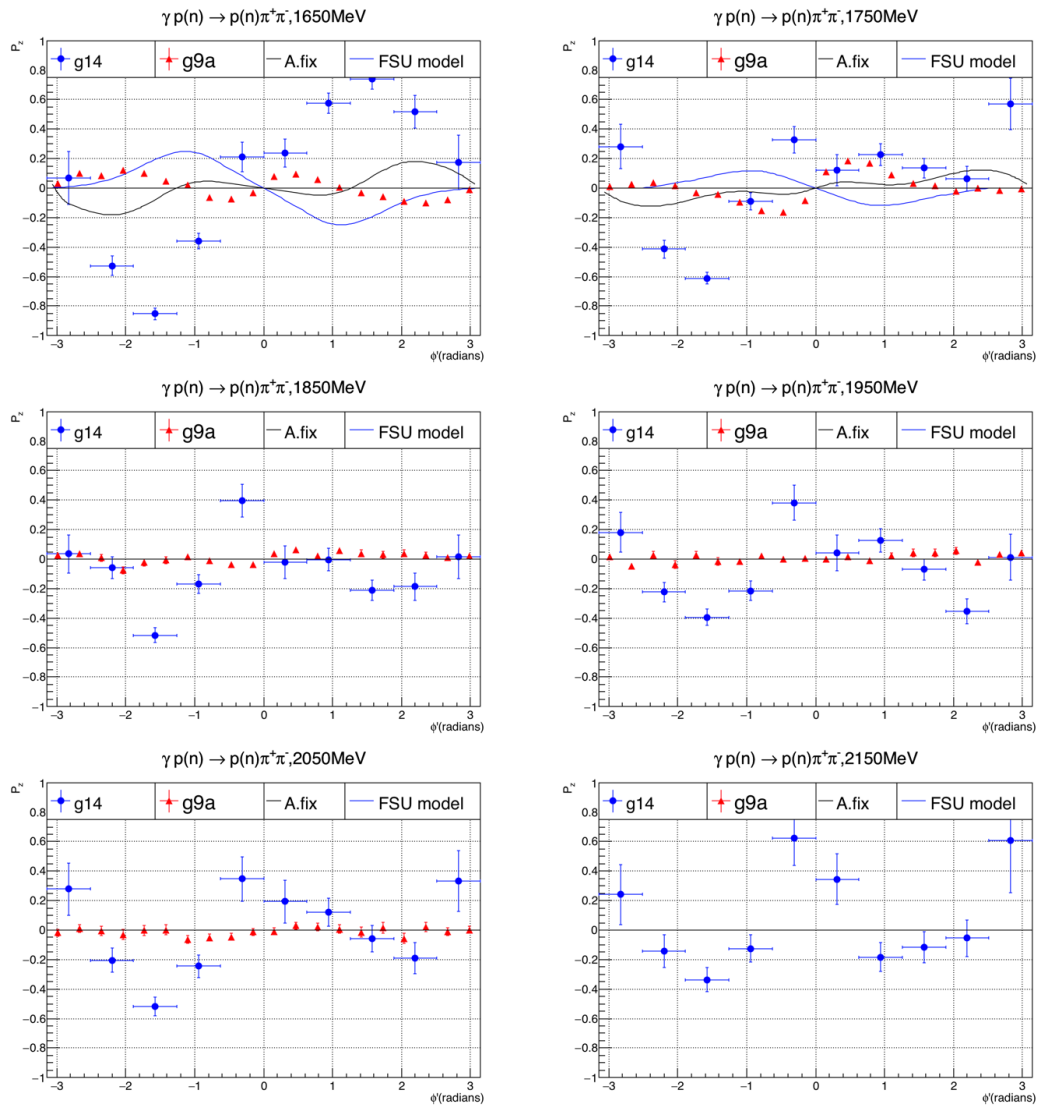
Figure 5.9: Target asymmetry vs. ϕ' for different center of momentum energy w.
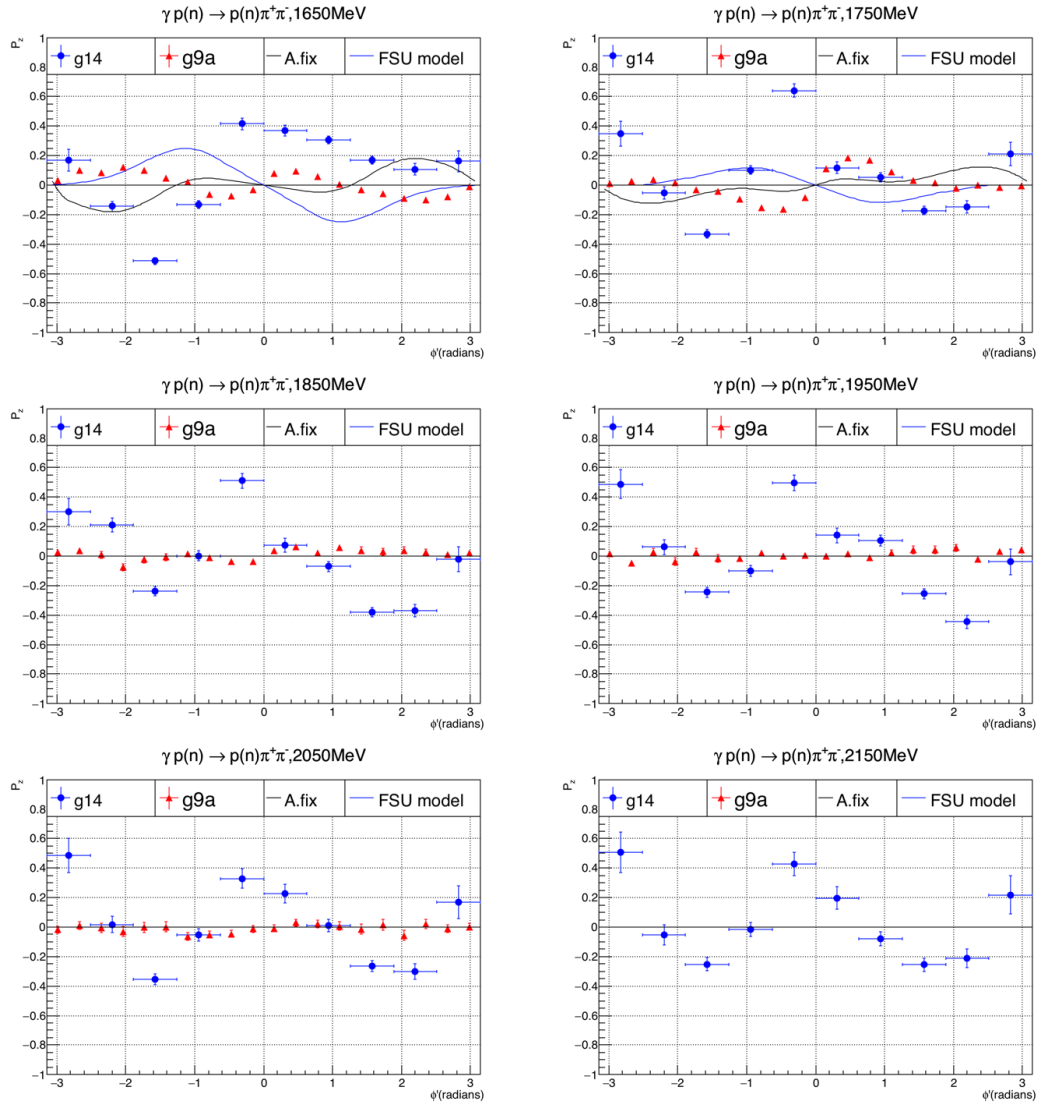
Figure 5.10: Target asymmetry vs. ϕ' for different center of momentum energy w, calculated under the assuption that $P_z(\phi')$ is independent of $\theta_{\pi\pi}$.
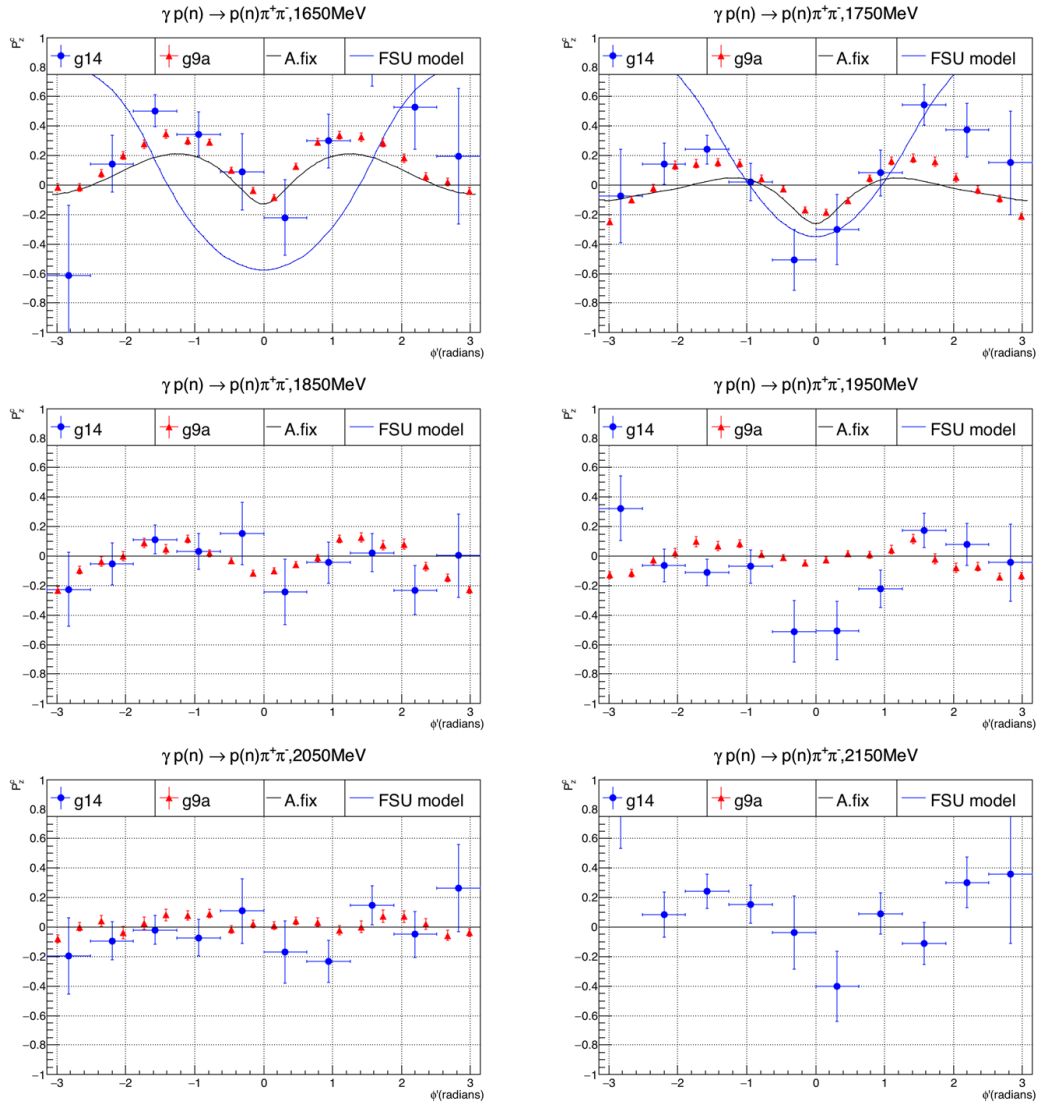
Figure 5.11: Beam target double asymmetry vs. ϕ' for different center of momentum energy w.
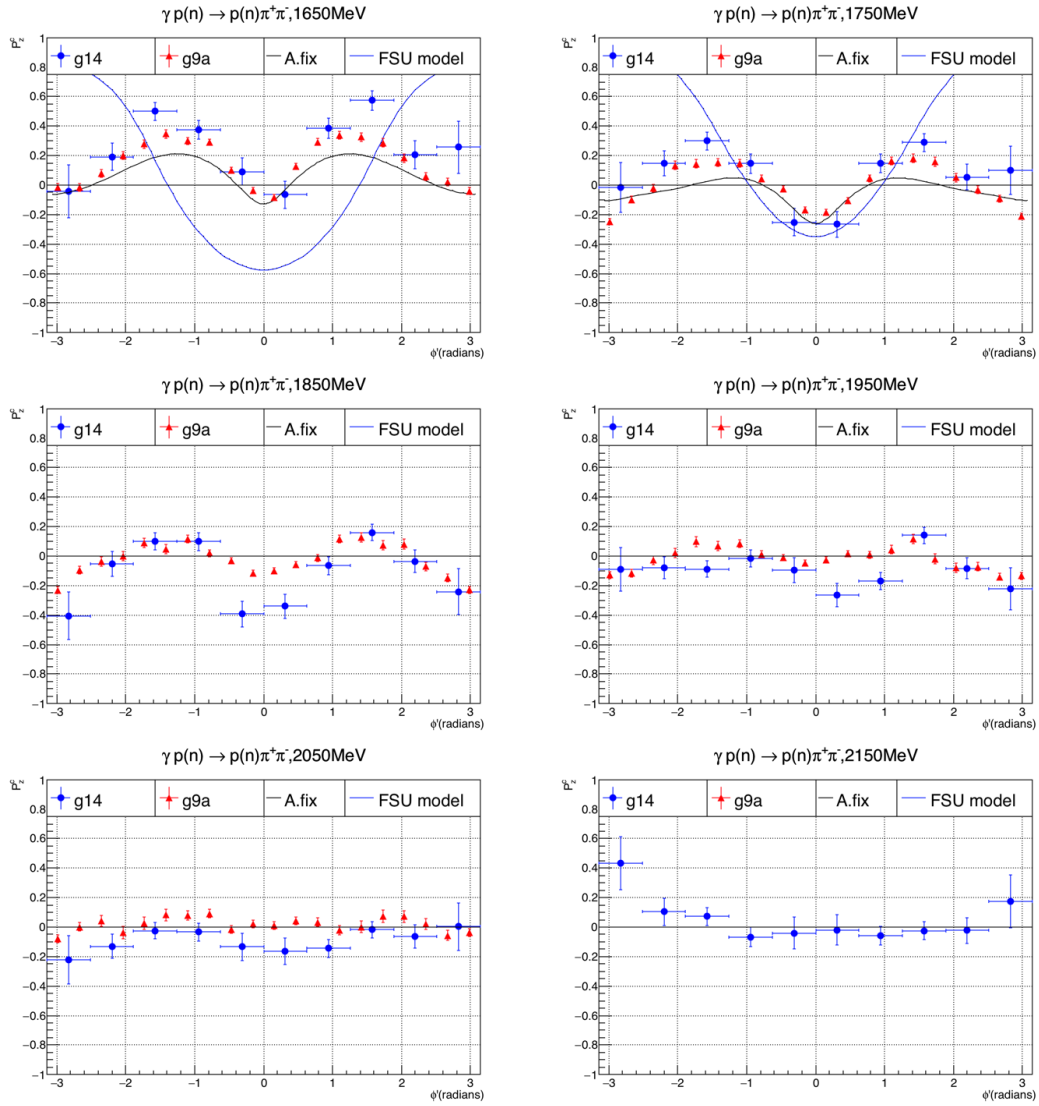
Figure 5.12: Beam target double asymmetry vs. ϕ' for different center of momentum energy w, calculated under the assuption that $P_z^\odot(\phi')$ is independent of $\theta_{\pi\pi}$.

Chapter 6

Polarization Observables for $\gamma n \to n\pi^+\pi^-$

The reaction of double pion photo-production from the neutron target has the same kinematics and polarization observables as the reaction using the proton target. The diagram for the reaction kinematics is shown in Figure 6.1.
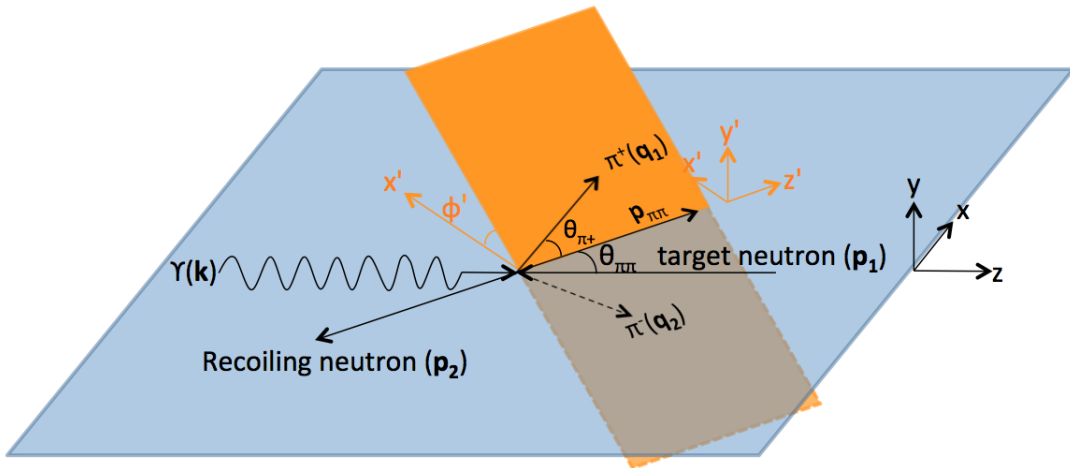

Figure 6.1: Kinemactics for the reaction of $\gamma n \to n\pi^+\pi^-$ in c.m. frame. $\boldsymbol{k}$, $\boldsymbol{p_1}$, $\boldsymbol{p_2}$, $\boldsymbol{q_1}$, $\boldsymbol{q_2}$ are the momenta of the incident photon, neutron target, recoiling neutron, and the two pions. $\theta_{\pi\pi}$ is the polar angle of the sum vector of the momenta of the two pions in center of momentum frame. $\theta_{\pi+}$ is the angle between $\boldsymbol{q_1}$ and $\boldsymbol{p_{\pi\pi}}$. ϕ' is then angle between the plane formed by the two pion momenta and the reaction plane.

6.1   Event selection

Similar filters are used in the neutron target channel as in the proton target channel.

6.1.1 Particle ID filters

The first set of filters are particle ID filters: PID = 8 for π^+, PID = 9 for π^-. For the identification of neutrons, CLAS uses the Electromagnetic Calorimeter to detect neutral particles. In the G14 experiment, there are two neutral particles involved: photons and neutrons. These two neutral particles are separated by a β cut at 0.9. The neutrons are identified with $\beta < 0.9$. (Figure 6.2).
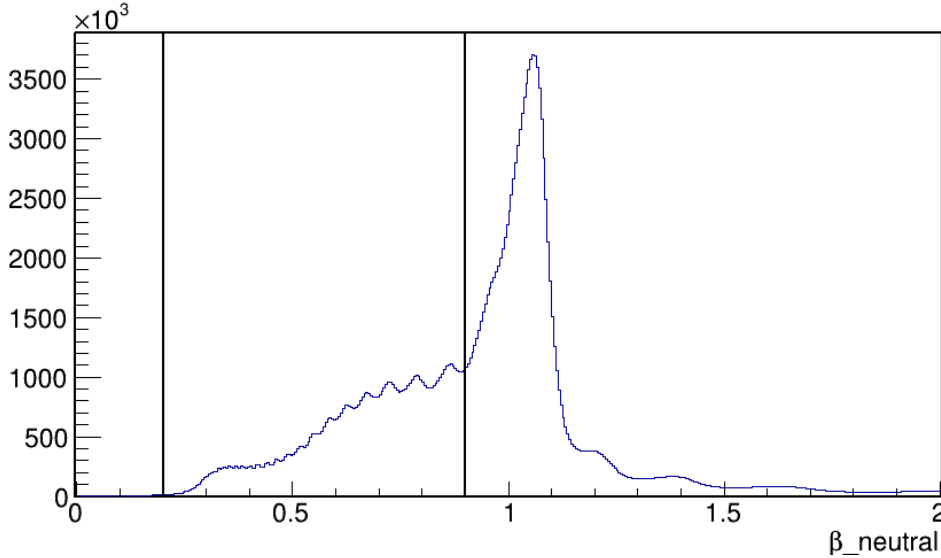

Figure 6.2: β value for neutral particles detected by the EC detectors, a cut of $\beta < 0.9$ is used to separate neutrons from photons.

Moreover, "targid" and "ngrf == 1" are used to better define the reaction channels. The "targid" filters require all the final state particles to come from the same tagged photon; and the "ngrf == 1" filter require the number of photons in the same RF bucket to be one.

6.1.2 $\Delta\beta$ cuts

Since the EC module of the CLAS detectors does not have high efficiency for detecting neutrons (Figure 6.3), we loosen the the $\Delta\beta$ cuts to increase statistics: $\Delta\beta$ cut for π^+ and π^- is chosen to be $|\Delta\beta| < 0.5$ instead of <0.3. Figure 6.5 gives the β vs momentum plot for π^+ and π^- particles after the $|\Delta\beta|$ cut.

6.1.3 Fiducial cuts

The same fiducial cuts are used for π^+ and π^- using the Equation 6.1, the angular distributions before and after the fiducial cuts for π^+ and π^- are shown in Figure 6.6.

$$\theta > 4.0 + \frac{510.58}{(30 - \phi)^{1.5518}} \tag{6.1}$$

For neutrons, extra cuts need to be used in order to remove some of the events that mis-identify protons as neutrons [58]. As shown in Figure 6.7, there are two peaks in the
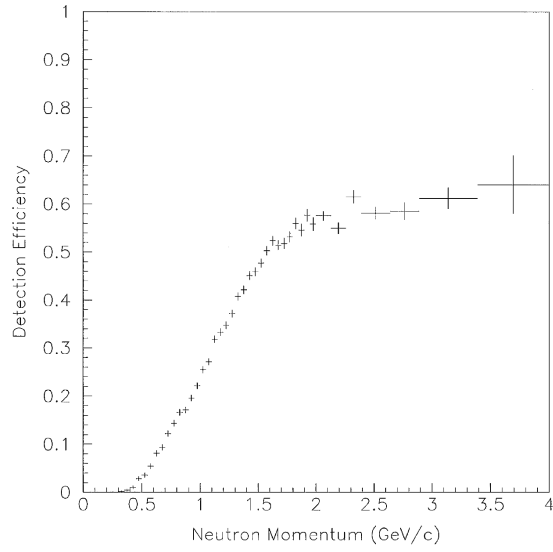
Figure 6.3: Measured neutron detection efficiency vs. neutron momentum in the EC detectors. Image Source: [39]

(a) π^+: abs($\Delta\beta$)<0.05.

(b) π^-: abs($\Delta\beta$)<0.05.
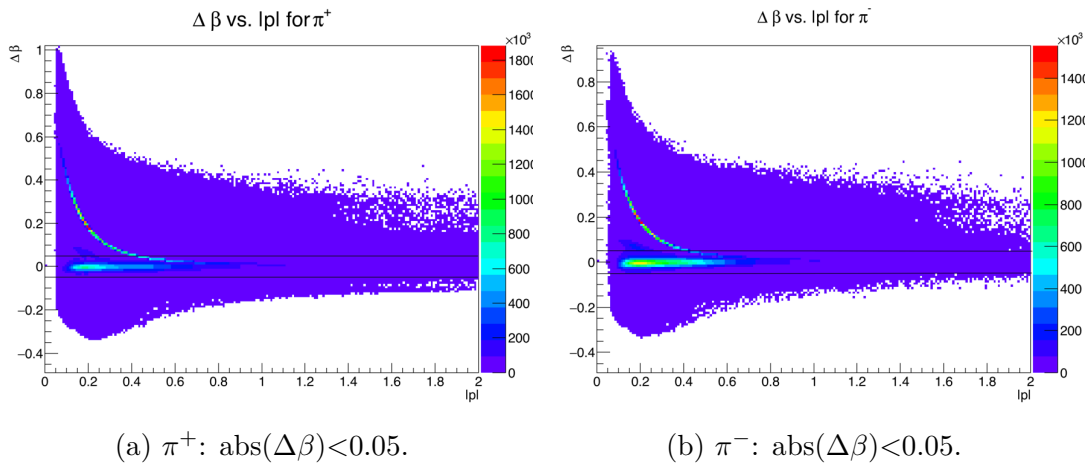
Figure 6.4: $\Delta\beta$ filter for π^+ and π^-
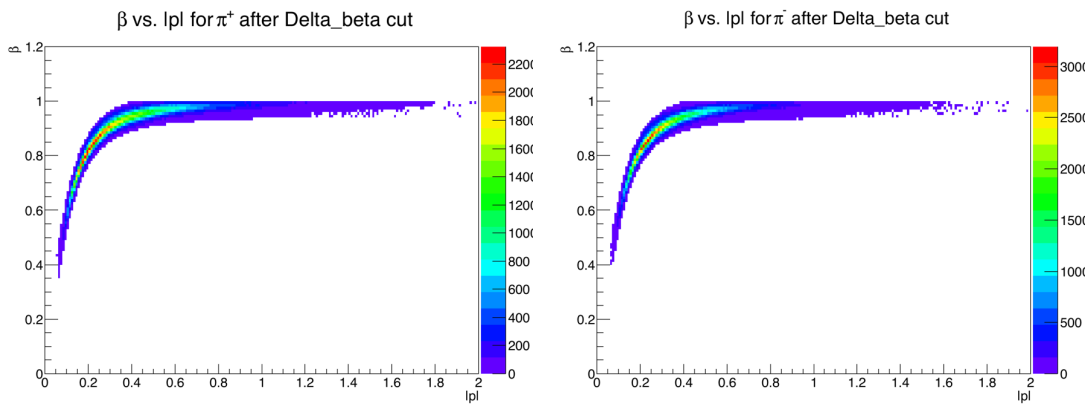
Figure 6.5: The β vs momemtum plots for π^+ and π^- after the $\Delta\beta$ cut.
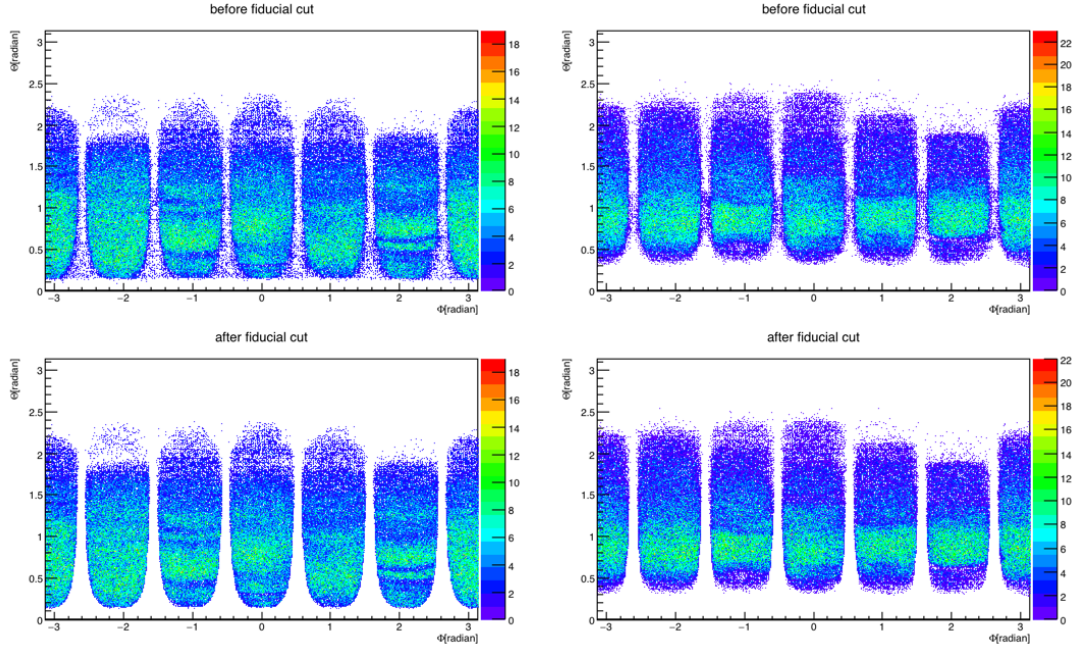
Figure 6.6: Fiducial cuts for π^+ and π^-. The top two plots are the angular distributions of π^+, π^- before fiducial cuts, the bottom two plots are the distributions after fiducial cuts

top right plot (b) for the θ collinear distribution, the peak on the right side indicates that there are some protons mis-identified as neutrons. In the center of momentum frame, the sum of the polar angles for the sum vector of π^+, π^- and the neutron should be 180° in the reaction: $\gamma + n \rightarrow n + \pi^+ + \pi^-$. However, since the DC(drift chamber) detectors have some bad regions, which cannot identify protons, these protons will hit the EC detectors and induce electromagnetic showers the same as neutrons. The method for CLAS to separate protons from neutrons detected by the EC detectors is to use the particle charge information from the DC. If part of the DC does not work, the protons that go through this part will be mis-identified as neutrons. Moreover, since protons will be bent in the torus magnetic field, the sum of θ for proton and $\pi^+\pi^-$ will not be 180°, which gives the right peak in Figure 6.7(b). The bottom two plots in Figure 6.7 show the regions of the EC detectors where the mis-identified protons are. Plot (c) uses a cut of $\theta_{\pi^+\pi^-} + \theta_{neu} - \pi > 0.1$, two regions of the angular distribution plot have more events than other regions. On the other hand, plot (d) with a cut of $\theta_{\pi^+\pi^-} + \theta_{neu} - \pi < 0.1$ (good neutron events) does not show the two enhanced regions. In order to remove the events with the mis-identified protons, we will make an extra fiducial cuts to remove the three regions with mis-identified protons in Figure 6.6(c). As shown in Figure 6.8, after the extra fiducial cuts for the mis-identified protons, the right peak in the θ collinear plot disappears. Since the protons bend in the torus magnetic field, the regions for mis-identified protons in the EC detectors should change position if the torus field changes direction, Figure 6.9 gives the change of the regions for positive and negative torus field. For the other magnetic field setting, the collinear θ plots before and after the extra fiducial cut for the mis-identified protons are shown in Figure 6.10.

137
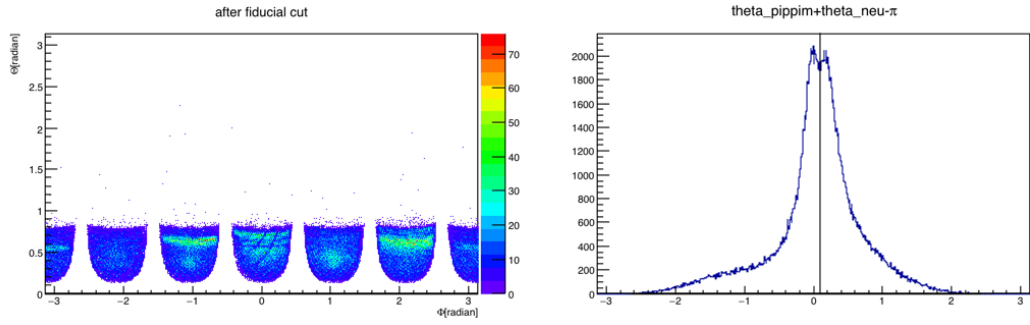
(a) Neutron angular distribution after normal fidicial cuts.

(b) $\theta_{\pi^+\pi^-} + \theta_{neu} - \pi$ in center of momentum frame
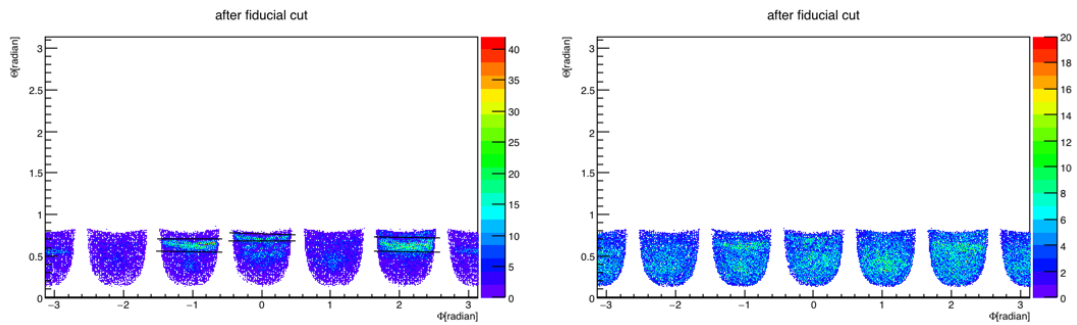

(c) Neutron angular distribution with cut of $\theta_{\pi^+\pi^-} + \theta_{neu} - \pi > 0.1$

(d) Neutron angular distribution with cut of $\theta_{\pi^+\pi^-} + \theta_{neu} - \pi < 0.1$

Figure 6.7: The problem of mis-identification of protons as neutrons.
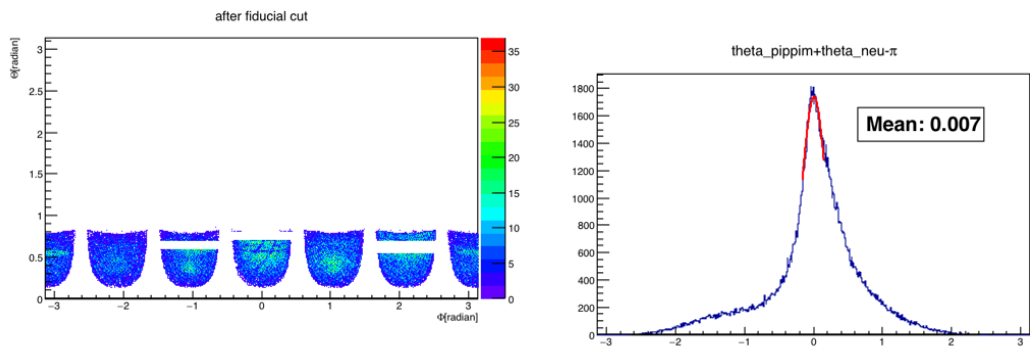
(a) The three regions where the mis-identified protons are are removed with extra cuts.

(b) $\theta_{\pi^+\pi^-} + \theta_{neu} - \pi$ in center of momentum frame after the extra fiducial cuts

Figure 6.8: Effect of the extra fiducial cuts on the removal of mis-identified protons.

138
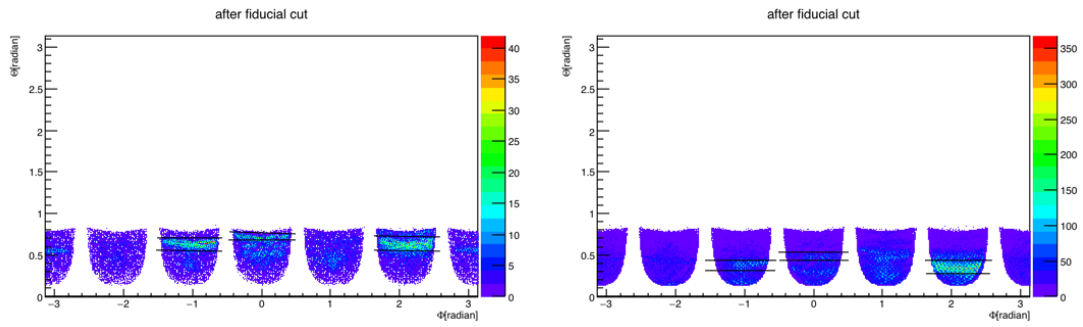
(a) Neutron angular distribution for positive torus magnetic field.

(b) Neutron angular distribution for negtive torus magnetic field.

Figure 6.9: The regions for mis-identified protons change positions for different torus field.
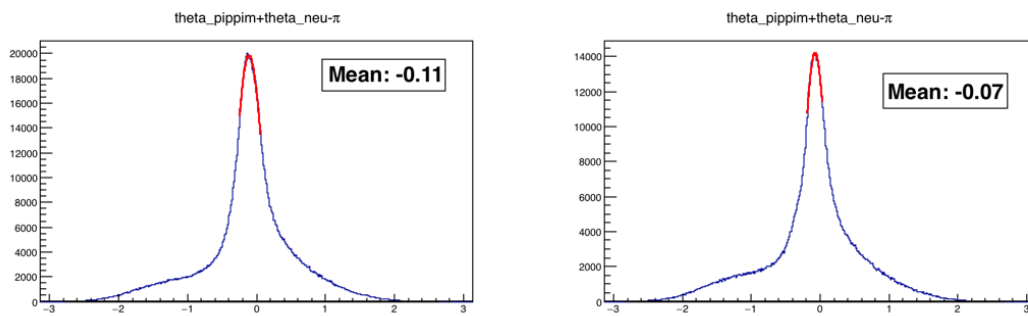
(a) $\theta_{\pi^+\pi^-} + \theta_{neu} - \pi$ in center of momentum frame before mis-identified protons region cut for negative torus field runs.

(b) $\theta_{\pi^+\pi^-} + \theta_{neu} - \pi$ in center of momentum frame after mis-identified protons region cut for negative torus field runs.

Figure 6.10: Effect of the extra fiducial cuts for negative torus field runs.

139

6.2 Kinematic Fitting for $\gamma n \to n\pi^+\pi^-$

For the kinematic fitting of this channel, since there is no information of the covariance matrix for the final state neutrons, we cannot apply the same kinematic fitting procedures as we did for $\gamma n \to p\pi^-$, $\gamma p \to p\pi^+\pi^-$, in which all the final state particles are detected with the information of the covariance matrix. We will use an approximate kinematic fitting for this channel, in which we assume the neutron target is a free neutron. The fitting is a "1C fit" as: $\gamma n \to (n)\pi^+\pi^-$, with the final state neutron missing (its 3 momentum are free parameters in the fitting). Even though the final state neutron is viewed as "missing", we have required that a neutron is detected in EC for the reaction in the event selection process. The pull distribution and confidence level are shown in Figure 6.11 and Figure 6.12. The cut of confidence level $CL > 2\%$, its effect on the missing mass, missing momentum and coplanairty plots are shown in Figure 6.13. The subplots in Figure 6.13 indicate that some background events are not removed by the confidence level cut, thus extra cuts for missing mass (0.8GeV < mm < 1.1 GeV) , coplanarity ($2.7<|\delta(\phi)|<3.5$) and vertex-z(-10.5 cm < z < -5.5 cm) are used after the confidence level cut.
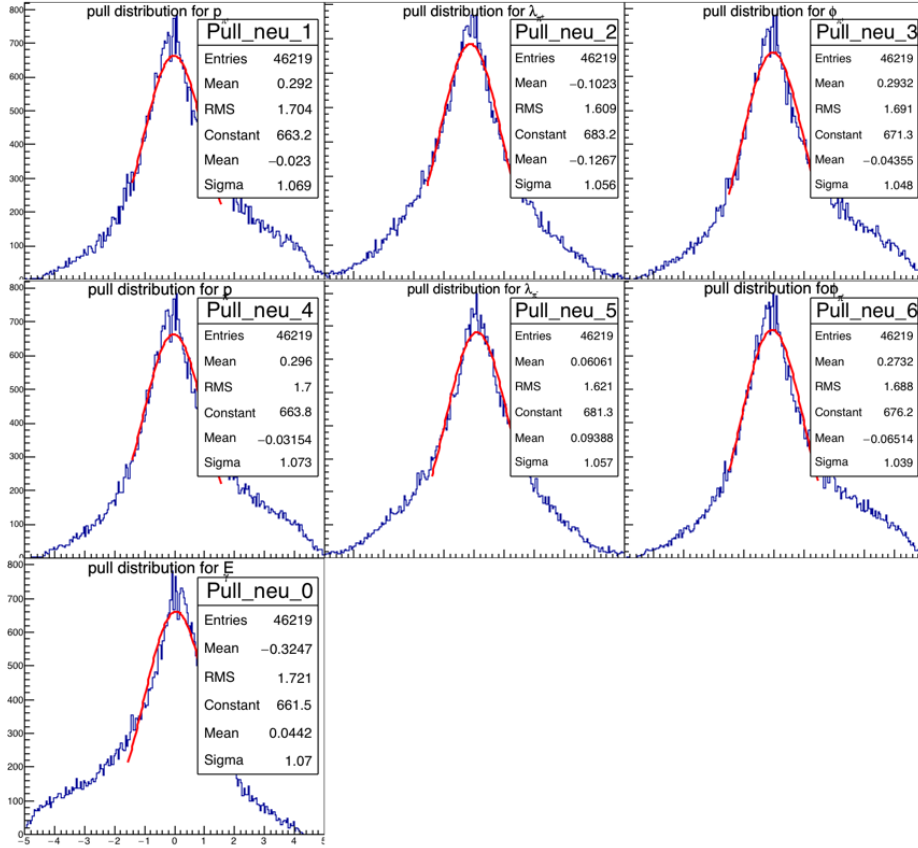


Figure 6.11: Pull distribution for $\gamma n \to (n)\pi^+\pi^-$.
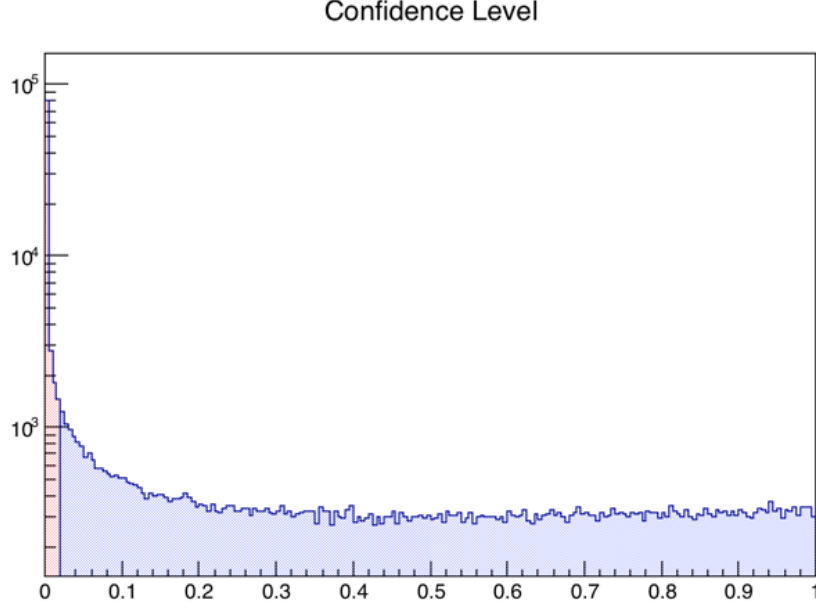
Figure 6.12: Confidence level for $\gamma n \to (n)\pi^+\pi^-$, a cut of CL $> 2\%$ are used to remove the background events.

(a) Missing mass: $\gamma n \to (n)\pi^+\pi^-$.

(b) Missing momentum: $\gamma n \to (n)\pi^+\pi^-$.

(c) Coplanarity: $|\phi(n) - \phi(\pi^+\pi^-)|$.

(d) Vertex z cut.
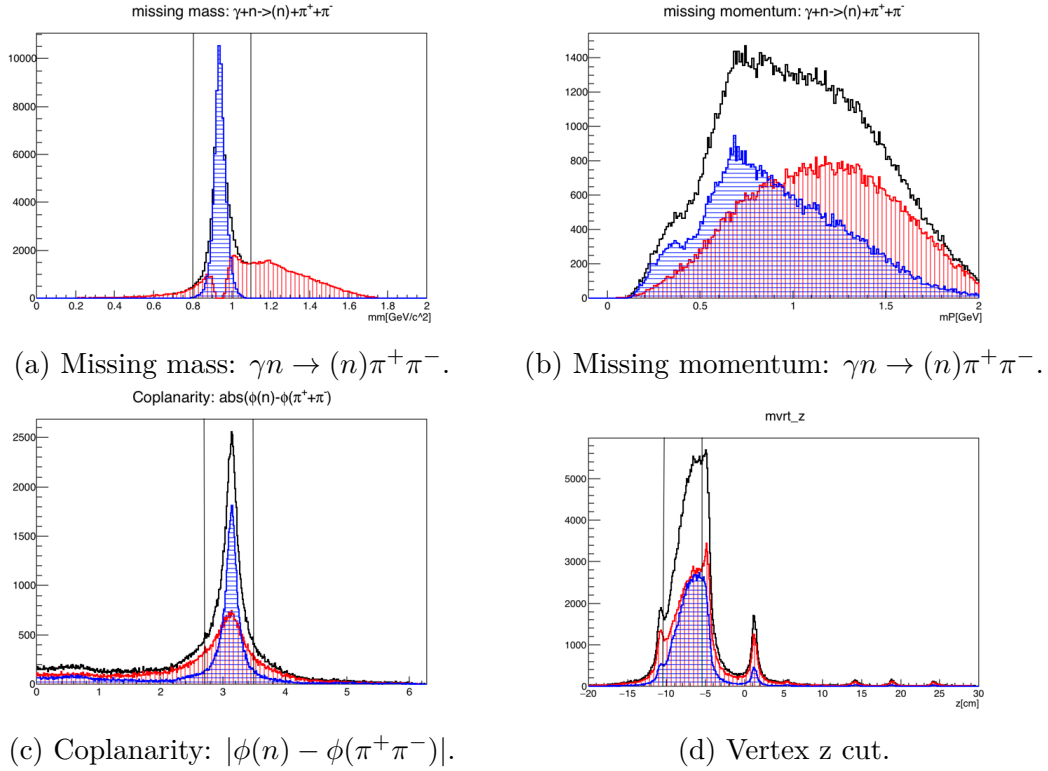
Figure 6.13: Effect of the kinematic fitting's confidence level cut on event selection for channel $\gamma n \to (n)\pi^+\pi^-$. For all the plots, the blue region is for good events that pass the cut, the red region is the background events that are removed by the confidence level cut. Extra cuts for missing mass ($0.8 GeV < mm < 1.1 GeV$), coplanarity ($2.7 < |\delta(\phi)| < 3.5$) and vertex-z(-10.5 cm $<$ z $<$ -5.5 cm) are used after the confidence level cut.

141

6.3 Results and discussion

The polarization observables for the channel $\gamma n \rightarrow n\pi^+\pi^-$ that can be extracted from the G14 data set are the same as the channel of $\gamma p \rightarrow p\pi^+\pi^-$ in Chapter 5. The observables are the beam helicity asymmetry $I^\odot$, target polarization asymmetry P_z, and beam-target double polarization asymmetry $P_z^\odot$. The data from two run periods of G14 experiment are used in this study: gold2 and silver5. The gold2 data set has a deuteron polarization $P_D = 26.9\%$, the silver5 data set has a deuteron polarization of $P_D = -5.1\%$.

6.3.1 Beam Helicity Asymmetry $I^\odot$

The results for beam helicity asymmetry are shown in Figure 6.14. The results are compared with $I^\odot$ with the proton target. From the plots, it is noticed that the beam helicity asymmetries are very close for higher c.m. energies of 1850 MeV, 1950 MeV, 2050 MeV, and 2150 MeV, but for lower c.m. energies of 1650 MeV, 1750 MeV, the differences is significant. This observation indicates that at lower c.m. energies, the resonances are different between the double pion reaction using the proton target and the neutron target. From Figure 1.7 in the first Chapter, we notice that $F_{15}(1680)$ is missing for the single pion photon-production with a neutron target. This situation could happen in the double pion photo-production, and our observation of the difference of $I^\odot$ between the proton target and neutron target provides useful information for groups using PWA to check the model for double pion photo-production.

6.3.2 P_z and $P_z^\odot$

The results for beam helicity asymmetries are shown in Figure 6.15, and the results for beam target double asymmetries are shown in Figure 6.16. These two sets of plots show the comparison for P_z and $P_z^\odot$ for the reaction of double pion photo-production using a polarized proton target and a polarized neutron target respectively. For both targets, since the run period (silver5) for target polarization along -z direction has a very small target polarization: -5.1% for neutron, and -2.55% for proton, there are big error bars on the measurement of P_z and $P_z^\odot$, which make it hard for us to extract useful information from the measurement of these two observables.
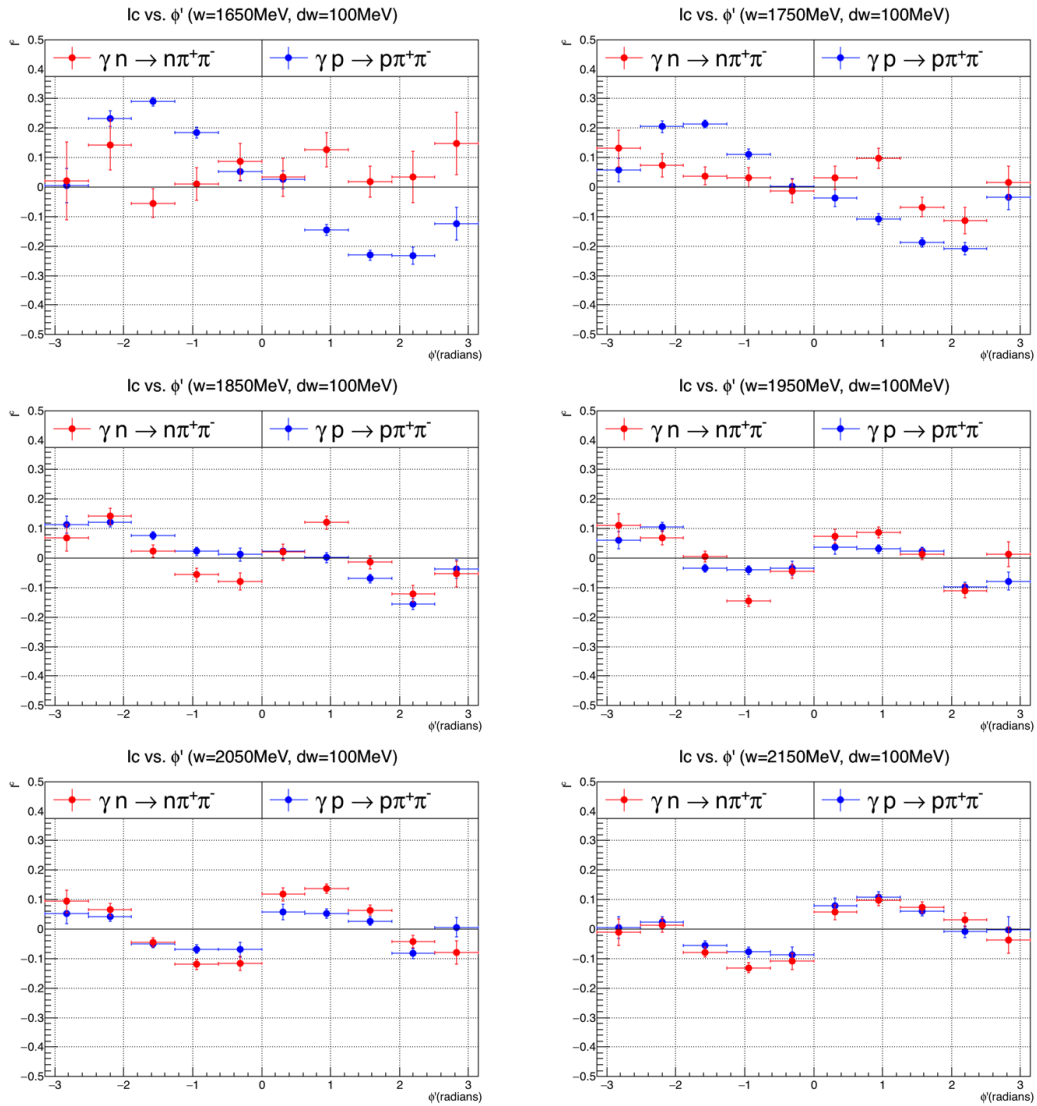
Figure 6.14: Beam helicity asymmetry $I^{\odot}$ vs. ϕ' for different center of momentum energy w.
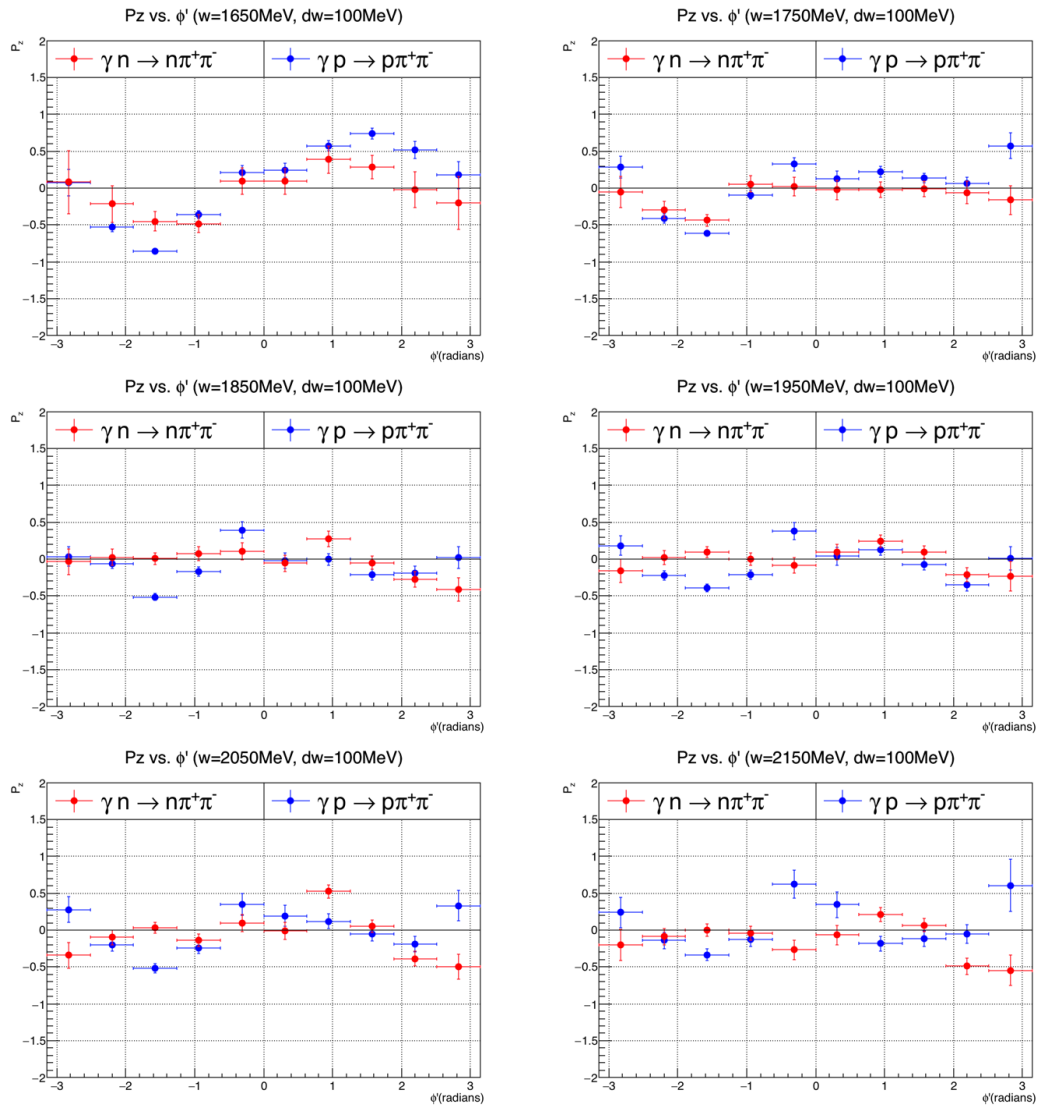
Figure 6.15: Target asymmetry P_z vs. ϕ' for different center of momentum energy w.
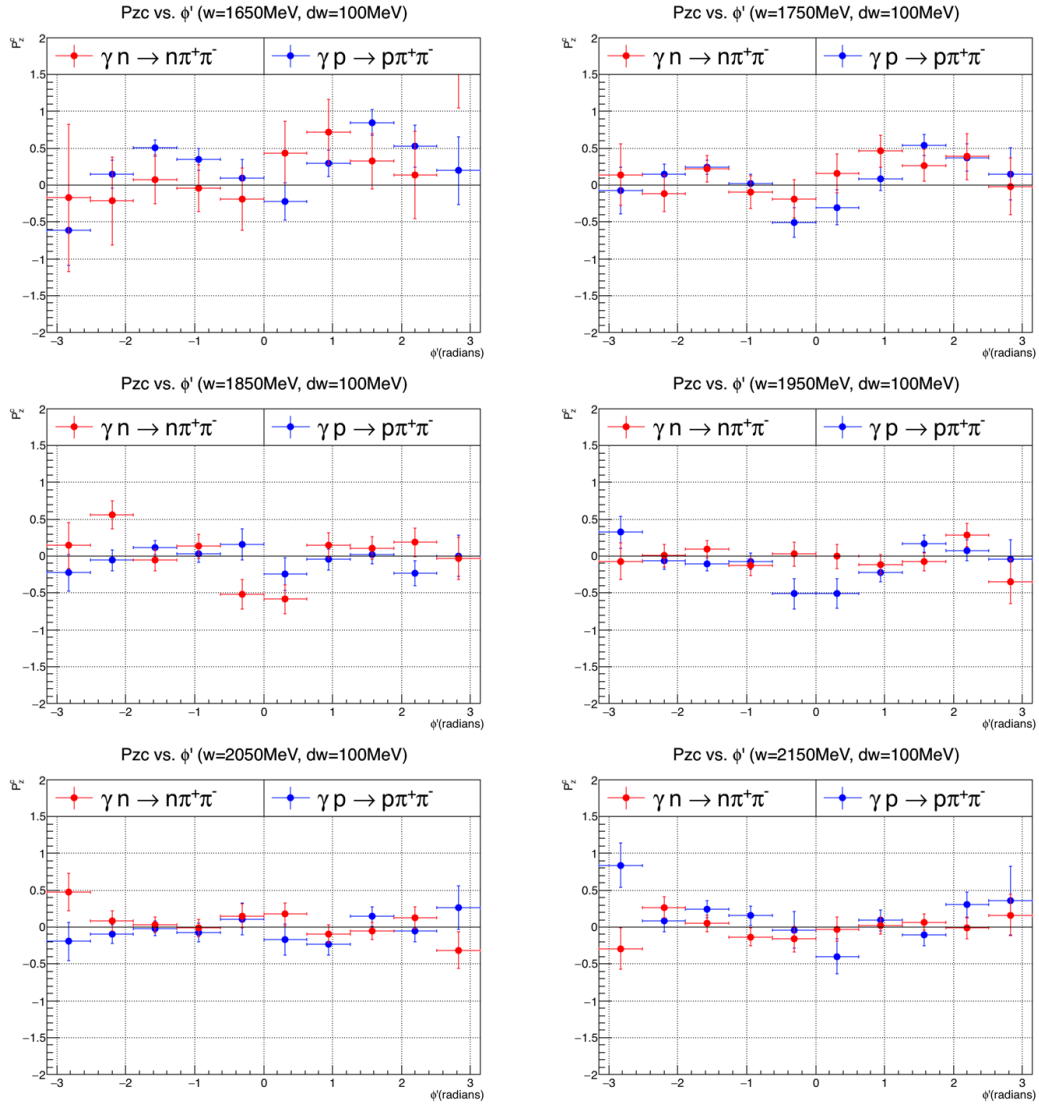
Figure 6.16: Beam target double asymmetry $P_z^{\odot}$ vs. ϕ' for different center of momentum energy w.

Chapter 7

Summary and Outlook

In this dissertation, we have introduced the first experiment using a polarized HD target at Jefferson Lab: the G14 experiment. In the experiment, a highly polarized photon beam and longitudinally polarized HD target were used. Both circularly polarized and linearly polarized photon beams were used in the experiment. Only the data set with circularly polarized beam has been analyzed in this study. The polarization of the photon beam was in a range from 76.2% to 88.8% depending on different run periods, the energy of the photon beam covers a range from 0.5 GeV to 2.2 GeV. During the circularly polarized photon beam runs, two polarized targets were used. The first target (target 21a) was operated in both "+z" direction and "-z" direction, the deuteron was polarized as high as 25.60% for "+z" mode. However, in the "-z" mode, the polarization is only -5.1%. The second target (target gold2) was operated only in the "+z" direction, and it had a higher deuteron polarization of 26.78%. The final state particles of the reaction were detected by the nearly 3π CLAS detectors located in Hall B.

Polarization observables from three reaction channels have been analyzed. They are: $\gamma + n \rightarrow p + \pi^-$, $\gamma + p \rightarrow p + \pi^+ + \pi^-$, $\gamma + n \rightarrow n + \pi^+ + \pi^-$. In the analysis procedure, a new method to remove the background events has been developed based on kinematic fitting. And the confidence level cut has proved to be a powerful tool to select separate events of interest from background events.

In the single pion channel ($\gamma + n \rightarrow p + \pi^-$), the beam target double asymmetry E has been analyzed, this is the first measurement for this observable on the polarized neutron target, and will be used to solve the discrepancy between different PWA models in the high center of momentum energy region.

For the double pion channels, three polarizations are measured: $I^\odot, P_z, P_z^\odot$. The beam helicity asymmetry $I^\odot$ using a proton target has been compared with two earlier measurements (G1c and G9a), and the results are agree. However, it was found that $I^\odot$ is not uniform along $\cos\theta_{\pi\pi}$. Thus the integration along $\cos\theta_{\pi\pi}$ should be done in a different way than the previous two experiments have done. Using the new way of integration, some discrepancies have been found between the new results from G14 and the results from G1c and G9a. Thus we suggest that the results in G1c and G9a should be checked again using the new way of integration of $I^\odot$ along $\cos\theta_{\pi\pi}$.

The beam helicity asymmetry $I^\odot$ using a neutron target has also been measured. This is the first measurement of this observable. The results from proton and neutron targets for $I^\odot$ have been compared, and a big difference has been found for two center

of momentum energy bins: 1650 MeV and 1750 MeV. It is possible that the difference comes from the missing of $F_{15}(1680)$ resonance in the reaction on the neutron target. Confirmation will await a detailed coupled channel partial wave analysis. For the other two observables $P_z, P_z^{\odot}$, since an unexpected small target polarization was found for the data set of target polarization along "-z" direction, the results have big error bars and we could not extract useful information from these two observables.

For the study of hadron spectroscopy, significant progress in experiments habe been made over the last decade, especially for reactions using photon beams. The new experimental results have helped us get a better understanding of the hadron system in the medium energy region. However, many more experimental measurements need to be done in order to get the complete picture for hadron spectroscopy. Especially for reactions with more than one final state pion, there are very few data available. The reaction channels with more than one final state pion have bigger cross sections than the single pion reactions in the energy region where most of the "missing resonances" are (above 2 GeV). This fact gives this reaction a higher priority in the study of the "missing resonance problem". The double pion channel is very promising for us to find those missing resonances, thus more experiments addressing this reaction are necessary.

Appendices

Appendix A

NMR signal analysis

A.1 Steps to prepare the four signals

Step1: Phase rotation. Figure A.1 and A.2 show that x and y signals mix the absorption signal and dispersion signal; a phase rotation is needed to get pure absorption and dispersion signals.

Step2: Background subtraction. Figure A.4 shows that if the background signal of the y channel is not zero, the Kramer Kronig transformed signal will have a slope.

Step3: Kramer-Kronig transformation. After the phase rotation and background subtraction(Figure A.4) , 4 clean absorption signals (Figure A.5) are ready to deduce the polarization value.

A.2 Background subtraction

While most of the NMR measurements have very clean and flat background signals, there are some measurements which have irregular background signals due to electrical or mechanical noises. There are four types of background that need to be corrected. The first type is as shown in the previous section, in which the X and Y signals are shifted away from zero by a constant value.

The second type of background is that the background line is linear with a slope (Figure A.6), then the Kramer-Kronig transformed signal will have an exponential tail (Figure A.7). The corrected signals are shown in Figures A.8, A.9.

The third type of background is the background with a step function (Figure A.10), the background subtracted signal is shown in Figure A.11.

The fourth type of background is the background with sharp peaks (Figure A.12), the background subtracted signal is shown in Figure A.13.
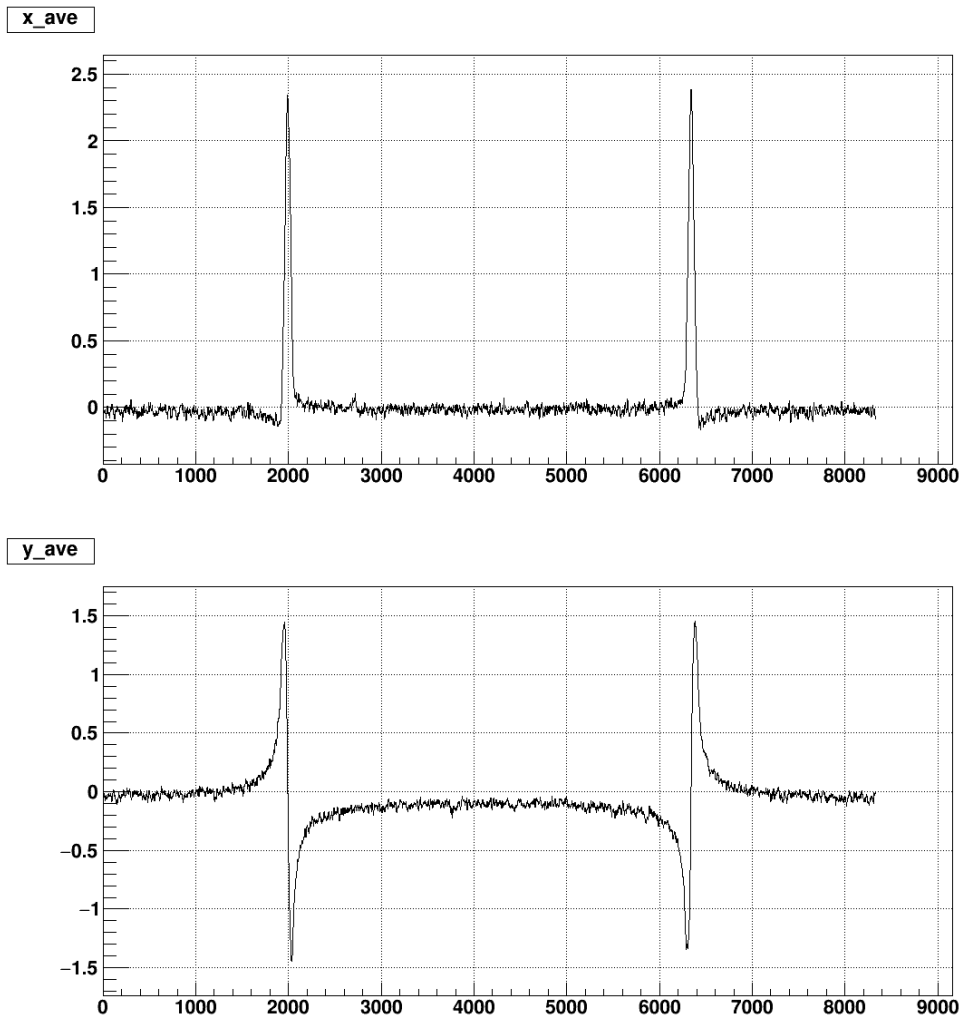
Figure A.1: Original signals from x- and y- channels of the NMR system.
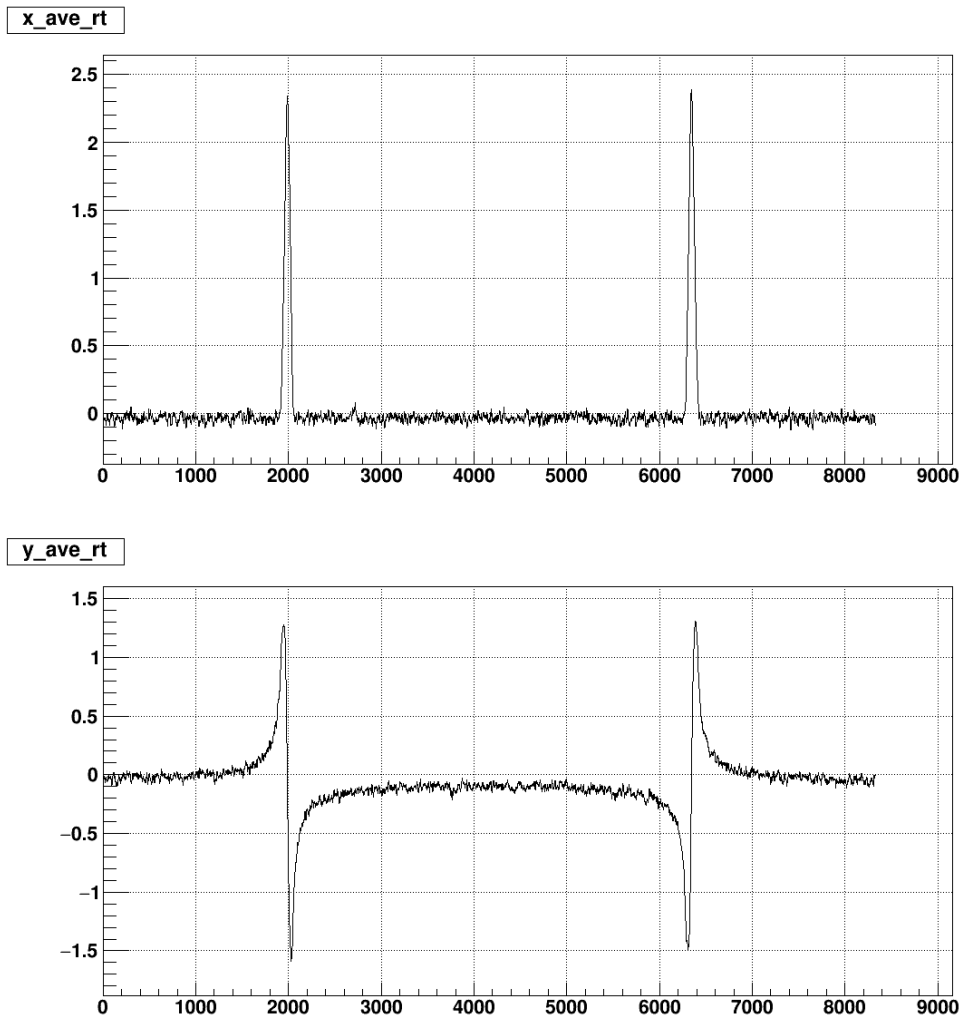
Figure A.2: Signals from x- and y- channels after phase roation.
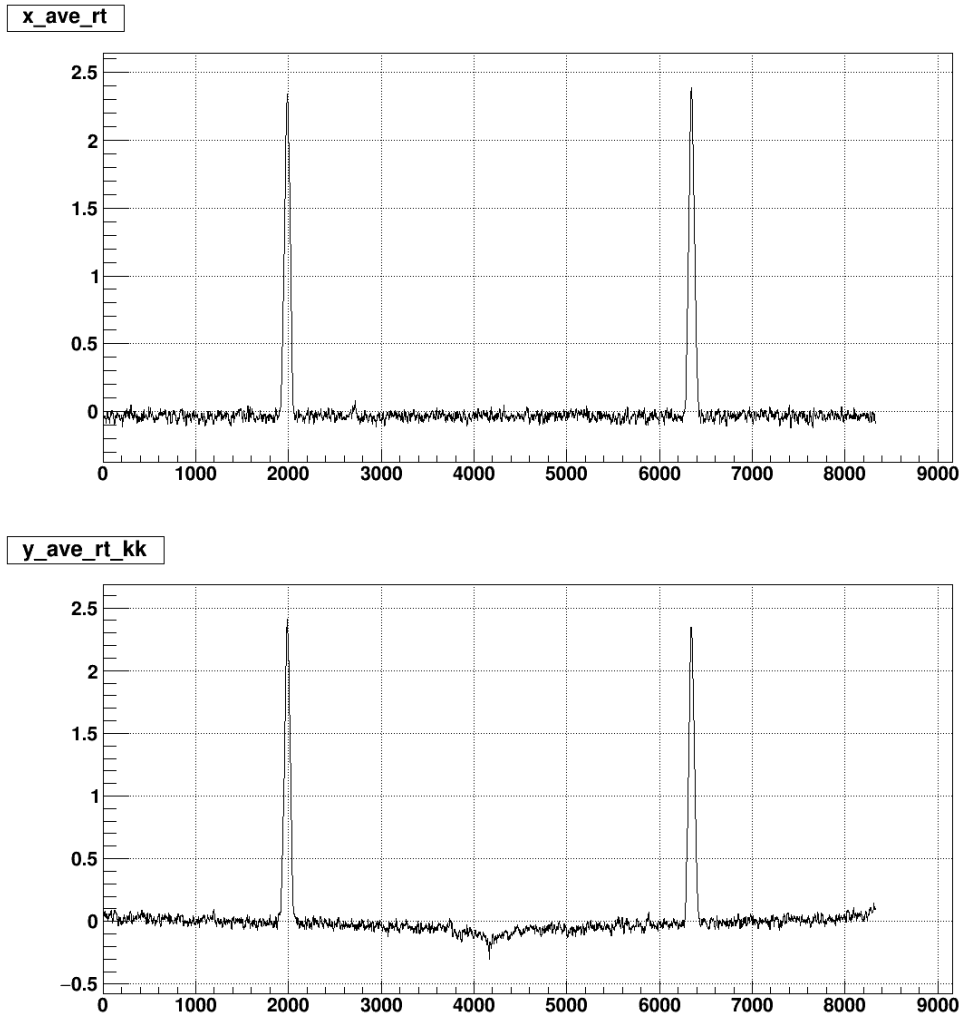
Figure A.3: Signals from x- and y- channels after phase rotation. y-channel signal has had the Kramer-Kronig transformation applied. There is a slope in the background, which is due to the nozero background of the y-channel signal before Kramer-Kronig transformation.

152
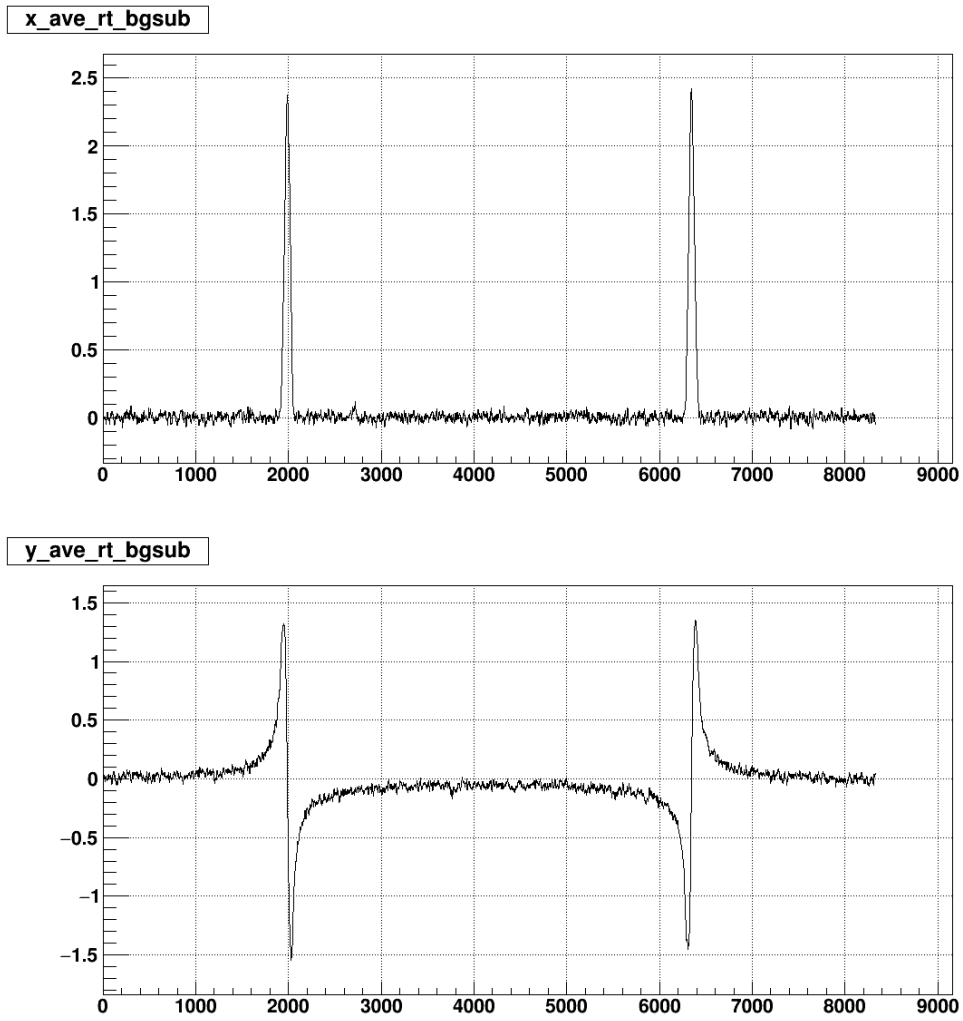
Figure A.4: Signals from x- and y- channels after phase rotation, the two signals have had background subtraction applied.
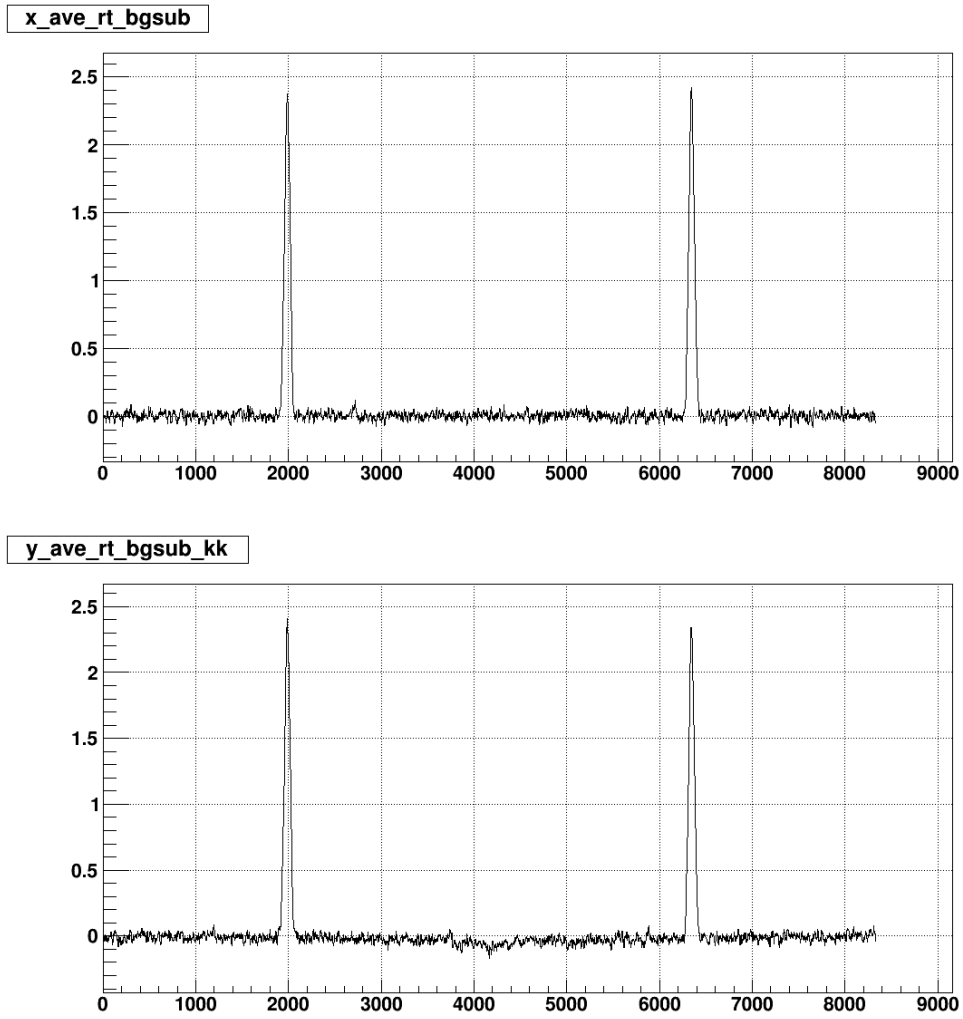
Figure A.5: Signals from x- and y- channels after phase rotation and background sub-traction, the background of the Kramer-Kronig transformed y-channel signal becomes flat.

154
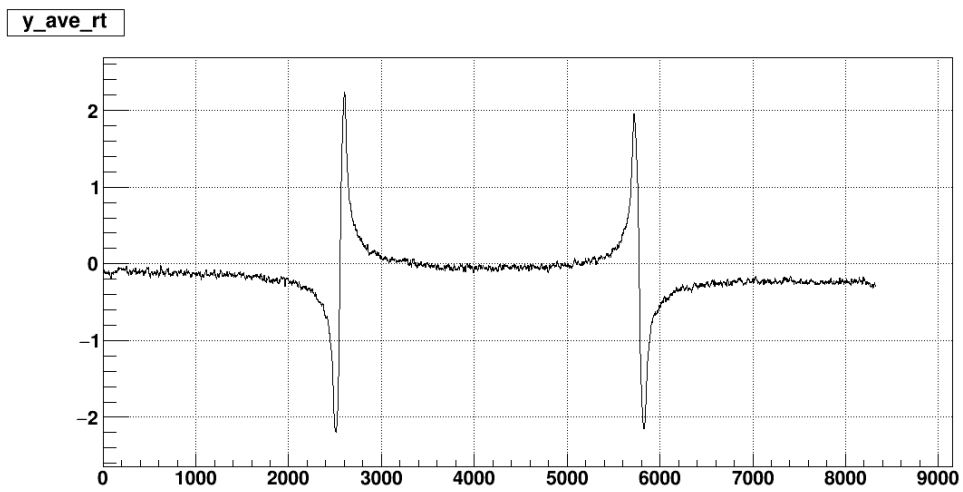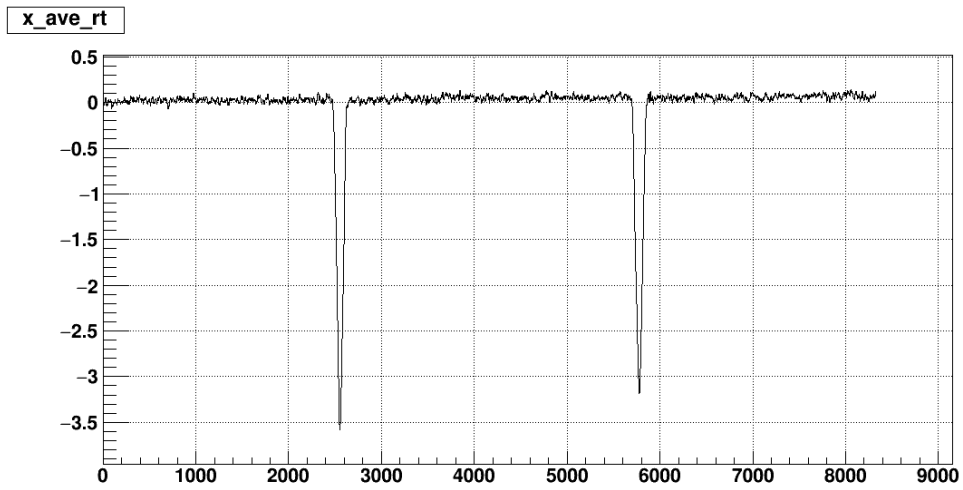
Figure A.6: Signals from x- and y- channels after phase rotation.
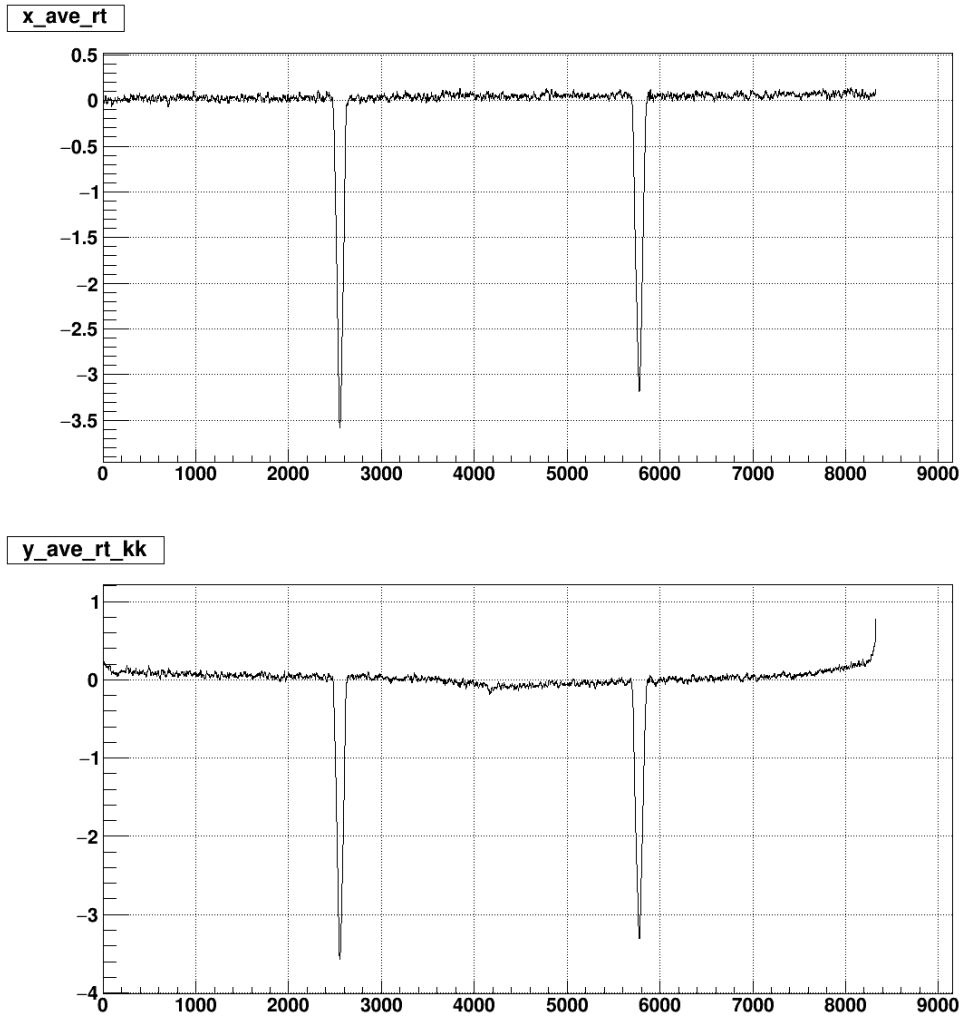
Figure A.7: Signals from x- and y- channels after phase rotation. The y-channel signal has had the Kramer-Kronig transformation applied. There is an exponential tail in the background, which is due to the linear background of the y-channel signal before the Kramer-Kronig transformation.
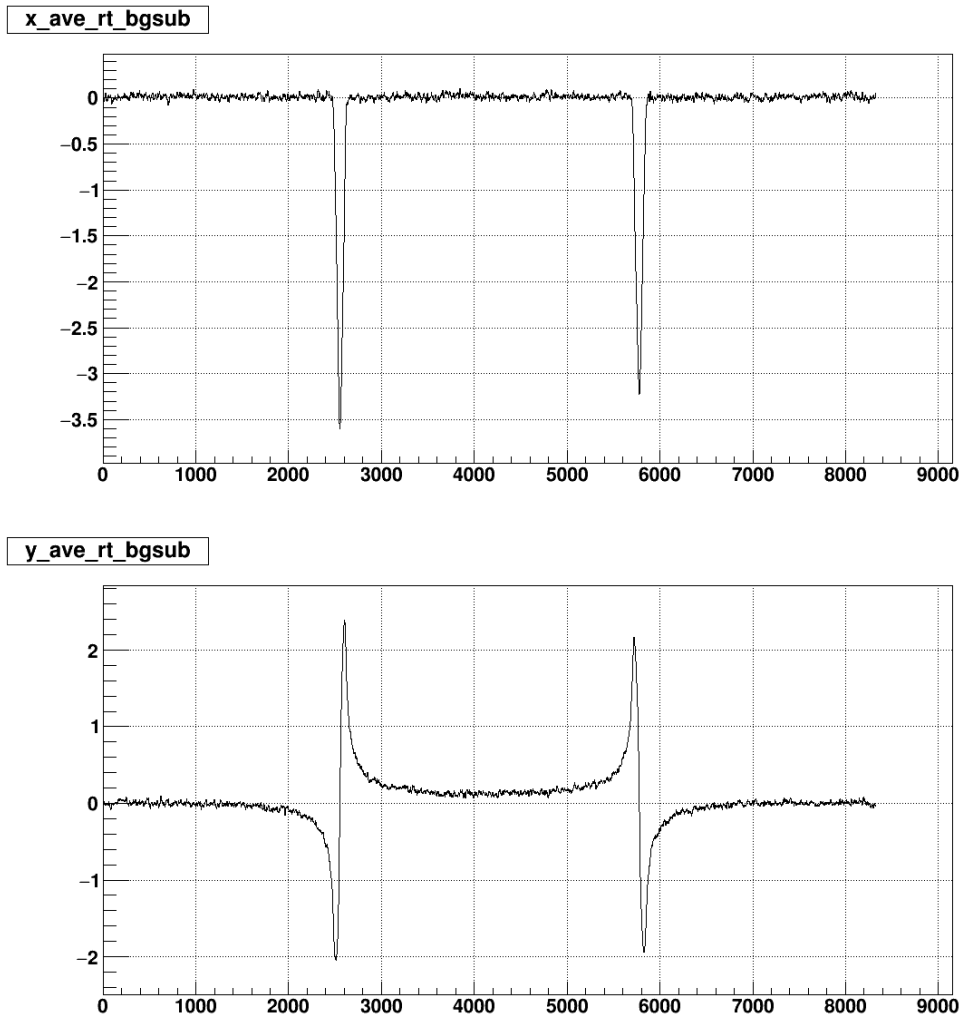
Figure A.8: Signals from x- and y- channels after phase rotation, the two signals have had background subtraction applied.
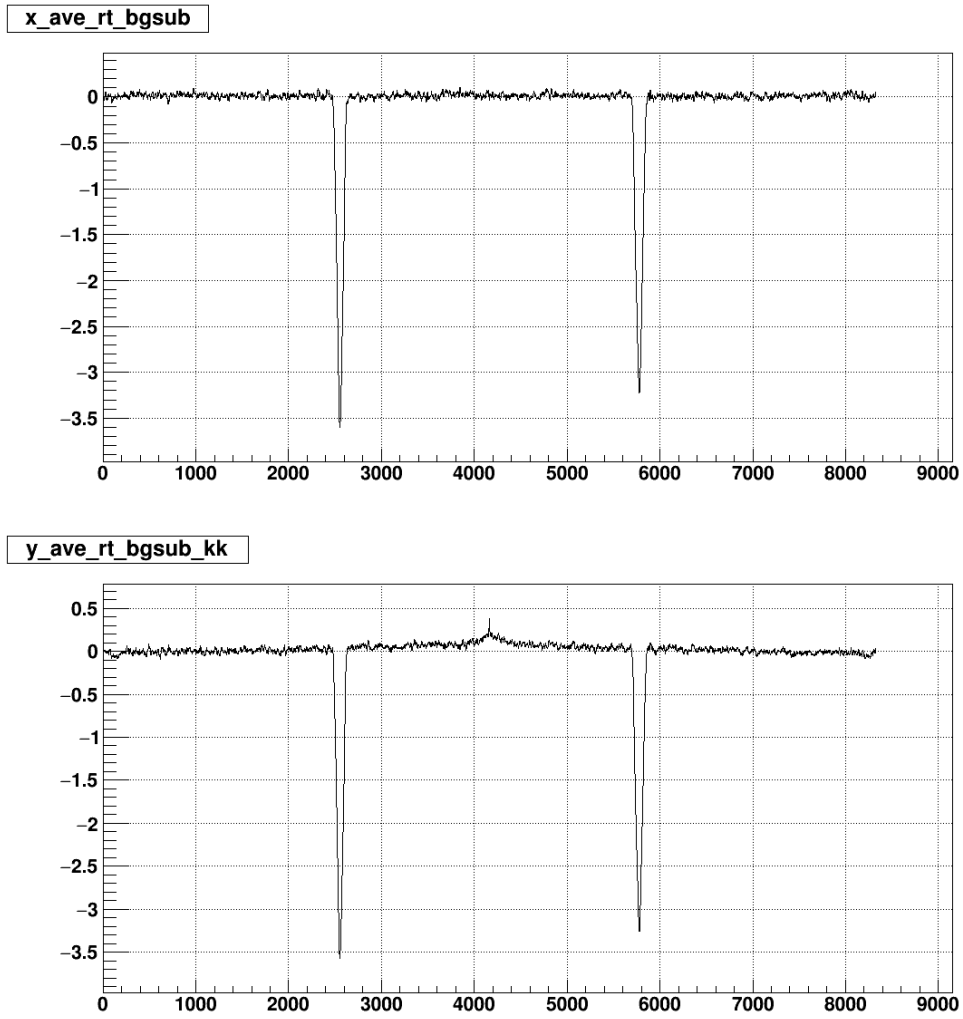
Figure A.9: Signals from x- and y- channels after phase rotation and background subtraction. The background of the Kramer-Kronig transformed y-channel signal becomes flat.

158
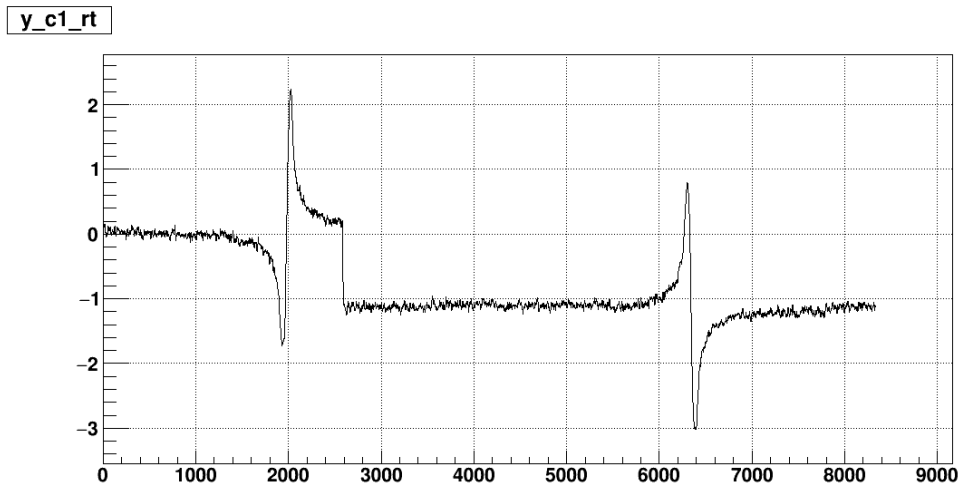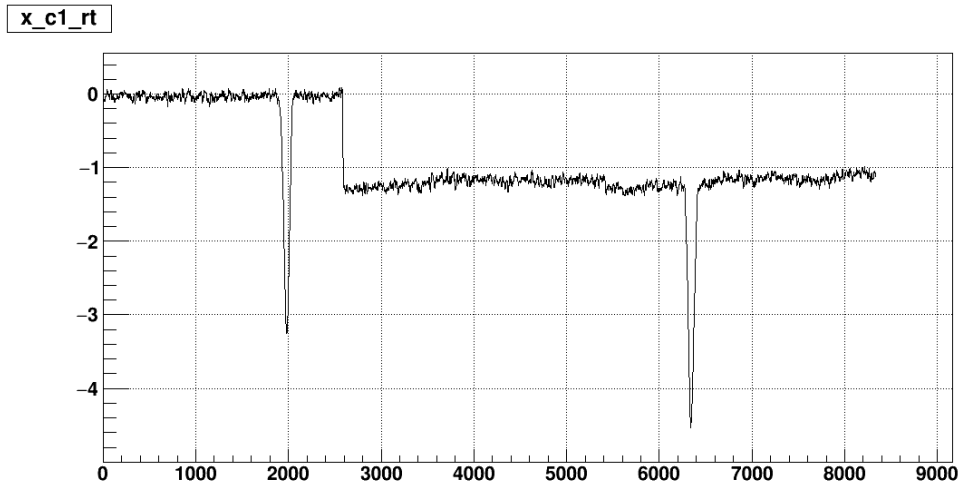
Figure A.10: Signal from x- and y- channels after phase rotation.
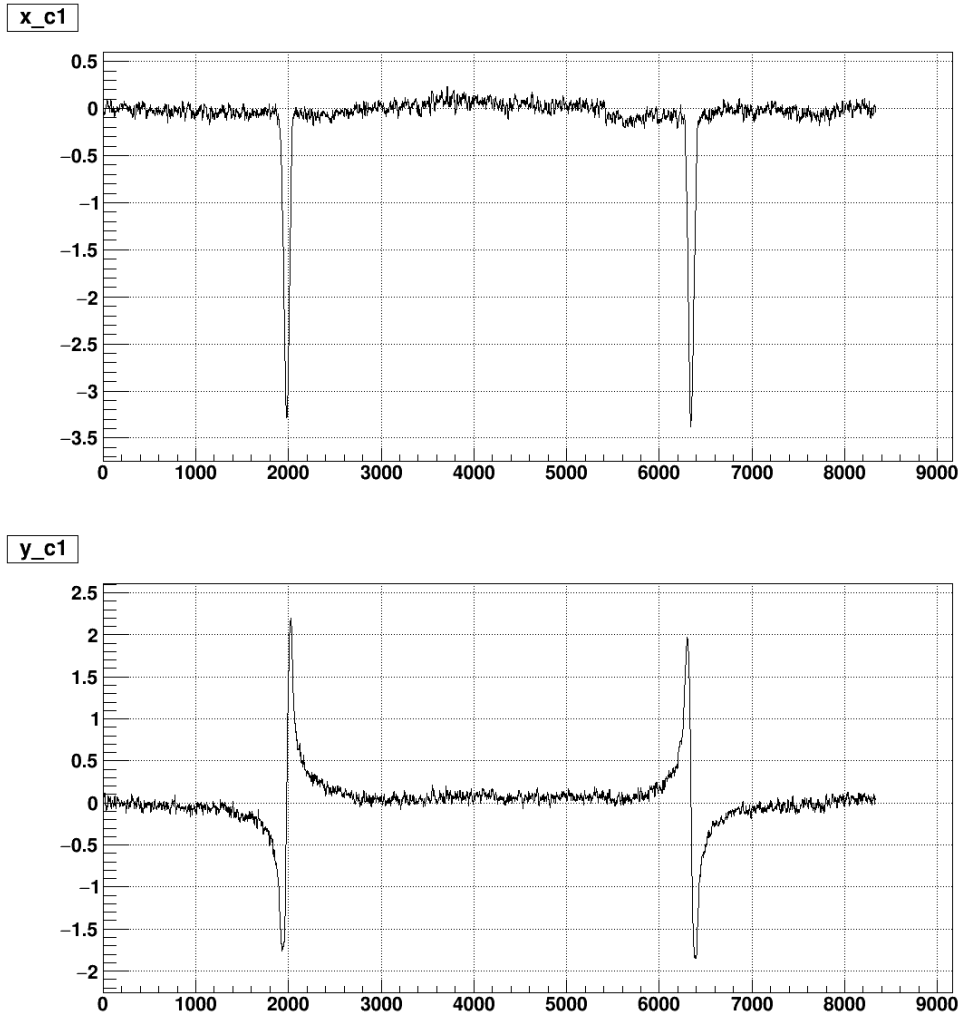
Figure A.11: Signals from x- and y- channels after phase rotation and background subtraction.
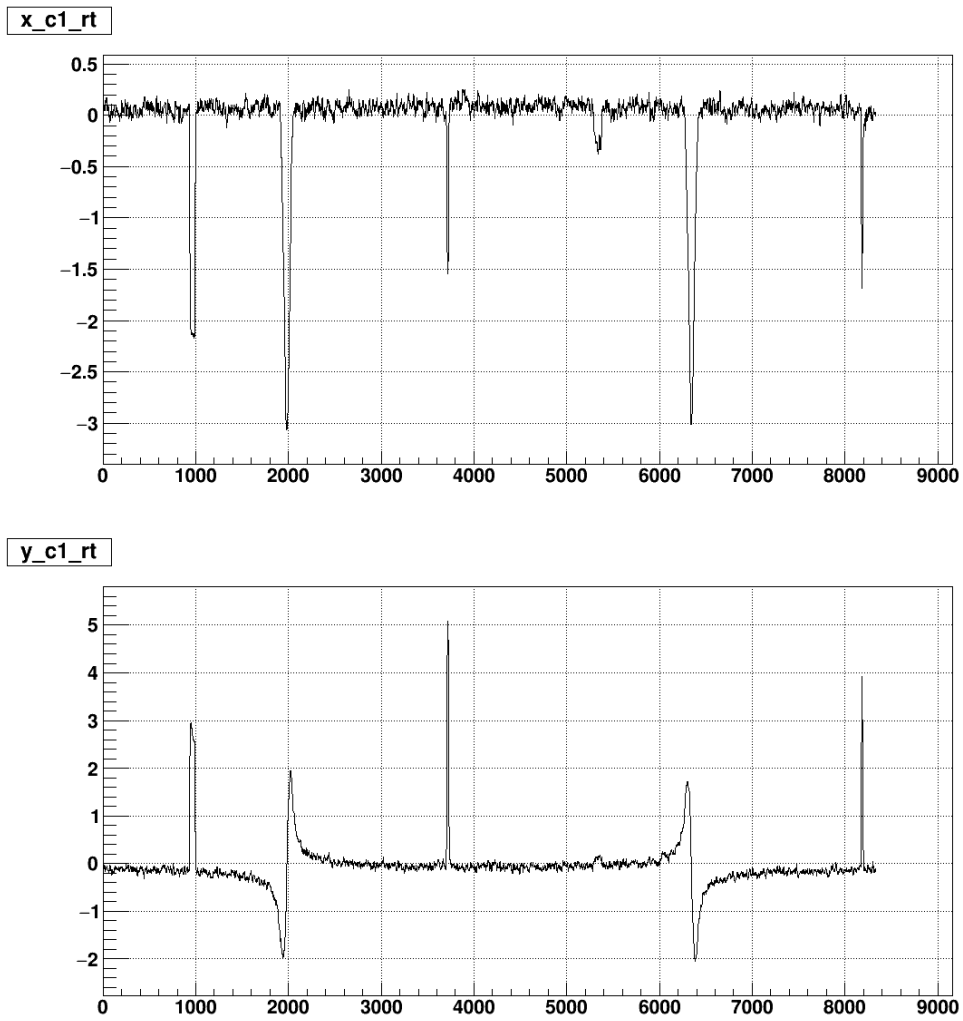
Figure A.12: Signals from x- and y- channels after phase rotation.
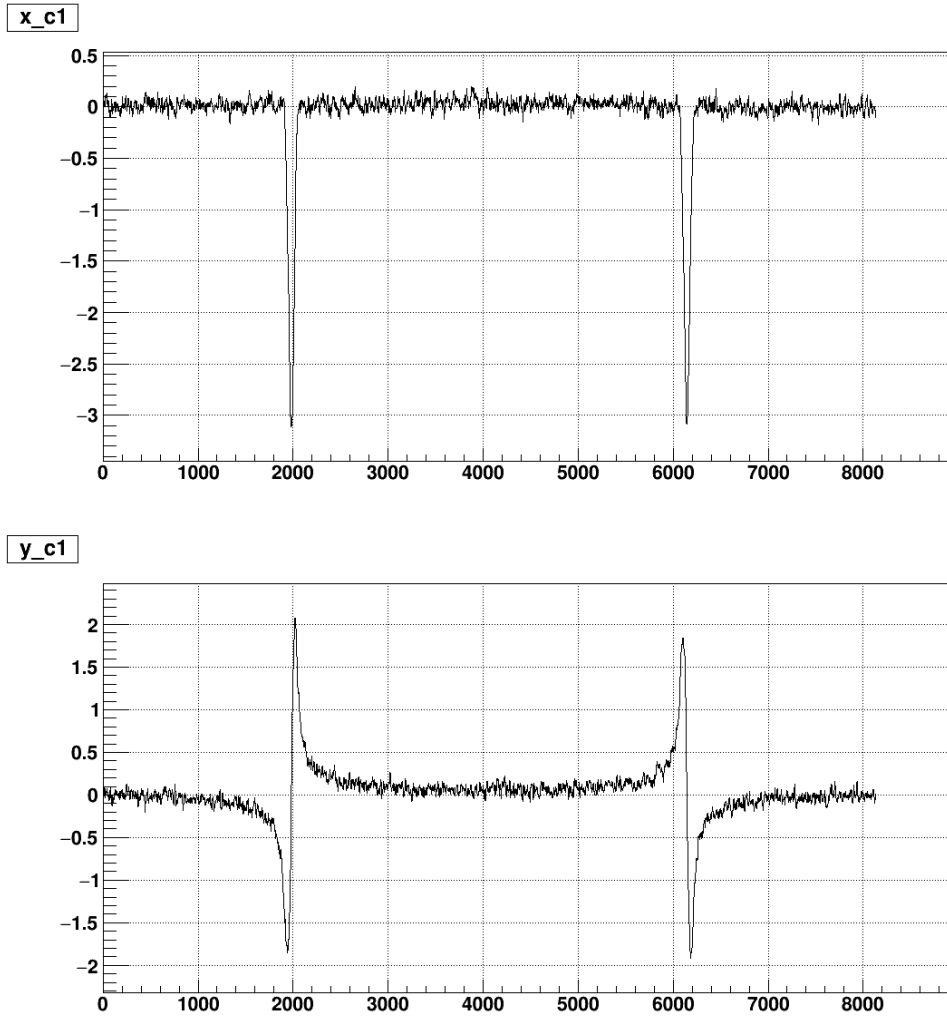
Figure A.13: Signals from x- and y- channels after phase rotation and background subtraction.

Appendix B

The effective mass of a nucleon inside the deuteron

The technique of reaction channel selection used in this study is 1-C kinematic fitting. One of the most important parameters used in this procedure is the effective mass of the nucleon inside deuteron. In the channel $\gamma(n) \to p\pi^-$, there are four constraint equations from the conservation of energy and momentum, and three unknown values for the target neutron's initial 3 momentum. A key component for the kinematic fitting to work is an accurate estimate of the effective mass for the quasi free neutron.

A straightforward solution to this problem is to use a Gaussian fit to find the centroid of the missing mass plot for this reaction, as in Figure B.1. However, as shown in the figure, the central values for the peaks from two different run periods are different. This difference is caused by an offset of the photon beam energy.
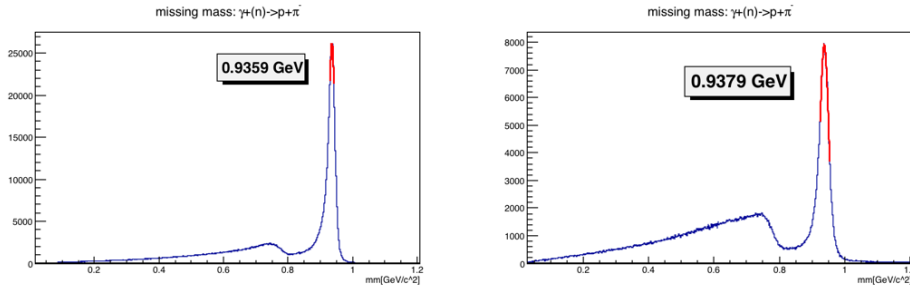

Figure B.1: Missing mass plot for the reaction of $\gamma(n) \to p\pi^-$ before the photon beam energy correction. The left plot is for the Silver1 period, the right plot is for the Gold2a period.

In order to correct the photon beam energy, the missing mass is plotted for the same reaction, but in a different way. Using the spectator model, the same reaction can be written as $\gamma D \to p(p)\pi^-$, with the p in parenthesis representing the spectator proton, which is not involved in the reaction. The spectator proton should have an on-shell mass of 0.9383 GeV. The missing mass plot for this reaction is shown in Figure B.2. Both of the central values for the missing mass peaks are not at 0.9383 GeV. This indicate the photon beam energy is not very accurate. For the Silver1 period, the photon beam energy should increase by 0.0030 GeV, and for the Gold2a period, the photon beam energy should

increase by 0.0082 GeV. The new missing mass plots for the reaction $\gamma D \to p(p)\pi^-$ after the photon beam correction are shown in Figure B.3.
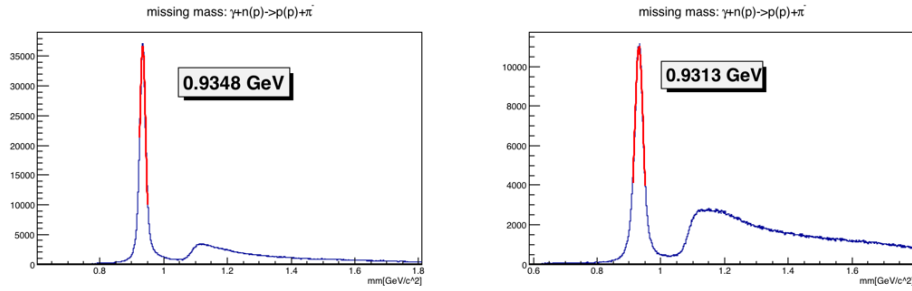
Figure B.2: Missing mass plot for the reaction of $\gamma D \to p(p)\pi^-$ before the photon beam energy correction. The left plot is for the Silver1 period, the right plot is for the Gold2a period.
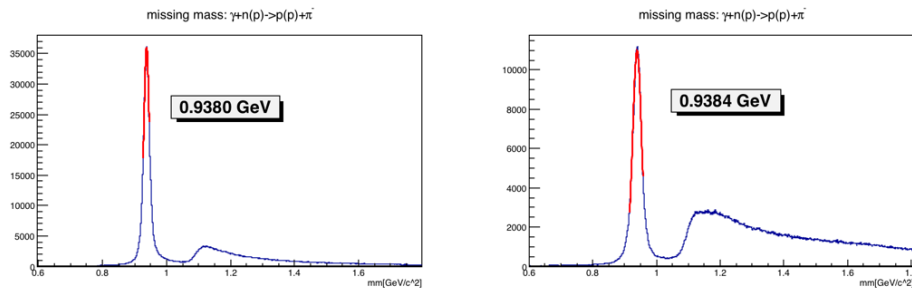
Figure B.3: Missing mass plot for the reaction of $\gamma D \to p(p)\pi^-$ after the photon beam energy correction. The left plot is for the Silver1 period, the right plot is for the Gold2a period.

The missing mass plots for the reaction after the photon beam energy correction is:

The energy correction for the photon beam and the calculated effective mass for quasi-free neutron for all circularly photon polarization run periods are shown in Table B.1. The average and statistical error for the effective mass is: $m^* = 0.9303 \pm 0.0003$ GeV.
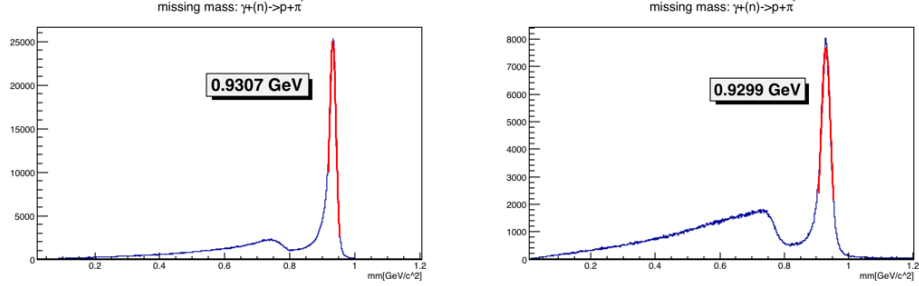
Figure B.4: Missing mass plot for the reaction of $\gamma(n) \to p\pi^-$ after photon beam energy correction. The left plot is for Silver1 period, the right plot is for Gold2a period.

Period	Δ E (GeV)	m^*(neutron) (GeV)
Silver1	0.003	0.9307
Silver2a	0.0015	0.9305
Silver2b	0.0015	0.9303
Silver3	0.0015	0.9303
Silver4	0.0015	0.9300
Silver5	-0.0015	0.9305
Gold2a	0.0082	0.9299
Gold2b	0.0082	0.9302

Table B.1: The photon beam energy offset and the effective mass of quasi free neutron for all circularly photon polarization run periods.

Appendix C

Empty target correction

As shown in Figure 2.31 in Chapter 2, there are aluminum wires inside the HD target cell. The channel selection procedures, especially the kinematic fitting will remove most of the events from the target cell, but there are still some background events that will pass the cuts. During the experiment, an empty target run was conducted for the study of the empty target subtraction. Figure C.1 gives the z vertex distribution for the Gold2a period and the Emptya period, the blue line in the target region on the right plot indicates that a small number of events from aluminum wires have passed the kinematic fitting cut.
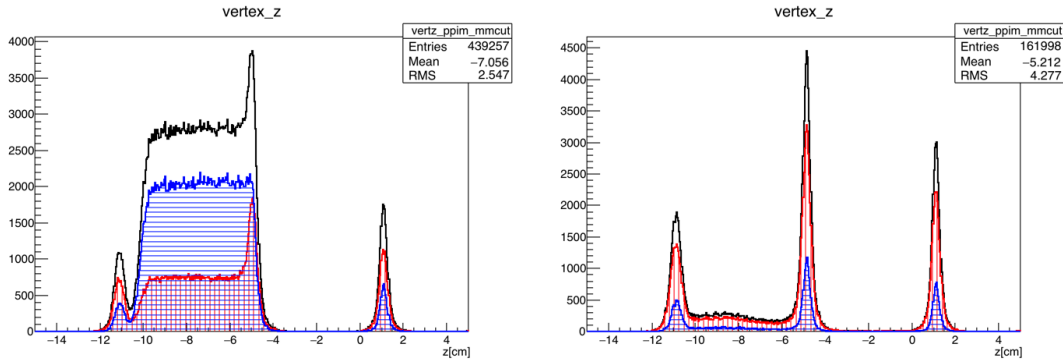

Figure C.1: Z vertex distribution for Gold2a(left) and Emptya(right). The black line is for all the events before the kinematic fitting cut, the blue line is for events that pass the cut, and the red line is for events fail the cut.

These background events will dilute the events from the HD target, and make the polarization observables smaller. And, this effect can be corrected using the following equation:

$$E = (1 + \frac{N_{empty}}{N_{HD}})E^{raw}, \tag{C.1}$$

where N_{empty} is for the events-normalized background events from the empty target run, and N_{HD} is for the events from the HD target.

A comparison of the z vertex distributions for the full target and empty target runs for different c.m. energy is shown in Figure C.2. It is noticed that the the ratios of events for the downstream Kel-F peak are different for different c.m. energies. Thus, an energy dependent background correction for the E asymmetry is needed.
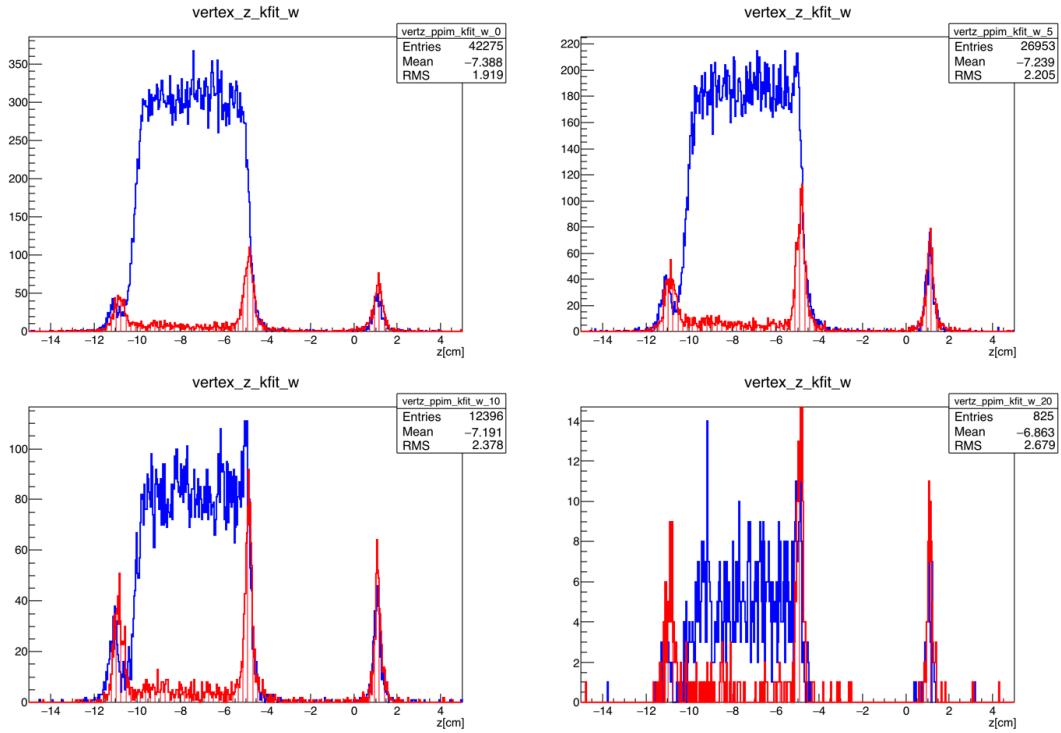
Figure C.2: Comparison of the z vertex between Gold2a(blue line) and Empty-a(red line) periods for different c.m. energies.

Figure C.3 shows the ratios of events from the full target run periods and the empty target run period for all circularly photon polarization runs.

The ratio of events from the empty target run and full target runs in the target region (-10.5 cm < z < -5.5 cm) can be obtained by using the scale constant from Figure C.3. For Gold2a and Gold2b periods, the fact that the target contained only 70% as many aluminum wires must be included in the calculation. The results are shown in Figure C.4.
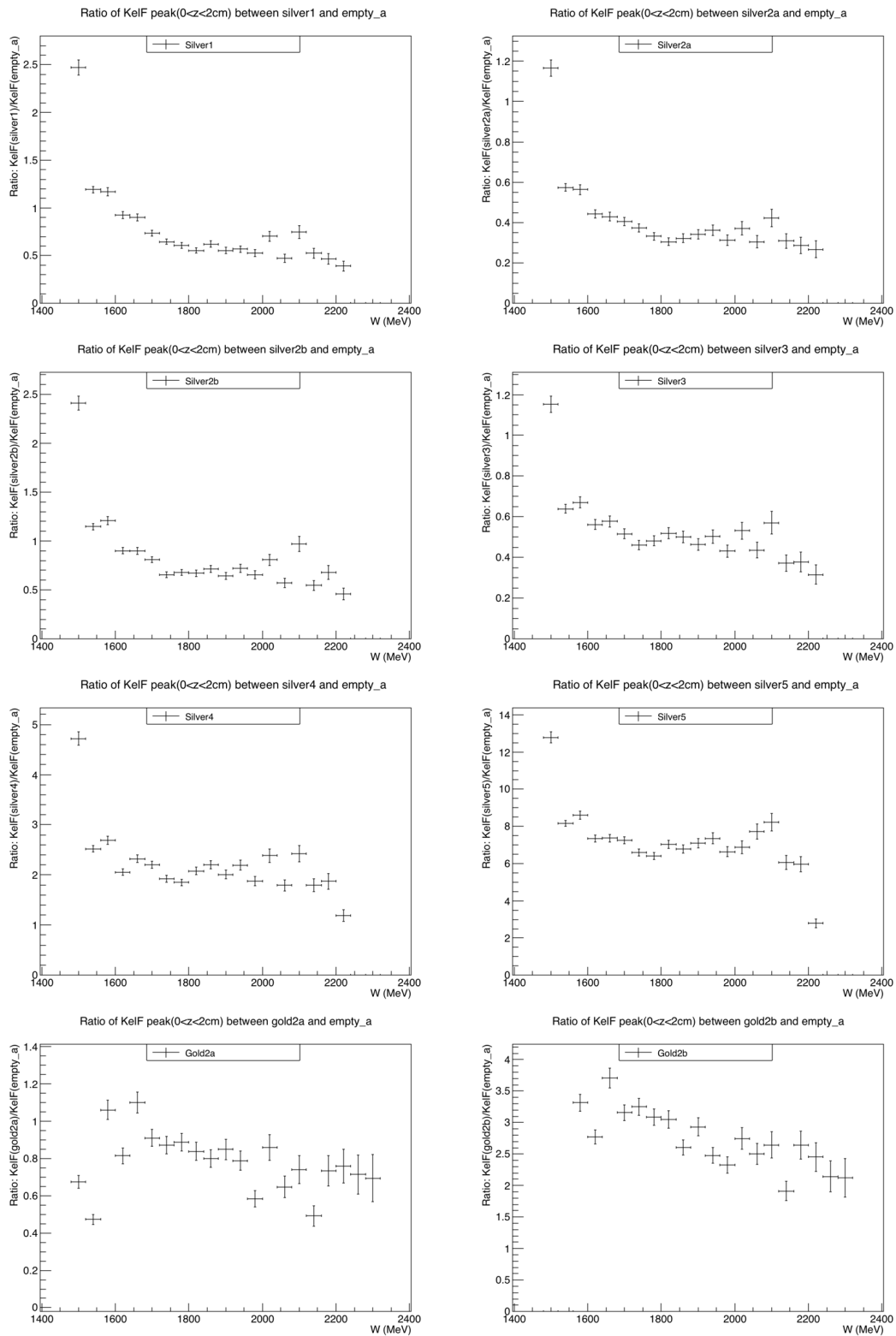
Figure C.3: Ratio vs. W(c.m.) for different run periods. Ratio = KelF(full target runs)/KelF(empty target runs)
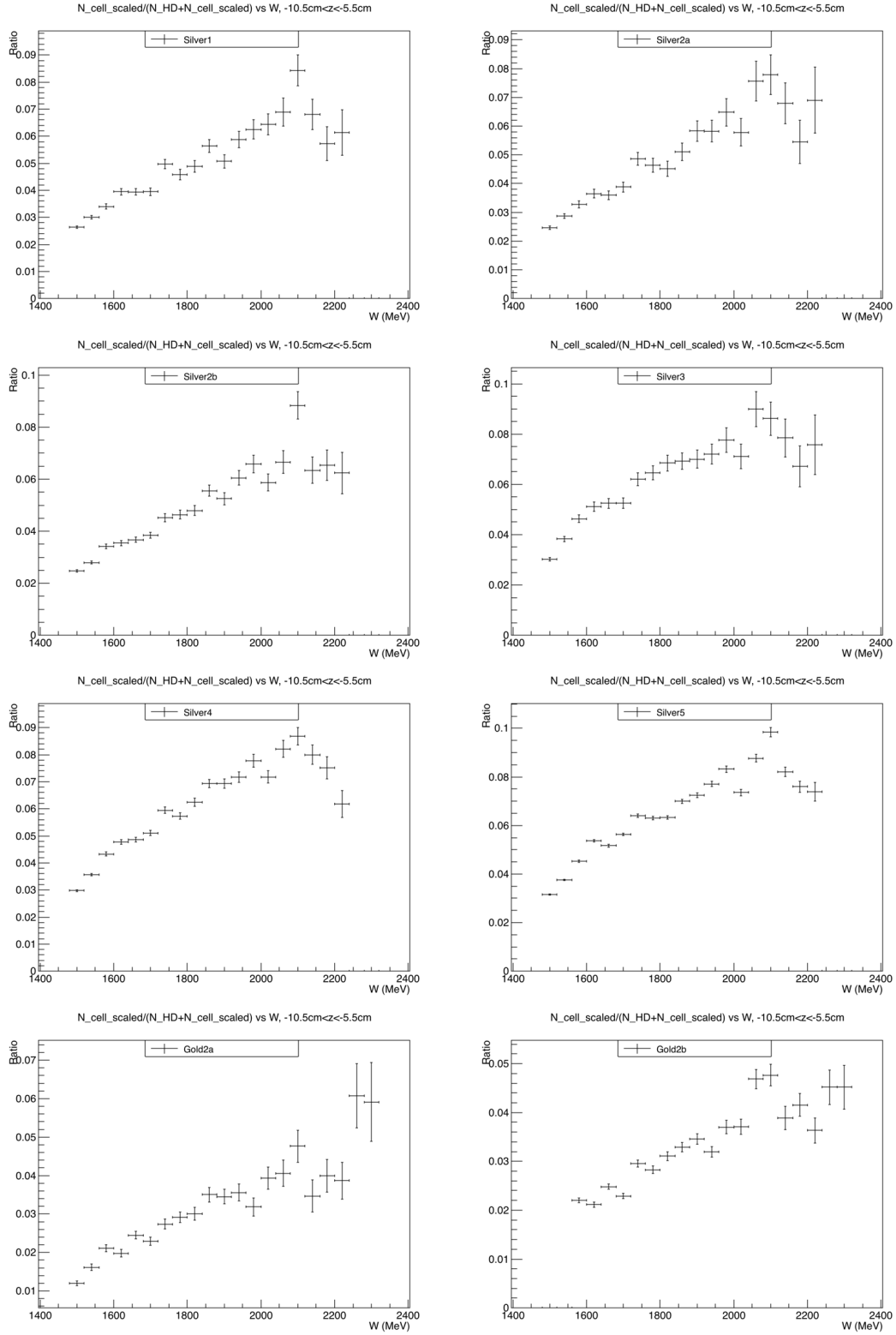
Figure C.4: Ratio vs. W(c.m.) for different run periods. Ratio $= \frac{N_{cell}}{(N_{HD}+N_{cell})}$, where N_{cell} is the scaled number of events from the empty target, N_{HD} is the number of events from the HD.

169

Bibliography

[1] C. Amsler, T. DeGrand, and B. Krusche, Review of quark model. The Review of Particle Physics (2014).

[2] S. Capstick and W. Roberts, Prog. Part. Nucl. Phys. 45, 241 (2000).

[3] N. Isgur and G. Karl, Phys. Lett. 72B, 109 (1977); 74B 353 (1978); Phys. Rev. D 18, 4187 (1978);N. Isgur and G. Karl, Phys. Rev. D 19, 2653 (1979).

[4] S. Capstick and N. Isgur, Phys. Rev. D 34,2809 (1986); S. Capstick and W. Roberts, Phys. Rev. D 47, 1994 (1993).

[5] R. Bijker et al., Ann. of. Phys. 236 69 (1994).

[6] M. Ferraris, M.M. Giannini, M. Pizzo, E. Santopinto and L. Tiator, Phys. Lett. B364, 231

[7] L. Ya. Glozman and D.O. Riska, Phys. Rep. C268, 263 (1996); L. Ya. Glozman, W. Plessas, K. Varga, R.F. Wagenbrunn, Phys. Rev. D 58, 094030 (1998).

[8] U. Loring, K. Kretzschmar, B. Ch. Metsch, H. R. Petry, Eur. Phys. J. A10, 309 (2001); U. Loring, B.Ch. Metsch, H. R. Petry, Eur. Phys. J. A10, 395 (2001); U. Loring, B.Ch. Metsch, and H. R. Petry, Eur. Phys. J. A10, 447 (2001).

[9] M. Anselmino et al. Rev. Mod. Phys. 65, 1199 (1993).

[10] B. Krusche and S. Schadmand. Study of Non-Strange Baryon resonances with Meson Photoproduction. Progress in Particle and Nuclear Physics 5, 399-485 (2003).

[11] G.F. Chew, M.L. Goldberger, F.E. Low, and Y. Nambu, Phys. Rev. 106, 1345 (1957).

[12] R.L. Walker, Phys. Rev. 182, 1729 (1969) .

[13] http://pwa.hiskp.uni-bonn.de

[14] http://portal.kph.uni-mainz.de/MAID/

[15] http://gwdac.phys.gwu.edu

[16] Igor Strakovsky. Radiative Decay Width of Neutral non-Strange Baryons from PWA. DMHPFP, Messian Italy, Sep. 2014.

[17] K.M. Watson, Phys. rev. 85, 852 (1952).

[18] M. Jacob and G.C. Wick. Ann. Phys. (N. Y.) 7, 404 (1959).

[19] A. M. Sandorfi, S Hoblit, H Kamano, T-S H Lee. Determining pseudoscalar meson photoproduction amplitudes from complete experiments. J. Phys. G: Nucl Part. Phys. 38, 053001 (2011) .

[20] S.Strauch, B.I Berman and the CLAS collaboration. Beam-Helicity Asymmetries in Double-Charged-Pion Photoproduction on the Proton. Phys. ReV. Lett 95, 162003 (2005).

[21] Sungkyun Park. Measurement of polarization observables in $\gamma p \to p\pi^+\pi^-$ using circular beam and longitudinal target polarization and the CLAS spectrometer at Jefferson Laboratory. PhD thesis (2013).

[22] C. Hanretty. Measurement of the polarization observables I^s and I^c for $\gamma p \to p\pi^+\pi^-$ using the CLAS spectrometer. PhD thesis (2011).

[23] A. Fix and H. Arenhovel. Double pion photoproduction on nucleon and deuteron. Eur. Phys. J. A 25, 115 (2005).

[24] W. Roberts and T. Oed. Polarization observables for two-pion production off the nucleon. Phys. Rev. C 71, 055201 (2005).

[25] Bonn-Gatchina partial wave analysis: search for missing baryon states. A. Sarantsev, Excited QCD 2010, Poprad, Slovakia.

[26] Bonn-Gatchina partial wave analysis. Comparison of the K-matrix and D-matrix (N/D based) methods. A. Sarantsev, PWA 2012, Beijing, China.

[27] https://www.flickr.com/photos/jeffersonlab.

[28] https://www.jlab.org.

[29] B. A. Mecking et al.The CEBAF Large Acceptance Spectrometer (CLAS). Nucl. Instrum. Meth. A 503, 513 (2003).

[30] M. Crofford et al. The RF System for the CEBAF Polarized Photoinjector. Technical Report, Thomas Jefferson National Accelerator Facility (1993).

[31] J. Grames et al. "Polarized Electron Sources @ JLAB"JLab Summer Science Series. July 7th, 2008.

[32] Subashini De Silva, Superconducting Parallel-Bar Deflecting/Crabbing Cavity Development and its Applications. Technical Report, Old Dominion University (2012).

[33] D.I. Sober, et al. The bremsstrahlung tagged photon beam in Hall B at JLab. Nucl. Instrum. Meth. A 440, 263 (2000).

[34] H. Olsen, L.C. Maximon. Photon and Electron Polarization in High-Energy Bremsstrahlung and Pair Production with Screening. Phys. Rev. 114, 887 (1959).

[35] F.J. Klein, et al. The Coherent Bremsstrahlung Facility in Hall B at Jefferson Lab (2005).

[36] F.A. Natter et al., Monte Carlo simulation and analytical calculation of coherent bremsstrahlung and its polarization. Nucl. Instr. and Meth. B 211, 465 (2003).

[37] Y.G. Sharabian, et al. A new highly segmented start counter for the CLAS detector. Nucl. Instr. and Meth. A 556, 246 (2006).

[38] E.S. Smith, et al. The time-of-flight system for CLAS. Nucl. Instr. and Meth. A 432 (1999) 265.

[39] M.Amarian, et al. The CLAS forward electromagnetic calorimeter. Nucl. Instr. and Meth. A 460, 239 (2001).

[40] A. Honig, Q. Fan, X. Wei, A. M. Sandorfi, C. S. Whisnant. New investigations of polarized solid HD targets. Nucl. Instrum. Meth. A 356, 39-46 (1995).

[41] Xiangdong Wei. HDice, the Polarized Solid HD Target in the Frozen Spin Mode for Experiments with CLAS. SPIN2012 (2012).

[42] C.E. Thorn, priv. comm.

[43] A. Deur. HD target PD polarimetry for 2011 (First batch of HD cells), CLAS notes (2011).

[44] Isaac F. Silvera. The solid molecular hydrogens in the condensed phase: Fundamentals and static properties. Rev. of Mod. Phys. Vol. 52. 393 (1980).

[45] Adalbert Farkas. Orthohydrogen, Parahydrogen and Heavy Hydrogen (1935).

[46] A. Honig and H. Mano. Enhanced nuclear polarization of D in solid HD. Phys. Rev. B 14 (5) 1858 (1976).

[47] Christopher M. Bade. RF methods to increase deuteron polarization in HD targets and NMR spin-polarization analysis at LEGS. (2006)

[48] C.D. Bass, et al. A portable cryostat for the cold transfer of polarized solid HD targets: HDice-I. Nucl. Instr. and Meth. A 737, 107 (2014).

[49] Vivien Laine. Polarimetry of the polarized hydrogen deuteride HDice target under an electron beam (2013).

[50] http://clasweb.jlab.org/bos/browsebos.php.

[51] A.G. Frodesen, O. Skjeggestad, Probability and Statistics in Particle Physics (1979).

[52] M. Williams, C.A. Meyer, "Kinematic Fitting in CLAS", CLAS-NOTE 2003-017 (2003).

[53] Dustin Keller, U-Spin Symmetry Test of the Σ^{*+} Electromagnetic Decay (2010).

[54] Dustin Keller, Techniques in Kinematic Fitting, CLAS-NOTE 2010-015 (2010).

[55] E. Pasyuk, "The CLAS ELOSS package", CLAS-NOTE 2007-016, the package is available from CLAS CVS repository.

[56] M. Williams, D. Applegate, C.A. Meyer, CLAS-NOTE 2004-017 (2004).

[57] A.M. Sandorfi, priv. comm..

[58] I. Zonta, priv. comm..